Darstellung und Charakterisierung von nanostrukturierten Eisen-basierten Übergangsmetall-Chalkogeniden mit Spinellstruktur für die Anwendung in der elektrokatalytischen Wasseroxidation und Kohlenstoffdioxidreduktion

Dissertation
zur Erlangung des akademischen Grades eines Doktors
der Naturwissenschaften (Dr. rer. nat.)

in der Bayreuther Graduiertenschule für Mathematik und Naturwissenschaften (BayNAT)
der Universität Bayreuth

vorgelegt von

Christopher Simon
aus Hadamar

Bayreuth, Juli 2022

Die vorliegende Arbeit wurde in der Zeit von Oktober 2018 bis September 2021 in Bayreuth am Lehrstuhl für Physikalische Chemie III unter Betreuung von Herrn Prof. Dr. Roland Marschall angefertigt.

Vollständiger Abdruck der von der Bayreuther Graduiertenschule für Mathematik und Naturwissenschaften (BayNAT) der Universität Bayreuth genehmigten Dissertation zur Erlangung des akademischen Grades eines Doktors der Naturwissenschaften (Dr. rer. nat.).

Dissertation eingereicht am: 22.07.2022

Zulassung durch das Leitungsgremium: 22.08.2022

Wissenschaftliches Kolloquium: 14.11.2022

Amtierender Direktor: Prof. Dr. Hans Keppler

Prüfungsausschuss:

Prof. Dr. Roland Marschall (Gutachter)
Prof. Dr. Birgit Weber (Gutachterin)
Prof. Dr. Matthias Breuning (Vorsitz)
JProf. Dr. Anna Schenk

Inhaltsverzeichnis

Abstract

Water splitting by electricity into molecular hydrogen and oxygen is a seminal approach for carbon-neutral and large-scale fuel production. However, the feasibility of electrochemical water splitting is still limited by the large overpotential of the oxygen evolution half reaction (OER). Nowadays, noble metal-based compounds like IrO_2 or RuO_2 are common electrocatalysts to reduce the kinetic barrier for the OER. They can be replaced by NiFe-based oxides such as spinel-type $NiFe_2O_4$. NiFe-based oxides can be synthesized from low-cost and abundant precursors. The following work will introduce two different strategies to prepare different single-phase $NiFe_2O_4$ nanomaterials: mesoporous $NiFe_2O_4$ (aqueous soft-templating method) and nanoparticulate $NiFe_2O_4$ (non-aqueous microwave synthesis).

In short, the soft-templating method makes use of a structure-directing agent (SDA) such as amphiphilic block-copolymer Pluronic® P-123 mixed with citric acid-complexed metal nitrate precursors to produce mesoporous $NiFe_2O_4$. The actual mesopore formation mechanism during subsequent thermal treatment was investigated systematically. Electron microscopy and nitrogen physisorption analysis reveal highly porous structures with highly accessible mesopores (diameters 5-12 nm) and specific surface areas up to 200 $m^2\ g^{-1}$.

The production of $NiFe_2O_4$ nanoparticles involves the dissolution of metal acetylacetonates in phenylethanol prior to microwave treatment at elevated temperatures. Applying this method, monodisperse $NiFe_2O_4$ nanoparticles in the size range of 4-11 nm with specific surface areas up to 250 $m^2\ g^{-1}$ can be synthesized easily within minutes. Due to the ultrasmall size of the particles, non-equilibrium conditions can be found. The spinel structure is significantly affected and deviates from the thermodynamically most stable inverse state, leading to changes in the degree of inversion, that in turn influence the material properties such as magnetism and conductivity, which was examined in detail by Mössbauer spectroscopy and magnetic measurements. Both $NiFe_2O_4$ nanopowders were finally tested for their abilities to electrocatalyze the oxygen evolution reaction in alkaline solution. By keeping the elemental composition of $NiFe_2O_4$ precisely constant, the influence of key parameters such as morphology, crystallinity, and degree of inversion on the electrocatalytic performance could be studied in detail. With the most active sample (7 nm nanoparticles), the overpotential for OER is successfully lowered to 380 mV, compared to 410 mV measured with optimized mesoporous $NiFe_2O_4$.

Other Fe-containing spinel oxides are accessible *via* application of the introduced microwave synthesis, which was illustrated exemplary for $MnFe_2O_4$.

Apart from water electrolysis, in times of rising carbon dioxide levels in the atmosphere, using electricity to convert the greenhouse gas into precious synthetic organic fuels such as carbon monoxide, methane, methanol, or formic acid (C_1-compounds) becomes another important matter in recent research. However, the realization of carbon dioxide electroreduction is still lacking due to practical issues. For instant, the solubility of carbon dioxide is low, limiting the reaction rate. Hydrogen evolution is a competing reaction, which often effects the selectivity for a certain C_1-component. Up to date, with the CO_2 reduction reaction (CO_2RR) requiring highly negative potentials, which also include overpotentials, the reaction is energy-intensive and therefore economically not feasible. Electrocatalysts can be used to significantly lower the overpotentials. Among the available materials, nature-inspired NiFe-based sulfides such as Ni_2FeS_4 as structural analogue to the carbon monoxide dehydrogenase are attractive candidates.

To prepare Ni_2FeS_4, a novel microwave synthesis was developed: prior to microwave treatment, parts of the organic solvent were displaced by benzyl mercaptane, which simultaneously acts as sulfur source. The resulting phase-pure Ni_2FeS_4 nanosheets with specific surface areas of 80 m^2 g^{-1} were applied as electrocatalyst for CO_2 reduction from neutral solution, evolving carbon monoxide and molecular hydrogen.

Kurzzusammenfassung

Die Elektrolyse von Wasser in Wasserstoff und Sauerstoff ist eine zukunftsträchtige Technologie zur nachhaltigen und großtechnischen Produktion von Brennstoffen. Allerdings ist die elektrochemische Wasserspaltung durch das hohe Überpotential der Sauerstoffentwicklung limitiert. Aktuell verwendete Elektrokatalysatoren zur Erniedrigung des Überpotentials, wie IrO_2 oder RuO_2, basieren jedoch auf dem Einsatz von kostspieligen Edelmetallen. Daher wird nach Alternativen gesucht, die zum Beispiel NiFe-basiert sein können. Solche Materialien, wie etwa $NiFe_2O_4$ mit Spinellstruktur, können unter niedrigem synthetischen Aufwand aus günstigen und gut verfügbaren Ausgangsstoffen hergestellt werden. Im Laufe der Arbeit werden zwei Strategien vorgestellt, um phasenreine $NiFe_2O_4$-Nanomaterialien zu synthetisieren: mesoporöses $NiFe_2O_4$ (wässrige Endotemplatsynthese) und $NiFe_2O_4$-Nanopartikel (nicht-wässrige Mikrowellensynthese).

Bei der wässrigen Endotemplatsynthese wird ein strukturgebendes Reagenz, wie das amphiphile Blockcopolymer Pluronic® P-123, eingesetzt, welches mit den durch Zitronensäure komplexierten Metallnitraten vermischt wird, um mesoporöses $NiFe_2O_4$ darzustellen. Der Mechanismus der Mesoporenbildung während der darauffolgenden Kalzinierung wurde zudem im Detail untersucht. Durch verschiedene Untersuchungsmethoden, inklusive Elektronenmikroskopie und Stickstoff-Physisorption, konnte bestätigt werden, dass es sich um hochporöse Strukturen mit gut zugänglichen Poren handelt. Die Mesoporen sind im Durchmesser 5-12 nm groß und es können spezifische Oberflächen bis zu 200 $m^2 g^{-1}$ realisiert werden.

Die Mikrowellensynthese zur Präparation von $NiFe_2O_4$-Nanopartikeln basiert auf den Metall-Acetylacetonaten, die vor der eigentlichen Temperaturbehandlung durch Aufheizen mit Mikrowellenstrahlung in Phenylethanol gelöst werden. Mit dieser Methode können monodisperse $NiFe_2O_4$-Nanopartikel schnell unter niedrigem synthetischen Aufwand mit Größen von 4-11 nm und spezifischen Oberflächen bis zu 250 $m^2 g^{-1}$ produziert werden. Im Fall solch kleiner Partikel liegt kein thermodynamisch stabiler Zustand vor. Daher weicht die Kationenverteilung in der Spinellstruktur von der thermodynamisch bevorzugten inversen Besetzung ab, was sich auf den sogenannten Inversionsgrad und auf die magnetischen Eigenschaften des Materials auswirkt. Um den Zusammenhang von Partikelgröße, Inversionsgrad und Magnetismus zu untersuchen, wurden Mössbauerspektren aufgenommen und Magnetmessungen durchgeführt. Die beiden hergestellten $NiFe_2O_4$-Nanopulver wurden als Elektrokatalysatoren für die alkalische Wasseroxidation getestet. Unter Beibehaltung der elementaren Zusammensetzung wurde der Einfluss von Schlüsselfaktoren, wie Morphologie, Kristallinität und Inversionsgrad, auf die Leistungsfähigkeit des Elektrokatalysators untersucht. Die aktivste Probe stellen die 7 nm großen $NiFe_2O_4$-Partikel dar, mit denen das Überpotential der Sauerstoffentwicklung auf 380 mV gesenkt werden kann. Im Vergleich dazu beträgt die Überspannung mit mesoporösem $NiFe_2O_4$ 410 mV.

Weiterhin konnte am Beispiel von $MnFe_2O_4$ festgestellt werden, dass die vorgestellte Mikrowellensynthese auch für andere eisenhaltige Spinelle anwendbar ist.

In Zeiten von steigenden Kohlenstoffdioxid-Konzentrationen in der Erdatmosphäre ist die CO_2-Elektroreduktion eine attraktive Methode, um das Treibhausgas in nutzbare synthetische organische Kraftstoffe umzuwandeln. Solche C_1-Brennstoffe sind zum Beispiel Kohlenstoffmonoxid, Methan, Methanol oder auch Ameisensäure. Die Elektroreduktion von Kohlenstoffdioxid wird allerdings aus praktischen Gründen noch nicht industriell umgesetzt. Ein Problem ist die schlechte Löslichkeit von CO_2 in Wasser, wodurch die Reaktionsrate stets niedrig ist.

Außerdem steht die Elektroreduktion von CO_2 bei den benötigten Potentialen in Konkurrenz zur Entstehung von Wasserstoff, was sich negativ auf die Produktselektivität für eine bestimmte C_1-Komponente auswirkt. Zudem sind bei der Elektroreduktion von Kohlenstoffdioxid stark negative Potentiale erforderlich. Durch die zusätzlich auftretenden Überpotentiale ist die Reaktion aktuell noch energieintensiv und unrentabel. Auch hier können Elektrokatalysatoren zur Senkung der Überpotentiale und zur Selektivitätssteuerung eingesetzt werden. Unter den verfügbaren Kandidaten sind NiFe-basierte Sulfide interessant, insbesondere das naturinspirierte Ni_2FeS_4 als strukturelles Analogon der Kohlenmonoxiddehydrogenase.

Um Ni_2FeS_4 herzustellen wurde in dieser Arbeit eine neuartige Synthese entwickelt. Dabei werden die Metallacetyl-Acetonate in einer Mischung aus Phenylethanol und Benzylmercaptan, welches simultan als Schwefel-Quelle dient, gelöst, bevor die Lösung durch Mikrowellenstrahlung aufgeheizt wird. Die resultierenden Ni_2FeS_4-Nanoschichten weisen eine spezifische Oberfläche von 80 m^2 g^{-1} auf und wurden erfolgreich als Elektrokatalysator in der Reduktion von CO_2 unter neutralen Bedingungen eingesetzt. Dabei sind Kohlenstoffmonoxid und molekularer Wasserstoff als Hauptprodukte entstanden.

1. Einleitung

1.1. Motivation

Bis heute basiert die weltweite Energieversorgung auf der Verbrennung von fossilen Energieträgern. Hierbei sind insbesondere die Primärenergieträger Kohle, Erdöl sowie Erdgas zu nennen. **Abbildung 1** enthält eine Graphik des Unternehmens BP (ehemals *British Petroleum*), in dem der primäre Gesamtenergieverbrauch von 1965 bis 2019 dargestellt ist. Den Daten ist zu entnehmen, dass der weltweite Energiebedarf mindestens seit 1965 stetig ansteigt und dass die oben genannten Primärenergieträger die Grundlage für die Versorgung der Menschheit mit Energie bilden. In den fossilen Ressourcen sind allerdings große Mengen an Kohlenstoff gespeichert, sodass die Verbrennung die Freisetzung großer Mengen an Kohlenstoffdioxid (CO_2) bewirkt, welches in der Atmosphäre als Treibhausgas fungiert und stark zur menschengemachten globalen Erwärmung beiträgt.[1,2]

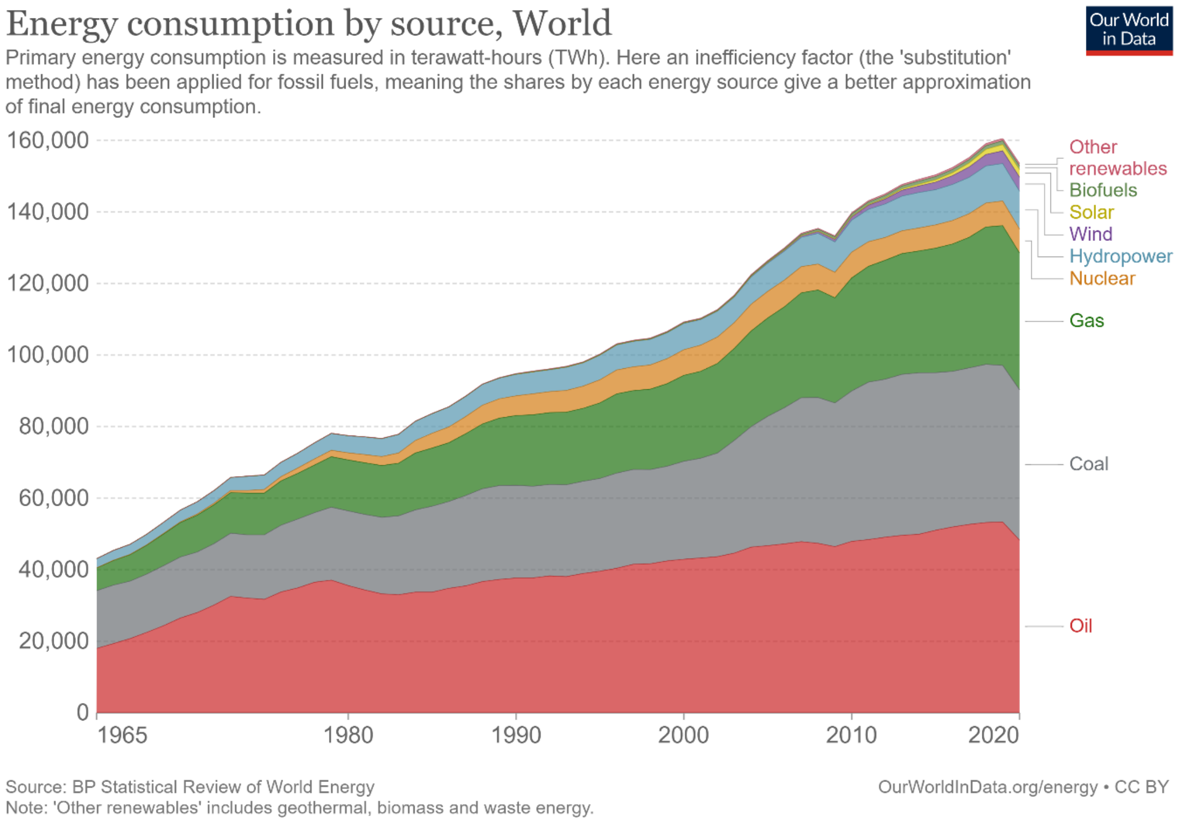

Energy consumption by source, World

Primary energy consumption is measured in terawatt-hours (TWh). Here an inefficiency factor (the 'substitution' method) has been applied for fossil fuels, meaning the shares by each energy source give a better approximation of final energy consumption.

Source: BP Statistical Review of World Energy

Note: 'Other renewables' includes geothermal, biomass and waste energy.

OurWorldInData.org/energy • CC BY

Abbildung 1: Weltweiter Primärenergieverbauch (in TWh) von 1965 bis 2020 für fossile, erneuerbare und nukleare Energieträger. Die Graphik basiert auf dem *bp Statistical Review of World Energy*[3] und wurde von der Internetseite ourworldindata.org übernommen mit CC BY 4.0 Lizenz, Copyright (2022) BP.[4]

Die Dekarbonisierung des Energiesektors ist demnach eine wichtige Aufgabe, um die Konsequenzen des anthropogenen Klimawandels zu beschränken. Dadurch ergibt sich die Notwendigkeit der Energieversorgung mit nachhaltigen, sauberen und effizienten Techniken. Insbesondere die erneuerbaren Energieträger spielen in diesem Kontext eine wichtige Rolle: Wasserkraft, Windenergie, Solarenergie, Geothermie und Bioenergie. **Abbildung 1** ist weiterhin zu entnehmen, dass der Anteil dieser erneuerbaren Energieträger bezogen auf die weltweite Energieerzeugung insbesondere in den 2000er und 2010er Jahren zugenommen hat. Verglichen mit den etablierten fossilen Energieträgern ist der Anteil allerdings noch gering, sodass ein weiterer Ausbau in den kommenden Jahren zwingend erforderlich ist, um die globale Erwärmung gemäß dem Übereinkommen von Paris von 2015 zu beschränken. Das Pariser Klima-Abkommen, das von 195 Vertragsparteien unterzeichnet wurde, legt das Ziel fest, die globale Erwärmung auf deutlich unter 2 °C gegenüber dem vorindustriellen Level zu beschränken.[5]

Ein Problem der erneuerbaren Energien ist allerdings, dass einige von ihnen zeitlich und räumlich nicht konstant verfügbar sind. Insbesondere die Versorgung mit Solar- und Windenergie unterliegt naturgemäß starken Schwankungen. **Abbildung 2** illustriert die Verfügbarkeit dieser beiden erneuerbaren Primärenergieträger bezogen auf den Standort Deutschland im Jahr 2020. Die Bereitstellung solarer Energie ist demnach für einen fixen Standort abhängig von der relativen Position der Sonne, ebenso vom Wetter, was zu täglichen und jahreszeitlichen Schwankungen führt. Die Windenergie ist ebenso vom vorherrschenden Wetter abhängig, welches sich stetig ändert. Tendenziell steht zudem im Winter mehr Windenergie zur Verfügung.

Es kann vorkommen, dass besonders in Zeiten starker Nachfrage, zum Beispiel in der frühen Nacht, nicht genug Energie vorhanden ist. Allerdings muss auch während dieser Energiespitzen der Bedarf sicher abgedeckt werden.

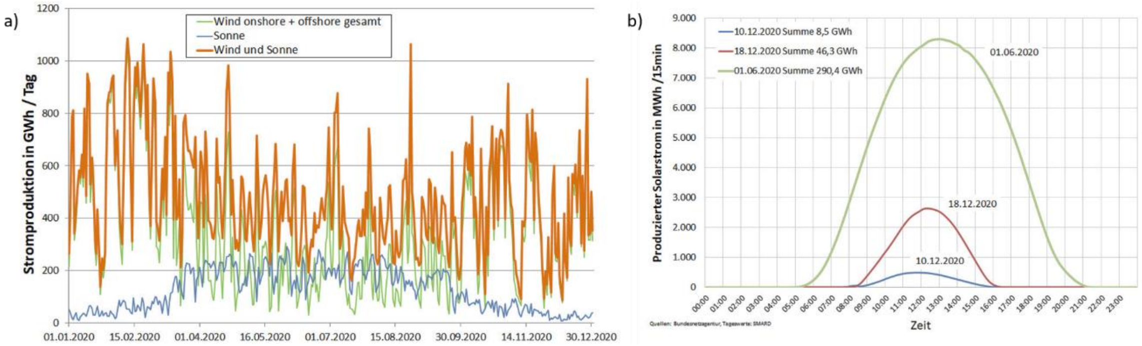

Abbildung 2: (a) Tagessummen der Stromproduktion aus Windenergie (grün) und Solarenergie (blau) im Jahr 2020 für Deutschland abhängt. (b) 15-Minuten-Summen der Stromproduktion aus Solarenergie am 01.06.2020 (grün), 10.12.2020 (blau) und 18.12.2020 (rot). Aus den Abbildungen wird ersichtlich, dass die Stromproduktion aus diesen erneuerbaren Energieträgern stark von der Jahreszeit, Tageszeit und auch von der Wetterlage abhängt. Die Daten stammen von der Bundesnetzagentur mit CC BY 4.0 Lizenz, Copyright (2021) Bundesnetzagentur[6]. Die Abbildungen wurden übernommen von der Internetseite nablaenergy.de mit Genehmigung, Copyright (2021) Harry Schüle.[7]

Daher ist es nötig, die durch erneuerbare Techniken gewonnene Energie zwischenzuspeichern. Hierfür wurden in den letzten Jahrzehnten verschiedene Lösungen entwickelt. Die Zwischenspeicher, die englisch auch als *power-to-X* bezeichnet werden, können grob in vier Kategorien eingeteilt werden: thermisch, mechanisch, chemisch und elektrochemisch.[8] Ein prominentes Exempel stellt die elektrochemische Speicherung von Energie dar, zum Beispiel in einem Akkumulator. In einem Pumpspeicherkraftwerk wird beispielsweise elektrische in potentielle Energie umgewandelt, was ein Beispiel für die mechanische Energiezwischenspeicherung darstellt. Bei der thermischen Methode wird die Primärenergie in Wärmeenergie umgewandelt, welche effektiv über längere Zeiträume gespeichert werden kann. Bei Bedarf kann die zwischengespeicherte Energie dann abgerufen werden.

Der Fokus dieser Arbeit liegt hingegen auf der chemischen Energiespeicherung in Form von Wasserstoff, welcher direkt aus Wasser hergestellt werden kann mit Sauerstoff als Nebenprodukt, oder weiteren synthetischen Kraftstoffen, welche direkt aus Kohlenstoffdioxid erzeugt werden. Dabei wird Primärenergie aus nachhaltigen Energiequellen dazu genutzt, um Strom zu erzeugen und elektrochemische Reaktionen, wie die Zerlegung von Wasser in die Elemente Sauerstoff und Wasserstoff oder die Reduktion von Kohlenstoffdioxid zu organischen Brennstoffen, zu ermöglichen. Die gewonnenen chemischen Energiespeicher können über längere Zeiträume gelagert werden und bei Bedarf wieder verbrannt beziehungsweise verstromt werden, um Energiespitzen, zum Beispiel am Abend, sicher abzudecken.

1.2. Chemische Energiespeicherung

Auf dem Gebiet der chemischen Energiespeicherung gilt vor allem Wasserstoff als Energieträger der Zukunft.[9] Unter Normalbedingungen liegt Wasserstoff als molekulares Gas (H_2) vor. Wasserstoff ist kein primärer Energieträger, das heißt, H_2 muss zunächst aus Primärenergie hergestellt werden. Der hergestellte Wasserstoff wird dann als nachhaltig oder „grün” bezeichnet, wenn er mithilfe von erneuerbaren Energien gewonnen wurde. Wasserstoff ist aufgrund der hohen gravimetrischen Energiedichte von *circa* 33 $\mathrm{kWh\,kg^{-1}}$ ein exzellenter Energiespeicher. Im Vergleich dazu weist Rohöl einen vergleichsweise niedrigen Wert von 12 $\mathrm{kWh\,kg^{-1}}$ auf.[10] Zu bemerken ist, dass Wasserstoff als sehr leichtes Gas unter Normalbedingungen eine geringe Dichte von $\rho = 0{,}9\ \mathrm{kg\,m^{-3}}$ besitzt,[11] was eine vergleichsweise geringe volumenbezogene Energiedichte zur Folge hat. Zur Erhöhung der volumetrischen Energiedichte kann Wasserstoffgas auch verflüssigt werden ($\rho = 71\ \mathrm{kg\,m^{-3}}$).[12] Im flüssigen Zustand wird H_2 zum Beispiel als Raketentreibstoff verwendet. Wasserstoff ist geeignet für die Langzeitspeicherung (Wochen bis Monate), wobei die Lagerung sowohl im kleinen als auch im großen Maßstab möglich ist, so wird H_2 als Gas bereits heute in industriellen Mengen in Salzkavernen gespeichert.[13] Zur Nutzung kann Wasserstoff erneut verstromt werden, aber auch die Verwendung als Kraftstoff für Brennstoffzellen-betriebene Transportmittel ist bereits realisiert.[14] Die konventionelle Gewinnung von Wasserstoff erfolgt seit den 1920er Jahren durch die Dampfreformierung (englisch *steam reforming*) von kohlenstoffhaltigen Energieträgern und Wasser.[15] Bei dem Verfahren werden allerdings Treibhausgase freigesetzt, weshalb alternative Verfahren zur Gewinnung von Wasserstoff erforscht werden. Möglichkeiten sind die Erzeugung von H_2 aus Biomasse oder die Elektrolyse von Wasser. Bei der elektrochemischen Zersetzung von Wasser kann Strom, gewonnen aus erneuerbaren Primärenergieträgern, eingesetzt werden, was die Emissionen an CO_2 bei dem Verfahren auf ein Minimum reduziert. Für die industrielle Nutzung der Wasserelektrolyse muss jedoch das Problem der hohen Energieverluste gelöst werden. In der Theorie muss für die Zerlegung von Wasser unter Normalbedingungen eine Spannungsdifferenz von 1,23 V aufgebracht werden, was einer freien Reaktionsenthalpie von + 237 $\mathrm{kJ\,mol^{-1}}$ entspricht. Allerdings liegt die tatsächlich benötigte Spannung aufgrund von kinetischen Effekten im Bereich von 2 V mit Beiträgen von beiden beteiligten Halbreaktionen: die Reduktion von Wasser zu Wasserstoff und die Oxidation zu Sauerstoff. Die Differenz von tatsächlich benötigter Spannung und dem Theoriewert wird auch als Überspannung bezeichnet. Es wird dementsprechend mehr Energie zur Produktion von Sauerstoff und Wasserstoff während der Wasserelektrolyse benötigt, als diese zu speichern in der Lage sind. Eine Überspannung senkt also die Effizienz der Speichermethode. Aktuell wird an der Reduktion dieser Überspannungen durch die Verwendung von entsprechenden Elektrokatalysatoren für beide Halbreaktionen geforscht, die allerdings effektiv und günstig verfügbar sein müssen, um die Wirtschaftlichkeit des Verfahrens zu garantieren.[16] In der vorliegenden Arbeit wird daher ein potentieller Elektrokatalysator für die kinetisch stark gehinderte Wasseroxidation näher beleuchtet: Nickelferrit ($NiFe_2O_4$). Es werden Strategien aufgezeigt, wie die Leistungsfähigkeit eines Elektrokatalysators für die Oxidation von Wasser wirksam optimiert werden kann.

Wasserstoff ist ein sogenannter synthetischer Kraftstoff: als solche werden allgemein Brennstoffe bezeichnet, die nicht mit Rohöl oder Erdgas als Rohstoff produziert wurden.[17] Eine weitere Strategie zur Gewinnung von solchen hochenergetischen Molekülen ist die Nutzung von atmosphärischem Kohlenstoffdioxid (CO_2) als Rohstoff. Zur Erzeugung von synthetischen organischen Brennstoffen, wie zum Beispiel Kohlenstoffmonoxid (CO), Methan (CH_4) oder Methanol (CH_3OH), muss das chemisch weitestgehend inerte Kohlenstoffdioxid-Molekül zunächst reduziert werden, was einen externen Energieeintrag erfordert. Eine Möglichkeit zur Verwertung von CO_2 ist die Reduktion mit Elektrizität, an der seit mehr als einem Jahrhundert geforscht wird.[18] Allerdings hat sich eine derartige Technologie aus verschiedenen Gründen bisher noch nicht etabliert. Zum einen erfordert die elektrochemische Reduktion von chemisch stabilem CO_2 das Anlegen von stark negativen Potentialen, sodass sich die benötigte Potentialdifferenz, je nach ablaufender Reaktion, ohne Betrachtung der Überpotentiale zu *circa* 1,0-1,5 V ergibt. Ein exakter Potentialwert ist nicht anzugeben, da verschiedene Reaktionen möglich sind, die zudem zu unterschiedlichen Reaktionsprodukten führen.[19] Die in der Praxis auftretende kinetische Hemmung führt wie bei der Wasserelektrolyse dazu, dass beidseitig Überpotentiale auftreten und sich die benötigte Spannung auf ≥ 2 V erhöht. Dadurch ist die CO_2-Reduktion aktuell noch nicht wirtschaftlich, da große Mengen an Energie benötigt werden.[20] Die Überspannung kann durch die Verwendung von Elektrokatalysatoren gesenkt werden. In dieser Arbeit wird der an die Natur angelehnte Elektrokatalysator Nickeleisensulfid (Ni_2FeS_4), der wie die Kohlenmonoxiddehydrogenase (CODH) die Elemente Nickel, Eisen und Schwefel enthält, für die elektrochemische Reduktion von CO_2 verwendet. Als Hauptprodukte entstehen hierbei Wasserstoff und Kohlenstoffmonoxid (CO). Bei dem erforderlichen Potential steht die CO_2-Reduktion in direkter Konkurrenz zu der Reduktion von Protonen.[21] Ein weiteres Problem ist die geringe Löslichkeit von Kohlenstoffdioxid in Wasser, was niedrige Reaktionsraten zur Folge hat.[22] Außerdem führt die Reduktion von CO_2 zu verschiedenen organischen Reaktionsprodukten, wodurch es schwierig ist, ein Molekül selektiv herzustellen. Die Selektivität kann aber zum Teil durch die Auswahl des Elektrokatalysators gesteuert werden.[23]

2. Theoretischer Hintergrund

2.1. Eisen-basierte Spinelle

2.1.1. Kristallstruktur

Spinelle sind anorganische Verbindungen mit der allgemeinen Summenformel MZ_2X_4.[24] In der Regel stehen M und Z für divalente beziehungsweise trivalente Kationen, während X Chalkogenid-Anionen repräsentiert. Spinellferrite sind Fe^{3+}-enthaltende oxidische Spinelle, die durch die Summenformel MFe_2O_4 beschrieben werden können, wobei M für divalente Metallkationen steht, wie zum Beispiel Mn^{2+}, Fe^{2+}, Co^{2+}, Ni^{2+}, Cu^{2+} oder Zn^{2+}. Die O^{2-}-Anionen bilden eine kubisch-dichteste Packung (englisch *cubic-close packed*, ccp). Die M^{2+}- und Fe^{3+}-Kationen besetzen in dieser Struktur die Tetraeder- (A) und Oktaederlücken (B). Folglich besteht die kubische Einheitszelle aus insgesamt 56 Atomen: 32 O^{2-}-Anionen, 8 A-Kationen und 16 B-Kationen (Raumgruppe $Fd\overline{3}m$, Nummer 227). Die Kristallstruktur ist in **Abbildung 3** beispielhaft für $NiFe_2O_4$ gezeigt. In der Spinellstruktur können die individuellen Kationen A- oder B-Plätze besetzen, was von den Ionenradien und der jeweiligen Ligandenfeldstabilisierungsenergie abhängt. In einem normalen Spinell, wie beispielsweise $ZnFe_2O_4$, besetzen die Fe^{3+}-Kationen Oktaederplätze und Zn^{2+}-Kationen bevorzugen die Tetraederplätze. Die Oktaederplätze sind insgesamt zu 50 % besetzt, während auf 12,5 % der Tetraederplätze Kationen zu finden sind. Im Fall von $NiFe_2O_4$ liegt eine veränderte Kationenverteilung vor, da Ni^{2+}-Kationen bevorzugt B-Plätze besetzen. Als Konsequenz besetzt die Hälfte der Fe^{3+}-Kationen dann A-Lücken, was als inverser Spinell bezeichnet wird.[25] Die Kationenverteilung wird charakterisiert durch den Inversionsparameter λ, der durch die Notation $[M_{1-\lambda}^{2+}Fe_{\lambda}^{3+}]^A[M_{\lambda}^{2+}Fe_{2-\lambda}^{3+}]^BO_4$ definiert ist. Drei Fälle können unterschieden werden: normaler Spinell ($\lambda = 0$), inverser Spinell ($\lambda = 1$) und partiell inverser Spinell beziehungsweise Mischspinell ($0 < \lambda < 1$).[26] Inversionsgrade werden experimentell üblicherweise mittels Neutronendiffraktion, Röntgenabsorptionsspektroskopie, Mössbauerspektroskopie oder magnetischen Messungen bestimmt.[26,27]

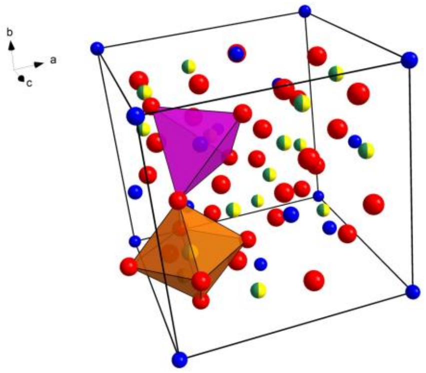

Abbildung 3: Kristallstruktur des inversen Spinells $NiFe_2O_4$ ($\lambda = 1$). Die O^{2-}-Anionen (rot) bilden eine kubisch-dichteste Packung. Die Hälfte der Fe^{3+}-Kationen (grün) befindet sich in Oktaederlücken (orange), während die andere Hälfte (blau) Tetraederlücken besetzt (magenta). Die Ni^{2+}-Kationen (gelb) befinden sich alle in Oktaederlücken.

2.1.2. Magnetische Eigenschaften

Die meisten Spinellferrite zeigen eine Reaktion auf ein extern angelegtes magnetisches Feld. Daher stellen solche Spinellferrite eine Gruppe von interessanten magnetischen Materialien dar, die für eine Reihe von Anwendungsfeldern geeignet sind. Sie finden etwa in der Biomedizin,[28] Katalyse,[29] Spintronik,[30] Magnetresonanztomographie (MRT)[31] oder Ferrofluid-Technologie Verwendung.[32] Für das Verständnis der magnetischen Eigenschaften von Spinellferriten ist der Elektronenspin, oft als Spin abgekürzt, von fundamentaler Bedeutung. Der Spin ist mit der Spinquantenzahl s verknüpft und kann die Werte +1/2 und -1/2 annehmen. Das magnetische Moment ist ein Maß für die Wirkung beziehungsweise Richtung der Spins der Elektronen. Die makroskopische Magnetisierung eines Festkörpers im externen Feld hängt stark mit der Ausrichtung der einzelnen magnetischen Momente zueinander (Kopplung) zusammen. Bei diamagnetischen Materialien sind die Atomschalen gefüllt und die jeweiligen magnetischen Momente heben sich gegenseitig auf, das heißt, es existieren gar keine ungepaarten

Spins.[33] Wenn magnetische Momente vorliegen, die aber nicht zueinander gekoppelt sind und auch keine Fernordnung vorliegt, wird von Paramagnetismus gesprochen. Die im Folgenden beschriebenen Spinkopplungen sind in **Abbildung 4a** schematisch dargestellt. Beim Ferromagnetismus liegen parallel ausgerichtete magnetische Momente vor, die sich in ihrer Größenordnung nicht voneinander unterschieden. Eine solche Anordnung liegt zum Beispiel in Materialien mit einer kristallinen Struktur vor, welche die direkte Kopplung der magnetischen Momente erlaubt. Ferromagnete können sich spontan ohne ein extern angelegtes Feld ausrichten. Antiferromagnetismus liegt vor, wenn die einzelnen Momente in ihrer Ausrichtung alternieren, aber sich in ihrer Größenordnung nicht voneinander unterscheiden. Dadurch ist die Magnetisierung ohne ein extern angelegtes Magnetfeld beim Antiferromagnetismus gleich Null. Die Spinausrichtung beim Ferrimagnetismus ist vergleichbar, jedoch heben sich die Einzelspins gegenseitig nicht vollständig auf. Eine derartige Situation liegt exemplarisch in Kristallen mit zwei unterschiedlichen ferromagnetischen Untergittern vor. Ein solches Verhalten kann zum Beispiel in vielen Spinellferriten wie Magnetit (Fe_3O_4) oder Nickelferrit ($NiFe_2O_4$) beobachtet werden und wird auch als Néel-Typ bezeichnet.[34,35] Für den Fall von zwei beteiligten Kationen liegen in den jeweiligen A- und B-Untergittern parallel ausgerichtete nicht-identische magnetische Momente vor, was einer ferromagnetischen Ordnung beider Untergitter entspricht. Beide Ferromagnete sind zueinander antiparallel angeordnet, löschen sich allerdings nicht gegenseitig, da es mehr B- als A-Kationen gibt. Die beschriebene Situation entspricht final einer ferrimagnetischen Anordnung[36,37] und ist in **Abbildung 4b** für die Fälle $\lambda = 0$ und $\lambda = 1$ schematisch gezeigt. Die Wahl der Kationen im Spinellsystem und die Kationenverteilung auf Tetraeder- und Oktaederplätze hat dementsprechend einen signifikanten Einfluss auf das magnetische Verhalten des Materials.[38]

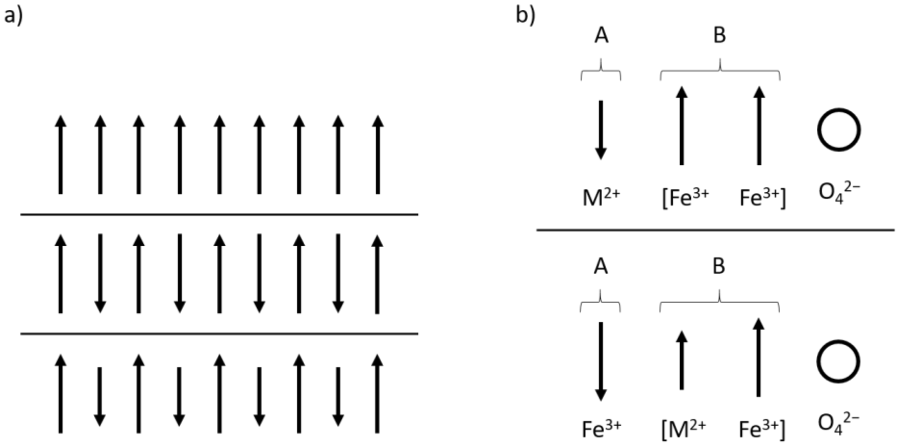

Abbildung 4: (a) Verschiedene Ausprägungsformen des Magnetismus mit jeweiliger Spinorientierung: Ferromagnetismus (oben), Antiferromagnetismus (mitte) und Ferrimagnetismus (unten). (b) Spinanordnung in normalen (oben) und inversen (unten) Spinellen. Voraussetzung für die dargestellte Situation ist, dass zwei Kationen mit ungepaarten Elektronen vorliegen. In beiden Untergittern bildet sich eine ferromagnetische Ordnung aus. Die antiparallele Ordnung dieser führt zum Ferrimagnetismus. Beides adaptiert von *Chem. Eng. J.* 2007 mit Genehmigung, Copyright (2006) Elsevier.[38]

2.1.3. Eisenoxid- und Eisensulfid-basierte Spinelle

Im folgenden Abschnitt sollen die in dieser Arbeit behandelten Eisen(III)oxid- und Eisen(III)sulfid-basierten Spinelle ($NiFe_2O_4$, $MnFe_2O_4$, Ni_2FeS_4) hinsichtlich ihrer Struktur und ihrer Eigenschaften näher beschrieben und potentielle Anwendungen thematisiert werden. Die genannten Spinelle wurden mittels verschiedener Methoden in unterschiedlicher Morphologie mit jeweils hoher spezifischer Oberflächen hergestellt: mesoporöses $NiFe_2O_4$, nanopartikuläres $NiFe_2O_4$, nanopartikuläres $MnFe_2O_4$ und Ni_2FeS_4-Nanoschichten.

2.1.3.1. $NiFe_2O_4$

Im thermodyamisch stabilen *Bulk*-Zustand besitzt Nickelferrit ($NiFe_2O_4$, Mineralname Trevorit) eine inverse Spinellstruktur, in der Ni^{2+}-Kationen B-Plätze besetzen und sich die Fe^{3+}-Kationen gleichmäßig auf A- beziehungsweise B-Plätze verteilen ($\lambda = 1$). Die Hälfte der sich im *high spin*-Zustand, der Konstitution mit der größtmöglichen Anzahl an ungepaarten Elektronen, befindlichen ferromagnetisch geordneten Fe^{3+}-Kationen mit einer $3d^5$ Elektronenkonfiguration besitzen folglich eine tetraedrische Koordination, was einem theoretischen magnetischen Sättigungsmoment von $\mu_B = 5{,}9$ entspricht. Die Vielfache des Bohrschen Magnetons μ_B beschreiben den Betrag eines magnetischen (Teil-)moments und sind demnach ein Maß für die Stärke der magnetischen Austauschwechselwirkung. Vom Sättigungsmoment wird dann gesprochen, wenn sich das System im Gleichgewicht befindet. Die B-Plätze werden von der anderen Hälfte der Fe^{3+}-Kationen eingenommen ($\mu_B = 5{,}9$) sowie von den ebenfalls ferromagnetisch geordneten $3d^8$ Ni^{2+}-Kationen ($\mu_B = 2{,}8$). Durch die ferrimagnetische Kopplung beider Untergitter (Néel-Konfiguration)[35] ergibt sich für $NiFe_2O_4$ eine theoretisches magnetisches Sättigungsmoment von 2,8 μ_B pro Formeleinheit.[39] Im Experiment wurden leicht niedrigere Werte im Bereich von 2,2-2,3 μ_B pro Formeleinheit beobachtet.[40–42] Allerdings kann der Inversionsgrad für einige Spinelle wie $NiFe_2O_4$ im Fall einer Strukturierung auf der Nanoebene variieren, wie von Ŝepelák *et al*. beschrieben.[43]

Solche $NiFe_2O_4$ Mischspinelle mit Inversionsgraden von $0 < \lambda < 1$ zeichnen sich durch veränderte Materialcharakteristika aus, was auch die magnetischen Eigenschaften betrifft. Durch die veränderte Kationenverteilung ergibt sich auch ein abweichendes magnetisches Moment. Für den Grenzfall der vollständig normalen Spinellstruktur ($\lambda = 0$) resultiert für $NiFe_2O_4$ ein hypothetisches magnetisches Moment von $\mu_B = 8{,}9$.[44] Für Mischspinelle werden deshalb magnetische Momente erwartet, die zwischen den beschriebenen Extrema liegen. Die Nanostrukturierung bietet deshalb im Fall solcher Verbindungen oftmals die Möglichkeit, durch die Modifizierung des Inversionsgrades die magnetischen Eigenschaften des Materials hinsichtlich einer bestimmten Anwendung zu optimieren. Allerdings ist zu beobachten, dass die Partikelgröße im Fall der Nanostrukturierung nicht mehr vernachlässigt werden kann, da Oberflächeneffekte unter anderem die Spinausrichtung beeinflussen.[45] Der Einfluss von Nanostrukturierung auf die magnetischen Eigenschaften von $NiFe_2O_4$ wird in dieser Arbeit anhand von größeneinstellbaren Nanopartikeln demonstriert.

Wie die meisten Ferrite ist $NiFe_2O_4$ gegenüber Säuren instabil, jedoch im Neutralen und Alkalischen stabil.[46] $NiFe_2O_4$ ist als günstig und einfach herzustellendes Material interessant für die heterogene Katalyse, wobei insbesondere die Elektrokatalyse und im Speziellen die Elektrolyse von Wasser in Wasserstoff und Sauerstoff zu erwähnen ist. Durch die Inkorperation von zwei redoxaktiven Metallen wie Nickel und Eisen ergeben sich zudem exzellente elektrochemische Eigenschaften. Die Oxidation von Wasser zu Sauerstoff wird aktuell zumeist im Alkalischen durchgeführt und erfordert die Verwendung von Elektrokatalysatoren, welche die benötigte Elektrolysespannung manipulieren, was die Wirtschaftlichkeit der Reaktion garantiert und die Einsparung von großen Energiemengen ermöglicht.[47] Die Grundlagen einer elektrokatalytischen Reaktion werden im späteren Verlauf der Arbeit näher diskutiert. $NiFe_2O_4$ ist ein geeignetes Material um die momentan genutzten Edelmetall-basierten Elektrokatalysatoren RuO_2 und IrO_2 für die alkalische Wasseroxidation zu ersetzen.[48] Die Verwendung eines Materials als Elektrokatalysator erfordert allerdings eine hohe elektrische Leitfähigkeit. In anderen Worten sollte das Material elektrischen Strom leiten können, was intrinsisch für *Bulk*-$NiFe_2O_4$ nicht gegeben ist.[49] Eine mögliche Lösung um diesen Nachteil entgegenzuwirken ist die Verkürzung der Ladungsträgerwege durch Nano- oder Mesostrukturierung, wobei durch die daraus resultierende Oberflächenerhöhung auch die Anzahl der aktiven Zentren signifikant erhöht wird. Daher stellt die alkalische Wasseroxidation auch eine Modellreaktion dar, um die Auswirkung der Oberflächenstrukturierung auf die elektrokatalytische Aktivität zu untersuchen. Dabei wurde in dieser Arbeit mesoporöses und nanopartikuläres $NiFe_2O_4$ dargestellt und die Auswirkung verschiedener Parameter wie Porengröße, Partikelgröße und Kristallinität auf die elektrokatalytische Aktivität in der alkalischen Wasseroxidation untersucht.

Die vielversprechenden Eigenschaften, wie zum Beispiel die gute chemische Stabilität, der Magnetismus, die Manipulierbarkeit der Kristallstruktur, die Inkorperation von zwei redoxaktiven Übergangsmetallen und die gute Verfügbarkeit von $NiFe_2O_4$ ermöglichen zudem die Erschließung weiterer Anwendungsfelder, wobei an dieser Stelle beispielhaft die Photokatalyse und die Gassensorik zu nennen sind. Beispielsweise berichten Rekhila *et al*. über die Anwendung von $NiFe_2O_4$ mit einer optischen Bandlücke von 1,6 eV in der photokatalytischen Wasserstoffentwicklung im sichtbaren Licht.[50] Jia *et al*. zeigen anhand der Detektion von Acetondampf weiterhin, dass $NiFe_2O_4$ auch als Material für die Gassensorik geeignet ist.[51]

2.1.3.2. $MnFe_2O_4$

Bei Manganferrit ($MnFe_2O_4$, Mineralname Jakobsit) handelt es sich im *Bulk*-Zustand um einen sogenannten partiell inversen Spinell oder Mischspinell mit einem Inversionsgrad $\lambda = 0{,}19$ nach Hastings und Corliss.[52] Damit befinden sich insgesamt 81 % der zweiwertigen Mangankationen und 10 % der dreiwertigen Eisenkationen auf Tetraederplätzen. Die restlichen 19 % an Mn^{2+} und 90 % an Fe^{3+} sind auf Oktaederplätzen lokalisiert. Auch im Fall von Manganferrit kann der Inversionsgrad zum Beispiel durch die partielle Oxidation von Mn^{2+} zu Mn^{3+} modifiziert werden, was dann zwangsläufig auch zur Einführung von Vakanzen führt, um die Ladungsneutralität zu gewährleisten.[53] Eine Abhängigkeit von Inversionsgrad und Partikelgröße ist hingegen bei $MnFe_2O_4$ in der Literatur umstritten.[54]

Beide inkorperierten Metallkationen (Mn^{2+} und Fe^{3+}) zeichnen sich durch eine $3d^5$ Elektronenkonfiguration aus. Dies hat zur Folge, dass $MnFe_2O_4$ im *Bulk*-Zustand ein vergleichsweise hohes magnetisches Sättigungsmoment von 3 μ_B für eine normale Kationenbesetzung beziehungsweise 5 μ_B für den inversen Fall aufweist.[55] Die Realität liegt zwischen diesen beiden Extrema, was berichtete experimentelle Werte von 3,3-4,5 μ_B pro Formeleinheit belegen.[56–58] Damit weist $MnFe_2O_4$ verglichen mit $NiFe_2O_4$ (2,2-2,3 μ_B)[40–42] und $MgFe_2O_4$ (1,1-1,4 μ_B)[59–61] ein deutlich höheres und mit Fe_3O_4 (3,7-3,9 μ_B)[62–64] und $CoFe_2O_4$ (3,6-4,0 μ_B)[40,65,66] vergleichbares Sättigungsmoment auf. Der Vergleich zeigt auch auf, dass die magnetischen Eigenschaften von Spinellferriten stark von der Wahl des divalenten Kations abhängen.

Manganferrit kann aus einfach aus gut verfügbaren Rohstoffen hergestellt werden. Die bemerkenswerten chemischen Eigenschaften, die denen von $NiFe_2O_4$ ähneln, ermöglichen die Verwendung des Materials für eine Vielzahl von relevanten Anwendungen. Beispielhaft erneut die elektrokatalytische Wasseroxidation im alkalischen Medium zu nennen.[67,68] $MnFe_2O_4$ wird, wie andere Ferrite auch, als zukünftiges Batteriematerial diskutiert.[69]

2.1.3.3. Ni_2FeS_4

Die Eisen-basierten Spinelle sind nicht auf oxidische Materialien beschränkt – es existiert unter anderem eine Reihe von sulfidischen Spinellen beziehungsweise Thiospinellen, wie zum Beispiel das binäre Magnetit-Analogon Fe_3S_4[70] oder die ternären Verbindungen Cr_2FeS_4, Mn_2FeS_4, Co_2FeS_4 und Ni_2FeS_4.[71,72] Selbst Eisen-enthaltende Selenospinelle sind bekannt, unter anderem das von Kim *et al*. beschriebene $Fe_xCu_{1-x}Rh_2Se_4$.[73]

Vom oben ausführlich beschriebenen $NiFe_2O_4$ leitet sich der Thiospinell Ni_2FeS_4 ab, auch bekannt als Mineral Violarit. Im Vergleich zum Nickelferrit sind die Oxidationsstufen der Ni- und Fe-Kationen vertauscht, das heißt, dass Ni als dreiwertiges und Fe als zweiwertiges Kation vorliegt. In der kubisch-dichtesten Packung der S^{2-}-Anionen besetzen die Fe^{2+}-Kationen Oktaederplätze (B), während die Ni^{3+}-Kationen jeweils zur Hälfte auf Tetraederplätze (A) und Oktaederplätze verteilt sind. Dies entspricht einer inversen Spinellstruktur, was in der Literatur durch theoretische Rechnungen und experimentelle Studien belegt ist.[74,75] Damit enthält der beschriebene Thiospinell Fe^{2+}-Kationen mit $3d^6$ Elektronenkonfiguration, während Ni^{3+} eine $3d^7$ Konfiguration aufweist. Folglich tragen beide Kationen mit ungepaarten Elektronenspins bei, was ähnlich wie bei den oxidischen Spinellen $NiFe_2O_4$ und $MnFe_2O_4$ zu einer ferrimagnetischen Gesamtkopplung führen dürfte. Die magnetischen Eigenschaften des Materials sind allerdings noch nicht im Detail untersucht worden.

Aus dem von Pring *et al*. veröffentlichten Phasendiagramm des Fe-Ni-S-O Systems (**Abbildung 5**) wird deutlich, dass Nickeleisensulfide wie Violarit tendenziell eher im Sauren beziehungsweise Neutralen stabil sind, jedoch nicht im Alkalischen.[46] Im Gegensatz dazu ist die oxidische Verbindung $NiFe_2O_4$ weniger stabil gegenüber Säuren. Dies führt dazu, dass eine Anwendung von Ni_2FeS_4 in der alkalischen Wasseroxidation nicht sinnvoll ist, womit unter diesen speziellen Bedingungen kein direkter Aktivitätsvergleich zwischen Oxid und Sulfid möglich ist.

Es ist bekannt, dass die Kohlenmonoxiddehydrogenase (CODH), welche Kohlenstoffdioxid (CO_2) enzymatisch zu Kohlenstoffmonoxid (CO) reduziert, als aktive Zentren [Ni-4Fe-5S] Cluster enthält.[76] Aus diesem Grund testeten Piontek *et al*. das nickel-, eisen- und schwefelhaltige Mineral Pentlandit ($Ni_{4.5}Fe_{4.5}S_8$) in der elektrokatalytischen Reduktion von CO_2 zu CO, wobei als Nebenprodukt auch Methan (CH_4) entsteht. Speziell in protischen Lösungsmitteln, wie zum Beispiel Wasser, steht die CO_2-Reduktion in Konkurrenz zur Reduktion von Protonen zu H_2.[77] Yamaguchi *et al*. haben gezeigt, dass Ni_2FeS_4-basierte Materialien dazu in der Lage sind, CO_2 elektrochemisch zu reduzieren.[78] Außerdem weisen die sulfidischen Materialien verglichen mit dem jeweiligen Oxid oft eine erhöhte intrinsische Leitfähigkeit auf,[79] was für die Anwendung in der Elektrokatalyse vorteilhaft sein kann.

Daher wurde in dieser Arbeit ebenfalls die elektrokatalytische CO_2-Umwandlung als Testreaktion für die hergestellten reinen Ni_2FeS_4-Nanoschichten ausgewählt. Anwendungen für solche Ni_2FeS_4-Thiospinelle sind in der Literatur nur wenige beschrieben. Neben der genannten Anwendung in der Elektrokatalyse sind hierbei der photokatalytische Abbau von Methylenblau und Rhodamin B zu erwähnen, ebenso die Nutzung für Superkondensatoren und die Glucose-Sensorik.[80–82]

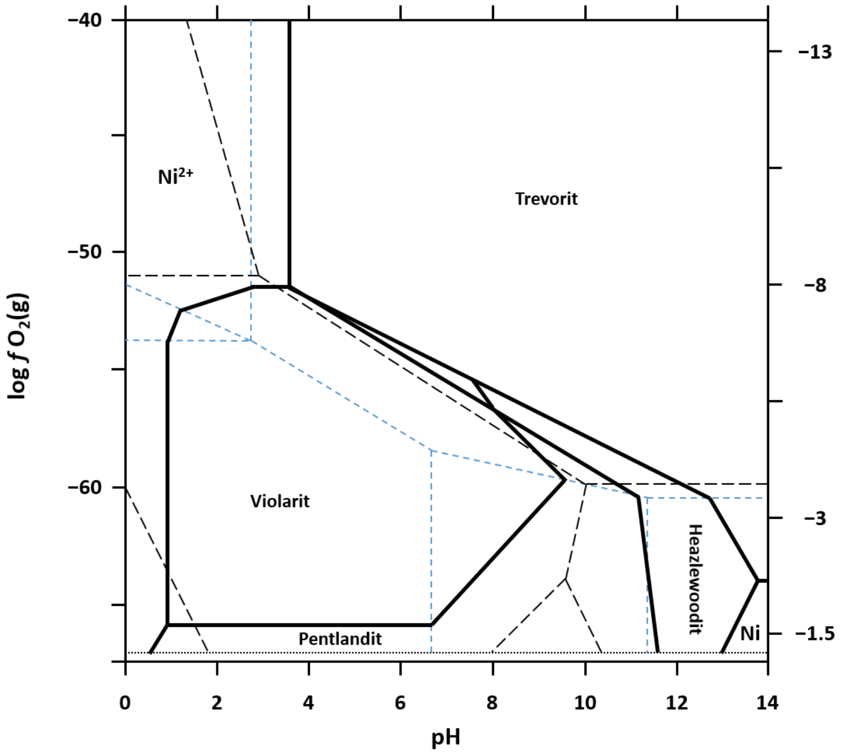

Abbildung 5: Stabilitätsdiagramm des Fe-Ni-S-O Systems in Abhängigkeit der Fugazitäten von Sauer- (O_2) sowie Wasserstoff (H_2) und des pH-Wertes. Die Nickeleisensulfide Violarit (Ni_2FeS_4) und Pentlandit ($Ni_{4.5}Fe_{4.5}S_8$) sind tendenziell eher im sauren Medium stabil. Im stark sauren Milieu können auch gelöste Ni^{2+}-Kationen vorliegen. Nickeleisenoxid (Trevorit, $NiFe_2O_4$) ist dagegen eher im Neutral und Alkalischen beständig. Unter stark alkalischen Bedingungen können auch Heazlewoodit (Ni_3S_2) und metallisches Nickel bestehen. Adaptiert von *Regolith* 2005 mit Genehmigung, Copyright (2005) Allan Pring[46] unter Berücksichtigung der Daten von *Hydrometallurgy* 1996 mit Genehmigung, Copyright (1996) Elsevier B.V.[83]

2.2. Elektrokatalyse

Die Elektrokatalyse ist eine Unterkategorie der heterogenen Katalyse und beschreibt allgemein die Reduktion von Aktivierungsenergien elektrochemischer Reaktionen an Elektrodenoberflächen (**Abbildung 6**). Damit eine elektrochemische Halbreaktion, wie zum Beispiel die Oxidation von Wasser, überhaupt ablaufen kann, ist das Anlegen eines charakteristischen Redoxpotentials notwendig, welches sich aus der Thermodynamik ergibt. Das Redoxpotential beschreibt die benötigte Potentialdifferenz, gemessen unter Standardbedingungen, damit die elektrochemische Reaktion gerade so ablaufen kann. In der Praxis ist die benötigte Spannung aus kinetischen Gründen meist höher als das Redoxpotential der entsprechenden Halbzellenreaktion. Die Differenz wird als Überspannung bezeichnet. Ein Elektrokatalysator verringert die Überspannung einer bestimmten Halbreaktion signifikant.[84,85] Dadurch kann in der Praxis die erforderliche Energiemenge minimiert werden, die notwendig ist, um die elektrochemische Reaktion durchzuführen.

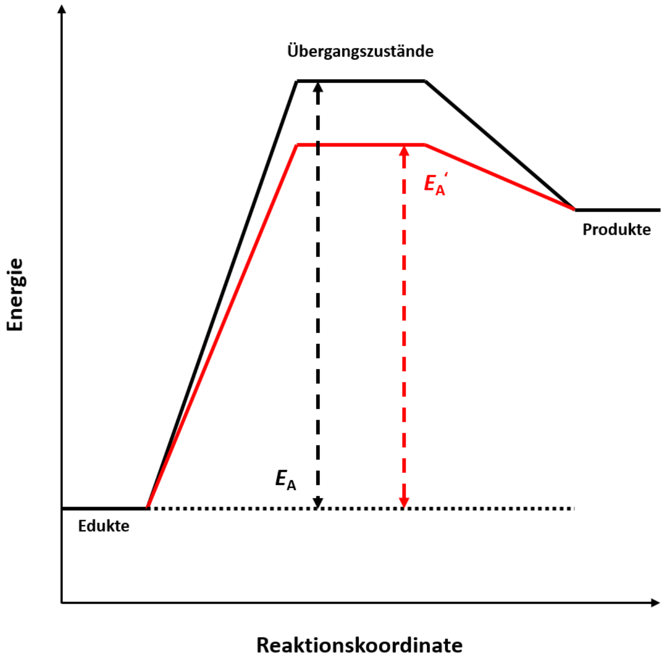

Abbildung 6: Potentialdiagramm für eine endergonische elektrochemische Reaktion, wie zum Beispiel die Protonenreduktion in der Wasserspaltung. Die Aktivierungsbarriere (schwarzer gestrichelter Pfeil) kann durch die Verwendung eines Elektrokatalysators erheblich gesenkt werden (roter gestrichelter Pfeil). Dies macht sich durch eine geringere notwendige Überspannung bemerkbar, was einer signifikanten Energieeinsparung entspricht. Adaptiert von *J. Mater. Chem. A* 2015 mit Genehmigung, Copyright (2015) Royal Society of Chemistry.[85]

2.2.1. Wasserelektrolyse

Unter Wasserelektrolyse wird die Spaltung von Wasser in die gasförmigen Elemente O_2 und H_2 durch elektrische Energie verstanden (**Gleichung 1**). Die Idee der Wasserzerlegung mit Strom wurde bereits im späten 18. Jahrhundert von van Troostwijk und Deimann beschrieben.[86] Durch die Methode kann potenziell grüner Wasserstoff gewonnen werden, sofern der verwendete Strom CO_2-neutral gewonnen wurde, zum Beispiel aus Solarenergie.

$$H_2O \rightarrow H_2 + 1/2\ O_2 \qquad (1)$$

Mit einer positiven freien Reaktionsenthalpie von +237 kJ/mol unter Standardbedingungen handelt es sich um eine endergonische Reaktion, die somit ohne externen Energieeintrag nicht abläuft. Die benötigte Potentialdifferenz für die Wasserelektrolyse ergibt sich ohne Betrachtung der Überpotentiale zu +1,23 V. Die Wasserelektrolyse umfasst zwei Teilreaktionen – die Reduktion von Protonen zu Wasserstoff (englisch *hydrogen evolution reaction*, HER) und die Wasseroxidation zu Sauerstoff (englisch *oxygen evolution reaction*, OER).[87] Die HER ist dabei eine einfache Reaktion und erfordert nur einen Zwei-Elektronen-Übertrag. Bei der OER werden dagegen vier Elektronen sowie vier Protonen übertragen und zusätzlich eine O—O Bindung geknüpft, wodurch die OER kinetisch vergleichsweise stark gehindert ist, was einem relativ hohen Überpotential entspricht.[88,89] Wie bereits angesprochen, verursacht ein zu hohes Überpotential im industriellen Maßstab enorme Energiekosten, was zur Unrentabilität der Wasserelektrolyse führen würde.

Zur praktischen Umsetzung der Wasserelektrolyse ist zudem ein Separator notwendig, der Kathoden- und Anodenraum voneinander trennt, damit sich die entstehenden Gase nicht vermischen können. Ein Ionenaustausch muss hingegen gewährleistet sein, da ein Ladungsausgleich erfolgen muss. Prinzipiell kann die Wasserelektrolyse bei jedem pH-Wert durchgeführt werden. In sauren Elektrolyten kann die Wasserelektrolyse dann durch die **Gleichungen 2a und b** beschrieben werden.

$$2\ H_3O^+ + 2\ e^- \rightarrow H_2 + 2\ H_2O \tag{2a}$$

$$3\ H_2O \rightarrow 1/2\ O_2 + 2\ H_3O^+ + 2\ e^- \tag{2b}$$

Im Fall der alkalischen Wasserelektrolyse gelten **Gleichungen 3a und b**.

$$2\ H_2O + 2\ e^- \rightarrow H_2 + 2\ OH^- \tag{3a}$$

$$2\ OH^- \rightarrow 1/2\ O_2 + H_2O + 2\ e^- \tag{3b}$$

Um die Wasserelektrolyse zu optimieren, wird für die Kathodenseite ein Elektrokatalysator benötigt, um die Überspannung der HER zu senken. Für saure und alkalische Elektrolyte wird zumeist Platin (Pt) verwendet, welches zwar eine gute Aktivität zeigt, aber in der Anschaffung aufgrund der beschränkten Verfügbarkeit vergleichsweise teuer ist. Deshalb werden aktuell neue, unkritische und säurestabile beziehungsweise basenstabile Elektrokatalystoren gesucht, um Platin zu ersetzen. Ein aktuelles edelmetallfreies Beispiel für saure Umgebungen stellt Molybdänphosphosulfid dar, welches aus kostengünstigen und reichlich vorhandenen Rohmaterialien hergestellt werden kann. Viele der Materialien sind auch unter stark sauren Bedingungen stabil und zeigen mit Edelmetallen vergleichbare Aktivitäten.[90] Auch für alkalische Elektrolyte werden alternative Elektrokatalysatoren benötigt. Zum Beispiel schlagen Hu *et al.* eine $Co_2N/Co_2Mo_3O_8$ Heterostruktur vor. Die Aktivität ist mit der von Platin vergleichbar.[91] Die Identifizierung und Testung von geeigneten Elektrokatalysatoren für die Halbreaktion der Protonenreduktion bleibt jedenfalls ein wichtiges Forschungsthema, was durch die Anzahl und Vielfältigkeit der Publikationen auf diesem Feld belegt wird.[92,93]

Die Verwendung eines Elektrokatalysators ist auch auf der Anodenseite notwendig, da die Überspannung der OER im Vergleich zur HER mechanistisch bedingt noch etwas höher ist. Speziell für die saure Wasseroxidation existieren zurzeit nur relativ wenige Alternativen zu den gängigen Iridium- und Rutheniumoxid-basierten Elektrokatalystoren. Ebenso wie bei Platin ist die Verwendung der Edelmetalle Iridium (Ir) und Ruthenium (Ru) kritisch, was eine Kommerzialisierung dieser Technik entgegensteht. Das Problem ist jedoch, dass die meisten edelmetallfreien Materialien, die eine hohe Aktivität aufweisen, unter den harschen Bedingungen der sauren Wasseroxidation nicht stabil sind, welche unter anderem in Brennstoffzellen mit Protonen-Austausch-Membranen (englisch *proton exchange membrane*, PEM) vorliegen. Eine Strategie besteht darin, den Anteil von Iridium beziehungsweise Ruthenium in den verwendeten Elektrokatalysatoren zumindest teilweise zu reduzieren. Gegenwärtig wird an Perowskit-basierten Elektrokatalysatoren mit reduziertem Edelmetall-Anteil wie $SrIrO_3$ oder $CaCu_3Ru_4O_{12}$ geforscht, welche säurestabil sind und eine intrinsische Aktivität in der Wasseroxidation aufweisen.[94–96] Für die alkalische Sauerstoffentwicklung werden unter anderen Übergangsmetalloxide auf Basis von

Eisen, Nickel, Cobalt und Mangan verwendet, die oft aufgrund ihrer Verfügbarkeit sehr günstig und einfach herzustellen sind.[97–99] Ein oft verwendetes Strukturmotiv ist hierbei die Spinellstruktur. Dabei werden binäre, ternäre und quartäre Spinelle eingesetzt, wie beispielsweise Co_3O_4,[100] $CoFe_2O_4$[101] oder auch $Ni_xCo_yMn_zO_4$.[102]

In dieser Arbeit wird der inverse Spinell $NiFe_2O_4$ in der Wasseroxidation getestet. Nickelferrit ist unter einem pH-Wert von *circa* 4 nicht stabil (siehe **Abbildung 5**), daher kann das Material ausschließlich im Neutralen oder Alkalischen eingesetzt werden. Ein anwendungsrelevantes Problem von solchen Übergangsmetalloxiden, wie zum Beispiel $NiFe_2O_4$, ist oftmals die schlechte elektrische Leitfähigkeit der Materialien.[49] Die Ladungsträger können nur vergleichsweise kurze Wege zurücklegen, sodass große Teile des *Bulk*-Materials gar nicht kontaktiert sind. Somit können die Ladungsträger die aktiven Zentren nicht oder nur schwer erreichen. Ein Lösungsansatz bietet hier die Meso- oder Nanostruktierung der Übergangsmetalloxidkatalysatoren, wodurch zusätzlich die Oberfläche und die Zahl der aktiven Zentren erhöht wird. Ein Parameter, der Oberfläche und Aktivität verknüpft, ist die elektrochemisch aktive Oberfläche (englisch *electrochemical active surface area*, ECSA). Jedoch ist eine Erhöhung der ECSA oftmals mit einem geringeren Kristallinitätsgrad verbunden, was sich negativ auf die elektrokatalytische Aktivität auswirken kann. Ein amorpher Elektrokatalysator ist allgemein schlecht elektrisch leitfähig und tendiert eher dazu, sich langsam zu zersetzen, weshalb die Langzeitstabilität ein wichtiger Faktor bei der Beurteilung der Güte eines Elektrokatalysators ist.[103] Die Tafel-Steigung als zusätzlicher Parameter gibt an, wie der Strom durch eine Elektrode von der Spannungsdifferenz zwischen Elektrode und Elektrolyt abhängt. Zur Ermittlung der Tafel-Steigung wird der Tafel-Plot herangezogen, für den die Stromdichte an der Elektrode gegen den dekadischen Logarithmus des Elektrodenpotentials aufgetragen wird.

Zusammenzufassend ist zu sagen, dass die elektrokatalytische Aktivität eines Materials schwierig vorherzusagen ist. Es sind sorgfältige Untersuchungen notwendig, um exakt festzustellen, welche Parameter die Performance bestimmen und wie diese für eine maximale Ausnutzung der bereitgestellten Energie optimiert werden müssen.

2.2.2. Reduktion von Kohlenstoffdioxid

Gegenüber dem vorindustriellen Niveau ist der Gehalt des Treibhausgases Kohlenstoffdioxid (CO_2) in der Atmosphäre um fast 150 ppm auf 419 ppm (Stand 14.07.2022) gestiegen.[104,105] Im Jahr 1960 betrug der atmosphärische CO_2-Gehalt noch 315 ppm.[106] Die elektrokatalytische Reduktion bietet eine vielversprechende Möglichkeit, in der Atmosphäre gebundenes CO_2 umzuwandeln beziehungsweise nutzbar zu machen. Damit leistet die elektrokatalytische Reduktion von CO_2 einen Beitrag zur Einhaltung des 2 °C-Ziels der Pariser Klimakonferenz (2015), insofern der verwendete Strom CO_2-neutral bereitgestellt wurde.[107]

Das CO_2-Molekül selbst ist äußerst stabil und chemisch weitestgehend inert. Zudem ist CO_2 schlecht in Wasser löslich, was bei der elektrochemischen Reduktion zu niedrigen Reaktionsraten führt. Kohlenstoff liegt in seiner höchstmöglichen Oxidationsstufe +IV vor. Die Ein-Elektronen-Reduktion zu $CO_2^{\cdot -}$ würde bei einem neutralen pH-Wert eine extrem negative Spannung von -1,90 V gegenüber der Standard-Wasserstoff-Elektrode (englisch *standard hydrogen electrode*, SHE) erfordern. Durch die Kopplung der Reduktion mit Protonenübergängen kann die notwendige Spannung gesenkt werden. Es können auf diese Weise wertvolle Rohchemikalien und Brennstoffe erzeugt werden, unter anderem Ameisensäure (HCOOH), Kohlenstoffmonoxid (CO), Methan (CH_4), Methanol (CH_3OH), Ethen (C_2H_4) oder Ethanol (C_2H_5OH). Die entsprechenden Reaktionsgleichungen sowie Standard-Halbzellenpotentiale E^0 bei einem pH-Wert von 7 sind den **Gleichungen 4a-f** zu entnehmen.[108,109] Es ist augenscheinlich, dass die Redoxpotentiale im Bereich von −0,6 bis −0,2 V *vs.* SHE liegen und damit einander sehr ähnlich sind, was die selektive Herstellung eines bestimmtes Produkts erschwert. Im Vergleich dazu liegt das Halbzellenpotential der Protonenreduktion (siehe **Gleichung 2a**) bei −0,41 V *vs.* SHE. Daher stellt die Reduktion von Protonen in protischen Medien immer eine Konkurrenzreaktion zur Reduktion von CO_2 dar. Als Gegenreaktion erfolgt in einem typischen CO_2-Elektrolyseur die Oxidation von Wasser an der Anode. Beide Reaktionskammern sind durch eine Ionenaustausch-Membran voneinander getrennt. Die Gesamtreaktion ist in jedem Fall endergonisch, sodass eine externe Spannung als Triebkraft zwingend benötigt wird.

$$CO_2 + 2\ H_3O^+ + 2\ e^- \rightarrow CO + 3\ H_2O,\ E^0 = -0{,}52\ \text{V}\ \textit{vs.}\ \text{SHE} \tag{4a}$$

$$CO_2 + 2\ H_3O^+ + 2\ e^- \rightarrow HCOOH + 2\ H_2O,\ E^0 = -0{,}61\ \text{V}\ \textit{vs.}\ \text{SHE} \tag{4b}$$

$$CO_2 + 6\ H_3O^+ + 6\ e^- \rightarrow CH_3OH + 7\ H_2O,\ E^0 = -0{,}38\ \text{V}\ \textit{vs.}\ \text{SHE} \tag{4c}$$

$$CO_2 + 8\ H_3O^+ + 8\ e^- \rightarrow CH_4 + 10\ H_2O,\ E^0 = -0{,}24\ \text{V}\ \textit{vs.}\ \text{SHE} \tag{4d}$$

$$2\ CO_2 + 12\ H_3O^+ + 12\ e^- \rightarrow C_2H_4 + 16\ H_2O,\ E^0 = -0{,}35\ \text{V}\ \textit{vs.}\ \text{SHE} \tag{4e}$$

$$2\ CO_2 + 12\ H_3O^+ + 12\ e^- \rightarrow C_2H_5OH + 15\ H_2O,\ E^0 = -0{,}32\ \text{V}\ \textit{vs.}\ \text{SHE} \tag{4f}$$

Da die Überpotentiale der Reaktionen zusätzlich betrachtet werden müssen, erfordert die Reduktion von Kohlenstoffdioxid demzufolge das Anlegen von stark negativen Potentialen. Daher sind die erforderlichen Energiemengen sehr hoch. Um die Wirtschaftlichkeit der Reaktion zu verbessern, ist die Verwendung von Elektrokatalysatoren notwendig. Hierfür werden zumeist metallhaltige Verbindungen eingesetzt.

Im Fall der CO_2-Reduktion können zudem verschiedene Produkte entstehen, die nach der Anzahl der Kohlenstoff-Atome in C_1-, C_2- und C_3-Produkte kategorisiert werden. Dabei kann die Selektivität durch die Wahl des Elektrokatalysators und dabei vor allem durch die inkorperierten Metalle gesteuert werden.[110] Enthalten die Elektrokatalysatoren die Metalle Gold (Au), Silber (Ag) oder Zink (Zn), wird tendenziell eher Kohlenstoffmonoxid als Hauptprodukt erhalten. Ein Beispiel hierfür sind elektrochemisch rekonstruierte Zinkoxid-Nanostrukturen, die von Luo *et al.* erfolgreich in der CO_2-zu-CO-Elektroreduktion eingesetzt wurden.[111] Ameisensäure kann durch die Verwendung von Metallen wie Zinn (Sn), Indium (In) und Blei (Pb) erhalten werden. Yuan *et al.* beschreiben beispielsweise zweidimensionale amorphe SnO_x Strukturen für die Herstellung von Ameisensäure aus Kohlenstoffdioxid.[112] Kupfer (Cu) nimmt eine gewisse Sonderrolle ein, da mit Cu-haltigen Elektrokatalysatoren eine Reihe von $C_{1/2/3}$-Produkten aus CO_2 dargestellt werden können, unter anderem Kohlenstoffmonoxid,[113] Ameisensäure,[114] Methanol,[115] Ethanol[116] und Ethen.[117] Wasserstoff-selektiv sind vor allem Elektrokatalysatoren, die Platin (Pt), Eisen (Fe) oder Nickel (Ni) enthalten. Darüber hinaus werden neben metallhaltigen Elektrokatalysatoren auch nicht-metallische Verbindungen oder molekulare Katalysatoren eingesetzt.[118]

Bezüglich der elektrokatalytischen CO_2 Reduktion liegt der Fokus der vorliegenden Arbeit auf ternären Übergangsmetallsulfiden mit spinellartiger Struktur. Im Speziellen wird der Thiospinell Ni_2FeS_4 thematisiert. Obwohl nickel- und eisenhaltige Elektrokatalysatoren in solchen Systemen eher dazu tendieren, Protonen zu Wasserstoff zu reduzieren, besteht die Möglichkeit, dass das Material auch in der CO_2-zu-CO-Elektroreduktion aktiv sein kann, da es sich von der Kohlenmonoxiddehydrogenase (CODH) ableitet. Es ist auch möglich, dass beide Reaktionen gleichzeitig ablaufen, was zu der Entstehung von Synthesegas führen würde.

2.3. Oberflächenstrukturierung von Elektrokatalysatoren

Die Oberflächenstruktur eines Elektrokatalysators kann für seine Aktivität und Stabilität ebenso essenziell sein wie die Zusammensetzung.[119] Eine Oberflächenerhöhung bietet in der heterogenen Katalyse generell den Vorteil der Maximierung der Anzahl an aktiven Zentren und damit eine Erhöhung der Reaktivität. Weiterhin sind Metalloxide wie $NiFe_2O_4$ oftmals nicht oder nur schlecht elektrisch leitfähig. Im Falle eines *Bulk*-Materials werden dementsprechend große Teile des Materials nicht kontaktiert. Das heißt, dass der Diffusionsweg eines Ladungsträgers zum nächsten Material-Elektrolyt-Kontakt zu lang ist, um diesen zu erreichen. Damit steht nur ein kleiner Teil des Materialvolumens für die Elektrokatalyse zur Verfügung. Die Nano- oder Mesostrukturierung bietet die Möglichkeit, die Diffusionswege deutlich zu verkürzen und damit die Kontaktierung zu verstärken, was oft mit einer verbesserten Performance einhergeht. Unabhängig von der Art der Strukturierung besteht allerdings das Problem der Diffusionslimitierung. Wenn die Transportwege im einem solchen Material für Elektrolyt, Reaktionsedukte und -produkte nur wenige Nanometer groß sind, ist der Transport beispielsweise durch Engstellen begrenzt. Dementsprechend ist der genaue Zusammenhang von Aktivität und Oberflächenstrukturierung nicht trivial und muss für jedes Katalysatorsystem empirisch untersucht werden.[120] Eine Möglichkeit der Oberflächenerhöhung bietet die Synthese von Nanoteilchen. Solche Teilchen besitzen Durchmesser zwischen 1 und 100 nm, wobei die Definition nicht eindeutig ist.[121] Die Formen von Nanoteilchen können mannigfaltig sein. Beispiele sind sphärische Partikel, plattenartige Strukturen oder stabartige Strukturen. Die Teilchen liegen oft agglomeriert vor.[122]

Durch die Erzeugung von porösen Strukturen kann die Oberfläche eines Materials ebenfalls erhöht werden. Die Porenkanäle weisen oft eine hohe Fernorndung auf. Durch die Porenkanäle können Elektrolyt, Edukte und Produkte sehr effektiv zum aktiven Zentrum transportiert werden, was ein Vorteil im Vergleich zu sphärischen Nanopartikeln darstellt. Nach der Internationalen Union für reine und angewandte Chemie *(International Union of Pure and Applied Chemistry*, IUPAC) weisen mikroporöse Stoffe einen Porendurchmesser D von < 2 nm auf. Liegt der Porendurchmesser zwischen 2 und 50 nm, wird von mesoporösen Materialien gesprochen. Sind die Poren noch größer, werden sie als Makroporen bezeichnet.[123] Poren können auch nach ihrer Zugänglichkeit und Form klassifiziert werden (**Abbildung 7**). Nicht jede Porenform ist für die heterogene Katalyse nützlich, wie zum Beispiel geschlossene Poren.[124]

Viele Elektrokatalysatoren werden in Form von Nanokatalysatoren eingesetzt, um die Aktivität zu erhöhen. Ein Beispiel stellt der Co_3O_4-Spinell dar. Nanopartikuläre und mesoporöses Co_3O_4-Pulver[125,126] wurden bereits für die elektrokatalytische Wasseroxidation eingesetzt. Es sind oft sorgfältige Untersuchungen notwendig, um festzustellen, welche Morphologie für den jeweiligen Elektrokatalysator und die spezifische Reaktion am besten geeignet ist.

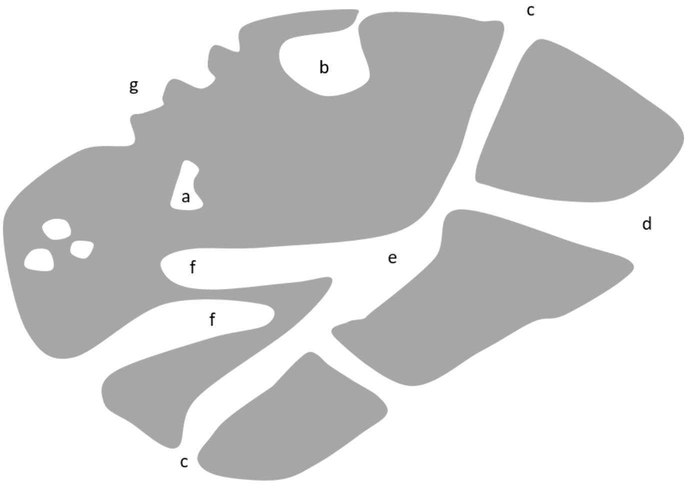

Abbildung 7: Schematische Darstellung verschiedener Porentypen. Geschlossene Poren (a) haben keine Verbindung zu Nachbarporen. Die Porentypen b-g werden als offene Poren bezeichnet und tragen zur spezifischen Oberfläche bei. Es existieren auch sogenannte Sackgassenporen (b und f). Rauigkeiten an der Oberfläche (g) können auch als Poren angesehen werden. Adaptiert von *Open Chem.* 2007 mit CC BY-NC-ND Lizenz, Copyright (2007) De Gruyter.[124]

2.3.1. Synthese von mesoporösen Metallchalkogeniden mit dem Templatverfahren

Zur Herstellung von mesoporösem $NiFe_2O_4$ (siehe Kapitel 3.1.) wurde in dieser Arbeit ein Templatverfahren angewandt. Die nasschemische Methode basiert auf dem Einsatz von Strukturgebern, den sogenannten Templaten. Es existieren zwei Arten von Templaten: Exo- und Endotemplate.

Beim Exotemplatverfahren (englisch *hard templating*), welches in **Abbildung 8a** schematisch dargestellt ist, wird der zu synthetisierende Feststoff um ein bereits bestehendes mesoporöses Gerüst herum aufgebaut, welche zu einem späteren Zeitpunkt wieder entfernt wird.[127] Als Exotemplat kann zum Beispiel mesoporöses Siliciumdioxid (SiO_2) fungieren, wie zum Beispiel SBA-15 (*Santa Barbara Amorphous-15*) mit hexagonaler 2D Porenstruktur oder KIT-6 (*Korean Advanced Institute of Science and Technology-6*), welches eine kubische 3D Porenstruktur aufweist. In den Poren des Gerüstmaterials wird der Feststoff durch eine Sol-Gel-Reaktion hergestellt und anschließend durch eine Kalzinierungsprozedur stabilisiert beziehungsweise auskristallisiert. Im abschließenden Schritt wird das Exotemplat wieder entfernt. Im Fall von SiO_2 kann dies durch eine Behandlung mit Säuren erfolgen.[128] Das finale Produkt ist demnach die negative Replika des Ausgangsmaterials. Vorteilhaft für die Herstellung eines geordnet porösen Festkörpers ist die Präsenz von Mikroporen im Exotemplat, denn dadurch wird die spätere Porenstruktur stabilisiert.[129] Eine Ordnung der Poren ist bei dem Verfahren demnach relativ einfach zu erreichen. Mit dem Exotemplatverfahren konnten Yen *et al*. bereits geordnet mesoporöses $NiFe_2O_4$ mit einer hohen spezifischen Oberfläche von 250 $m^2\,g^{-1}$ herstellen.[130] Bei dem Exotemplatverfahren finden während der Kalzinierung allerdings oft unerwünschte chemische Prozesse zwischen Templat und den Reagenzien statt. Im Fall der Verwendung von SiO_2-Templaten können sich beispielsweise Silicate bilden. Weiterhin sind die Porenparameter, wie zum Beispiel Größe, Form und Anordnung, schlecht einstellbar, da diese von der Morphologie des Exotemplats bestimmt werden. Die morphologische Vielfalt der Exotemplate ist jedoch beschränkt.[131]

Die Alternative zur Porenerzeugung mit dem Exotemplatverfahren stellt das Endotemplatverfahren dar (englisch *soft templating*), dessen Ablauf in **Abbildung 8b** schematisch gezeigt ist. Der Vorteil bei dem Verfahren ist, dass die Porenparameter bei dem Verfahren leicht durch die Änderung verschiedener Reaktionsparameter variiert werden können. Als Template bei dem Verfahren werden Tenside oder Blockcopolymere eingesetzt. Solche amphiphilen Substanzen haben die Eigenschaft, in Lösung unter bestimmten Bedingungen Aggregate zu bilden, die sogenannten Mizellen. Mehrere Mizellen können sich zufällig arrangieren oder auch durch Van-der-Waals-Kräfte und Wasserstoffbrückenbindungen geordnete Strukturen entwickeln.[132] Mizellen können von amphiphilen Verbindungen gebildet werden, das heißt, sie bestehen aus einem hydrophilen und hydrophoben Teil.

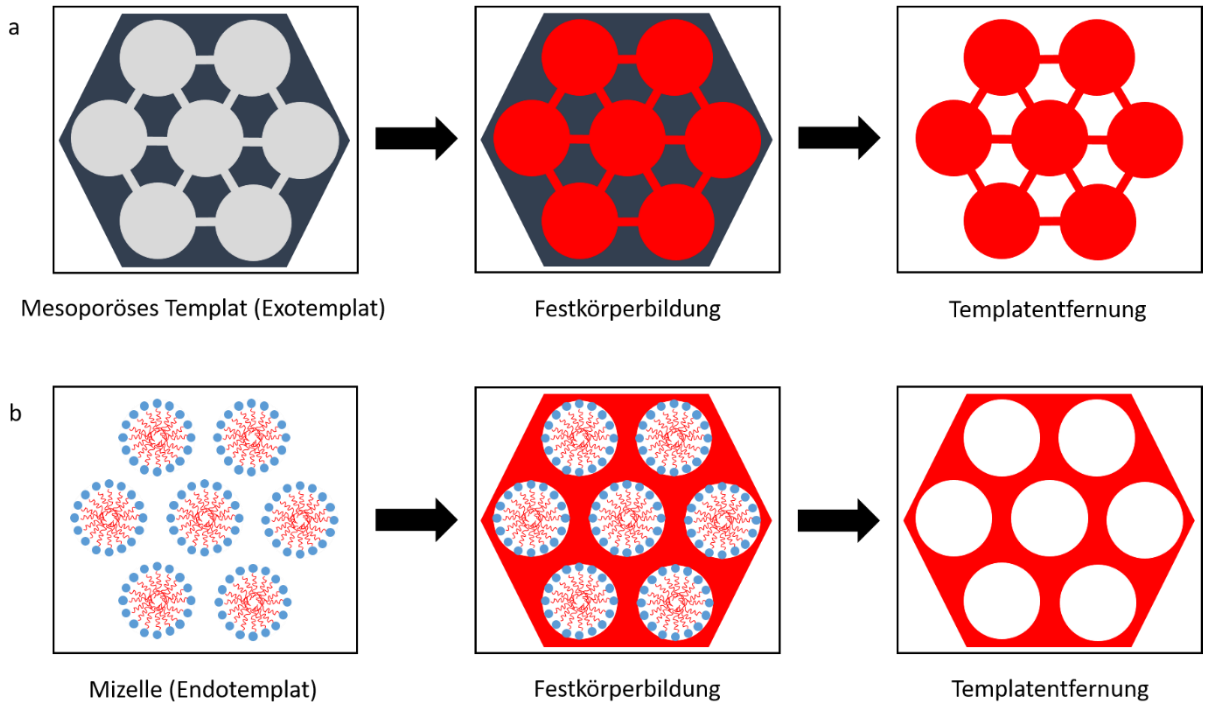

Abbildung 8: Schematische Darstellung der Templatverfahren zur Herstellung mesoporöser Feststoffe. (a) Beim Exotemplatverfahren wird der zu synthetisierende Feststoff in einem bereits porösen Gerüstmaterial aufgebaut, welches zu einem späteren Zeitpunkt wieder entfernt wird. (b) Das Endotemplatverfahren basiert auf dem Einsatz von strukturdirigierenden Reagenzien, wie zum Beispiel grenzflächenaktive Tenside oder Blockcopolymere. Diese können in Lösung Agglomerate (Mizellen) bilden, um die sich der gewünschte Feststoff bilden kann. Das Endotemplat wird durch Extraktion oder Temperaturbehandlung zu einem späteren Zeitpunkt entfernt, wodurch final der poröse Feststoff erhalten wird. Adaptiert von *Chem. Soc. Rev.* 2011 mit Genehmigung, Copyright (2011) Royal Society of Chemistry.[133]

Ein Beispiel für eine solche amphiphile Substanz stellt das in dieser Arbeit verwendete symmetrische Blockcopolymer Pluronic® P-123 dar,[134] welches hydrophile Polyethylenoxid- (PEO) und hydrophobe Polypropylenoxid-Einheiten (PPO) enthält (**Abbildung 9a**). In Lösungsmitteln kann P-123 mizellenartige Strukturen entwickeln. In wässrigen Medien zeigen dabei die PEO-Blöcke zum Wasser hin und bilden damit das Äußere der Mizelle, während die PPO-Blöcke im Inneren der Mizelle keinen direkten Wasserkontakt aufweisen (**Abbildung 9b**). Die Mizellen können abhängig von Temperatur und Konzentration eine hexagonale 2D oder eine kubische 3D Anordnung ausbilden[135,136] und werden unter anderem zur Herstellung der Exotemplate SBA-15 und KIT-6 verwendet.

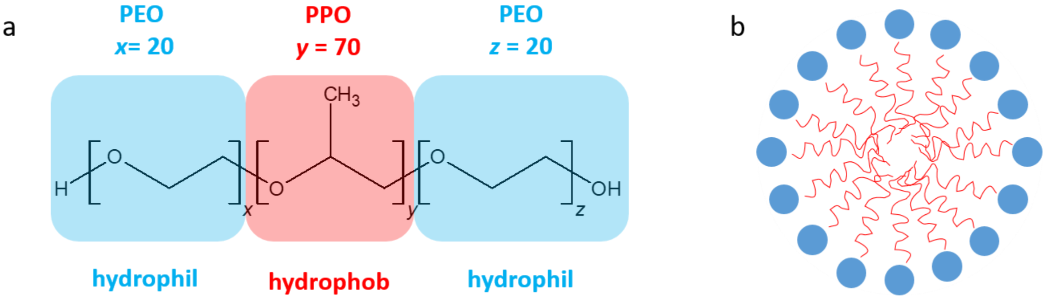

Abbildung 9: (a) Struktur des amphiphilen Blockcopolymers Pluronic® P-123 mit hydrophilen Polyethylenoxid- (PEO) und hydrophoben Polypropylenoxid-Blöcken (PPO). (b) In Lösungsmitteln, wie zum Beispiel Wasser, können sich mizellenartige Strukturen bilden, indem sich die Baueinheiten gemäß ihrer hydrophilen oder hydrophoben Eigenschaften ausrichten.[135]

Um diese Endotemplatstruktur kann sich in einem Sol-Gel-Prozess durch Hydrolyse und einer sich anschließenden Kondensation der amorphe Feststoff ausbilden. Oft wird die Reaktion so geführt, dass die Reaktionsmischung langsam eingetrocknet wird, sodass dabei die kritische Mizellbildungskonzentration (englisch *critical micelle concentration*, CMC) erreicht wird. Die CMC beschreibt genau die Konzentration der amphiphilen Verbindungen, bei der sich Mizellen bilden können. Durch das langsame Verdampfen des Lösungsmittels wird auch die Sol-Gel-Reaktion beschleunigt, wodurch sich schließlich ein dreidimensionales Netzwerk ausbildet, welches auch als Flüssigkristall bezeichnet wird. Das beschriebene Verfahren heißt verdampfungsinduzierte Selbstassemblierung (englisch *evaporation-induced self-assembly*, EISA). Das organisch-anorganische Hybridmaterial wird schließlich vollständig getrocknet und abschließend temperaturbehandelt, was dazu führt, dass das gewünschte Metalloxid auskristallisiert und das organische Templat entfernt wird. Bei der Kalzinierung darf kein Lösungsmittel mehr vorhanden sein, da sonst Quellung oder Druckerhöhung durch plötzlich entstehende Gasmoleküle die Porenstruktur zerstören können. Die Templatentfernung kann alternativ auch durch Extraktion zum Beispiel mit Salzsäure erfolgen,[128] insofern das herzustellende Material gegenüber dem Extraktionsmedium chemisch stabil ist. Die Morphologie des Metalloxids entspricht dann der negativen Replika der vorausgehenden Mizellenstruktur. Die Kalzinierung des Metalloxids darf nur bei solchen Temperaturen erfolgen, bei denen noch kein ausgeprägtes Kristallitwachstum zu erwarten ist. Kristallitwachstum ausgehend von den Porenwänden würde dazu führen, dass die Poren kollabieren. Dementsprechend muss die Kalzinierungstemperatur gemäß dem Kristallisationsverhalten des herzustellenden Materials und der thermischen Zersetzung des Templats ausgewählt werden. Bei dem Endotemplatverfahren können Porengröße, Porenvolumen und Porenordnung durch verschiedene Parameter eingestellt beziehungsweise optimiert werden, wie zum Beispiel durch die Wahl des Lösungsmittels oder -gemisches, die Konzentrationen von Endotemplat und Metall-Präkursoren, die Art der Trocknungsprozedur und die Art der Kalzinierungsprozedur.[137,138]

Aus diesem Grund wird in der vorliegenden Arbeit das Endotemplatverfahren zur Synthese von mesoporösem $NiFe_2O_4$ verwendet. Dieses basiert auf dem Einsatz der Template Pluronic® P-123 (Poly-(ethylenglykol)-*block*-poly-(propylenglykol)-*block*-poly-(ethylenglykol)) und Zitronensäure, welche in Wasser gelöst werden. Ausgehend von den Nitratsalzen kann sich dann um die Templatstruktur ein Netzwerk aus amorphem $NiFe_2O_4$ ausbilden. Durch Kalzinierung werden abschließend die Templat-Moleküle entfernt und das mesoporöse ternäre Übergangsmetalloxid erhalten. Der Einsatz von Zitronensäure hat bei der Kalzinierung den zusätzlichen Vorteil, dass sich dabei amorphe Carbonate bilden können. Die Bildung von amorphen Carbonaten verzögert hier die Oxidbildung, was ein mögliches Kristallitwachstum des Oxids und den Porenkollaps verhindern kann.[139,140] Durch die Wahl der Template und der Kalzinierungstemperatur kann die Materialmorphologie leicht modifiziert werden. Dies ermöglicht die Untersuchung des Zusammenhangs zwischen Morphologie und Aktivität in der elektrokatalytischen Wasseroxidation, bei gleichzeitig konstanter Zusammensetzung der Proben.

2.3.2. Mikrowellensynthese von Metallchalkogenid-Nanopartikeln und -Nanoschichten

Eine Alternative zur mesoporösen Morphologie stellen Nanopartikel dar. Durch die Verkleinerung der Partikelgröße auf < 100 nm kann die spezifische Oberfläche signifikant erhöht werden. Allerdings tendieren Nanopartikel dazu, Agglomerate zu bilden.[129] Der Kontakt von Nanopartikeln verringert die zugängliche Oberfläche. Die Agglomeration kann durch den Einsatz von verschiedenen Funktionalisierungsreagenzien wie beispielsweise Betain-Hydrochlorid, Ölsäure, Oleylamin, Zitronensäure oder Polyvinylpyrrolidon (PVP) wirksam vermieden werden. Solche Substanzen lagern sich an der Partikeloberfläche an und verhindern durch verschiedene Abstoßungsmechanismen deren Annäherung.[141]

Für die Synthese von Nanopartikeln existieren mehrere etablierte nasschemische Methoden, unter anderem die Co-Ausfällung, Thermaldekomposition, Mikrowellensynthese oder Solvothermalsynthese.[142] Die Co-Ausfällung basiert zunächst auf dem Lösen der Reaktionsedukte, um diese zu homogenisieren. Die Reaktion und Fällung erfolgt schließlich durch Zugabe einer weiteren Lösung. Mit dieser Methode stellen Krishnakanth *et al.* Nickel(II)-oxid-Nanopartikel (NiO) her. Dabei wird das Nitrat-Salz zunächst in Wasser gelöst und mit einer basischen Lösung als Hydroxid gefällt, welches dann durch eine Temperaturbehandlung in das Oxid überführt wird.[143] Bei der thermalen Zersetzung werden die Metall-Präkursoren meist in einem Solvens gelöst, welches einen Siedepunkt aufweist, der höher ist als die Zersetzungstemperaturen der Metall-Präkursoren, was dann zur Bildung eines Metalloxids führt. Ein Beispiel für eine solche Synthese stellt die von Wang *et al*. vorgestellte Methode zur Herstellung von nanopartikulärem Mangan(II,III)-oxid (Mn_3O_4) dar, die auf der Thermaldekomposition des Nitrats mit einer Zersetzungstemperatur von 37 °C gelöst in Octadecylamin basiert, welches bei 349 °C siedet.[144] Bei der Solvothermalsynthese wird das Solvens mit den gelösten Reaktionsedukten durch Temperaturerhöhung über den Siedepunkt einem hohen Druck ausgesetzt. Unter solchen Bedingungen werden Interaktionen zwischen den Reaktanden intensiviert, wodurch das kristalline Produkt entsteht. Für solche Solvothermalsynthesen werden gasdichte Reaktoren eingesetzt, die Autoklaven. Mit dieser Methode sind viele Metalloxide zugänglich. Chen und Xu beschreiben beispielsweise die Synthese von nanopartikulärem Fe_3O_4. Dazu wird Eisen(II)-methoxyethoxid in einer Mischung aus Wasser und 2-Methoxyethanol gelöst und bei einer vergleichsweise niedrigen Reaktionstemperatur von 140 °C zu Fe_3O_4 umgesetzt.[145] Die Mikrowellensynthese ist mit der Solvothermalsynthese verwandt, jedoch wird Mikrowellenstrahlung zum Aufheizen genutzt. Dadurch kann eine rasche Erwärmung innerhalb von einigen Sekunden realisiert werden, wobei die Erhitzung der Reaktionslösung homogen erfolgt. Der optimale Energietransfer führt zu verkürzten Reaktionszeiten, wodurch auch der Energiebedarf signifikant gesenkt werden kann. Die Reaktionsparameter können bei der Mikrowellensynthese exakt gesteuert werden.[146] In einigen Fälle ist die *post*-synthetische Temperaturbehandlung der gewonnenen Nanopartikel sinnvoll, um zum Beispiel die Kristallisation des Metalloxids abzuschließen oder organische Rückstände der Reaktionsedukte zu entfernen.

Die Vorteile der Mikrowellensynthese werden in dieser Arbeit dazu genutzt, um $NiFe_2O_4$-Nanopartikel effizient herzustellen. Durch eine anschließende Kalzinierung können morphologische Parameter, wie zum Beispiel die Partikelgröße oder der Kristallisationsgrad, variiert werden und die Auswirkungen auf die Aktivität in der elektrokatalytischen Wasseroxidation untersucht werden. Die nicht-wässrige Methode basiert auf einem nukleophilen Angriff von Benzylalkohol oder eines Derivats an ein Metall-Acetylacetonat, infolgedessen es zur Bildung von Benzylacetat kommt (**Abbildung 10a**). Ein weiteres Benzylalkohol-Molekül koordiniert schließlich an das Metallzentrum des entstandenen Enolats, wodurch unter Freisetzung von Aceton ein Ligandenaustausch erfolgt (**Abbildung 10b**). Mit einem weiteren Benzylalkohol-Molekül kommt es zur Eliminierung eines Ethers, welche zusätzlich durch das Metallzentrum katalysiert wird (**Abbildung 10c**). Zurück bleibt das hydrolysierte Metallzentrum, das nun mit einem weiteren hydrolysierten Metallzentrum unter Abspaltung von Wasser kondensieren kann, was für die Bildung einer ausgedehnten Metalloxid-Struktur notwendig ist.[147,148]

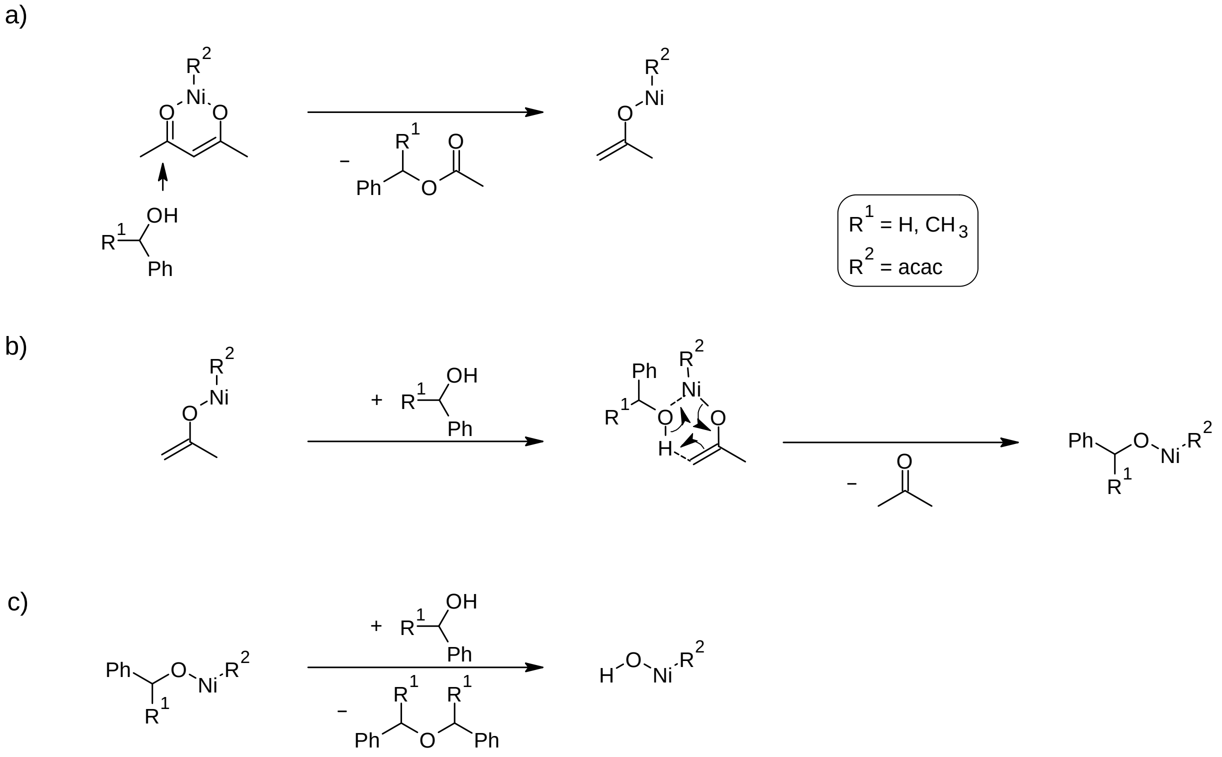

Abbildung 10: Postulierter Mechanismus der Reaktion von Metall-Acetylacetonaten mit Benzylalkohol, hier gezeigt für Nickel(II)-acetylacetonat ($Ni(acac)_2$). (a) Zuerst wird durch den nukleophilen Angriff von Benzylalkohol an $Ni(acac)_2$ ein Metall-Enolat gebildet. (b) Ein weiteres Benzylalkohol-Molekül koordiniert dann an das gebildete Enolat, wodurch unter Freisetzung von Aceton ein Ligandenaustausch erfolgt. (c) Mit einem weiteren Molekül Benzylalkohol wird zuletzt unter Abspaltung eines Ethers das Nickel-Hydroxid gebildet, welches nun mit weiteren hydrolysierten Metallzentren unter Wasserabspaltung kondensieren kann (c). Adaptiert von *Chem. – An Asian J.* 2008 mit Genehmigung, Copyright (2008) WILEY-VCH Verlag GmbH & Co. KGaA, Weinheim.[147]

Die beschriebene Reaktion wurde bereits für verschiedene spinellartige Ferrite angewandt, wie zum Beispiel $ZnFe_2O_4$[149,150] und $MgFe_2O_4$.[59,141] Die in dieser Arbeit thematisierte Mikrowellen-basierte Darstellung von phasenreinen $NiFe_2O_4$-Nanopartikeln (Kapitel 3.2.) basiert auf der Reaktion von Nickel(II)-acetylacetonat (Ni(acac)$_2$) und Eisen(III)-acetylacetonat (Fe(acac)$_3$) mit dem Lösungsmittel *rac*-1-Phenylethanol, einem Benzylalkohol-Derivat. Dabei sind morphologische Parameter justierbar über die Synthesetemperatur in der Mikrowelle (200-240 °C) und die Kalzinierungstemperatur (300-500 °C). Die Reaktion ist auch auf das aufgrund der ausgeprägten magnetischen Eigenschaften interessante Manganferrit ($MnFe_2O_4$) anwendbar, was detailliert in Kapitel 3.3. erläutert wird.

Aus dem Reaktionsmechanismus wird ersichtlich, dass das Sauerstoff-Atom des Benzylalkohols direkt in das entstehende Metalloxid eingebaut wird. Aus diesem Grund kann durch den Austausch von Benzylalkohol mit einem Schwefel-Analogon ein entsprechendes Sulfid hergestellt werden, was Ludi *et al.* bereits für die binären Sulfide Zink(II)-sulfid (ZnS) und Zinn(IV)-sulfid (SnS_2) zeigen konnten.[151] Kapitel 3.4. beschreibt die Darstellung des ternären Thiospinell-Elektrokatalysators Ni_2FeS_4 ausgehend von Ni(acac)$_2$ und Fe(acac)$_3$ bei 200 °C. Als Lösungsmittel wird ein Gemisch aus *rac*-1-Phenylethanol und Benzylmercaptan verwendet (**Abbildung 11**). Auffallend ist, dass bei dieser Reaktion Nickel oxidiert ($Ni^{2+} \rightarrow Ni^{3+}$) und Eisen reduziert ($Fe^{3+} \rightarrow Fe^{2+}$) wird. Außerdem bilden sich hier keine Nanopartikel, sondern plättchenartige Strukturen, die auch als Nanoschichten bezeichnet werden.

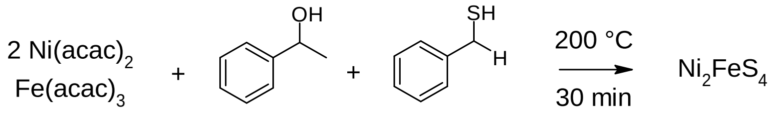

Abbildung 11: Mikrowellen-basierte Herstellung des Thiospinells Ni_2FeS_4 als Nanoschichten. Dazu werden die Metall-Acetylacetonate in einem Gemisch aus *rac*-1-Phenylethanol und Benzylmercaptan gelöst und bei 200 °C in einem Mikrowellenreaktor behandelt. Der postulierte Mechanismus läuft ähnlich dem in **Abbildung 10** gezeigten Mechanismus für die Bildung von Metalloxiden ab. Entnommen aus *ACS Appl. Energy Mat.* 2021 mit Genehmigung, Copyright (2021) American Chemical Society.

2.3. Problemstellung und Kurzüberlick über die verwendeten Untersuchungsmethoden

Die vorliegende Arbeit "Darstellung und Charakterisierung von nanostrukturierten Eisen-basierten Übergangsmetall-Chalkogeniden mit Spinellstruktur für die Anwendung in der elektrokatalytischen Wasseroxidation und Kohlenstoffdioxidreduktion" beschäftigt sich zunächst mit der Herstellung der vorgestellten Materialien $NiFe_2O_4$, $MnFe_2O_4$ und Ni_2FeS_4. Den Materialien ist gemeinsam, dass sie zwei- oder dreiwertiges Eisen enthalten, wobei Eisen eines der am häufigsten vorkommenden Elemente in der Erdkruste ist (Massenanteil $w = 6{,}20\ \%$).[152,153] Die Elemente Nickel ($w = 0{,}008\ \%$)[154] und Mangan ($w = 0{,}106\ \%$)[152] sind auch vergleichsweise gut verfügbar. Dadurch ist eine kostengünstige Herstellung der aufgeführten Spinelle möglich. Grundlage für weitergehende Untersuchungen an den hergestellten Materialien ist zunächst die Phasenreinheit, denn Fremdphasen können Eigenschaften der Spinelle verfälschen und andere elektro(katalytische) Aktivitäten aufweisen. Dementsprechend wird in den vier folgenden Veröffentlichungen die Phasenzusammensetzung der hergestellten Spinelle detailliert mit verschiedenen Analysemethoden betrachtet. Die wichtigste Methode stellt hierbei die Röntgendiffraktometrie dar, womit die kristalline Struktur einer Probe erforscht werden kann. Um potenzielle

Fremdphasen wie α-Fe_2O_3 (Mineralname Hämatit) sicher auszuschließen, sind zudem weitere Experimente mit anderen Methoden wie Ramanspektroskopie oder energiedispersiver Röntgenspektroskopie (englisch *energy dispersive X-ray spectroscopy*, EDXS) enthalten. Die durchgeführten Synthesen haben weiterhin das Ziel, die Spinelle in Form von Nanopulvern zu erhalten. Der oxidische Spinell $NiFe_2O_4$ wird daher mithilfe einer Templatierungsreaktion als mesoporöser Festkörper und durch eine Mikrowellensynthese in Form von Nanopartikeln hergestellt, deren Größe über eine thermische Nachbehandlung einstellbar ist. Die Mikrowellensynthese von $MnFe_2O_4$ führt ebenfalls zu sphärischen Nanopartikeln, die sich aber durch eine thermische Nachbehandlung in die binären Komponenten zersetzen können. Mit einer modifizierten Mikrowellen-basierten Synthese können Ni_2FeS_4-Nanoschichten erfolgreich hergestellt werden. Zur Analyse der erzeugten Nanostrukturen werden insbesondere Physisorptionsmessungen und die Elektronenmikroskopie (englisch *scanning electron microscopy*, SEM und *transmission electron microscopy*, TEM) herangezogen. Die Physisorptionsmessung ist insbesondere im Falle des mesoporösen $NiFe_2O_4$ äußerst leistungsstark, weil nicht nur die spezifische Oberfläche ermittelt werden kann, sondern anhand der Form der sogenannten Isotherme die Porenmorphologie beurteilt werden kann.[155] So lässt sich mit Hysterese-Scans beweisen, dass im Fall von $NiFe_2O_4$ ein unabhängiges Porensystem vorliegt, dessen Poren unabhängig voneinander mit Gas befüllt beziehungsweise entleert werden können, was für die spätere Anwendung in der Wasseroxidation von Vorteil ist. Zur Untersuchung von porösen Materialien mit Hysterese-Scans werden die Poren durch Einstellung von bestimmten Relativdrücken nur teilweise gefüllt. Die Charakteristika der Desorptions-Scans lassen dann Rückschlüsse auf die Porenkonnektivität zu.[156] Ein weiterer Schwerpunkt der Veröffentlichungen liegt auf der Analyse der magnetischen Eigenschaften der hergestellten Spinelle, insbesondere der $NiFe_2O_4$- und $MnFe_2O_4$-Nanopartikel. Dazu sind SQUID-Messungen (englisch *superconducting quantum interference* device) inkludiert. Die Art der Kationen und die Verteilung in der Spinellstruktur führt zu hohen Sättigungsmagnetisierungen, die zudem teilweise durch die Wahl der Partikelgröße einstellbar sind. Die hergestellten $NiFe_2O_4$ Pulver sind potenzielle Elektrokatalysatoren für die alkalische Wasseroxidation. Allerdings hängt die Performance des Materials stark von verschiedenen Faktoren ab, wie zum Beispiel Morphologie, Inversionsgrad oder potentielle Verunreinigungen. Das Exempel des mesoporösen $NiFe_2O_4$ zeigt, dass eine poröse Struktur mit einem Porensystem, dessen Poren unabhängig voneinander befüllt und entleert werden können, eine Performanceverbesserung bewirkt. Die Experimente an den $NiFe_2O_4$-Nanopartikeln zeigen darüberhinausgehend, dass eine Partikelgröße von 7 nm optimal für die Aktivität als Elektrokatalysator ist. Bei größeren Partikeln ist die spezifische Oberfläche zu niedrig, bei kleineren Partikeln ist die Aktivität ebenfalls herabgesetzt, was aus einem veränderten Inversionsgrad oder einer isolierenden organischen Schutzschicht resultiert. Eine Anwendung in der alkalischen Wasseroxidation ist für die Ni_2FeS_4-Nanoschichten, die auch durch eine Mikrowellensynthese dargestellt wurden, aufgrund von Stabilitätsproblemen zunächst nicht sinnvoll. Allerdings ist als anorganisches Analogon der Kohlenmonoxiddehydrogenase (CODH) mit den [Ni-4Fe-5S] Zentren eine Aktivität in der elektrochemischen Reduktion von Kohlenstoffdioxid denkbar. Tatsächlich zeigen erste Untersuchungen, dass die Herstellung von Synthesegas aus einer wässrigen mit CO_2 gesättigten Lösung mit Ni_2FeS_4 möglich ist.

3. Resultate

3.1. Elektrokatalytische Wasseroxidation mit mesoporösem $NiFe_2O_4$

3.1.1. Synopsis

In den Kapiteln 3.1. und 3.2. wird der $NiFe_2O_4$-Spinell und die Anwendung in der elektrokatalytischen Wasseroxidation in alkalischen Elektrolyten behandelt. $NiFe_2O_4$ dient hierbei als Modellsubstanz, um den Einfluss einer Oberflächenstrukturierung auf die elektrokatalytische Aktivität detailliert zu untersuchen. Die Veröffentlichung in *ChemElectroChem* beschreibt die einfache Herstellung von mesoporösem $NiFe_2O_4$ durch eine Endotemplatsynthese, welche auf dem Einsatz der strukturdirigierenden Reagenzien Pluronic® P-123 (Poly-(ethylenoxid)-*block*-poly-(propylenoxid)-*block*-poly-(ethylenoxid)), im Folgenden als P-123 abgekürzt, und Zitronensäure ($C_6H_8O_7$) basiert (siehe Kapitel 2.3.1.). Die Synthese geht von den Nitratsalzen als Metall-Präkursoren aus, die in Wasser gelöst werden. Nach der Zugabe von P-123, Zitronensäure oder beiden Substanzen kombiniert erfolgt das langsame Eintrocknen der Reaktionsmischung und anschließend die Behandlung des Rückstands in einem Vakuumtrockenschrank, um letzte Lösungsmittelreste zu entfernen. Wären bei der späteren Kalzinierung noch Lösungsmittelreste anwesend, würde das simultane Verdampfen dieser eine Druckerhöhung bewirken, wodurch es zu einem Kollaps der erzeugten Porenstruktur kommen könnte. Ist Zitronensäure bei der Temperaturbehandlung an Luft zugegen, bilden sich während des Aufheizprozesses bei *circa* 230 °C amorphe Carbonate aus, was durch thermogravimetrischen Messungen und Infrarotspektroskopie bewiesen werden kann. Die postulierten Carbonate sind bis etwa 340 °C präsent und können die poröse Struktur während der Kalzinierung stabilisieren, da kein Kristallitwachstum stattfindet. Die weitere Temperaturerhöhung bewirkt eine Umwandlung zum oxidischen Material, welches bei 400 °C noch eine amorphe Charakteristik aufweist. Die Kalzinierung bei 450 °C und 550 °C führt zu einer Umwandlung zum kristallinen $NiFe_2O_4$. Es konnte zudem festgestellt werden, dass die Zugabe von Zitronensäure als Komplexbildner notwendig ist, um $NiFe_2O_4$ phasenrein herzustellen. Andernfalls ist die Vermischung der Metall-Präkursoren inhomogen, was nach der Kalzinierung zur Bildung einer thermodynamisch stabilen Nebenphase (α-Fe_2O_3) führt. Die Variation der Reagenzien und der Kalzinierungstemperatur bietet die Möglichkeit, die Mesostruktur des Materials zu modifizieren. Auf diesem Weg können phasenreine $NiFe_2O_4$-Pulver mit spezifischen Oberflächen von 44-220 $m^2\,g^{-1}$ dargestellt werden, mit Porengrößen von 5-12 nm und Porenvolumina von 0,13-0,31 $cm^3\,g^{-1}$. Eine besondere Charakteristik, welche durch Stickstoff-Physisorptionsmessungen kombiniert mit Hysterese-Scans detailliert untersucht wurde, ist das offen zugängliche Porensystem der Festkörper, in dem die Poren unabhängig von Nachbarporen mit Gas befüllt und wieder entleert werden können. Die mesoporösen $NiFe_2O_4$-Pulver, kalziniert bei 400 °C, 450 °C und 550 °C, wurden hinsichtlich ihrer Aktivität in der elektrokatalytischen Wasseroxidation untersucht, speziell im Hinblick auf den Einfluss der Oberflächenmorphologie. Es zeigte sich, dass die Aktivität stark von Parametern wie der Porenhomogenität, Porengröße, zugänglichen Oberfläche und Kristallinität abhängt. Um die Aktivität zu optimieren, ist eine Maximierung der spezifischen Oberfläche essentiell. Die Kristallinität spielt nur eine untergeordnete Rolle. Für die Erzeugung einer solchen Struktur ist eine Kalzinierungstemperatur von 400 °C ausreichend, wodurch eine energieintensive Temperaturbehandlung bei 550 °C vermieden werden kann. Mit dem mesoporösem $NiFe_2O_4$-Elektrokatalysator, hergestellt mit Zitronensäure als einzigem strukturgebenden Templat und kalziniert bei 400 °C, kann das Überpotential für die Wasseroxidation auf 410 mV gesenkt werden.

3.1.2. Veröffentlichung in *ChemElectroChem*

Christopher Simon,[a] Jana Timm,[a] David Tetzlaff,[b,c] Jonas Jungmann,[a] Ulf-Peter Apfel,[b,c] Roland Marschall[a]

Mesoporous $NiFe_2O_4$ with Tuneable Pore Morphology for Electrocatalytic Water Oxidation

Veröffentlicht in: *ChemElectroChem* **2021**, *8*, 227-239.

Einflussfaktor *ChemElectroChem* (2021): 4,590
https://doi.org/10.1002/celc.202001280

[a] Department of Chemistry, University of Bayreuth, Universitaetsstrasse 30, 95447 Bayreuth, Germany
[b] Inorganic Chemistry I – Bioinorganic Chemistry, Ruhr-University Bochum, Universitaetsstrasse 150, 44801 Bochum, Germany
[c] Fraunhofer Institute for Environmental, Safety, and Energy Technology, Osterfelder Strasse 3, 46047 Oberhausen, Germany

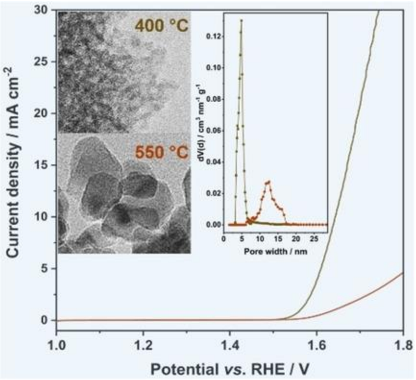

Individuelle Beiträge:

Das Konzept des Manuskripts wurde entwickelt von Prof. Dr. Ulf-Peter Apfel, Prof. Dr. Roland Marschall und mir. Es wurde verfasst von Dr. Jana Timm, Prof. Dr. Roland Marschall und mir mit Beiträgen von allen Co-Autoren. Die Syntheseexperimente wurden alle von mir durchgeführt, ebenso wie die grundlegende Charakterisierung der mesoporösen Pulver (Röntgendiffraktometrie, Ramanspektroskopie, Infrarotspektroskopie, Rasterelektronenmikroskopie gekoppelt mit energiedispersiver Röntgenspektroskopie und Transmissionselektronenmikroskopie gekoppelt mit Elektronenbeugung). Dr. Jana Timm und Jonas Jungmann haben die Physisorptionsmessungen und die dazugehörige Datenauswertung durchgeführt. David Tetzlaff war verantwortlich für die Durchführung der elektrokatalytischen Tests und hat bei der Datenanalyse geholfen. Die Mössbauerspektren wurden gemessen und gefittet von Dr. Florian Wittkamp (Ruhr-Universität Bochum). Die thermogravimetrischen Analysen wurden durchgeführt von Dr. Kevin Turke und Sebastian Werner (beide Justus-Liebig-Universität Gießen). Alle Autoren haben mit wissenschaftlicher Diskussion zum Manuskript beigetragen.

Mein Beitrag zum Manuskript beträgt ca. **70 %**.

ChemElectroChem
Articles
doi.org/10.1002/celc.202001280
Chemistry Europe
European Chemical Societies Publishing

Special Collection

Mesoporous $NiFe_2O_4$ with Tunable Pore Morphology for Electrocatalytic Water Oxidation

Christopher Simon,[a] Jana Timm,[a] David Tetzlaff,[b, c] Jonas Jungmann,[a] Ulf-Peter Apfel,*[b, c] and Roland Marschall*[a]

Mesoporous $NiFe_2O_4$ for electrocatalytic water splitting was prepared via soft-templating using citric-acid-complexed metal nitrates as precursors. The mesopore evolution during thermal treatment was examined systematically giving insights into the formation process of mesoporous $NiFe_2O_4$. Detailed nitrogen physisorption analysis including desorption scanning experiments reveal the presence of highly accessible mesopores generating surface areas of up to 200 m^2/g. The ability of the $NiFe_2O_4$ powders to perform electrocatalytic oxygen evolution reaction under alkaline conditions was investigated, highlighting the advantages of mesopore insertion. The most active samples reach a current density of 10 $mA\,cm^{-2}$ at an overpotential of 410 mV with a small Tafel slope of 50 $mV\,dec^{-1}$, indicating an enhanced activity that originated from the increased catalyst surface.

1. Introduction

Electrocatalytic water splitting using renewable energies to form green hydrogen and oxygen has attracted a widespread interest to replace fossil fuels as major energy carrier. Currently, the oxygen evolution half reaction (OER) is regarded to be the major bottle-neck of water splitting due to its hampered kinetics involving a multi-step proton and electron transfer. Noble metal electrocatalysts, such as RuO_2 and IrO_2 are widely used for OER, however, their prohibitive scarcity and cost limit their potential widespread use in electrolyzers. Therefore, researchers have focused on first-row transitions metal oxides like Co_xO_y,[1,2] Mn_xO_y,[3,4] Fe_xO_y,[5,6] Ni_xO_y,[7,8] and combinations thereof[9–11] as potential electrocatalysts for OER.

Among the multiple transition metal oxides, ferrites with the general formula $M^{II}Fe_2O_4$ (M = Ca, Zn, Mg, Ni, Co, Mn *etc.*) have gained considerable attention due to their compositions made up from earth-abundant elements and widespread application fields besides electrocatalysis[12–15] in gas sensing,[16,17] and photocatalysis/photoelectrochemistry.[18–27] Especially nickel ferrite has been considered as efficient OER electrocatalyst, with outstanding high stability in alkaline media, excellent redox properties, and ferromagnetism facilitating the catalyst separation from solution.[28,29] Already in 1999, N. K. Singh and R. N. Singh showed that the inverse spinel $NiFe_2O_4$ is a highly active material in the electrocatalytic water oxidation with an overpotential of 379 mV at a current density of 100 $mA\,cm^{-2}$, which outcompetes pure iron oxide (spinel Fe_3O_4).[30]

A common approach to optimize the performance of an electrocatalyst is based on the preparation of materials with high surface-to-volume ratio by means of nano-/mesostructuring.[31,32] Such porous structures provide large accessible active surface areas, and mass transport characteristics can be tailored. However, downsizing the pore size and therefore increasing the surface area limits the rate of mass transport of reactants and products influencing the overall performance. Likewise, ordering of the pores can influence mass transport characteristics during this type of reactions, too.[33] Due to the variety of parameters influencing the formation and activity of mesoporous electrocatalysts, detailed studies are necessary to understand the structure/activity relationships of mesoporous electrocatalysts.[34] Since many transition metal oxides are intrinsically poorly conductive,[35,36] shortening the diffusion pathways by nano-/mesostructuring can improve the transport of charge carriers through the material.

Various mesoporous $NiFe_2O_4$ were described in literature. For example, Haetge *et al.* reported a soft-templating route to prepare ordered mesoporous $NiFe_2O_4$ thin films with pore widths of around 16 nm, using a non-commercial KLE polymer (poly(ethylene-co-butylene)-b-poly(ethylene oxide) diblock copolymer[37]) for pseudocapacitive charge storage.[38] Jia *et al.* used a similar soft-templating approach based on the commercial Pluronic® P-123 block copolymer to synthesize non-ordered

---

[a] *C. Simon, Dr. J. Timm, J. Jungmann, Prof. R. Marschall*
Department of Chemistry
University of Bayreuth
Universitaetsstrasse 30, 95447 Bayreuth, Germany
E-mail: roland.marschall@uni-bayreuth.de
[b] *D. Tetzlaff, Prof. U.-P. Apfel*
Inorganic Chemistry I – Bioinorganic Chemistry
Ruhr-University Bochum
Universitaetsstrasse 150, 44801 Bochum, Germany
[c] *D. Tetzlaff, Prof. U.-P. Apfel*
Fraunhofer Institute for Environmental, Safety, and Energy Technology
Osterfelder Strasse 3, 46047 Oberhausen, Germany
E-mail: ulf-peter.apfel@umsicht.fraunhofer.de

Supporting information for this article is available on the WWW under https://doi.org/10.1002/celc.202001280

An invited contribution to a Special Collection dedicated to GDCh Electrochemistry: At the Interface between Chemistry and Physics

mesoporous $NiFe_2O_4$ powders for acetone detection with two major types of pores with 7 and 33 nm in diameter.[39]

Further, Gu *et al.*, Li *et al.*, and Yen *et al.* reported on ordered mesoporous $NiFe_2O_4$ (pore diameters of 7 nm, 5–25 nm, and 3–8 nm), which can be used as microwave adsorber material or bifunctional catalyst for Li-O_2 batteries. Here, the generation of the ordered mesoporous structures was based on a multi-step hard-templating strategy (nanocasting) using mesoporous silica (KIT-6, SBA-15, MCM-48) as template, which can be a time-consuming synthesis and leaves residual silica in the material.[40–42]

To avoid the disadvantages of having tedious polymer synthesis or impurities of insulating SiO_2, we herein focused on a simple, rapid, one-step soft-templating route, based on the evaporation-induced self-assembly process (EISA) using the commercially available triblock copolymer Pluronic® (P-123) and citric acid, to synthesize ordered mesoporous phase-pure $NiFe_2O_4$ powders with tunable pore sizes in the range of 5–12 nm for application in electrocatalytic oxygen evolution reaction. The porosity, pore accessibility, phase composition and crystallinity of the powders were tuned by the calcination temperature, giving insights into the importance of these parameters for application. Detailed morphological investigations including nitrogen physisorption, electron microscopy, and X-ray diffraction were performed to understand the results from electrocatalytic water oxidation studies, which reveal the influence of accessible surface area, connected pores, and crystallinity on the overall activity.

2. Results and Discussion

Micelle-templated ordered mesoporous transition metal oxides, and carbonates as their intermediates during thermal treatment, are known to be easily available *via* the formation of metal complexes with citric acid.[31,43] Therefore, this approach was followed to prepare the mixed metal oxide $NiFe_2O_4$ with highly homogeneous mesopores here by using Pluronic P-123® (P-123) with citric acid calcined at various temperatures (275 °C, 400 °C, 450 °C, 550 °C). For comparison, samples were also prepared using only P-123 and only citric acid as templates, to reveal their influence on the pore generation and activity.

The mesoporous structure of $NiFe_2O_4$ is largely affected by the calcination temperature and the synthesis conditions, in general. The concentrations of P-123 (0.03 equivalents concerning the Ni precursor) and citric acid (4.3 equivalents concerning the Ni precursor) were kept constant in order to stay well below the critical micelle concentration (cmc) before the solvent evaporation step, and to investigate the role of the templating/chelating agents and the calcination temperature. To understand the occurring processes and to investigate mesopore evolution during the synthesis in detail, we performed thermogravimetric analysis coupled with online mass spectrometry (TG-MS) with as-synthesized samples before calcination (Figure 1). Pristine P-123 shows the highest mass loss between 200 and 350 °C with maxima of the CO_2 and H_2O MS traces at 334 °C, while nickel iron oxide samples prepared only with P-123 start decomposing already at 87 °C and show then a slow decay ending at 358 °C. The corresponding CO_2 and H_2O MS traces show therefore a broad distribution in the temperature range between 87 °C and 358 °C with no distinguishable maxima. The difference in the decomposition decays of pristine P-123 and the hybrids can be explained by the different decomposition steps of precursors iron(III) nitrate and nickel(II) nitrate. Here, the decomposition of both nitrate salts is quite complex and takes place in several stages via metastable intermediates like $Ni(NO_3)_{1.5}O_{0.25}\cdot H_2O$ or $Fe_4O_4(OH)_2(NO_3)_2\cdot 2H_2O$.[44,45]

The TG curve of a nickel iron oxide sample prepared only with citric acid shows a mass loss at 130–153 °C that can be

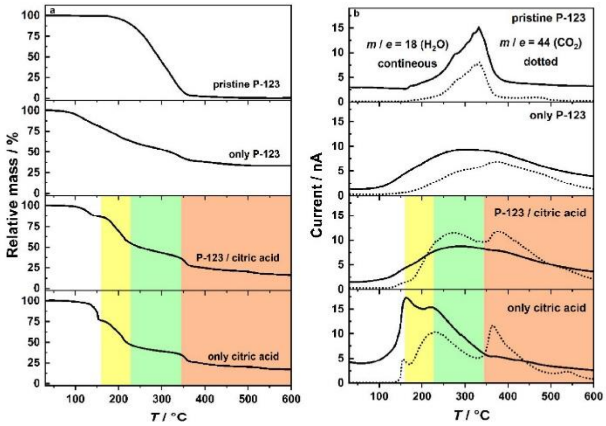

Figure 1. a) TG measurements of as-prepared $NiFe_2O_4$ samples and the pristine P-123, b) H_2O (*m/e* = 18, continuous lines) and CO_2 (*m/e* = 44, dotted lines) evolution during TG analysis monitored *via* mass spectrometry.

assigned to the loss of surface-adsorbed water, and further to a partial decomposition of citric acid, which is confirmed by the signals in the corresponding mass spectra of H_2O and CO_2 at 156/162 °C, respectively. In this case, synthesis only with citric acid, the CO_2 MS trace must result from the partial decomposition of citric acid due to the absence of any other carbon source. The 2nd decomposition step at 173–226 °C marks the decomposition of the precursor complex into intermediate carbonate species (yellow zone in Figure 1), as explained below. The 3rd decomposition step at 343–363 °C can be assigned to the transformation of these carbonates into the metal oxide (red zone in Figure 1), causing a prominent peak in the CO_2 MS trace at 364 °C, while a peak in the H_2O MS trace is missing at this temperature. Bernicke *et al.* observed a similar behavior during the citric acid-supported templating strategy of mesoporous NiO thin films.[31]

The two decomposition steps at 173–226 °C and 343–363 °C are separated by a plateau. Stable amorphous carbonate intermediates like $NiCO_3$ might be present at this temperature range (green zone in Figure 1).[31] Combination of P-123/citric acid results in a similar TG curve, compared to the TG curve of samples prepared only with citric acid, indicating the presence of intermediate carbonate species. According to the results from TG analysis, carbonates may be present between ~230 °C and ~340 °C. Furthermore, the presence of amorphous carbonates can facilitate polymer removal without sintering of pore walls.[43]

To check the presence and amorphous nature of intermediate carbonate species, as-synthesized samples were calcined at 275 °C and investigated using Cu PXRD and DRIFT spectroscopy. PXRD patterns of samples calcined at 275 °C show no reflections indicating crystalline phases (dotted line, Figure 2a). For all samples calcined at 275 °C, a prominent double peak at 1600–1400 cm^{-1} is present in the DRIFT spectra indicating carbonate anions (Figure S1).[43,46,47] When calcining these samples at 400 °C or above, no IR bands belonging to carbonate anion vibrations are present anymore, which is in agreement with the results from TG-MS analysis. Additionally, at calcination temperature 400 °C or higher an IR signal at 3699 cm^{-1} is detectable and can be attributed to O–H vibrations of isolated O–H groups on metal oxide surfaces.[48] This vibration is only IR active if no or weak hydrogen bridge bonds are present in the material. P-123 is a polar block copolymer with O–H and ether bounds, which could form strong hydrogen bridge bonds with O–H groups on the metal oxide surface.[49,50] Therefore, the appearance of the IR signal at 3699 cm ^{1} can be correlated to the complete removal of P-123. TG-MS analysis and IR spectroscopy demonstrate the role of citric acid as carbonate source in the presented synthesis. These amorphous carbonates are stable in a relatively wide temperature range of 226–343 °C.

PXRD patterns are shown in Figure 2a. As expected and in accordance with literature data,[51] the $NiFe_2O_4$ samples crystallize between 400 °C and 550 °C, which is indicated by the rise of reflections at 450 °C and especially 550 °C. In this temperature range, the carbonates are already decomposed. PXRD patterns indicate the presence of single-phase, nanocrystalline $NiFe_2O_4$ when citric acid is present during the synthesis. All reflections can be indexed according to the $NiFe_2O_4$ reference pattern (ICOD, no. 00-044-1485). In contrast, samples prepared only with P-123 without citric acid are not completely phase-pure. The impurity identified from PXRD is hematite (α-Fe_2O_3), as marked in Figure 2a.[52] SAED patterns (Figure S2) further confirm these findings. Citric acid might act as chelating agent of the cations, also preventing phase separation.[53] This finding goes in line with a decreased Ni:Fe ratio below the optimum value of 0.5 (Figure S3), which can be detected *via* EDXS for samples prepared only with P-123. Even the errors for the EDXS data of the prepared only with P-123 are remarkably higher compared to the samples where citric acid was used. These findings go in line with the already mentioned phase impurity of the samples only prepared with P-123.

For samples prepared at 550 °C, calculated averaged crystallite sizes L_{hkl} from the integral width of the (220), (400), (511) and (440) reflections are 7.6 ± 0.6 nm (sample prepared only with P-123), 12.0 ± 0.7 nm (sample prepared only with

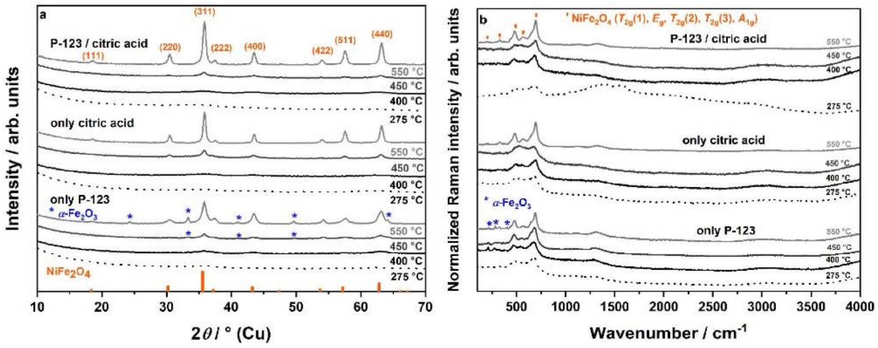

Figure 2. a) Cu PXRD patterns and b) Raman spectra of mesoporous $NiFe_2O_4$ samples calcined at 275 °C, 400 °C, 450 °C, and 550 °C. Samples were prepared only with P-123, only with citric acid, and with P-123 plus citric acid combined.

citric acid), and 10.6 ± 0.6 nm (sample prepared with P-123/citric acid).

Phase-purity was also checked by Raman spectroscopy, especially to exclude the presence of hematite by-phases, since small amounts of hematite in spinel nanocrystals might not be detected by PXRD. For cubic spinels with $Fd3m$ space group, five Raman active lattice modes were expected: A_{1g} (691 cm^{-1}) $+ E_g$ (332 cm^{-1}) $+ 3\ T_{2g}$ (201 cm^{-1}, 487 cm^{-1}, 570 cm^{-1}).[54–57] The A_{1g} signal corresponds to the symmetric stretching mode of M–O bonds in tetrahedral units. The $T_{2g}(2)$ and $T_{2g}(3)$ signals can be assigned to the asymmetric stretching mode and to the asymmetric bending of M–O bonds in octahedral units, respectively. The E_g and $T_{2g}(1)$ signals match with the symmetric bending and stretching modes of metal oxygen bonds, also located in octahedral voids. In contrast, trigonal hematite (space group R$\bar{3}$c) exhibits seven active lines in the Raman spectrum: 2 A_{1g} (225 cm^{-1}, 498 cm^{-1}) + 5 E_g (247 cm^{-1}, 293 cm^{-1}, 299 cm^{-1}, 412 cm^{-1}, 613 cm^{-1}).[58] Thus, spinel-type $NiFe_2O_4$ and trigonal hematite can clearly be distinguished by their Raman profiles. As presented in Figure 2b, the Raman modes of $NiFe_2O_4$ are present for all samples calcined at 550 °C. Additionally, the Raman spectrum of sample prepared only with P-123 additionally features prominent signals of hematite, including the intense signal at 293/299 cm^{-1}. Typically, the materials calcined at lower temperature suffer from a lack of crystallinity, thereby signal intensity decreases. However, the most intense $T_{2g}(2)$ and A_{1g} modes are visible in all Raman spectra. Occurring signals at 1100–1500 cm^{-1} can be interpreted as 2nd order peaks.[59] No signals of crystalline or amorphous carbonate species could be detected by this technique. Raman spectroscopy supported the results obtained from PXRD, pointing out that the addition of citric acid as chelating agent is mandatory to get pure $NiFe_2O_4$ materials. However, due to the small crystallites and therefore only poor Raman intensities, quantification of the occupancy of the tetrahedral and octahedral sites is not reliable.

Additionally, ^{57}Fe Mössbauer spectra of samples calcined at 550 °C, taken at ambient temperature, are presented in Figure S4. Isomer shifts (δ) of 0.32 mm/s (only citric acid, Figure S4b) and 0.25 mm/s (P-123/citric acid, Figure S4c) exhibit the presence of Fe(III) cations in two different local surroundings in the $NiFe_2O_4$ lattice. Ferric cations are coordinated tetrahedral or octahedral by oxygen anions, respectively. For those phase-pure samples, the observed sextets (hyperfine splitting) are typical of Fe cations in a permanent magnetic state. Detailed analysis display the presence of two overlapping sextets, corresponding to two iron sites. The inversion parameter X can be estimated by fitting both sextets separately.[61,62] Resulting values of 0.68 (only citric acid) and 0.35 (P-123/citric acid) indicate the presence of a partially inverse spinel. However, Agouriane *et al.* have postulated a value of $X = 0.95$–0.97 for $NiFe_2O_4$, determined by Rietveld refinement and Mössbauer spectroscopy. The significant deviations may originate from the different calcination temperature (1000 °C *vs.* 550 °C), since the calcination temperature and therefore crystallinity can have a major influence on the inversion parameter.[63,64] For sample prepared only with P-123, a third iron site is present since the sample is a phase mixture of $NiFe_2O_4$ and α-Fe_2O_3. To exclude the impact of P-123 on the formation of phase mixtures of $NiFe_2O_4$ and α-Fe_2O_3, we investigated samples in which no P-123 and no citric acid was used in the synthesis, and we find the same phase mixture of $NiFe_2O_4$ and α-Fe_2O_3 after calcination (Figure S5). Due to phase-impurities, samples prepared only with P-123 and without P-123/without citric acid will thus no longer be discussed in the following. To summarize, the phase-purity of samples prepared with citric acid as chelating agent is proven by PXRD, SAED, Raman spectroscopy, EDXS, and Mössbauer spectroscopy. The chelation of metal cations with citric acid ensures their uniform distributions, preventing phase separation successfully.

TEM images and SEM images of mesoporous $NiFe_2O_4$ samples are shown in Figure 3 and Figure S5 and S6, respectively. Generally, both TEM and SEM images show big agglomerates in the μm size range, which are characterized by sub-structures in the nm size range. The SEM images of the sample only with citric acid (Figure S6) and the sample with P-123 and citric acid (Figure S7) show nanosized spherical particles as sub-structures. Nevertheless, these sub-structures can be better resolved using TEM analysis, allowing detailed analysis of the generated morphology. TEM image of sample prepared only citric acid and calcined at 275 °C (Figure 3a) clearly demonstrates a bulk material with regularly changing material contrast, verifying a high porosity even at 275 °C. If the P-123 polymer is additionally used in the synthesis combined with citric acid (P-123/citric acid), the brighter spots are more pronounced, showing that the P-123 possibly still blocks the pores at 275 °C (Figure 3e). Increasing the temperature to 400 °C affects the transformation of the amorphous carbonates to the amorphous metal oxide (*cf.* Figure 2). The morphology of the sample with only citric acid is completely conserved at 400 °C (Figure 3b). For the sample prepared with P-123/citric acid, the voids can now be interpreted as mesopores, since the P-123 is decomposed (Figure 3f). At 450 °C, the crystallization of $NiFe_2O_4$ starts, but samples maintain their remarkable porosities (Figure 3c,g). Interestingly, morphologies of samples only with citric acid and P-123/citric acid do not distinguish significantly at 400 °C and 450 °C, showing non-ordered mesopores. This indicates that the porosity is also introduced by the use of citric acid, not solely by the P-123. At 550 °C (Figure 3 d,h), the morphologies have changed to nanoparticular structures with interparticular pores between singular nanoparticles (Scheme 1).

According to the results from PXRD, initial crystal growth occurs in this temperature range (450–550 °C), causing morphological transformations. When the synthesis is performed only with citric acid, particles with a size of (21.0 ± 4.1) nm can be observed. However, the particles are strongly agglomerated,

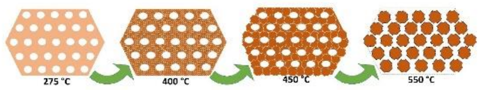

Scheme 1. Morphological transformation of mesoporous $NiFe_2O_4$ upon annealing.

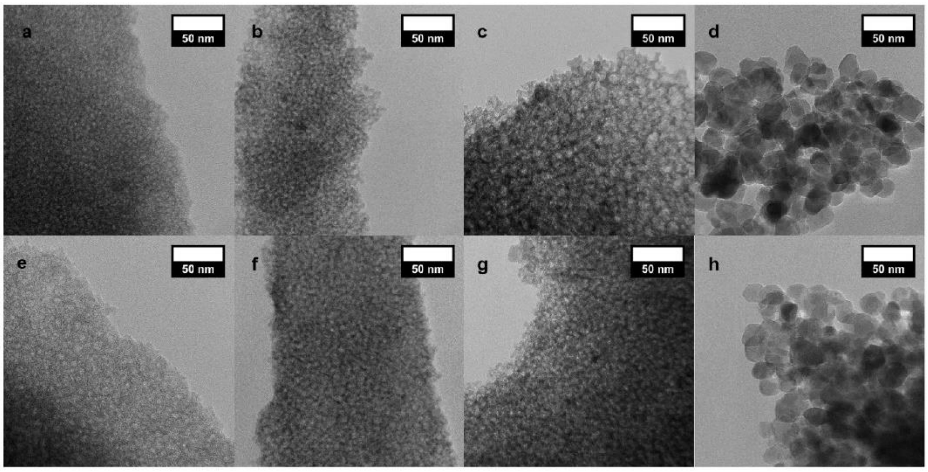

Figure 3. TEM images of mesoporous $NiFe_2O_4$ samples prepared only with citric acid calcined at 275 °C (a), 400 °C (b), 450 °C (c), and 550 °C (d). TEM images of mesoporous $NiFe_2O_4$ samples prepared with P-123/citric acid calcined at 275 °C (e), 400 °C (f), 450 °C (g), and 550 °C (h).

which impedes accurate particles size estimation. When P-123 and citric acid are combined in the synthesis, particles of a relatively uniform spherical shape with diameters of around (14.3 ± 2.4) nm are observed. The particle sizes are also slightly larger than the calculated crystallite sizes from PXRD. In general, $NiFe_2O_4$ tends to form a particular nanosized structure at 550 °C. The addition of P-123 further seem to inhibit the particle growth, resulting in different particle sizes at a calcination temperature of 550 °C (14.3 nm vs. 21.0 nm).

Detailed physisorption studies were performed to reveal the evolution of mesopores during the synthesis of $NiFe_2O_4$ (Figure 4). In Figure 4, the nitrogen physisorption isotherms of the mesoporous $NiFe_2O_4$ samples prepared under various conditions are shown. The corresponding pore size distributions and cumulative pore volumes are presented in Figure 4. The analyzed data of the nitrogen physisorption measurements are summarized in Table 1.

Physisorption isotherms show hysteresis loops clearly indicating the presence of mesopores in each prepared sample (type 4(a) isotherms, *cf.* Table 1).[65] The shape and starting p/p_0 values of the hysteresis of the physisorption isotherms differ depending on the synthesis conditions, indicating a morphological transformation in the relevant temperature range. The isotherms of the samples which were calcined only at 275 °C show already hysteresis loops indicating mesopores. The adsorption and the desorption isotherm branches of the samples prepared with P-123/citric acid are not overlapping at low relative pressure in contrast to isotherm branches of the samples without P-123 (only citric acid). This effect can be attributed to polymer residues due to swelling processes and irreversible nitrogen adsorption.[66] The specific surface area of the sample prepared with P-123/citric acid is only 53 $m^2 g^{-1}$, while the sample prepared only with citric acids exhibits a specific surface area of 285 $m^2 g^{-1}$. Residuals of P-123, which are present at 275 °C (*cf.* TG-MS and TEM analysis (Figure 1, Figure 3b)) inhibit the accessibility of the pores/ sample surface for nitrogen gas molecules and lead therefore to lower surface areas and also decreased pore volumes compared to the samples prepared only with citric acid (0.05 $cm^3 g^{-1}$ *vs.* 0.28 $cm^3 g^{-1}$). It confirms that the loss of carbonate species due to citrate addition already leads to a highly porous mesostructure. This could be further proven by the analysis of the pore sizes. Both samples with/without P-123 (P-123/citric acid and only citric acid) are already mesoporous with narrow pore size

Table 1. Results obtained from nitrogen physisorption measurements presented in Figure 4. The averaged values of three different samples and the standard deviation are presented in Table S3.

	Only citric acid				P-123/citric acid			
	275 °C	400 °C	450 °C	550 °C	275 °C	400 °C	450 °C	550 °C
Surface area [$m^2 g^{-1}$]	285	220	208	44	53	190	202	67
Pore width [nm]	5.0	5.0	5.1	12.0	4.6	6.0	5.1	10.0
Pore volume [$cm^3 g^{-1}$]	0.28	0.27	0.24	0.13	0.05	0.31	0.22	0.15

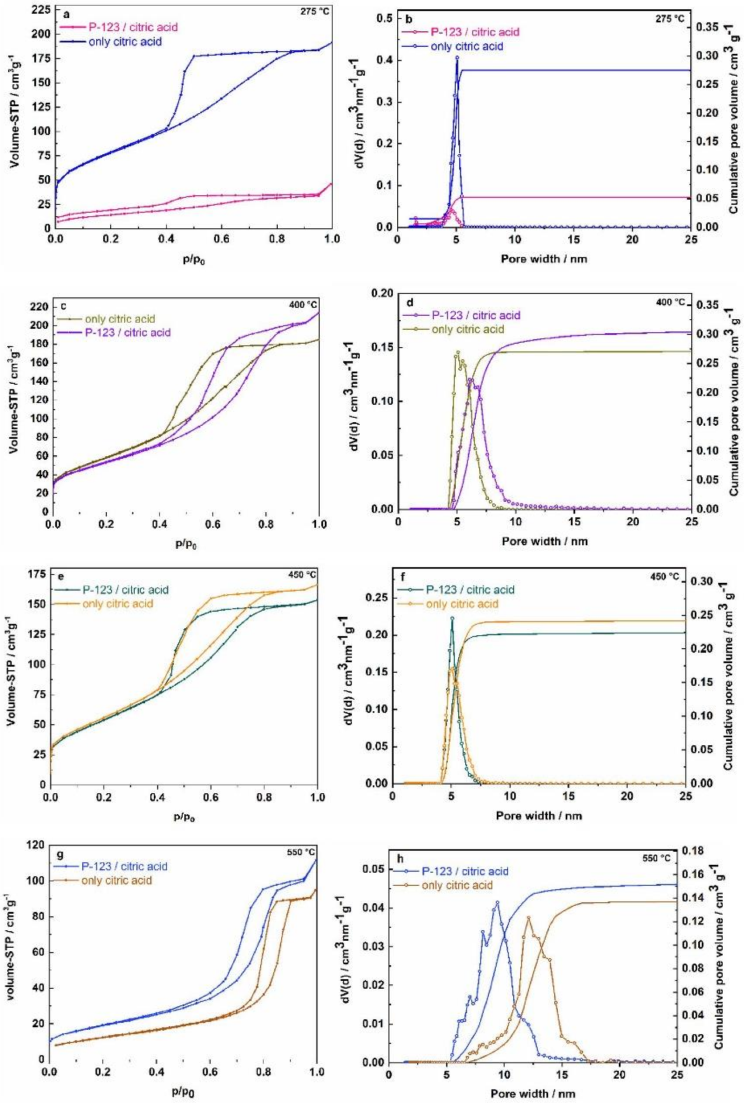

Figure 4. a, c, e, g) N_2 physisorption isotherms of samples calcined at 275 °C, 400 °C, 450 °C and 550 °C, respectively, and b, d, f, h) corresponding pore size distributions plus cumulative pore volumes (obtained by NLDFT analysis).

distribution with maxima at 4.6 nm and resp. 5.0 nm, but the pore volume is much larger when only citric acid is used. In summary, the highly mesoporous morphology of amorphous $NiFe_2O_4$ can already be gained by the usage of citric acid.

At higher calcination temperature the P-123 residues are removed, and therefore the specific surface area of the samples prepared with/without P-123 (P-123/citric acid and only citric acid) approach each other. Samples calcined at 400 °C and 450 °C have very high specific surface area of around 200 $m^2 g^{-1}$. Furthermore, the pore size distributions are very narrow. As already observed by TEM analysis, morphologies of both types of samples are quite similar at this temperature range (*cf.* Figure 3b,c,f,g). Despite the non-ordered porosity found in TEM images, the pore sizes achieved are highly homogeneous at this temperature treatment, peaking at 5–6 nm. At a calcination temperature of 550 °C, the templated-like morphology transform to a nanoparticular structure, as indicated by PXRD and TEM analysis (*cf.* Figure 2a and Figure 3d,h). These particles also form interparticular voids, which could be detected in the mesoporous range *via* nitrogen physisorption. The sample prepared only with citric acid exhibits larger pores than the sample with P-123/citric acid combined (12 nm *vs.* 10 nm), which can be correlated to larger particles seen in TEM images.

To further underline the relation between the crystallization and the porosity of the materials, samples with citric acid and P-123 were calcined to temperature up to 800 °C (Figure S7). The maxima of the pore size distribution of these samples shift towards larger pores (see Table S1), and the pore size distribution gets broader with increasing calcination temperatures (Figure S7). The higher calcination temperature promotes the transformation of smaller mesopores into larger but more non-ordered mesopores due to crystallite growth, as can be seen in the broadening of the pore size distribution (Figure 4). As a result, surface areas decrease strongly with increasing median pore size in all cases (*cf.* Table 1).

To further investigate the influence of the different calcination temperatures, the varying shapes of the hysteresis loops of the nitrogen physisorption isotherms due to modified mesoporosity were investigated *via* hysteresis scans. This method can unfold the pore connectivity of mesopores in a material, and therefore the origin of the mesopores of the different samples can be revealed. The pore connectivity is a very important property of functional porous materials for transport-related applications, *e.g.* electrocatalytic water oxidation. Additionally, the detection of different pore systems in one material is possible by this method.[67]

The desorption scanning method was used to investigate the desorption behavior of the pores in dependence of the neighboring pores. In general, if the desorption behavior of pores is dependent on the neighboring pore and the pore filling grade, the desorption of different isotherm desorption scans intersect in only one point at the p/p_0 value of the start/end of the hysteresis. If the desorption behavior of the pores is independent of the neighboring pores and the pore filling, the desorption of different isotherm scans shows hysteresis curves comparable to each other. Furthermore, the pore size distribution resulting from the different scans is comparable to each other.[68] For the desorption scanning isotherms, the adsorption was only run to a particular p/p_0 value in every cycle, and the desorption characteristics of the sample were detected. In Figure 5a,c,e, the hysteresis scans of samples prepared only with citric acid and calcined at different temperatures are presented. The first scan was measured over the whole range of p/p_0 up to 0.995 (*cf.* Figure 4). The other maximum adsorption points were chosen due to the hysteresis occurring in this range. The measured desorption branch of all scanning isotherms was then analyzed concerning the pore size distribution *via* NLDFT method (Figure 5b,d,f). In Figure 5b and d, the analyzed data of the hysteresis scans of the samples calcined at 400 °C and 450 °C are presented. The pore size distributions of the second scans are similar to that of the first scan. The maximum in the pore size distribution is located at 4.9 (Figure 5b) and 5.1 nm (Figure 5d). For the samples calcined at 550 °C, the pore size distribution (Figure 5f) is slightly broader compared to the samples calcined at 400 °C and 450 °C and the maximum in pore size distribution is located at larger pores (around 12 nm). For all three samples, the first three pore size distribution shapes are comparable to each other only with a slight shift towards smaller pores and further first three scans exhibit a hysteresis loop indicating mesopores (IUPAC: type 4 isotherm[65]).

These minor differences show that the pores are not affected by neighboring pores during ad- and desorption process for all presented samples prepared only with citric acid. Additionally, the filling level of the pores is not influencing the desorption behavior of every individual pore, which can be seen in the almost horizontal courses of the desorption branches of all isotherms and the existence of hysteresis in all isotherms. In case of the isotherms of the samples calcined at 400 °C this behavior is best observable for the second scan. Here, the desorption branch of hysteresis of the first scan and the desorption branch of the second scan intersect in the area of the hysteresis of the first scan at 0.48 p/p_0. The isotherms of the different scans further show hysteresis and comparable pore size distributions. Therefore, all isotherms show independent behavior from each other as well as the pores. This is a very important fact for applicability in processes where gases are evolved. The broadening in the pore size distribution in the fourth hysteresis scan of all different samples prepared only with citric acid indicates small amounts of smaller mesopores in the materials. This effect was already investigated on carbon materials.[69] To summarize, the materials synthesized only with citric acid show excellent characteristics of their pore structure for applicability. The pores are independent from each other and gas molecules can desorb completely at every p/p_0 value. The calcination temperature plays no role for the accessibility of the pore network.

Hysteresis scans with the desorption scanning method were also carried out for the materials prepared using citric acid combined with P-123 (Figure S8). The first scan of every sample is again the isotherm with p/p_0 values up to 0.995 (*cf.* Figure 4).

In this NLDFT data evaluation of the samples calcined at different temperatures (Figure S8b,d,f), it can be observed that the pore size distribution of the 1st and the 2nd scan exhibit almost the same values. The maxima in the pore size distributions are located at 4.9 nm (400 °C), 5.0 nm (450 °C) and 10.5 nm (550 °C). Furthermore, the presence of hysteresis loops in the first and second scan are clearly visible. This shows again that the pores are independent from each other in this p/p_0 region and could be filled and emptied at every p/p_0 value. Still the third scan of every samples has the maximum in pore size distribution comparably to the first and second scan only with a slight broadening towards same smaller mesopores. The fourth scan shows the presence of smaller mesopores more clearly.[69]

The materials synthesized with P-123 and citric acid also exhibit excellent characteristics in the pore structure regarding applicability. The pore characteristics and pore connectivity are

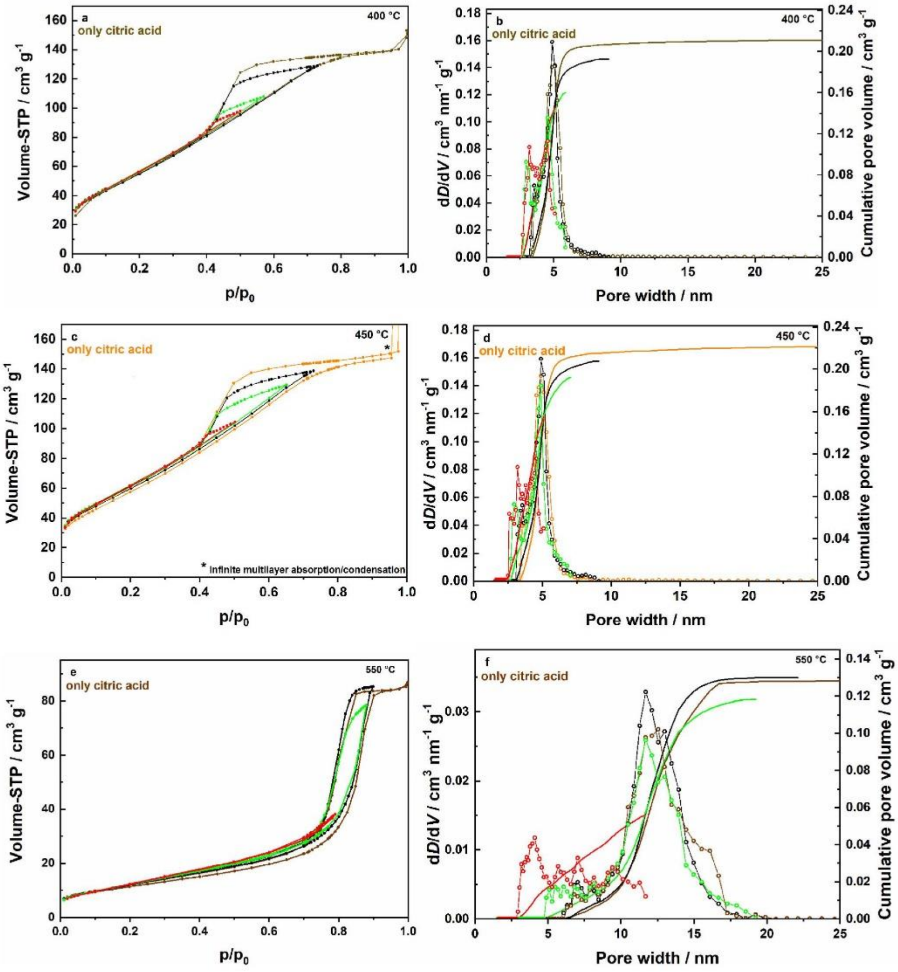

Figure 5. Hysteresis scanning isotherms of mesoporous $NiFe_2O_4$ samples prepared only with citric acid (a, c, e) and the corresponding pore size distribution plots analyzed by using the NLDFT method (b, d, f). Different scans were indicated with second scan: black, third scan: green and fourth scan: red.

comparable for the samples prepared only with citric acid and with a mixture of citric acid and P-123. Therefore, the detailed analysis of the mesopores of the materials shows the high potential of all prepared materials in application where the pore filling plays a major role, *e.g.* electrocatalytic water splitting.

Concluding all analytical investigations, an overall formation mechanism can be proposed for the presented synthesis strategy. The first step is the complexation of Ni^{2+} and Fe^{3+} cations in aqueous solution by citric acid,[70,71] which is essential for their uniform distribution.[72] Otherwise, cations are distributed unevenly, resulting in the formation of an undesired hematite by-phase during heat treatment (*cf.* Figure 2). These hybrid structures are conserved during evaporation and drying, respectively. During heat treatment, citric acid metal complexes are converted into amorphous metal carbonate species, *via* several intermediate steps (*cf.* Figure 1). At 275 °C, metal carbonates start to decompose by introducing porosity into the material (*cf.* Figure 1 and Figure 4). Increasing temperature to 400 °C effects the transformation of the amorphous carbonates to the amorphous metal oxide (*cf.* Figure 2b). Investigations on the porosity of the samples (Figure 4) show that the presence of carbonates allows partially removal of organic residues (P-123) before crystal growth of $NiFe_2O_4$, associated with the formation of thick crystalline pore walls taking place. Highly porous semi-crystalline nickel iron oxides with large surface area and very narrow pore size distribution can be achieved at 450 °C. Moreover, the pores achieved are highly accessible at each pressure, as determined by hysteresis scans (Figure 5 and S8). Through crystallite growth, the generated porous structure of the samples transforms into a particular structure with interparticular voids. Interestingly, the pore size distribution remains relatively narrow even at 550 °C when P-123 and citric acid were used, although TEM images clearly reveal nanoparticle agglomerates. Due to detailed investigations on the formation mechanism, phase-pure mesoporous $NiFe_2O_4$ samples with fully accessible pore system were obtained. Apparently, the presence of a block copolymer like P-123 during the initial step of the synthesis does not result in micelle formation. Rather, citric acid and the corresponding carbonates arrange as a scaffold, introducing uniform pores in the materials during thermal removal of organic compounds, whereas the P-123 polymer is able to prevent aggregation of obtained particles during crystallite growth and densification. In Figure S5, X-ray diffraction pattern, Raman spectrum, physisorption isotherm and pore size distribution plot of a 550 °C treated sample prepared without P-123 and without citric acid are shown. The already mentioned presence of the hematite phase shows the need of using citric acid as chelating agent. Further, a loss of pore homogeneity can be observed, since the shape of the isotherm changes significantly and the pore size distribution gets broader compared to the samples prepared with P-123 and citric acid. Larger pores with sizes >20 nm are present, proving the role of P-123 to prevent particle aggregation during densification and crystallite growth even further.

After elucidating the composition and morphology of the samples, we investigated our materials for their applicability in OER electrocatalysis in alkaline media (1 M KOH) using a three-electrode system. A glassy carbon rotating disk electrode modified with 1.4 mg cm^{-2} electrocatalyst was applied as working electrode. First, CV measurements were performed to determine the electrochemical surface area (ECSA) of the electrocatalysts (Figure S10). Figure 6a and b display the obtained slopes corresponding to the double layer capacity, which is proportional to the ECSA. The ECSA measurements indicate overall comparable ECSAs for all samples, however the ECSA tends to be higher if samples were calcined at lower temperatures. This trend is in good accordance with the obtained specific surface areas determined *via* physisorption measurements. However, nickel ferrite synthesized using only citric acid at 550 °C displays a similar value ($C_{DL} = 0.73$ mF cm^{-2}) compared to the nickel ferrite with added both P-123 and citric acid ($C_{DL} = 0.74$ mF cm^{-2}) while exploiting a specific surface area smaller by factor 1.6, meaning that a direct correlation between the ECSA and the specific surface area is not generally possible. Interestingly, the sample synthesized using only citric acid at 400 °C displays the smallest values, which contradicts the previously described trend. The reason for this remains elusive. Inaccuracies in the ECSA analysis itself were excluded by performing EIS measurements with the sample with P-123 and citric acid calcined at 400 °C in a non-faradaic region as a representative example. The obtained data was fitted using a Randles circuit including a constant phase element (CPE) (Figure S11). The calculated capacitance using the fit is 0.85 mF cm^{-2} which is only slightly higher than the capacitance obtained by CV measurements (0.81 mF cm^{-2}). Thus, the EIS data is in good agreement with the data obtained by CV measurements and shows the validity of our data.

The OER performance of the prepared samples was evaluated by performing linear sweep voltammetry experiments (Figure 6c). Samples calcined at 550 °C display a poor activity with a current density of ca. 2.1 mA cm^{-2} at 1.7 V. The activity does not increase through the use of P-123 with citric acid with specific surface areas 1.6 times higher, meaning that the ECSA determines the electrochemical activity instead of the specific surface area. Samples calcined at 400 °C or 450 °C display an improved activity, which is influenced by the increased ECSA. In general, crystallinity has only a subordinate role for the activity, since amorphous or semi-crystalline samples calcined at 400 °C or 450 °C exhibit significantly higher current densities. Hence, our results hint that a lower degree of crystallinity by heating at a moderate calcination temperature can be favorable for the overall performance, which agrees with recent literature.[34,73] Hereby, crystallinity and porosity/surface area are coupled directly, since a higher degree of crystallinity implies pore shrinkage or even pore collapse due to crystallite growth. In fact, samples prepared only with citric acid and P-123/citric acid calcined at 400 °C or 450 °C show similar performances in the electrocatalytic water oxidation experiments, which can clearly be correlated to their comparable morphologies. The most active sample, which was prepared only with citric acid and calcined at 400 °C, reaches a current density of 20.8 mA cm ^{2} at 1.7 *vs.* RHE. Overpotentials range from 410 mV to 430 mV, which are acceptable values for OER. In Table 2 the results of the electrochemical measurements are summarized.

Tafel plots of mesoporous $NiFe_2O_4$ samples are shown in Figure 6e and f and display similar Tafel slopes (50–94 mV dec^{-1}) compared to other spinel-type electrocatalysts in literature.[30,74] The lower Tafel slopes can probably be correlated to the accessible mesopore systems (*cf.* Figure 5 and S8), allowing mass transport through our materials, which is often beneficial for transport-related application like electrocatalytic water

Table 2. Results obtained from electrochemical measurements.

	Only citric acid			P-123/citric acid		
	400 °C	450 °C	550 °C	400 °C	450 °C	550 °C
Overpotential for OER [mV]	410	420	>570	420	430	>570
Tafel slope [mV dec^{-1}]	50	51	94	52	55	87
c_{DL} [10^{4} F cm^{-2}]	4.53	8.36	7.26	8.14	7.84	7.38

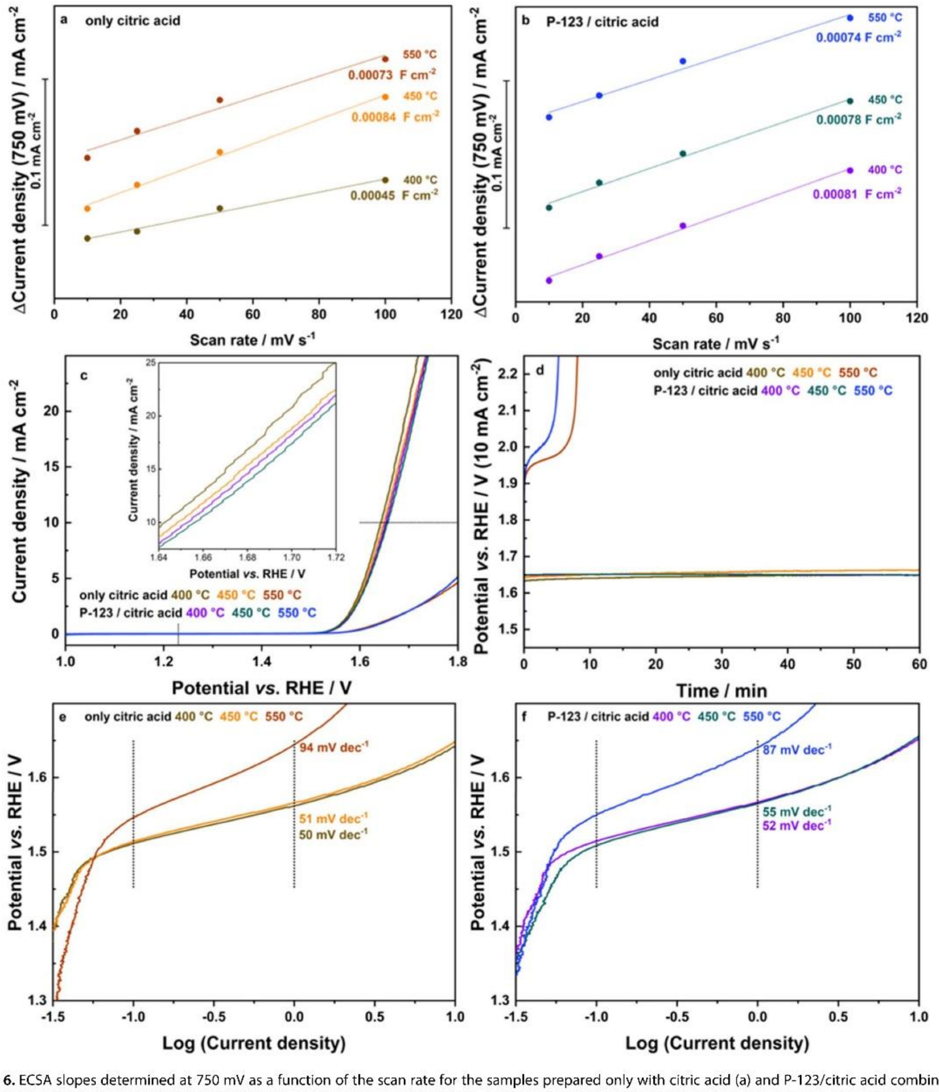

Figure 6. ECSA slopes determined at 750 mV as a function of the scan rate for the samples prepared only with citric acid (a) and P-123/citric acid combined (b). The linear slope representing the capacitance c_{DL} is proportional to the ECSA. c) Linear sweep voltammograms (LSV) measured with a scan rate of 1 mV s^{-1} in 1 M KOH and d) long-term chronopotentiometric (CPC) stability tests measured for one hour at a constant current density of 10 mA cm^{-2}. Tafel plots of mesoporous $NiFe_2O_4$ samples synthesized only with citric acid (e) and P-123/citric acid combined (f).

oxidation. To investigate the long-term stability of the mesoporous materials a constant current density of 10 mA cm^{-2} (chronopotentiometric mode) for the OER was applied (Figure 6d, Figure S12). For all samples calcined at 400 °C and 450 °C, the potential does not change significantly, demonstrating stable performance for at least one hour. In contrast, samples calcined at 550 °C do not steadily catalyze the OER as the potential increases significantly after approx. 5 minutes. The required high potential for these materials to reach a current density of 10 mA cm^{-2} may lead to corrosion of the glassy carbon surface triggering electrocatalyst detachment of the electrode. The same effect could be observed of the samples calcined at 400 °C and 450 °C but only after approx. 6 h. These additional long-term stability tests in Figure S13 further underline the assumption of electrocatalyst detachment caused by corrosion of the glassy carbon electrode surface. Electrochemical impedance spectroscopy (EIS) data obtained at 1.6 V *vs.* RHE display the smallest resistance of samples calcined at 450 °C. However, EIS data can be easily misinterpreted and thus leave open, whether the resistances are caused either by altered electrolyte interactions or a minimized charge transfer resistance (Figure S14).

In conclusion, we have demonstrated an altered OER activity depending on the morphology of the synthesized nickel ferrites. In general, high specific surface area materials reveal a trend in increased ECSAs alongside with increased activities. The minimum overpotential reached of 410 mV show the potential of $NiFe_2O_4$ as an electrocatalyst for water oxidation, since previously reported overpotentials for water oxidation with unmodified NiO or Fe_2O_3 are much higher.[56]

3. Conclusions

We present a simple synthesis strategy to prepare phase-pure $NiFe_2O_4$ electrocatalysts with highly accessible mesopores. The materials were prepared by a modified soft-templating strategy using citric acid as scaffold and the optional addition of the commercially available block copolymer Pluronic® P-123, followed by calcination. The formation of intermediate carbonate species induced by the use of citric acid in the synthesis plays a key role in the formation mechanism of the mesoporous structure. Furthermore, citric acid is also crucial to obtain phase-pure $NiFe_2O_4$. The synthesis procedure is easy to handle, low-cost and maybe industrial scalable in the future. Parameters like crystallinity and porosity/surface area can be controlled by the calcination procedure. By keeping the composition constant, the influence of often-neglected parameters like pore homogeneity, pore width, (accessible) surface area, and crystallinity can be investigated precisely. Our results highlight the relation between morphology/crystallinity and performance, demonstrating that high accessible surface areas are essential for high performances, while crystallinity only plays a subordinate role. Hence, the materials can be treated at moderate temperatures, avoiding an energy-consuming heating step at elevated temperatures. Morphological investigations including the hysteresis scanning method can substantially help to fully understand the activity of a nanostructured electrocatalyst. However, the performances of our materials are still limited compared to other $NiFe_2O_4$ nanomaterials like -cubes or -particles[56,75,76] and further to other mixed transition metal oxides.[77] However, our materials are of high purity, while materials described in literature often contain α-Fe_2O_3[76] or NiO,[78] which prevents complete comparability. In contrast to, for example faceted NiFe-oxide nanocubes,[75] controlling the exposed facets in the pore channels is not possible, resulting in a weaker activity of mesoporous $NiFe_2O_4$. More importantly, the incorporated elements are cheap and available, in contrast to cobalt-containing mixed metal oxide electrocatalysts.[79] Long-term stability as another important parameter for application is also provided, contrary to manganese-containing compounds.[80]

Experimental Section

Synthesis

Mesoporous $NiFe_2O_4$ samples were prepared using the well-known EISA process,[81] coupled with the addition of citric acid during the synthesis, inspired by the works of Kraehnert *et al.*[31,43] Therefore, 116.3 mg (0.4 mmol) nickel(II) nitrate hexahydrate (*SigmaAldrich*, 99.999 %) were dissolved in 2 mL of deionized water, and stirred for 10 minutes (500 rpm). Afterwards, 323.2 mg (0.8 mmol) iron(III) nitrate nonahydrate (*AcrosOrganics*, 99+%) were added, followed by stirring for 1 hour. Meanwhile, 52.2 mg (0.009 mmol, 0.03 equivalents concerning the Ni precursor) of the commercially available triblock copolymer $PEO_{20}PPO_{70}PEO_{20}$ (Pluronic® P-123, *Sigma-Aldrich*) and 271.1 mg (1.3 mmol, 4.3 equivalents concerning the Ni precursor) citric acid monohydrate (*CarlRoth*, ≥99,5 %) were dissolved in 12 mL of deionized water, and stirred for 1 hour. Then, six portions of 2 mL of polymer and 0.25 mL precursor solutions were each combined. After 2 hours of stirring (500 rpm), the solutions were transferred into 5 mL polytetrafluoroethylene (PTFE) cups, followed by water evaporation under a glass dome at 65 °C on a heating plate for at least 2 days and final drying at 50 °C using a vacuum drying oven. Calcination of the obtained hybrid material was performed at 275 °C/400 °C/450 °C/550 °C for 1 hour in air (heating rate 1 °C/min). For comparison, the synthesis procedure was also performed in the absence of Pluronic® P-123 and/or citric acid, respectively. In the following Pluronic® P-123 will be abbreviated as P-123. Synthesis variations and their labels are summarized in Table S1.

Materials Characterization

Powder X-ray diffraction (PXRD) measurements were performed on a Malvern PANanlytical Empyrean diffractometer with a PixCel 1D detector operating at 40 kV acceleration voltage and 40 mA emission current using Cu K-α radiation (wavelength $\lambda = 1.54060$ Å). For the measurements, the lower level of the pulse-height discrimination (PHD) was set to 8.05 keV, and the upper level to 11.27 keV. Data were recorded in a range from 10–70° 2θ. Crystallite sizes were calculated from the integral width using (220), (400), (511) and (440) reflections of $NiFe_2O_4$. For this purpose, the intensity of the diffraction pattern was plotted versus the scattering vector *S* (Eq. 1) and the ratio between area and height of an isolated reflex (integral width B_{hkl}) determined. The crystallite size L_{hkl} is then obtained as the inverse value of the integral width B_{hkl}.[82]

$$S = \frac{2 \cdot \sin\left(\frac{\pi}{180^\circ} \cdot \theta\right)}{\lambda} \quad (1)$$

Raman spectra were recorded using a LABRAM I Raman spectrometer from Horiba Jobin Yvon GmbH equipped with an Olympus BX41 microscope using LabSpec 5.78.24 software for data evaluation. For the measurements, a HeNe laser ($\lambda = 632.82$ nm) was used, operated with a laser power of 1.15 mW. Samples were measured at 50x magnification within a range of 100–4000 cm^{-1}, 5 co-additions, and 25 s exposure time. Raman spectra were de-spiked manually and smoothed using a FFT filter, before normalizing the data.

N_2 physisorption analysis were performed at 77 K using an Anton Paar QuantaTec ASiQ-MP-MP-AG instrument (scanning curves) and an Anton Paar QUADRASORB evo surface area & pore size analyzer (standard isotherms). Pore size distributions were calculated using NLDFT equilibrium model assuming cylindrical pores and silica like surface. Specific surface areas were estimated by applying the Brunauer-Emmett-Teller (BET) model. All samples were degassed in vacuum at 120 °C for at least 12 hours prior to the measurements. Data evaluation was carried out with the program ASiQwin 4.0®.

For recording transmission electron microscopy (TEM) images and selected area electron diffraction (SAED) patterns, a 200 kV JEOL JEM-2200FS EFTEM equipped with Schottky FEG and In-Column Omega Energyfilter from JEOL GmbH was used. Prior to each measurement, 1-2 mg of the sample were suspended in 1 mL of ethanol (*AcrosOrganics*, extra dry, 99.5 %). Then, 4-8 µL of the suspension were dropped on a carbon film coated Cu TEM grid (200 Mesh). TEM (and also SEM) images were processed using ImageJ 1.52a. Particle sizes were measured from at least 30 independent particles, before averaging the values.

Scanning electron microscopy (SEM) was performed on a Zeiss Leo 1530 instrument at an acceleration voltage of 3.0 kV (working distance 2.5–5 mm). Samples were sputtered with Pt using a Cressington Sputter Coater 208 HR. For the energy-dispersive X-ray spectroscopy (EDXS) experiments, an UltraDry-EDX detector (Thermo Fisher Scientific NS7) was used, while the acceleration voltage was set to 15 kV (working distance 8 mm). For each sample, Ni to Fe ratios were measured at several points, before averaging the values.

For thermogravimetric analysis (TGA), a Netzsch STA409PC thermoscale in combination with a QMG421 quadrupole mass spectrometer from Balzers was utilized. Data were recorded in a range from 30 °C to 800 °C, with a heating rate of 5 °C/min in synthetic air (80 % N_2, 20 % O_2).

Diffuse reflectance infrared Fourier transform spectroscopy (DRIFTS) data were collected using a Bruker alpha II in a range of 400–4000 cm^{-1} with a spectral resolution of 10 cm^{-1} and 200 co-additions per scan.

^{57}Mössbauer spectra were recorded at room temperature using a ^{57}Co radiation source in a Rh matrix in a SeeCo constant acceleration spectrometer. Isomer shifts are referred to α-Fe metal at room temperature. Data were fit to a single line superposed on a symmetric Hyperfine Field Distribution using a Voigt profile based adaptive least-square routine with the WMOSS program. For the estimation of the inversion degree X, the ratio between the areas under the fits for the two iron sites (tetrahedral, octahedral) was calculated. This ratio is equal to the term $X/(2\text{-}X)$.

Electrochemical measurements were performed using a Gamry Interface 1010B or a Gamry Reference 600+ potentiostat. A three-electrode setup was employed utilizing a catalyst modified glassy carbon electrode (GC, diameter 3.0 mm) equipped with an Autolab RDE-2 working, a platinum wire counter and a reversible hydrogen reference electrode (RHE, HydroFlex mini, Gaskatel GmbH). All measured potentials were given against RHE. Catalyst inks were prepared by dispersing 3.3 mg of the catalyst in a 100 µL mixture of water, ethanol and Nafion solution (5 % in aliph. alcohols, *Sigma -Aldrich*) in the volume ratio of 8 : 1 : 1. Subsequently, the catalyst ink was sonicated for 30 min and a drop of 3 µL (1.4 mg cm^{-2} catalyst loading) was applied to the pre-polished GC electrode surface and was left to dry under air for 30 min. Polishing of the GC electrode was performed with alumina suspensions (0.3 and 0.05 µm, *Buehler*) for 3 min, respectively, followed by ultra-sonication of the GC electrode in Milli-Q water for 5 min.

A 1 M KOH solution (*Fisher Scientific*, 85.3 %, used without purification) was used as electrolyte, which was purged with N_2 prior to each electrochemical experiment for 10 min. Linear sweep voltammograms were recorded under N_2 atmosphere with a scan rate of 1 mV s^{-1} and a rotation speed of 1600 rpm. Chronopotentiometry was carried out by applying a constant current of 10 mA cm^{-2} with a rotation speed of 1600 rpm. For evaluation of electrochemical active surface areas (ECSA), a method presented by McCrory *et al.* was applied.[83] First, cyclic voltammograms were measured in a non-faradaic region (0.65–0.85 V *vs.* RHE) with various scan rates (100, 50, 25, 10 mV s^{-1}). Current density differences of forward and backward scans at 750 mV were plotted against the scan rate. The slope of the resulting linear fit is proportional to the electrochemical double-layer capacitance c_{DL}, and thus proportional to the ECSA. Electrochemical impedance spectroscopy (EIS) measurements were performed at 1.6 V vs. RHE from 100 kz–1 Hz with an amplitude of 1 mV and 10 points per decade.

Acknowledgments

The authors gratefully acknowledge funding by the German Research Foundation DFG (AP242/6-1, MA 5392/7-1). U.-P. A. is grateful for financial support from the Deutsche Forschungsgemeinschaft (Emmy Noether grant AP242/2-1 & AP242/6-1; under Germany's Excellence Strategy – EXC-2033 – Project number 390677874), the Fraunhofer Internal Programs under Grant no. Attract 097-602175 as well as the Fraunhofer Cluster of Excellence CINES. The authors thank Dr. Florian Wittkamp for performing Mössbauer spectroscopy, and Dr. Rafael Meinusch together with Kevin Turke (both Justus-Liebig University Giessen) for executing TG-MS analysis. Further thanks go to the Bavarian Polymer Institute KeyLab Electron and Optical Microscopy for deployment of TEM/SEM devices, and especially Dr. Markus Drechsler and Martina Heider for their support in recording EM images. Open access funding enabled and organized by Projekt DEAL.

Conflict of Interest

The authors declare no conflict of interest.

Keywords: electrocatalysis · oxygen evolution reaction · mesoporous materials · soft templating · ferrite spinels

[1] N. H. Chou, P. N. Ross, A. T. Bell, T. D. Tilley, *ChemSusChem* **2011**, *4*, 1566–1569.
[2] A. S. Schenk, S. Eiben, M. Goll, L. Reith, A. N. Kulak, F. C. Meldrum, H. Jeske, C. Wege, S. Ludwigs, *Nanoscale* **2017**, *9*, 6334–6345.
[3] A. Ramírez, P. Hillebrand, D. Stellmach, M. M. May, P. Bogdanoff, S. Fiechter, *J. Phys. Chem. C* **2014**, *118*, 14073–14081.
[4] M. Huynh, C. Shi, S. J. L. Billinge, D. G. Nocera, *J. Am. Chem. Soc.* **2015**, *137*, 14887–14904.
[5] M. E. G. Lyons, R. L. Doyle, *Int. J. Electrochem. Sci.* **2012**, *7*, 9488–9501.
[6] Q. Liu, A. M. Asiri, X. Sun, *Electrochem. Commun.* **2014**, *49*, 21–24.
[7] F. Chekin, H. Tahermansouri, M. R. Besharat, *J. Solid State Electrochem.* **2014**, *18*, 747–753.
[8] J. C. B. Nadesan, A. C. C. Tseung, *J. Electrochem. Soc.* **1985**, *132*, 2957–2959.
[9] A. Kargar, S. Yavuz, T. K. Kim, C. H. Liu, C. Kuru, C. S. Rustomji, S. Jin, P. R. Bandaru, *ACS Appl. Mater. Interfaces* **2015**, *7*, 17851–17856.
[10] X. Lv, Y. Zhu, H. Jiang, X. Yang, Y. Liu, Y. Su, J. Huang, Y. Yao, C. Li, *Dalton Trans.* **2015**, *44*, 4148–4154.
[11] X. Kong, T. Zhu, F. Cheng, M. Zhu, X. Cao, S. Liang, G. Cao, A. Pan, *ACS Appl. Mater. Interfaces* **2018**, *10*, 8730–8738.
[12] X. F. Lu, L. F. Gu, J. W. Wang, J. X. Wu, P. Q. Liao, G. R. Li, *Adv. Mater.* **2017**, *29*, 1604437.

[13] G. Liu, K. Wang, X. Gao, D. He, J. Li, *Electrochim. Acta* **2016**, *211*, 871–878.
[14] Q. Qin, L. Chen, T. Wei, Y. Wang, X. Liu, *Catal. Sci. Technol.* **2019**, *9*, 1595–1601.
[15] M. Li, Y. Xiong, X. Liu, X. Bo, Y. Zhang, C. Han, L. Guo, *Nanoscale* **2015**, *7*, 8920–8930.
[16] A. Sutka, M. Kodu, R. Pärna, R. Saar, I. Juhnevica, R. Jaaniso, V. Kisand, *Sens. Actuators B* **2016**, *224*, 260–265.
[17] J. Wu, D. Gao, T. Sun, J. Bi, Y. Zhao, Z. Ning, G. Fan, Z. Xie, *Sens. Actuators B* **2016**, *235*, 258–262.
[18] K. Kirchberg, R. Marschall, *Sustain. Energy Fuels* **2019**, *3*, 1150–1153.
[19] S. Ida, K. Yamada, T. Matsunaga, H. Hagiwara, Y. Matsumoto, T. Ishihara, *J. Am. Chem. Soc.* **2010**, *132*, 17343–17345.
[20] T. Peng, X. Zhang, H. Lv, L. Zan, *Catal. Commun.* **2012**, *28*, 116–119.
[21] D. Tetzlaff, C. Simon, D. S. Achilleos, M. Smialkowski, K. junge Puring, A. Bloesser, S. Piontek, H. Kasap, D. Siegmund, E. Reisner, et al., *Faraday Discuss.* **2019**, 216–226.
[22] K. Kirchberg, S. Wang, L. Wang, R. Marschall, *ChemPhysChem* **2018**, *19*, 2313–2320.
[23] N. Guijarro, P. Bornoz, M. S. Prévot, X. Yu, X. Zhu, M. Johnson, X. A. Jeanbourquin, F. Le Formal, K. Sivula, *Sustain. Energy Fuels* **2017**, *2*, 103–117.
[24] A. G. Hufnagel, K. Peters, A. Müller, C. Scheu, D. Fattakhova-Rohlfing, T. Bein, *Adv. Funct. Mater.* **2016**, *26*, 4435–4443.
[25] L. I. Granone, A. C. Ulpe, L. Robben, S. Klimke, M. Jahns, F. Renz, T. M. Gesing, T. Bredow, R. Dillert, D. W. Bahnemann, *Phys. Chem. Chem. Phys.* **2018**, *20*, 28267–28278.
[26] D. Peeters, D. H. Taffa, M. M. Kerrigan, A. Ney, N. Jöns, D. Rogalla, S. Cwik, H. W. Becker, M. Grafen, A. Ostendorf, et al., *ACS Sustainable Chem. Eng.* **2017**, *5*, 2917–2926.
[27] K. Kirchberg, A. Becker, A. Bloesser, T. Weller, J. Timm, C. Suchomski, R. Marschall, *J. Phys. Chem. C* **2017**, *121*, 27126–27138.
[28] R. Galindo, E. Mazario, S. Gutiérrez, M. P. Morales, P. Herrasti, *J. Alloys Compd.* **2012**, *536*, S241–S244.
[29] Z. Wu, Z. Zou, J. Huang, F. Gao, *ACS Appl. Mater. Interfaces* **2018**, *10*, 26283–26292.
[30] N. K. Singh, R. N. Singh, *Indian J. Chem. Sect. A* **1999**, *38 A*, 491–495.
[31] M. Bernicke, B. Eckhardt, A. Lippitz, E. Ortel, D. Bernsmeier, R. Schmack, R. Kraehnert, *ChemistrySelect* **2016**, *1*, 482–489.
[32] N. Menzel, E. Ortel, R. Kraehnert, P. Strasser, *ChemPhysChem* **2012**, *13*, 1385–1394.
[33] F. J. Keil, *Catal. Today* **1999**, *53*, 245–258.
[34] T. Priamushko, R. Guillet-Nicolas, M. Yu, M. Doyle, C. Weidenthaler, H. Tüysüz, F. Kleitz, *ACS Appl. Mater. Interfaces* **2020**, *3*, 5597–5609.
[35] G. Ou, F. Wu, K. Huang, N. Hussain, D. Zu, H. Wei, B. Ge, H. Yao, L. Liu, H. Li, et al., *ACS Appl. Mater. Interfaces* **2019**, *11*, 3978–3983.
[36] Q. Chen, R. Wang, F. Lu, X. Kuang, Y. Tong, X. Lu, *ACS Omega* **2019**, *4*, 3493–3499.
[37] A. Thomas, H. Schlaad, B. Smarsly, M. Antonietti, *Langmuir* **2003**, *19*, 4455–4459.
[38] J. Haetge, C. Suchomski, T. Brezesinski, *Inorg. Chem.* **2010**, *49*, 11619–11626.
[39] C. Jia, Y. Zhang, Q. Kong, Q. Wang, G. Chen, H. T. Guam, C. Dong, *J. Mater. Sci. Mater. Electron.* **2020**, *31*, 6000–6007.
[40] X. Gu, W. Zhu, C. Jia, R. Zhao, W. Schmidt, Y. Wang, *Chem. Commun.* **2011**, *47*, 5337.
[41] Y. Li, K. Guo, J. Li, X. Dong, T. Yuan, X. Li, H. Yang, *ACS Appl. Mater. Interfaces* **2014**, *6*, 20949–20957.
[42] H. Yen, **n.d.**
[43] B. Eckhardt, E. Ortel, D. Bernsmeier, J. Polte, P. Strasser, U. Vainio, F. Emmerling, R. Kraehnert, *Chem. Mater.* **2013**, *25*, 2749–2758.
[44] W. Brockner, C. Ehrhardt, M. Gjikaj, *Thermochim. Acta* **2007**, *456*, 64–68.
[45] P. Melnikov, V. A. Nascimento, I. V. Arkhangelsky, L. Z. Zanoni Consolo, L. C. S. De Oliveira, *J. Therm. Anal. Calorim.* **2014**, *115*, 145–151.
[46] S. Mehrabani, J. P. Singh, R. Bagheri, A. G. Wattoo, Z. Song, K. H. Chae, M. M. Najafpour, *Nanoscale Adv.* **2019**, *1*, 686–695.
[47] D. Esken, H. Noei, Y. Wang, C. Wiktor, S. Turner, G. Van Tendeloo, R. A. Fischer, *J. Mater. Chem.* **2011**, *21*, 5907–5915.
[48] X. Wang, L. Andrews, *J. Phys. Chem. A* **2006**, *110*, 10035–10045.
[49] J. P. Gallas, J. M. Goupil, A. Vimont, J. C. Lavalley, B. Gil, J. P. Gilson, O. Miserque, *Langmuir* **2009**, *25*, 5825–5834.
[50] M. Ide, M. El-Roz, E. De Canck, A. Vicente, T. Planckaert, T. Bogaerts, I. Van Driessche, F. Lynen, V. Van Speybroeck, F. Thybault-Starzyk, et al., *Phys. Chem. Chem. Phys.* **2013**, *15*, 642–650.
[51] K. V. P. M. Shafi, Y. Koltypin, A. Gedanken, R. Prozorov, J. Balogh, J. Lendvai, I. Felner, *J. Phys. Chem. B* **1997**, *101*, 6409–6414.
[52] M. Zainuri, *IOP Conf. Ser.: Mater. Sci. Eng.* **2017**, *196*, 1–4.
[53] K. K. Lee, Y. C. Kang, K. Y. Jung, J. H. Kim, *J. Alloys Compd.* **2005**, *395*, 280–285.
[54] W. B. White, B. A. DeAngelis, *Spectrochim. Acta Part A* **1967**, *23*, 985–995.
[55] A. Ahlawat, V. G. Sathe, *J. Raman Spectrosc.* **2011**, *42*, 1087–1094.
[56] N. Dalai, B. Mohanty, A. Mitra, B. Jena, *ChemistrySelect* **2019**, *4*, 7791–7796.
[57] P. R. Graves, C. Johnston, J. J. Campaniello, *Mater. Res. Bull.* **1988**, *23*, 1651–1660.
[58] D. L. A. de Faria, S. Venâncio Silva, M. T. de Oliveira, *J. Raman Spectrosc.* **1997**, *28*, 873–878.
[59] V. Bartůněk, D. Sedmidubský, Š. Huber, M. Švecová, P. Ulbrich, O. Jankovský, *Materials* **2018**, *10*, 1–11.
[60] C. Zhao, H. Li, J. Jiang, Y. He, W. Liang, *High Press. Res.* **2018**, *38*, 212–223.
[61] E. De Grave, A. Govaert, D. Chambaere, G. Robbrecht, *Physica B+C* **1979**, *96*, 103–110.
[62] E. Greenberg, W. M. Xu, M. Nikolaevsky, E. Bykova, G. Garbarino, K. Glazyrin, D. G. Merkel, L. Dubrovinsky, M. P. Pasternak, G. K. Rozenberg, *Phys. Rev. B* **2017**, *95*, 1–13.
[63] E. Agouriane, A. Essoumhi, A. Razouk, M. Sahlaoui, M. Sajieddine, *J. Mater. Environ. Sci.* **2016**, *7*, 4614–4619.
[64] H. S. C. O'Neill, H. Annersten, D. Virgo, *Am. Mineral.* **1992**, *77*, 725–740.
[65] M. Thommes, K. Kaneko, A. V. Neimark, J. P. Olivier, F. Rodriguez-Reinoso, J. Rouquerol, K. S. W. Sing, *Pure Appl. Chem.* **2015**, *87*, 1051–1069.
[66] J. Jeromenok, J. Weber, *Langmuir* **2013**, *29*, 12982–12989.
[67] K. A. Cychosz, R. Guillet-Nicolas, J. García-Martínez, M. Thommes, *Chem. Soc. Rev.* **2017**, *46*, 389–414.
[68] R. Cimino, K. A. Cychosz, M. Thommes, A. V. Neimark, *Colloids Surf. A* **2013**, *437*, 76–89.
[69] K. A. Cychosz, X. Guo, W. Fan, R. Cimino, G. Y. Gor, M. Tsapatsis, A. V. Neimark, M. Thommes, *Langmuir* **2012**, *28*, 12647–12654.
[70] G. R. Hedwig, J. R. Liddle, R. D. Reeves, *Aust. J. Chem.* **1980**, *33*, 1685–1693.
[71] C. F. Timberlake, *J. Chem. Soc.* **1964**, 5078–5085.
[72] A. E. Danks, S. R. Hall, Z. Schnepp, *Mater. Horiz.* **2016**, *3*, 91–112.
[73] S. S. Nkabinde, Z. B. Ndala, N. P. Shumbula, T. Kolokoto, O. Nchoe, G. N. Ngubeni, K. P. Mubiayi, N. Moloto, *New J. Chem.* **2020**, *44*, 14041–14049.
[74] K. Chakrapani, G. Bendt, H. Hajiyani, I. Schwarzrock, T. Lunkenbein, S. Salamon, J. Landers, H. Wende, R. Schlögl, R. Pentcheva, et al., *ChemCatChem* **2017**, *9*, 2988–2995.
[75] A. Kumar, S. Bhattacharyya, *ACS Appl. Mater. Interfaces* **2017**, *9*, 41906–41915.
[76] D. Lim, H. Kong, N. Kim, C. Lim, W. S. Ahn, S. H. Baeck, *ChemNanoMat* **2019**, *5*, 1296–1302.
[77] Z. P. Wu, X. F. Lu, S. Q. Zang, X. W. Lou, *Adv. Funct. Mater.* **2020**, *30*, 1–20.
[78] B. K. Kang, M. H. Woo, J. Lee, Y. H. Song, Z. Wang, Y. Guo, Y. Yamauchi, J. H. Kim, B. Lim, D. H. Yoon, *J. Mater. Chem. A* **2017**, *5*, 4320–4324.
[79] V. Maruthapandian, M. Mathankumar, V. Saraswathy, B. Subramanian, S. Muralidharan, *ACS Appl. Mater. Interfaces* **2017**, *9*, 13132–13141.
[80] F. D. Speck, P. G. Santori, F. Jaouen, S. Cherevko, *J. Phys. Chem. C* **2019**, *123*, 25267–25277.
[81] T. Weller, L. Deilmann, J. Timm, T. S. Dörr, P. A. Beaucage, A. S. Cherevan, U. B. Wiesner, D. Eder, R. Marschall, *Nanoscale* **2018**, *10*, 3225–3234.
[82] H. G. Jiang, M. Rühle, E. J. Lavernia, *J. Mater. Res.* **1999**, *14*, 549–559.
[83] C. C. L. McCrory, S. Jung, J. C. Peters, T. F. Jaramillo, *J. Am. Chem. Soc.* **2013**, *135*, 16977–16987.

Manuscript received: October 1, 2020
Revised manuscript received: December 7, 2020
Accepted manuscript online: December 17, 2020

ChemElectroChem

Supporting Information

Mesoporous $NiFe_2O_4$ with Tunable Pore Morphology for Electrocatalytic Water Oxidation

Christopher Simon, Jana Timm, David Tetzlaff, Jonas Jungmann, Ulf-Peter Apfel,* and Roland Marschall*

Table S1: Label and weighted portions for the preparation of mesoporous $NiFe_2O_4$.

label	additional agents		mass / mg			
	P-123	Citric acid	nickel(II) nitrate hexahydrate	iron(III) nitrate nonahydrate	Pluronic® P-123	citric acid monohydrate
without P-123/citric acid	-	-	116.3	323.2	-	-
only P-123	x	-	116.3	323.2	52.2	-
only citric acid	-	x	116.3	323.2	-	271.1
P-123/citric acid	x	x	116.3	323.2	52.2	271.1

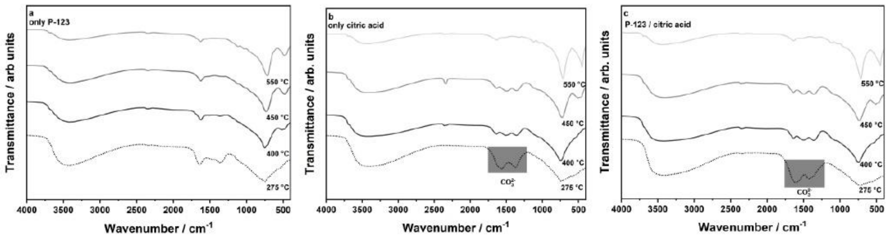

Figure S1: DRIFT spectra of mesoporous $NiFe_2O_4$ samples. Samples were calcined at 275 °C, 400 °C, 450 °C, and 550 °C. The carbonate anion shows a prominent double peak at 1500 - 1700 cm^{-1} (marked in grey). Further signals belong to water (O-H stretching mode at ~ 3400 cm^{-1}, H-O-H bending vibration at ~ 1650 cm^{-1}), carbon dioxide (asymmetric stretching mode at ~ 2350 cm^{-1}), and to the $NiFe_2O_4$ metal oxide (~ 700 cm^{-1} and ~ 450 cm^{-1}).[1–4] Peaks at ~1360 cm^{-1} and ~1500 cm^{-1} belong to N=O containing species like NO_2 or nitrate.[5,6] The increasing signal at 3699 cm^{-1} could be attributed to free O-H vibrations at the metal oxide surface.[7]

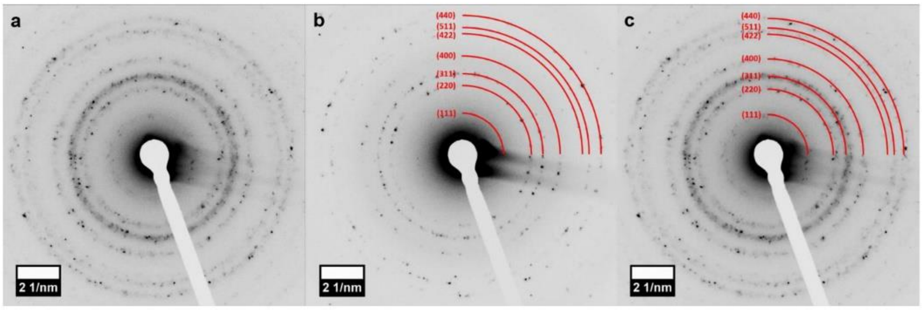

Figure S2: SAED patterns of $NiFe_2O_4$ samples prepared (a) only with P-123, (b) only with citric acid, and (c) with P-123/citric acid combined, all calcined at 550 °C. They show rings consisting of many small spots, each spot arising from a Bragg reflection from an individual crystallite. For phase-pure samples (only citric acid and P-123/citric acid), drawn rings can be assigned to (111), (220), (311), (400), (511), and (440) reflections of $NiFe_2O_4$.

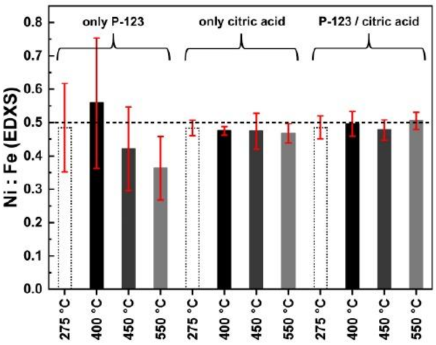

Figure S3: Ni to Fe ratio of various mesoporous $NiFe_2O_4$ samples calcined at 275 °C, 400 °C, 450 °C, and 550 °C. Ni to Fe ratios were estimated *via* EDXS. For phase-pure nickel ferrite, the expected value is 0.5. For each sample, several points were investigated, before averaging the Ni to Fe ratios. The standard deviations are shown as error bars. For samples prepared with only P-123, Ni to Fe ratios are lower than expected, indicating hematite impurities. The corresponding large errors bars are related to the inhomogeneous distributions of metal cations.

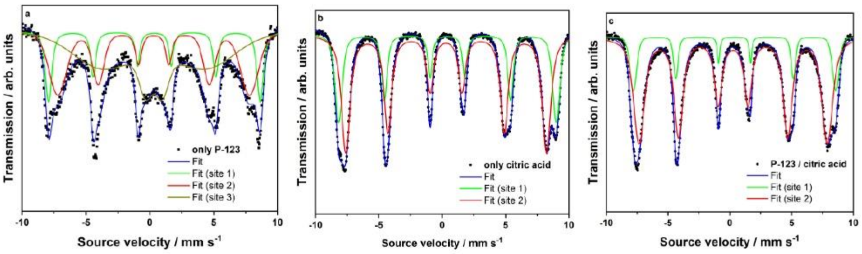

Figure S4: Mössbauer spectra of mesoporous $NiFe_2O_4$ samples prepared (a) only with P-123, (b) only with citric acid, and (c) with P-123/citric acid combined, all calcined at 550 °C. Site 1 represents tetrahedral iron sites, site 2 octahedral iron sites. For the sample prepared only with P-123, a third iron site is present, since the sample is a phase mixture of nickel ferrite and hematite. From these data, the degrees of inversion X can be calculated using the areas under the fits for the tetrahedral and octahedral coordinated iron species, respectively.

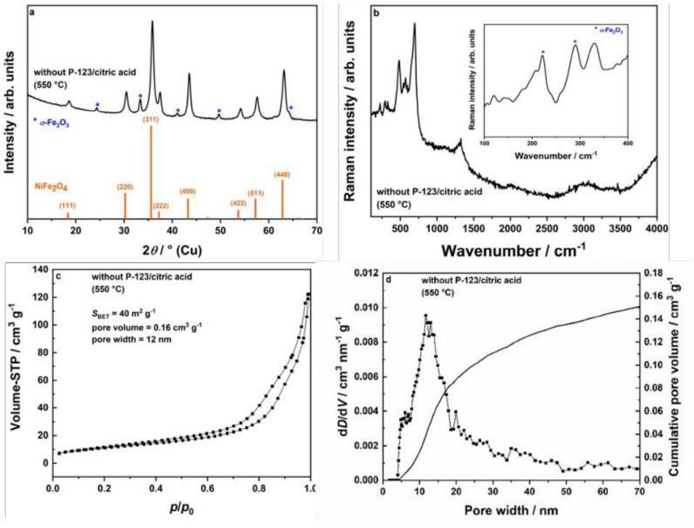

Figure S5: X-ray diffraction pattern (a), Raman spectrum (b), nitrogen physisorption isotherm (c), and corresponding pore size distribution (d) of mesoporous NiFe$_2$O$_4$ prepared without P-123 and without citric acid (calcination temperature 550 °C).

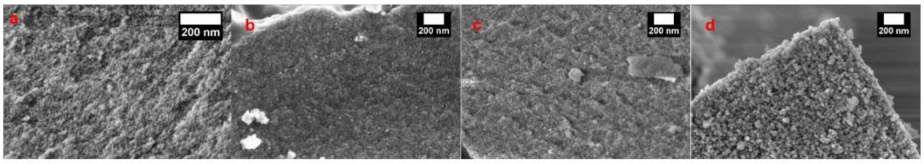

Figure S6: SEM images of mesoporous NiFe$_2$O$_4$ prepared only with citric. Samples were calcined at 275 °C (a), 400 °C (b), 450 °C (c), and 550 °C (d).

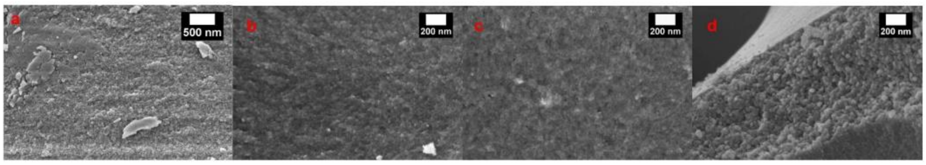

Figure S7: SEM images of mesoporous NiFe$_2$O$_4$ prepared with P-123 plus citric acid. Samples were calcined at 275 °C (a, only low magnification possible due to high polymer content), 400 °C (b), 450 °C (c), and 550 °C (d).

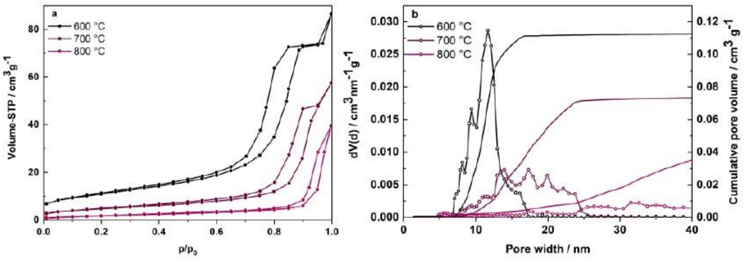

Figure S8: (a) N_2 physisorption isotherms of samples prepared with P-123 and citric acid calcined at 600 °C, 700°C and 800 °C and (b) corresponding pore size distributions plus cumulative pore volumes (obtained by NLDFT analysis). The pores of the sample calcined at 800 °C are partly in a region where gas physisorption measurements are not suitable (> 40 nm).

Table S2: Results obtained from nitrogen physisorption (Figure S8).

	P-123/citric acid		
	600 °C	700 °C	800 °C
Specific surface area / m^2 g^{-1}	39.1	16.8	6.6
Pore width / nm	9.5 / 11.7	11-24	24->40
Pore volume / cm^3 g^{-1}	0.11	0.07	0.03

Table S3: Averaged results obtained from nitrogen physisorption measurements. The averaged values of three different samples and the standard deviation of the catalysis-relevant samples.

	only citric acid				P-123/citric acid			
	275 °C	400 °C	450 °C	550 °C	275 °C	400 °C	450 °C	550 °C
surface area / m^2 g^{-1}	218±47	210±11	178±22	44±1	68±27	207±17	199±12	67±5
pore width / nm	4.9±0.1	4.9±0.2	4.8±0.2	11.5±0.7	4.7±0.2	5.2±0.6	5.0±0.1	9.5±0.4
pore volume / cm^3 g^{-1}	0.20±0.06	0.21±0.05	0.17±0.05	0.13±0.01	0.08±0.05	0.24±0.06	0.23±0.01	0.16±0.02

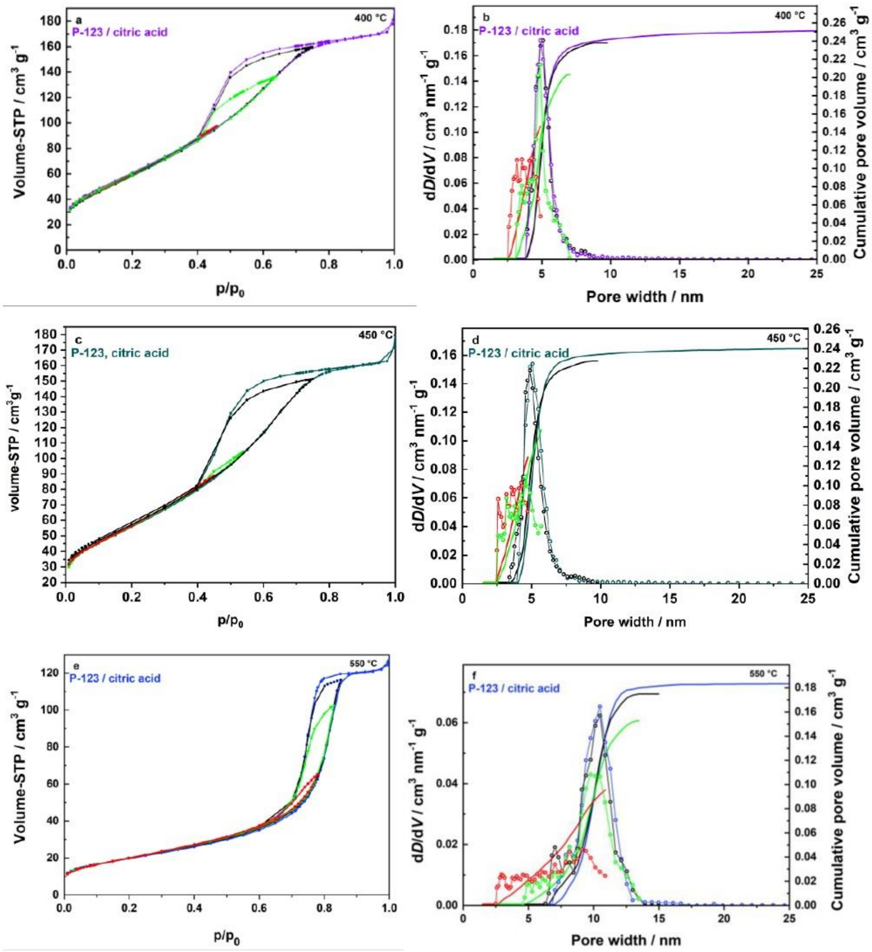

Figure S9: Hysteresis scanning isotherms of mesoporous $NiFe_2O_4$ samples prepared with P-123 and citric acid combined (a, c, e) and the corresponding pore size distribution plots analyzed via NLDFT method (b, d, f).

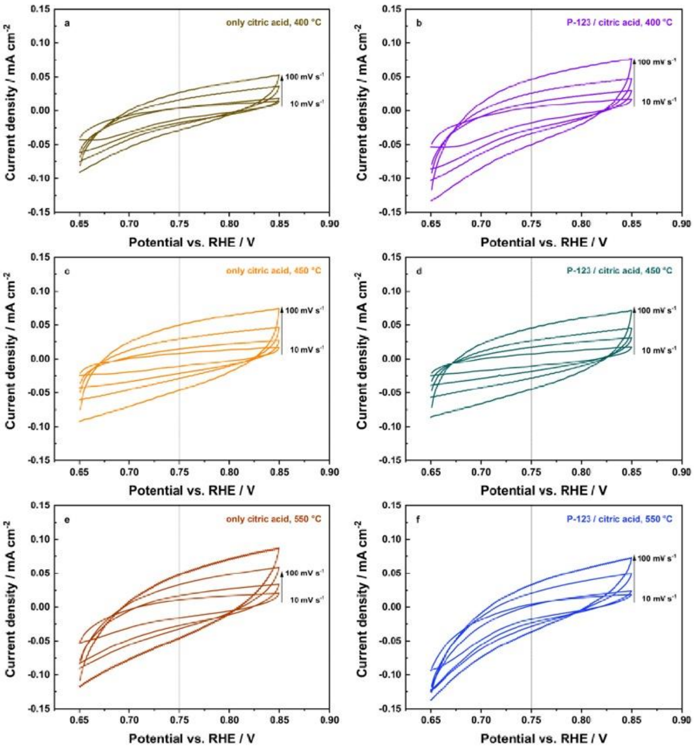

Figure S10: Cyclovoltammograms of mesoporous $NiFe_2O_4$ samples measured at variable scan rates (100, 50, 25, 10 mV s^{-1}). From the current density differences at 750 mV, the double-layer capacitance c_{CL} can be estimated, representing the electrochemical active surface area (ECSA).

The fitting provided a set of parameters like Y_0, R_p, R_s and a and the capacitance was calculated according to the following equation[8]:

$$C = \frac{(Y_0 \cdot R_p)^{a^{-1}}}{R_p}\,.$$

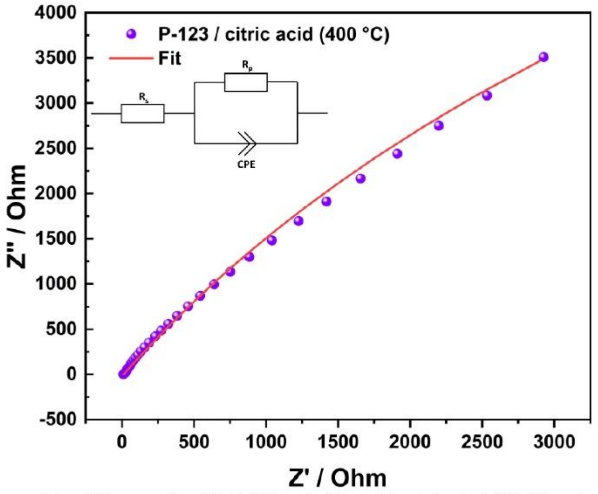

Figure S11: Impedance data of the sample with P-123 and citric acid calcined at 400 °C and simulation.

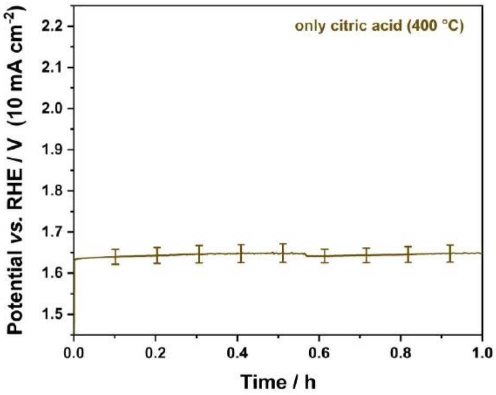

Figure S12. Long term stability test with error bars for the sample only with citric acid calcined at 400 °C. The error was calculated on the basis of three measurements of the sample and leads to an average standard error of 19 mV.

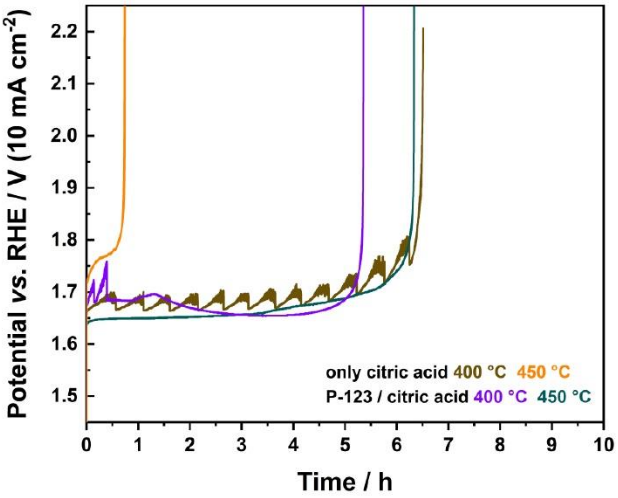

Figure S13. Long-term stability testing of the employed catalyst utilizing RDEs.

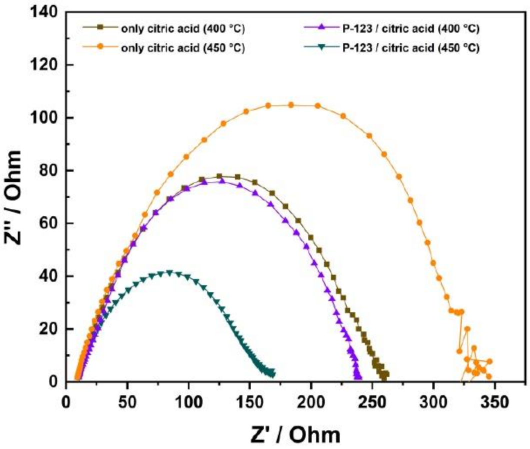

Figure S14. **EIS measurements with the various catalyst materials obtained at 1.6 V vs. RHE**.

Additional literature

[1] S. Mehrabani, J. P. Singh, R. Bagheri, A. G. Wattoo, Z. Song, K. H. Chae, M. M. Najafpour, *Nanoscale Adv.* **2019**, *1*, 686–695.

[2] A. Bloesser, R. Marschall, *ACS Appl. Energy Mater.* **2018**, *1*, 2520–2525.

[3] J. Timm, R. Marschall, *Adv. Sustain. Syst.* **2018**, *2*, 1700170.

[4] C. A. Poteet, K. M. Pontoppidan, S. T. Megeath, D. M. Watson, K. Isokoski, J. E. Bjorkman, P. D. Sheehan, H. Linnartz, *Astrophys. J.* **2013**, *766*, 1–14.

[5] G. Socrates, *Infrared and Raman Characteristic Group Frequencies: Tables and Charts*, **2004**.

[6] F. A. Miller, C. H. Wilkins, *Anal. Chem.* **1952**, *24*, 1253–1294.

[7] X. Wang, L. Andrews, *J. Phys. Chem. A* **2006**, *110*, 10035–10045.

[8] P. Connor, J. Schuch, B. Kaiser, W. Jaegermann, *Zeitschrift fur Phys. Chemie* **2020**, *234*, 979–994.

3.2. Elektrokatalytische Wasseroxidation mit $NiFe_2O_4$-Nanopartikeln

3.2.1. Synopsis

Der folgende Abschnitt beschreibt die Verwendung sphärischen $NiFe_2O_4$-Nanopartikeln für die elektrokatalytische Wasseroxidation in alkalischen Elektrolyten. Der Fokus soll zudem auf den magnetischen Eigenschaften von $NiFe_2O_4$ liegen. Die Veröffentlichung in *Chem. Eur. J.* thematisiert die schnelle und effiziente Synthese von nanopartikulärem $NiFe_2O_4$ durch eine Mikrowellen-basierte Methode. Verglichen mit der in Kapitel 3.1. diskutierten Templatsynthese beansprucht die Mikrowellenmethode eine Reaktionszeit von nur 30 Minuten, während die Templatsynthese aufgrund des langsamen Eintrocknens der Reaktionsmischung einige Tage benötigt. Eine sich anschließende thermische Behandlung der Nanopartikel ist zudem bei der Mikrowellensynthese optional, um die Partikelgröße einzustellen, was sich auch auf die katalytische Aktivität auswirken kann. Bei der Methode werden $Ni(acac)_2$ und $Fe(acac)_3$ als Metall-Präkursoren eingesetzt, die vor der eigentlichen Synthese in *rac*-1-Phenylethanol gelöst werden. Das Aufheizen erfolgt in einem geschlossenen System. Bei der Standardreaktionstemperatur von 225 °C entwickelt sich ein Druck von einigen bar (<10 bar). Niedrigere Temperaturen sind möglich, allerdings sind die Pulver dann hauptsächlich amorph. Die maximal mögliche Temperatur beträgt 240 °C, denn bei noch höheren Temperaturen kann sich metallisches Nickel am Gefäßrand bilden, welches Mikrowellenstrahlung gut absorbieren kann,[157] was zu einem unkontrollierbaren Temperaturanstieg führt. Nach der Fällung und der Waschprozedur können die Nanopartikel temperaturbehandelt werden, um die Partikelgröße anzupassen und etwaige organische Reste zu entfernen. In der Veröffentlichung sind Temperaturen für die thermische Nachbehandlung unter Luft von 300 °C, 400 °C und 500 °C gewählt. Durch die Synthese können phasenreine, sphärische $NiFe_2O_4$-Partikel mit Durchmessern von 4-11 nm und spezifischen Oberflächen von 63-243 $m^2\ g^{-1}$ präpariert werden. Anhand von Mössbauerspektren, die bei 80 K gemessen wurden, lassen sich Inversionsgrade λ bestimmen, die von der Partikelgröße abhängig sind. Es zeigt sich, dass $NiFe_2O_4$ nach einer thermischen Behandlung bei 500 °C einen Inversionsgrad von 0,66 aufweist und somit ein partiell inverser Spinell ist. Allgemein tendiert das System bei niedrigeren Kalzinierungstemperaturen zu einer Kationenbesetzung, die vom thermodynamisch bevorzugten inversen Zustand abweicht. Aus theoretischen Überlegungen ergibt sich, dass ein normaler $NiFe_2O_4$-Spinell eine gesteigerte Sättigungsmagnetisierung aufweisen müsste, was im Experiment nicht zu beobachten ist. Die maximal gemessene Sättigungsmagnetisierung bei 10 K beträgt 41,8 emu g^{-1} (1,75 μ_B pro Formeleinheit) für die bei 500 °C getemperte Probe. Es zeigt sich, dass die Sättigungsmagnetisierung bei den bei niedrigeren Temperaturen behandelten Proben deutlich reduziert ist, was mit Oberflächeneffekten zusammenhängt. Somit sind die magnetischen Eigenschaften des Materials dennoch über die Partikelgröße einstellbar. Die Aktivität in der Wasseroxidation hängt ebenso von der Partikelgröße ab. Die maximale Aktivität wird durch eine thermische Nachbehandlung bei 400 °C erreicht, was die niedrige OER Überspannung von 380 mV belegt (vergleiche mesoporöses $NiFe_2O_4$ 410 mV aus Kapitel 3.1.). Bei einer höheren Temperatur kommt es durch den Verlust von Oberfläche zu einem Aktivitätseinbruch. Entgegen der Erwartung liegt das Überpotential der kleineren Nanopartikel, die nicht oder nur bei 300 °C nachbehandelt wurden, ebenfalls höher (487 mV und 464 mV). Dies könnte mit organischen Resten oder einem ungünstigen Inversionsgrad und schlechter Leitfähigkeit zusammenhängen. Die Hauptaussage ist, dass die elektrokatalytische Aktivität durch verschiedene Variationen optimiert werden kann und ein Elektrokatalysator ein passendes Zusammenspiel verschiedener Eigenschaften benötigt.

3.2.2 Veröffentlichung in *Chemistry – A European Journal*

Christopher Simon,[a] Mohamed Barakat Zakaria,[b,c] Hannah Kurz,[a] David Tetzlaff,[b,d] André Blösser,[a] Morten Weiss,[a] Jana Timm,[a] Birgit Weber,[a] Ulf-Peter Apfel,[b,d] Roland Marschall[a]

Magnetic $NiFe_2O_4$ Nanoparticles Prepared *via* Non-aqueous Microwave-assisted Synthesis for Application in Electrocatalytic Water Oxidation

Veröffentlicht in: *Chemistry – A European Journal* **2021**, *27*, 16990-17001.

Einflussfaktor *Chemisty – A European Journal* (2021): 5,236
https://doi.org/10.1002/chem.202101716

[a] Department of Chemistry, University of Bayreuth, Universitaetsstrasse 30, 95447 Bayreuth, Germany
[b] Inorganic Chemistry I – Bioinorganic Chemistry, Ruhr-University Bochum, Universitaetsstrasse 150, 44801 Bochum, Germany
[c] Department of Chemistry, Faculty of Science, Tanta University, Tanta 31527, Egypt
[d] Fraunhofer Institute for Environmental, Safety, and Energy Technology, Osterfelder Strasse 3, 46047 Oberhausen, Germany

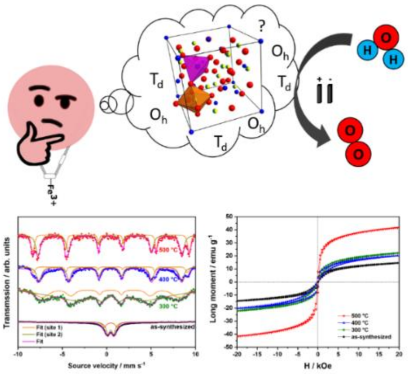

Individuelle Beiträge:

Das Konzept des Manuskripts stammt von Prof. Dr. Roland Marschall und mir. Es wurde verfasst von Prof. Dr. Roland Marschall und mir mit Beiträgen von allen Co-Autoren. Sämtliche Proben wurden von mir hergestellt, ebenso war ich verantwortlich für die Charaktersierung mittels Röntgendiffraktometrie, Raman- sowie Infrarotspektroskopie, Rasterelektronenmikroskopie gekoppelt mit energiedispersiver Röntgenspektroskopie und Transmissionselektronenmikroskopie gekoppelt mit Elektronenbeugung. Die Physisorptionsmessungen an den Pulvern wurden von Dr. Jana Timm und Jonas Jungmann (AG Marschall, Universität Bayreuth) durchgeführt und ausgewertet. Die Messung und Auswertung der Röntgenphotoelektronenspektren erfolgte durch Dr. Morten Weiß. Dr. Hannah Kurz und Prof. Dr. Birgit Weber waren verantwortlich für die Untersuchungen der magnetischen Eigenschaften der Materialien. Die Messung und Auswertung der Mössbauerspektren oblag David Tetzlaff, während die elektrokatalytischen Experimente von Dr. Mohamed Barakat Zakaria durchgeführt und in Zusammenarbeit mit mir intepretiert wurden. Die thermogravimetrischen Analysen wurden durchgeführt von Lena Geiling (AG Roth, Universität Bayreuth). Alle Autoren haben mit wissenschaftlicher Diskussion beigetragen. Mein Beitrag zum Manuskript beträgt ca. **60 %**.

Chemistry–A European Journal
Full Paper
doi.org/10.1002/chem.202101716
Chemistry Europe
European Chemical Societies Publishing

Magnetic $NiFe_2O_4$ Nanoparticles Prepared via Non-Aqueous Microwave-Assisted Synthesis for Application in Electrocatalytic Water Oxidation

Christopher Simon,[a] Mohamed Barakat Zakaria,[b, c] Hannah Kurz,[a] David Tetzlaff,[b, d] André Blösser,[a] Morten Weiss,[a] Jana Timm,[a] Birgit Weber,[a] Ulf-Peter Apfel,[b, d] and Roland Marschall*[a]

Abstract: Phase-pure spinel-type magnetic nickel ferrite ($NiFe_2O_4$) nanocrystals in the size range of 4 to 11 nm were successfully synthesized by a fast and energy-saving microwave-assisted approach. Size and accessible surface areas can be tuned precisely by the reaction parameters. Our results highlight the correlation between size, degree of inversion, and magnetic characteristics of $NiFe_2O_4$ nanoparticles, which enables fine-tuning of these parameters for a particular application without changing the elemental composition. Moreover, the application potential of the synthesized powders for the electrocatalytic oxygen evolution reaction in alkaline media was demonstrated, showing that a low degree of inversion is beneficial for the overall performance. The most active sample reaches an overpotential of 380 mV for water oxidation at 10 $mA\,cm^{-2}$ and 38.8 $mA\,cm^{-2}$ at 1.7 V vs. RHE, combined with a low Tafel slope of 63 $mV\,dec^{-1}$.

Introduction

Electrocatalytic water splitting can be regarded as a promising method to store electrical energy in form of hydrogen as a sustainable green energy carrier. However, water splitting typically suffers from the sluggish reaction kinetics of the oxygen evolution half reaction (OER). By employing electrocatalysts, the required overpotential of the OER can be decreased significantly.[1,2] However, up-to-date benchmark electrocatalysts like RuO_x or IrO_x are based on expensive and scarce noble metals, which is the reason why recent research focuses on their substitution.[3,4]

Spinel-type first-row transition metal oxides (TMOs) or their composite compounds containing nickel, manganese, iron, or cobalt are attractive materials for the electrocatalytic oxygen evolution reaction in alkaline media.[5–9] However, Mn-based electrocatalysts are often neglected due to stability issues.[10,11] The use of cobalt is further discussed critically due to its toxicity hazards and limited availability.[12] Therefore, low cost and highly abundant bimetallic NiFe spinel oxides with the elemental composition $NiFe_2O_4$ have gained attention in the field of alkaline water electrolysis, combining remarkable stability in alkaline media with excellent redox properties.[13,14] Their ferrimagnetism enables a simple way to recover the electrocatalyst from solution, making the material interesting for future large-scale industrial applications.[15]

$NiFe_2O_4$ is a representative of the spinel group with the general formula AB_2O_4. Typically, the inversion parameter λ is utilized to describe the particular cationic distributions in tetrahedral and octahedral sites according to the notation $[A_{1-\lambda}B_\lambda]_{tet}[A_\lambda B_{2-\lambda}]_{oct}O_4$. According to thermodynamics, the typical arrangement is either a normal spinel with an inversion degree of $\lambda = 0$ (e.g. $ZnFe_2O_4$, $CdFe_2O_4$)[16,17] or an inverse spinel with $\lambda = 1$ (e.g. $NiFe_2O_4$, $CoFe_2O_4$),[18,19] depending on cationic sizes and crystal field splitting energies. However, deviating situations can be found for non-equilibrium conditions, for example in the case of nanosized materials.[20,21] Thus, values for λ of 0.6 and 0.35–0.68 were reported for sol-gel derived $NiFe_2O_4$ nanomaterials by Atif et al. and Simon et al.,[22,23] which is then referred as a partially inverse spinel.

---

[a] *C. Simon, H. Kurz, Dr. A. Blösser, Dr. M. Weiss, Dr. J. Timm, Prof. B. Weber, Prof. R. Marschall*
Department of Chemistry
University of Bayreuth
Universitaetsstrasse 30
95447 Bayreuth (Germany)
E-mail: roland.marschall@uni-bayreuth.de

[b] *Dr. M. B. Zakaria, D. Tetzlaff, Prof. U.-P. Apfel*
Inorganic Chemistry I
Ruhr-University Bochum
Universitaetsstrasse 150
44801 Bochum (Germany)

[c] *Dr. M. B. Zakaria*
Department of Chemistry
Faculty of Science
Tanta University
Tanta 31527 (Egypt)

[d] *D. Tetzlaff, Prof. U.-P. Apfel*
Fraunhofer Institute for Environmental, Safety, and Energy Technology
Osterfelder Strasse 3
46047 Oberhausen (Germany)

Supporting information for this article is available on the WWW under https://doi.org/10.1002/chem.202101716

Part of a Special Issue on Contemporary Challenges in Catalysis.

The ferrimagnetic nature of bulk $NiFe_2O_4$ arises from the magnetic moment of anti-parallel spins between ferromagnetically ordered Fe^{3+} ions ($3d^5$, $\mu=5.9$) located at tetrahedral voids and ferromagnetically ordered Ni^{2+} ($3d^8$, $\mu=2.8$) plus Fe^{3+} ions ($3d^5$, $\mu=5.9$) on octahedral sites. The two sublattices are coupled antiferromagnetically, resulting in a magnetic moment of $\mu=2.8$ per formula unit. In case of a normal spinel arrangement of the cations, ferromagnetically ordered Fe^{3+} ions ($2\times 3d^5$) would couple antiferromagnetically with the Ni^{2+} ($3d^8$) ions resulting in a theoretically expected total spin of $S=4$ ($\mu=8.9$) per formula unit, which is significantly higher. Consequently, the magnetic characteristics of $NiFe_2O_4$ strongly depend on the cationic distribution, providing a simple access to tune the magnetic properties of nanosized $NiFe_2O_4$ materials, thus establishing a widespread range of possible magnetic applications, for example in biomedicine[24] or electromagnetic devices.[25]

Further, preparation of nanoparticular materials enables high surface-to-volume ratios. The increased number of active sites and shortened charge carrier pathways make them attractive for surface-depending processes like the electrocatalytic water splitting.[26,27]

$NiFe_2O_4$ nanoparticles with different morphological characteristics can be prepared by manifold preparation techniques: for example, Zhou et al. prepared $NiFe_2O_4$ nanoparticles with tuneable sizes of 10–120 nm via a low temperature hydrothermal method,[28] whereas Wang et al. chose a solvothermal approach in ethylene glycol producing $NiFe_2O_4$ nanoparticles with adjustable sizes of 7–200 nm.[29] $NiFe_2O_4$ nanoparticles with sizes of 8–28 nm are further available using co-precipitation methods, which is shown by Maaz et al.[30] Among the various preparation techniques, the applied microwave-assisted method offers an efficient and controlled heating, shortened reaction times, reproducibility, and improved yields.[31–33]

Following this experimental procedure, we present a simple one-step, non-aqueous microwave-based synthesis of magnetic $NiFe_2O_4$ nanoparticles, which is also applicable for related compounds such as $MgFe_2O_4$, $ZnFe_2O_4$, and $CaFe_2O_4$.[34–39] The as-synthesized powders already contain slightly nanocrystalline $NiFe_2O_4$, while organic residues originating from the metal precursors and the solvent can be removed easily by an additional calcination step at moderate temperatures. Phase-pure $NiFe_2O_4$ nanoparticles can be prepared by applying the microwave-based synthesis, with adjustable sizes and surface areas ranging from 4–11 nm and 63–243 $m^2\,g^{-1}$, respectively. The magnetic properties of the obtained materials can be controlled by adjusting the degree of inversion as described above. Thorough characterization of the powders was performed by transmission electron microscopy (TEM), selected area electron diffraction (SAED), X-ray diffraction (PXRD), Raman spectroscopy, energy dispersive X-ray spectroscopy (EDXS), nitrogen and water vapor physisorption analysis, diffuse reflectance infrared Fourier transform spectroscopy (DRIFTS), thermogravimetric analysis coupled with online mass spectrometry (TGA-MS), X-ray photoelectron spectroscopy (XPS), Mössbauer spectroscopy, and superconducting quantum interference device (SQUID) magnetometry. Additionally, the application potential of the powders was investigated for electrocatalytic oxygen evolution in alkaline media.

Results and Discussion

Nanocrystalline spinel-type $NiFe_2O_4$ particles were prepared by a water-free microwave-assisted synthesis starting from acetyl acetonate precursors dissolved in *rac*-1-phenylethanol as high boiling point solvent. Subsequent thermal treatment was executed to remove organic precursor residues and to adjust the crystallize size precisely. The microwave reaction temperature was set to 225 °C, with subsequent calcination steps at 300, 400, or 500 °C, respectively.

Morphology and crystal structure of as-synthesized as well as calcined $NiFe_2O_4$ nanoparticles were studied in detail by TEM and SAED (Figure 1). Low-magnification TEM images generally show randomly shaped particle agglomerates of a few hundred nanometers consisting of small nanoparticles. Hence, the degree of agglomeration is relatively high, which is expected, since no stabilization strategy like surface capping was applied.[34] Lattice planes are visible in the high-resolution TEM images, even for the as-synthesized sample. SAED patterns further demonstrate the crystallinity even of the as-synthesized sample, which is further increasing with the higher calcination temperatures. Patterns of obtained nanoparticles show rings consisting of small dots, each arising from a set lattice planes of an individual nanocrystallite. Upon calcination, the rings/dots are clearly more pronounced, due to the significantly higher crystallinity. Exemplary for the sample calcined at 500 °C, rings were assigned to spinel-type $NiFe_2O_4$ according to the reference pattern (JCPDS, no. 00-044-1485).

Particle size distributions estimated via particle counting can be fitted using a LogNormal function, demonstrating a sharp size distribution for as-synthesized particles, peaking at 3.6 nm. As expected, particle size distributions get broader when performing a subsequent thermal annealing procedure due to crystallite growth. However, particle size distributions of samples calcined at 300 and 400 °C are still relatively sharp, compared to the 500 °C sample. The averaged nanoparticle size could be estimated to be 4.9 nm (300 °C), 7.3 nm (400 °C), and 11.4 nm (500 °C).

Syntheses of $NiFe_2O_4$ are sometimes accompanied by the formation of thermodynamically stable α-Fe_2O_3 as secondary phase,[40] which can have a significant influence on the material properties. Therefore, a thorough control of phase-purity by PXRD (Figure 2a), Raman spectroscopy (Figure 2b), and EDXS (Table S1) is indispensable.

Even as-synthesized samples exhibit relatively wide reflections in the corresponding PXRD pattern that can unequivocally be assigned to spinel-type $NiFe_2O_4$ with $Fd\bar{3}m$ space group (JCPDS, no. 00-044-1485). By calcination, reflections get sharper, which is consistent with an increased crystallite size. From the integral breadth of the (220), (400), (511), and (440) reflections, the mean crystallite domain sizes could be calculated to 4 nm (as-synthesized), 6 nm (300 °C), 7 nm (400 °C), and 11 nm (500 °C), demonstrating nanocrystallinity of the samples. These

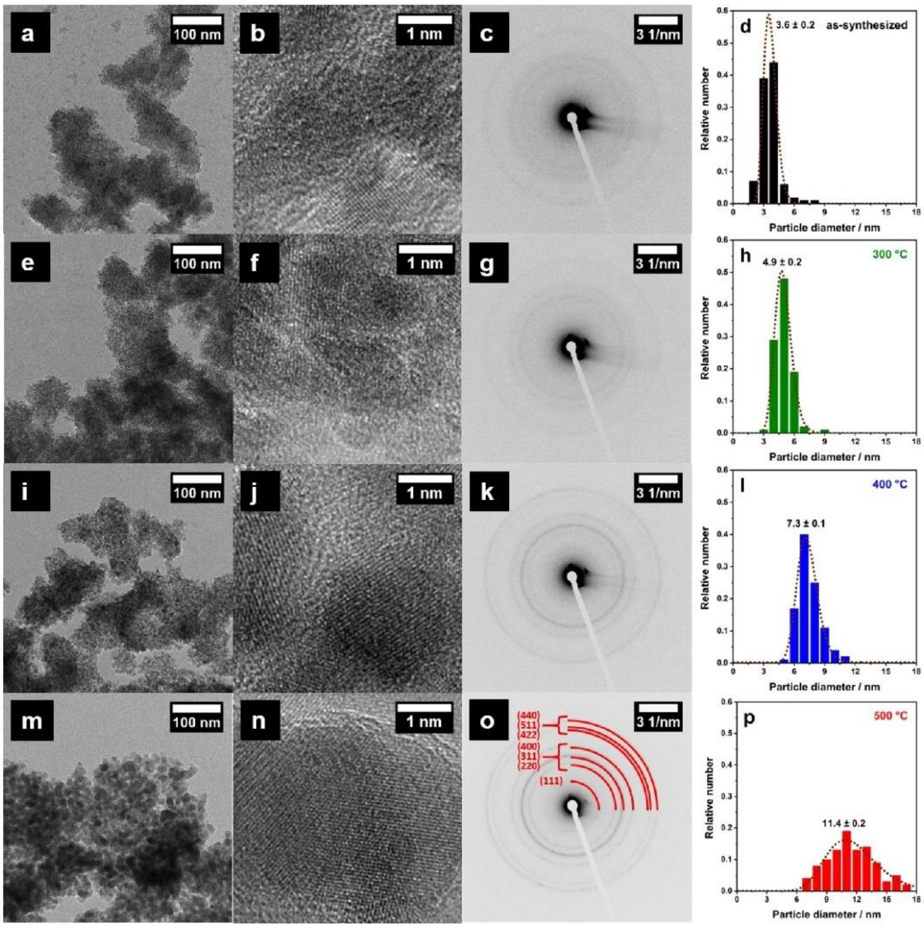

Figure 1. (HR-)TEM images (first and second column), SAED patterns (third column) plus particle size distributions (right column) of as-synthesized (a–d) and calcined (300 °C: e–h, 400 °C: i–l, 500 °C: m–p) $NiFe_2O_4$ nanoparticles.

values coincide with the particle sizes obtained from TEM analysis and display the single-crystalline nature of the $NiFe_2O_4$ nanoparticles.

The phase-purity of the prepared nanocrystals was additionally investigated by Raman spectroscopy, since small amounts of α-Fe_2O_3 might not be detected via PXRD due to the broad reflections caused by the nanosized crystals or the potentially amorphous nature of this oxide. Notably, the cationic distributions in tetrahedral and octahedral sites can also be estimated using this technique if high quality data can be obtained.[41] Figure 2b shows the expected five active Raman modes of spinel-type $NiFe_2O_4$, even before calcination: T_{2g} (200 cm^{-1}, 475 cm^{-1}, 565 cm^{-1}), E_g (320 cm^{-1}), and A_{1g} (685 cm^{-1}).[42] The most intense A_{1g} signal can be assigned to metal-oxygen symmetric stretching modes located in tetrahedral sites. The additional signals (T_{2g}, E_g) are due to the symmetric and asymmetric stretching and bending modes of metal-oxygen units located in octahedral voids.[43] The absence of characteristic Raman modes of hexagonal α-Fe_2O_3 also suggests the single-phase nature of the prepared $NiFe_2O_4$ nanoparticles.[44]

The Ni to Fe ratios that were calculated from EDX spectra of the $NiFe_2O_4$ nanoparticles (Table S1, Supporting Information) are close to the expected value of 0.5 for $NiFe_2O_4$, further underlining the single-phase nature of the prepared nanoparticles. The correct stoichiometry reveals that use of an excess of one precursor component in the synthesis is not necessary, as known for $MgFe_2O_4$.[36] As-synthesized samples exhibit higher

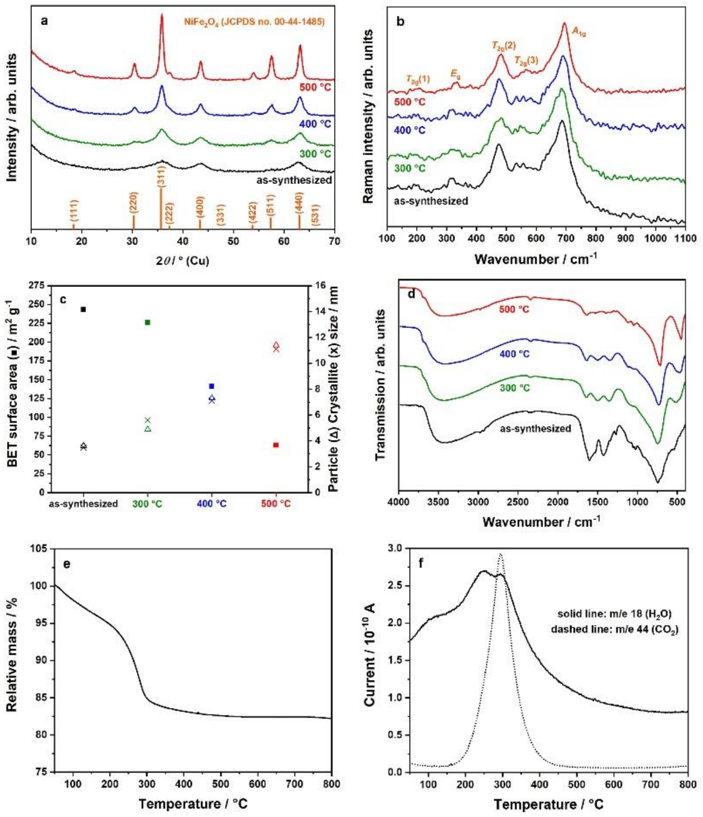

Figure 2. (a) PXRD patterns of calcined samples starting from the as-synthesized powder prepared at 225 °C via the microwave-based synthesis strategy, plus (b) corresponding Raman spectra; (c) relations between BET surface area (■), particle size (Δ), and crystallite size (x); (d) DRIFT spectra of corresponding samples; (e) TG analysis of as-synthesized sample prepared at 225 °C, plus (f) H_2O (solid line) and CO_2 (dashed line) evolution curves during heating monitored by MS.

carbon contents compared to the calcined samples, due to remaining organic residues from precursors and solvent.

BET surface areas of $NiFe_2O_4$ nanoparticles are summarized in Figure 2c. The maximum surface area achieved is 243 $m^2 g^{-1}$ for the as-synthesized sample, which is an unexpectedly high value for this type of material. As expected, BET surface areas decrease upon calcination because of crystallite growth, which has been proven due to enlarged nanocrystallite sizes. Samples treated at 500 °C still exhibit a high surface area of 63 $m^2 g^{-1}$.

Further investigations by DRIFTS (Figure 2d) show metal-oxygen vibrational modes of the spinel ferrite between 540–470 cm^{-1} and 750–740 cm^{-1}, respectively. Apparently, these modes are more pronounced after the additional calcination step. For the as-synthesized samples, two prominent signals are present at 1440–1410 cm^{-1} and 1620–1585 cm^{-1}, which can be assigned to carbonyl groups of precursor residues and adsorbed water molecules. Upon calcination at 300–500 °C, these signals mostly disappear, which corresponds to the decomposition of these precursor-derived surface carbonyl groups. Signals at 2350–2340 cm^{-1}, 3500–3000 cm^{-1}, and 3700–3690 cm^{-1} can be attributed to carbon dioxide, water, and O–H surface vibrations, respectively. Peaks appearing at 2980–2930 cm^{-1} are due to C–H vibrations.[36,41,45]

The presence of surface hydrocarbons is additionally indicated by TGA-MS of as-synthesized samples (Figure 2e and f), revealing a significant mass loss of nearly 15 % in the heating range of 250–300 °C. Still, in the range of 300–500 °C samples lose another 2 % of their masses. The first mentioned mass loss originates from the continuing decomposition of remaining organics or carbonates, since H_2O and CO_2 traces are detected by in situ MS analysis in exactly this temperature range (Figure 2f).

Conclusively, phase-pure $NiFe_2O_4$ with tuneable morphology can be prepared by a non-aqueous microwave-assisted synthesis, coupled with subsequent thermal annealing step. Aggregated nanocrystals exhibit sizes of 3.6–11.4 nm, resulting in high surfaces up to 243 $m^2 g^{-1}$.

Compositions of microwave-derived $NiFe_2O_4$ nanoparticles prepared at 225 °C were investigated via XPS, considering C 1s, O 1s, Ni $2p_{3/2}$, Fe $2p_{3/2}$ signals (**Figure S1**). High-resolution XP spectra of Ni $2p_{3/2}$ and Fe $2p_{3/2}$ are complex due to multiplet splitting and shake-up satellite peaks. The obtained spectra have been fitted with the parameters for $NiFe_2O_4$ as proposed by Biesinger et al.[46] Herein, FWHM and binding energies have been allowed to relax slightly ($\pm$0.2 eV for FWHM and $\pm$0.2 eV and 0.4 eV for Fe and Ni binding energies, respectively) in order to compensate for different instrumental resolutions, different pass energies and errors resulting from charge corrections. The measured Ni $2p_{3/2}$ and Fe $2p_{3/2}$ spectra are in good agreement with the fits, indicating the presence of $NiFe_2O_4$. O 1s spectra can be fitted with three different peaks at 529.9 eV, 531.4 eV and 533.4 eV, which can be attributed to lattice oxygen, oxygen atoms adjacent to defects, and oxygen from water molecules.[47] The peak at 531.4 eV is decreasing in intensity with increasing annealing temperature, indicating that the amount of defects is reduced by annealing in air.

Elemental compositions obtained from XPS analyses are summarized in Table S2. Compared to the calcined samples, the as-synthesized powders contain a significantly higher carbon content, because of remaining organic residues. Ni to Fe ratios in the nanocrystals are close to 0.5, which correlates well with previous findings from EDXS.

The described microwave-based preparation route was also performed at 200, 240, 250, and 275 °C instead of 225 °C, showing that the synthesis procedure works in a temperature range of 200–240 °C (Figure S2). At 250 and 275 °C, the syntheses mostly result in the formation of additional Ni nuclei. Since metallic Ni is an excellent microwave absorbing material, superheating can occur, which is coupled with an unusual pressure increase (Figure S3).[48] Additionally, the time-dependency of the presented synthesis strategy was studied exemplary for a reaction temperature of 240 °C (the highest possible reaction temperature without Ni nuclei formation and superheating effects). Therefore, the reaction time was varied between 5–30 min. Corresponding PXRD patterns of the as-synthesized nanopowders are presented in Figure S4. Already after 5 min, extremely wide reflections with low intensities of spinel-type $NiFe_2O_4$ are observable, demonstrating very small crystallites already forming after this short reaction time. With increasing reaction times, samples become more and more crystalline, which is demonstrated by the increasing crystallite sizes and decreasing BET surface areas (Figure S5). Comparable microwave-based experiments were performed for $ZnFe_2O_4$ spinels by Dolcet et al.,[37] obtaining highly crystalline phase-pure $ZnFe_2O_4$ nanoparticles already after 5 min of reaction time. Due to restricted yields at 200 °C and the potential danger of superheating at 240 °C, the standard reaction temperature was chosen to be 225 °C for full analysis.

In the thermodynamically most stable state, the crystal structure of $NiFe_2O_4$ can be described as inverse spinel with an inversion degree of $\lambda = 1$. The anti-parallel spin arrangement of cations located in tetrahedral and octahedral sites results in the overall ferrimagnetic nature of the Neél collinear type.[49,50] Non-equilibrium conditions can be induced by preparing nanosized $NiFe_2O_4$ materials, resulting in a deviation of cationic distributions ($0 < \lambda < 1$), which is then referred as partially inverse spinel. Cationic distributions of such iron-based spinels can be estimated by ^{57}Fe Mössbauer spectroscopy, which was performed at 298 K and 80 K for microwave-derived $NiFe_2O_4$ nanoparticles prepared at 225 °C (Figure 3). For the inverse spinel $NiFe_2O_4$ with a permanent magnetic moment, a magnetic hyperfine splitting into two sextets is expected, corresponding to Fe^{3+} cations located in tetrahedral and octahedral voids, respectively. At room temperature, Mössbauer spectra of the nanoparticles depend strongly on the synthesis conditions. The as-synthesized sample shows two very similar doublets with an isomer shift δ of 0.35 mm/s (both) and a quadrupole splitting ΔE_Q of 0.98 and 0.55 mm/s, respectively,[51] indicating the presence of Fe^{3+} in tetrahedral and octahedral sites and superparamagnetic behavior. A reliable assignment of the doublets to the different sites and thus determination of λ is not possible with the data available. A subsequent thermal annealing step at temperatures of 300 or 400 °C does not change the described situation significantly. A calcination

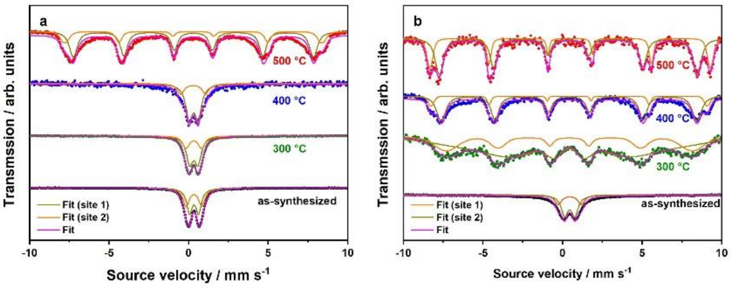

Figure 3. ^{57}Fe Mössbauer spectra of $NiFe_2O_4$ nanoparticles taken at 298 K (a) and 80 K (b). Generally, data points were fitted for both Fe^{3+} cations located in tetrahedral (site 1) and octahedral (site 2) voids, giving the overall fit.

temperature of 500 °C is necessary to observe a sextet due to the magnetic hyperfine splitting in the room temperature Mössbauer spectrum. The increased particle size results in a reduced fluctuation of the magnetization and the magnetization reversal is now slow compared to the time resolution of the Mössbauer spectrum. Please note that the blocking temperature for the magnetization reversal determined by magnetic measurements, which will be shown below, is lower due to the different time scales of the two methods. Notably, the sextet is a superposition of two individual sextets arising from Fe^{3+} cations located in tetrahedral and octahedral sites. The above findings suggest changing cationic distributions and blocking temperatures by varying nanoparticle sizes. From the relative areas of these sextets, the inversion degree λ can be determined approximately, by equalizing the areas (tetrahedral, octahedral) with the term $\lambda/(2-\lambda)$.[52] For this purpose, measurements were repeated at 80 K. Here, the sextets become observable for the three calcined samples, showing that the blocking temperatures are above 80 K on the Mössbauer time scale. The estimation of λ is only meaningful for samples calcined at 400 and 500 °C. For the sample calcined at 300 °C the small particle size leads to a significant broadening of the lines due to the iron centers at the surface that prevent a reliable determination of the areas. Obtained values for λ (400 °C : 0.30, 500 °C : 0.66) suggest the presence of partially inverse spinels and further underline the strong relation between nanoparticle size and cationic distributions. A higher calcination temperature results in a more inverse $NiFe_2O_4$ spinel, which is in agreement with thermodynamics. Thereof, cationic distributions of $NiFe_2O_4$ nanoparticles are easily adjustable by the chosen calcination temperature. Further details obtained from ^{57}Fe Mössbauer spectroscopy (isomer shifts, quadrupole splittings, internal magnetic fields) are summarized in Table S3.

Magnetization curves of $NiFe_2O_4$ nanoparticles measured at 300 K and 10 K obtained by SQUID magnetometry are presented in Figure 4a and b. To include the mass portion of diamagnetic components, original data sets were corrected by 22.0 % (as-synthesized), 3.6 % (300 °C), 1.5 % (400 °C), and 0.8 % (500 °C), which is in accordance with TGA analysis (cf. Figure 2e). Uncorrected magnetization plots are additionally presented in Figure S6. The saturation magnetizations M_S (with/without mass correction) are further summarized comparatively in Table 1. Determined M_S values are generally higher for the 10 K measurements compared to the room temperature measurements, indicating that complete saturation is not reached at room temperature. Additionally, magnetization curves taken at 10 K feature a narrow hysteresis, in line with the determined blocking temperature that is for all samples above 10 K. Comparing the differently treated samples, the saturation magnetizations estimated at 300 K and 10 K increase with the calcination temperature by tendency. The as-synthesized particles exhibit a saturation magnetization of 14.6 emu g^{-1}, compared to 41.8 emu g^{-1} of samples treated at 500 °C. This is in line with the increase in particle size. Effects like surface spins, spin canting, spin glass structures, and dead layers, depending mainly on the size of $NiFe_2O_4$ nanoparticles, may

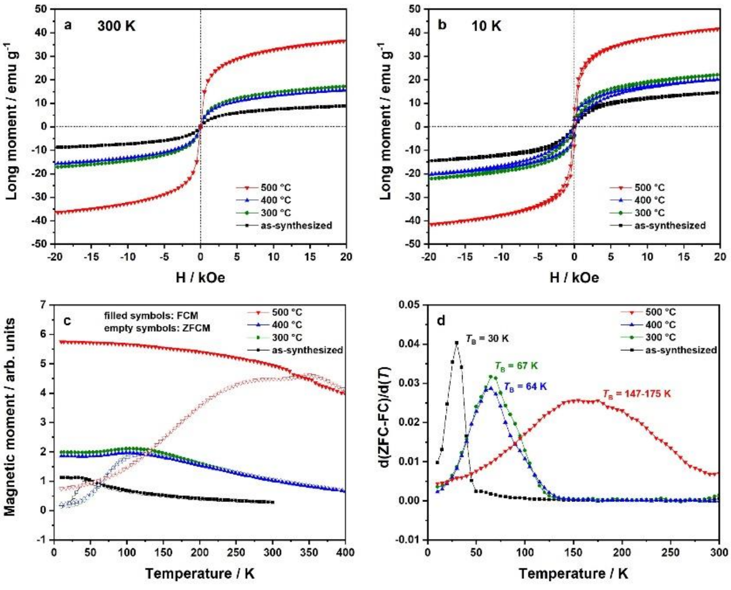

Figure 4. Mass loss corrected magnetization curves of $NiFe_2O_4$ nanoparticles at 300 K (a) and 10 K (b), measured via SQUID magnetometry. The field-cooled (FCM) (applied field 100 Oe) and zero-field-cooled magnetization (ZFCM) curves are shown in (c), the corresponding d(ZFC-FC)/d(T) plots in (d). Here, the local maxima represent the blocking temperatures.

Table 1. Saturation magnetization at 20 kOe obtained from SQUID magnetometry experiments. The assumed unit cell is $Ni_8Fe_{16}O_{32}$ with M = 1875.05 g mol^{-1}.

	size/nm	300 K			10 K		
		M_s/emu g^{-1}	M_s (corr)/emu g^{-1}	M_s/Kemu mol^{-1}	M_s/emu g^{-1}	M_s (corr)/emu g^{-1}	M_s/Kemu mol^{-1}
as-synthesized	3.6	7.2	8.8	16.6	11.9	14.6	27.3
300 °C	4.9	16.6	17.2	32.3	21.4	22.2	41.6
400 °C	7.3	15.5	15.7	29.5	20.0	20.3	38.0
500 °C	11.4	36.3	36.6	68.5	41.4	41.8	78.3

contribute to the significantly changed, for smaller particles usually reduced, magnetic properties.[53] However, for samples treated at 300 and 400 °C a deviation from this trend is observed; the saturation magnetization after calcination at 300 °C is higher (22.2 emu g^{-1}) than after calcination at 400 °C (20.3 emu g^{-1}) and does not go in line with the particle size. This indicates a change in the inversion degree already at those temperatures, thus λ (300 °C) $<$ λ (400 °C).

Using Neel's sublattice theory, the calculated saturation magnetization of bulk $NiFe_2O_4$ (thermodynamically stable state) is 50 emu g^{-1}.[54] According to $M_S = N_A \mu_B S$, this value strongly depends on the expected total spin per formula unit, a reduced λ will lead to an increased saturation magnetization. With $\lambda = 0.66$ after calcination at 500 °C and a particle size of 11.4 nm, a comparison with the achieved saturation magnetization indicates that near-bulk magnetization is reached despite the small nanocrystals size of $NiFe_2O_4$. A relation of the magnetic properties with both, inversion degree and nanoparticle size, is therefore obvious. Thus the magnetism of ultrasmall $NiFe_2O_4$ nanoparticles is reduced due to the large particle surface, but the changed cationic distributions can counteract this effect, which was shown already for $NiFe_2O_4$[55,56] and other spinel-type materials, like $MgFe_2O_4$[36] or $CoFe_2O_4$.[57]

The field-cooled (FCM) and zero-field-cooled (ZFCM) magnetization curves are depicted in Figure 4c. Blocking temperatures T_B could be estimated via the d(ZFC-FC)/d(T) plots shown in Figure 4d. ZFCM-FCM plots of magnetic $NiFe_2O_4$ as-synthesized nanoparticles and those calcined at 300 °C and 400 °C show the expected behavior for soft magnetic nanomaterials with narrow particles size distributions.[58] However, ZFCM-FCM curves exhibit differences depending on the particle size. The d(ZFC-FC)/d(T) plot of the as-synthesized powder is characterized by a sharp signal with a maximum at 30 K, giving the mandatory temperature for the spin flip, which is referred as blocking temperature T_B. Thermal treatment results in a signal broadening, which correlates to the loss of particles size homogeneity (cf. Figure 1d, h, l, p) and an increasing degree of magnetic anisotropy. Blocking temperatures of calcined samples could be estimated to 67 K (300 °C), 64 K (400 °C), and 147–175 K (500 °C). For the particles calcined at 500 °C the signal is very broad indicating a significantly broader particle size distribution. A relation between blocking temperature and calcination temperature/particle size is obvious. When performing Mössbauer spectroscopy at 80 K (cf. Figure 3b), the blocking temperature is near or above 80 K for all calcined samples, resulting in sextets due to magnetic hyperfine splitting. Since as-synthesized particles feature a blocking temperature of 30 K, only a doublet due to superparamagnetism can be observed at 80 K.

To conclude, particle size, crystallite size, surface area, and following cationic distributions can easily be controlled by the synthesis conditions. Consequently, the magnetic properties of nanoparticular $NiFe_2O_4$ strongly depend on the subsequent thermal annealing procedure. By adjusting particle sizes precisely, inversion degree and magnetic characteristics of obtained $NiFe_2O_4$ nanomaterials can be tailored for any particular application.

Alongside the magnetic applications, $NiFe_2O_4$ is a promising material to catalyze the oxygen evolution reaction, combining remarkable surface areas (in case of nanoparticle or mesoporous morphology) with an outstanding stability in alkaline media. For electrochemical oxygen evolution to take place at $NiFe_2O_4$ nanoparticles, the presence of a preferably bulk hydrophilicity and wettability is beneficial.[59] Therefore, water vapor physisorption isotherms of $NiFe_2O_4$ nanoparticles prepared at 225 °C were recorded (Figure S7a) and for better comparison corrected with regard to the respective specific BET surface area (Figure S7b). For a metal oxide, $NiFe_2O_4$ nanocrystal powders generally exhibit relatively high water vapor uptakes of 0.77 cm^3 m^{-2} (as-synthesized), 1.00 cm^3 m^{-2} (300 °C), 1.63 cm^3 m^{-2} (400 °C), and 2.16 cm^3 m^{-2} (500 °C) at a relative pressure of 0.95 (95 % humidity).[60] Thus, a higher calcination temperature results in a higher overall water uptake, which can be correlated to the decomposition of hydrophobic carbon surface residues (cf. Figures 2e and f). From this point of view, the calcination of $NiFe_2O_4$ powder further promotes the applicability in electrochemical water splitting.

The ferrimagnetism of spinel-type $NiFe_2O_4$ enables a simple method to recover the electrocatalyst for catalyst reuse. Due to nanostructuring, an improved electrical conductivity is ensured, which is also beneficial for electrocatalysis.[61,62] Hence, the application potential of $NiFe_2O_4$ nanocrystals for the oxygen evolution reaction (OER) was investigated, examining the influence of surface area and crystallinity on the overall activity in detail. For this purpose, a glassy carbon (GC) electrode modified with 0.35 mg cm^{-2} $NiFe_2O_4$ was used as working electrode. Experiments were performed under alkaline conditions (1 M KOH). To compare surface areas obtained by physisorption measurements with the corresponding electrochemical active surface area (ECSA), cyclic voltammetry data measured at various scan rates in the non-faradaic region (1.31–1.41 V vs. RHE) were considered (Figure S8). Differences of forward and backward scans at 1.36 V vs. RHE were plotted against the scan rate (mV s^{-1}). Linear extrapolation of the data

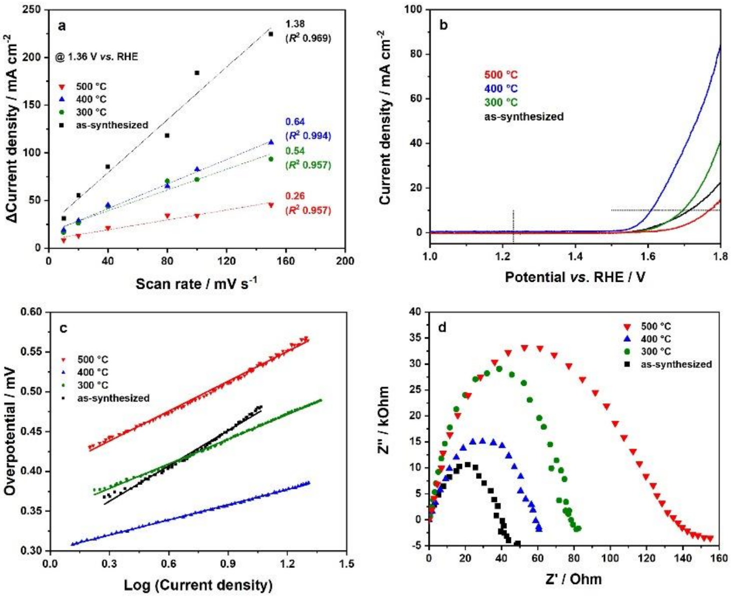

Figure 5. Electrochemical characterization of microwave-derived $NiFe_2O_4$ nanoparticles prepared at 225 °C. (a) Estimation of the electrochemical double-layer capacitance c_{DL} as slope of the linear fit, which is proportional to ECSA, (b) Linear sweep voltammograms (LSV) without iR compensation measured with a scan rate of 50 mV s^{-1} in 1 M KOH, corresponding Tafel plots are further shown in (c). EIS Nyquist plots of electrodes at applied potential (1.7 V vs. RHE) are presented in (d).

points gives the electrochemical double-layer capacitance c_{DL} as slope. Normalization on the surface area of the GC electrode (0.071 cm^2) and division of c_{CL} with the specific capacitance (c_S, typical value 0.03 mF cm^2 for alkaline solutions) finally gives the electrochemical active surface area (Figure 5a).[3,63,64] Parameters obtained from electrochemical measurements are further summarized in Table 2. As-synthesized nanoparticles exhibit an electrochemical active surface of 3.27 cm^2. Upon calcination, ECSA values decrease, which can be correlated to the enlarged crystallite size. These observations go in line with a decreased BET surface area (cf. Figure 2c). Comparing as-synthesized and 500 °C samples, the electrochemical active surface decreases by 81 % (3.27 cm^2 vs. 0.62 cm^2), comparable to the observed BET surface area change by likewise 73 % (243 m^2 g^{-1} vs. 63 m^2 g^{-1}). Interestingly, samples treated at 300 and 400 °C exhibit comparable ECSA. Linear sweep voltammograms (LSVs) of $NiFe_2O_4$-modified glassy carbon working electrodes presented in Figure 5b reveal a dependency of the OER activity and morphology. The current densities read at 1.7 V vs. RHE are 8.7 mA cm^{-2} (as-synthesized), 10.8 mA cm^{-2} (300 °C), 38.8 mA cm^{-2} (400 °C), and 3.4 mA cm^{-2} (500 °C). Accordingly, $NiFe_2O_4$ nanoparticles calcined at 400 °C show the highest OER activity. Apart from that, the as-synthesized and 300 °C samples perform worse compared to the sample calcined at 400 °C. Thus, observed activities partly mismatch the estimated electrochemical double-layer capacitances, providing that other factors also influence the activity for the electrocatalytic water oxidation. The reason for the relatively low OER activity of the uncalcined sample is the organic surface coating, which originates from precursor (acetylacetonate) and solvent (*rac*-1-phenylethanol) residues, decreasing the surface hydrophilicity significantly. Notably, a calcination temperature of 300 °C is not sufficient to remove these organic surface layers, contrary to 400°, which is reflected by the significantly increased OER performance at 400 °C. Interestingly, the breakdown in activity towards the sample calcined at 500 °C not only correlates with a lower BET surface area, but also with the doubling of the degree of inversion observed from Mössbauer spectroscopy (0.30 to 0.66, cf. Figure 3). For $NiFe_2O_4$ nanoparticles, a more inverse spinel seems to lower the activity for the electrocatalytic oxygen evolution reaction in alkaline media. Such an influence of λ on the OER activity was earlier observed for spinel

Table 2. Parameters obtained from electrochemical investigations on $NiFe_2O_4$ nanoparticles prepared at 225 °C. The overpotential for the oxygen evolution reaction was read at a current density of 10 mA cm^{-2}.

	Overpotential/mV	Tafel slope/mV dec^{-1}	ECSA/cm^2
as-synthesized	487	148	3.27
300 °C	464	103	1.28
400 °C	380	63	1.52
500 °C	539	125	0.62

manganese ferrite ($MnFe_2O_4$) nanoparticles.[65] Since both magnetic properties and OER activity are therefore correlated to the inversion degree, λ can be considered as one key factor to establish a function-tailored spinel-type material.

To sum up, a thermal annealing step at moderate temperatures like 400 °C results in the maximum activity, but higher calcination temperatures result in a breakdown of activity, which is influenced by a lower surface area[66] and an increased degree on inversion. Overpotentials (at 10 mA cm^{-2}) of 487 mV (as-synthesized), 464 mV (300 °C), 380 mV (400 °C), and 539 mV (500 °C) are acceptable values for the electrocatalytic water oxidation, and further go in line with previous results. From this point of view, an energy-consuming annealing step at temperatures higher than 400 °C is not recommended for a high electrocatalytic activity. The potential-dependent kinetics of the oxygen evolution reaction (OER) with $NiFe_2O_4$ nanoparticles were studied via Tafel analysis (Figure 5c). Tafel slopes of 148 mV dec^{-1} (as-synthesized), 103 mV dec^{-1} (300 °C), 63 mV dec^{-1} (400 °C), and 125 mV dec^{-1} (500 °C) reveal favorable kinetics for the oxygen evolution reaction, especially for nanoparticles calcined at 400 °C. In addition, electrochemical impedance spectroscopy on material electrodes was performed (Figure 5d). $NiFe_2O_4$ nanoparticles calcined at 500 °C possess a relatively high resistance, which could be correlated to the slightly increased crystallite size but can ultimately be correlated to the larger degree of inversion of the spinel as well as to their altered magnetic behavior, resulting in a decreased activity for electrocatalytic water oxidation. When the calcination temperature is reduced to 400 °C, the resistance is much lower, which can be correlated to the remarkably better performance of the corresponding sample. The sample calcined at 300 °C shows a similar resistance comparable to samples calcined at 400 and 500 °C, although the particle size is smaller. However, a carbon layer on the nanoparticle surface seems to influence their electrocatalytic behavior. The as-synthesized particles exhibit the lowest resistance of all samples, possibly due to the smallest particle surface, which contradicts to the worse OER performance. However, the four samples show quite small Nyquist arcs (50–140 Ω), indicating a fast charge transfer at the interface of electrode and electrolyte for high performance.

For future industrial applications, stable performances over longer periods of time are essential, combined with high activities. Therefore, a chronoamperometric long-term stability test was performed with the most active 400 °C-treated sample. Therefore, a constant potential of 1.56 V vs. RHE was applied, which is near to the experimental onset (overpotential) of the sample (Figure S9). In the first three hours, it is obvious that there is a significant increase in the current density, which might be attributed to the electrochemical activation of the electrode, which were not conditionalized by cyclic voltammetry prior to chronoamperometry. After the activation process, a fast current density drop can be observed, before reaching a relatively constant level after around 10 hours. After one day, the current density is reduced to 38%, compared to the start. A part of the current density loss originates possibly from the detachment of the catalyst from the electrode surface during the long-term stability test. Notably, after the course of the experiment, fine particles could be observed in the electrolyte visually.

To outline the electrochemical measurements, microwave-derived $NiFe_2O_4$ nanoparticles synthesized at 225 °C are able to electrocatalyze the oxygen evolution reaction. The overall performances are strongly influenced by the subsequent thermal annealing procedure, with samples treated at 400 °C being the most active nanocrystals, reaching an overpotential of 380 mV for water oxidation. Thus, a high surface area combined with a low crystallinity and suitable bulk hydrophilicity seem to be key factors for a high performance in the oxygen evolution reaction. However, a temperature treatment at 400 °C is necessary to achieve the maximum activity. In fact, temperature treatment below 400 °C or omitting the calcination step entirely results in smaller particle sizes, but carbon residues originating from the synthesis procedure are not decomposed completely, hindering the electrocatalytic water oxidation.

Conclusions

We introduced a non-aqueous microwave-assisted sol-gel synthesis for the preparation of $NiFe_2O_4$ nanocrystals. The reaction operates in a temperature window of 200–240 °C, yielding crystalline nanopowders directly after the synthesis. By a subsequent thermal annealing step at 300–500 °C, the morphology of the nanoparticles can be tuned preciselyand their surface area is also cleaned from residual hydrocarbon impurities. Applying for example a reaction temperature of 225 °C, phase-pure spinel-type $NiFe_2O_4$ nanoparticles with sizes of 3.6–11.4 nm and surface areas 63–243 m^2 g^{-1} can be produced.

Due to the preparation of such ultrasmall $NiFe_2O_4$ nanocrystals, non-equilibrium site occupations can be found, which is indicated by changed cationic distributions. The structure changes from a complete inverse spinel (thermodynamically stable state) to a partially inverse spinel upon nanostructuring. Due to the changed occupation of tetrahedral and octahedral sites in the $NiFe_2O_4$ nanoparticles, the magnetic properties can be tailored precisely by adjusting the degree of inversion. Thus, $NiFe_2O_4$ nanocrystals are applicable for a widespread range of magnetic applications.

In addition, $NiFe_2O_4$ nanoparticles were tested for their ability to perform the electrocatalytic oxygen evolution reaction in alkaline media. Keeping the composition of the materials constant, the influence of morphology, crystallinity, and degree of inversion on the activity was investigated, revealing that heating above 400 °C is not necessary to get high electrochemical activity. Moreover, we can correlate the breakdown in activity at higher calcination temperatures to the higher degree of inversion of the spinel crystal. The most active sample, which was treated at 400 °C, reaches a remarkable activity (overpotential 380 mV, Tafel slope 63 mV dec^{-1}). It is worth to mention that in context of recent literature about $NiFe_2O_4$ in water oxidation electrocatalysis, and although we used unmodified and phase-pure $NiFe_2O_4$ nanoparticles, our as-synthesized materials exhibit a comparable performance (Table S4). No strategies like faceting,[67] modification with other compounds,[68] surface functionalization,[69] or introduction of vacancies[70] were applied, underlining the high potential of our facile synthesis to prepare active electrocatalysts and showing the importance of the inversion degree, λ on the overall performance.

Experimental section

For each synthesis of $NiFe_2O_4$ nanoparticles, 128.5 mg (0.5 mmol) $Ni(acac)_2$ (*SigmaAldrich*, for synthesis) and 353.2 mg (1 mmol) $Fe(acac)_3$ (*Acros Organics*, +99%) were dissolved in 15 mL of *rac*-1-phenylethanol (*SigmaAldrich*, 98%) using ultrasonication. The obtained solution was transferred into a 30 mL borosilicate microwave glass vessel. The solution was then heated as fast as possible to a maximum temperature of 200–275 °C (standard 225 °C) for typically 30 min using microwave irradiation (Anton Paar Monowave 400 equipped with MAS24 autosampler) under constant stirring (600 rpm). Next, the reaction mixture was cooled down to 55 °C using compressed air. To study the influence of the reaction time, the reaction was performed additionally for 5–25 min (5 min steps) at 240 °C. Obtained nanoparticles were precipitated with *n*-pentane and washed for three times with water/acetone mixtures (3:1, 12:1, 12:1) and diethyl ether. The resulting powder was dried at 80 °C overnight. To remove remaining organic residues and to adjust the crystallite size, the as-synthesized samples were further calcined in a Nabertherm muffle furnace under air atmosphere at 300/400/500 °C (heating rate 5 °C/min, holding time 5 h).[34,37]

Characterization techniques

Transmission electron microscopy (TEM) and selected area electron diffraction (SAED) were performed on a 200 kV JEOL-JEM-2200FS EFTEM with Schottky FEG and In-Column Omega Energyfilter from JEOL GmbH. For sample preparation, samples were dispersed in ethanol (*Merck, LiChrosolv®, gradient grade for liquid chromatography*), before dropping a small amount of the dispersion on a carbon film coated Cu TEM grid (200 Mesh). Images were edited using ImageJ 1.52a.

X-ray powder diffraction (PXRD) was measured with a Malvern PANalytical Empyrean device equipped with a PixCel 1D detector using Cu Kα radiation (wavelengths $\lambda_1 = 1.54046$ Å and $\lambda_2 = 1.54439$ Å). Acceleration voltage and emission current were set to 40 kV and 40 mA, respectively. Data were collected in a range of 10–70° 2θ, with a step size of 0.144° and a scan step time of 883 s. To minimize X-ray fluorescence, detector pulse height distribution (PHD) settings were changed to 8.05 keV (lower level) and 11.27 keV (upper level). From PXRD data, the crystallite domain size could be estimated using the integral breadth β.[71] Therefore, 2Θ values were transformed to units of s ($s = (2\sin\Theta/\lambda)$. Then, dividing the area under an individual reflection by its height gives the integral breadth β_{hkl}, which is the reciprocal of the crystallite size L_{hkl}.

Raman spectra were collected on a LABRAM I Raman spectrometer from Horiba Jobin Yvon GmbH, additionally modified with an Olympus BX41 microscope (50x magnification). A HeNe laser ($\lambda = 632.82$ nm) was utilized, operated with a power of 2 mW. For each sample, three spots were measured with 15 s integration time and 10 co-additions. Subsequently, individual spectra were averaged, normalized and smoothed using a FFT filter. Data were measured within a range of 100–1000 cm^{-1} with a step size of 1.02 cm^{-1}.

Energy-dispersive X-ray spectroscopy (EDXS) experiments were performed using a Zeiss Leo 1530 instrument equipped with an UltraDry-EDX detector (ThermoFisher Scientific NS7). A working distance of 8 mm was applied, while the acceleration voltage was set to 15 kV in order to detect Ni, Fe, and O. Prior to the analysis, samples were sputtered with 1.3–2 nm of Pt with a Cressington Sputter Coater. For each sample, four points were investigated, before averaging the values, with the standard deviation as error bar.

Diffuse reflectance infrared Fourier transform spectroscopy (DRIFTS) was measured on Bruker alpha II device within a range of 400–4000 cm^{-1}, applying a spectral resolution of 10 cm^{-1} and 200 co-additions for a single scan.

Surface areas were estimated with N_2 at 77 K using an Anton Paar QUADRASORB evo surface area & pore size analyzer. For surface area evaluation, the BET (Brunauer-Emmett-Teller) theory was applied. Prior to the measurements, samples were degassed in vacuum at 120 °C for 12 h to remove surface adsorbed water.

Volumetric H_2O vapor physisorption measurements were performed with the ASiQMP-MP-AG setup (Anton Paar QuantaTec, Boynton Beach, USA) at 20 °C and constant $p_0 = 2317.67$ Pa (17.384 Torr). The samples were also degassed at 120 °C for 12 h prior to the measurement.

Thermogravimetric analysis (TGA) in synthetic air was carried out on a Netsch Jupiter STA 449 C thermo-balance, additionally coupled with a Netzsch Aeolos QMS 403 C mass spectrometer (MS). Data were collected in a range of 30–1000 °C with a heating rate of 5 °C min^{-1}. MS traces of H_2O (*m/e* 18) and CO_2 (*m/e* 44) were recorded.

X-ray photoelectron spectroscopy (XPS) was performed with a Physical Electronics PHI VersaProbe III Scanning XPS Microprobe equipped with a monochromatic aluminum Kα source in the KeyLab "Device Engineering" of the Bavarian Polymer Institute (BPI). Survey scans were measured with a pass energy of 224 eV, a step size of 0.8 eV and a time of 50 ms per step, whereas high-resolution spectra were recorded with a pass energy of 26 eV, a step size of 0.1 eV and a step time of 50 ms; beam diameter was set to 100 μm for all measurements. All samples were flooded with low energy electrons and argon ions to prevent surface charging. Argon ion sputtering before measuring was omitted to prevent reduction of iron and nickel species.[47] The recorded data was evaluated with CasaXPS using Gaussian-Lorentzian GL(30) line shapes and Shirley backgrounds; the C 1s signal was set to 284.8 eV for charge correction.

^{57}Fe Mössbauer spectroscopy at room temperature and 80 K was performed on a SeeCo constant acceleration spectrometer with temperature controller, equipped with a ^{57}Co source in a Rh matrix. Isomer shifts are referred to α-Fe at room temperature. Data sets were fitted with the WMOSS program by applying a Voigt profile-based (hyperfine field distribution) or Lorentzian profile-based (quadrupole doublets) least-square routine.

Magnetic experiments were performed on a superconducting quantum interference device (SQUID) MPMS-XL5 device from Quantum Design. Samples were measured in gelatin capsules held in a plastic straw. Field measurements at 10 and 300 K were performed from 0.1 to 20 to −20 kOe in the hysteresis mode (step width 0.5 kOe). The scans were corrected for the diamagnetism of the sample holder and the sample mass loss during calcination, which was estimated via TGA. ZFCM/FCM (zero-field-cooled/field-cooled magnetization) curves were collected at 0.1 kOe from 10 to 300/400 K and back to 10 K in the sweep mode with a velocity of

5 K min^{-1}. For this purpose, samples were first cooled in the SQUID cavity without applying an external magnetic field.

For OER measurements, a conventional three-cell with a glassy carbon electrode-coated with the catalyst was used as working electrode, saturated calomel electrode (SCE) as reference electrode, and platinum wire as counter electrode. For preparing the working electrodes, 5 mg of the catalyst was dispersed in a water/ethanol mixture (950 µL, 3:1 v/v) under sonification for 30-minutes, followed by adding Nafion (50 µL, 5 wt%) with a sonification process for another 1 h to afford a homogeneous ink. The ink was dropped onto the surface on the glassy carbon electrode with a geometric area of 0.071 cm^2 and dried at room temperature. LSV was performed at a potential range between 0.0 V and 1.0 V vs. SCE for the OER with a scan rate of 50 mV s^{-1} in 1 M KOH. The overpotential was determined at a current density of 10 mA cm^{-2}. The electrochemical impedance spectroscopy (EIS) was performed at 0.7 vs. SCE from 0.01 to 20 kHz. The cyclic voltammetry (CV) data were collected at the potential range from 0.3 to 0.4 V vs. SCE at different scan rates (10, 20, 40, 80, 100, and 150 mV s^{-1}) to calculate the electrochemical double-layer capacitance, which is proportional to ECSA. The collected potential *versus* the reversible hydrogen electrode (RHE) was calculated according to the following formula: E(RHE) = E(SCE) + 0.241 V + 0.059 V*pH.

Acknowledgements

The authors gratefully acknowledge funding by the German Research Foundation DFG (AP242/6-1, MA 5392/7-1). U.-P.A. is grateful for financial support from the German Research Foundation DFG (Emmy Noether grant AP242/2-1; under Germany's Excellence Strategy EXC-2033 – Project number 390677874), from the Fraunhofer Internal Programs under Grant no. Attract 097-602175 as well as the Fraunhofer Cluster of Excellence CINES. The authors thank Lena Geiling (University of Bayreuth, group of Prof. C. Roth) for TGA-MS analysis, and Jonas Jungmann for physisorption measurements. Further thanks go to the Bavarian Polymer Institute KeyLab Electron and Optical Microscopy for deployment of TEM/SEM devices, and especially Dr. Markus Drechsler and Martina Heider for their support in recording EM images. We also thank the XPS/UPS facility at the Bavarian Polymer Institute KeyLab Device Engineering for use of the XPS system. H.K. gratefully acknowledges financial support from the MINT Lehramt Plus and the BayNAT program. Open access funding enabled and organized by Projekt DEAL.

Conflict of Interest

The authors declare no conflict of interest.

Keywords: degree of inversion · microwave synthesis · nanoparticles · oxygen evolution reaction · spinel ferrites

[1] N. T. Suen, S. F. Hung, Q. Quan, N. Zhang, Y. J. Xu, H. M. Chen, *Chem. Soc. Rev.* **2017**, *46*, 337–365.

[2] J. Song, C. Wei, Z.-F. Huang, C. Liu, L. Zeng, X. Wang, Z. J. Xu, *Chem. Soc. Rev.* **2020**, *49*, 2196–2214.

[3] C. C. L. McCrory, S. Jung, J. C. Peters, T. F. Jaramillo, *J. Am. Chem. Soc.* **2013**, *135*, 16977–16987.

[4] Y. Matsumoto, E. Sato, *Mater. Chem. Phys.* **1986**, *14*, 397–426.

[5] L. Han, S. Dong, E. Wang, *Adv. Mater.* **2016**, *28*, 9266–9291.

[6] S. Watzele, P. Hauenstein, Y. Liang, S. Xue, J. Fichtner, B. Garlyyev, D. Scieszka, F. Claudel, F. Maillard, A. S. Bandarenka, *ACS Catal.* **2019**, *9*, 9222–9230.

[7] T. Priamushko, R. Guillet-Nicolas, M. Yu, M. Doyle, C. Weidenthaler, H. Tüysüz, F. Kleitz, *ACS Appl. Mater. Interfaces* **2020**, *3*, 5597–5609.

[8] M. Li, Y. Xiong, X. Liu, X. Bo, Y. Zhang, C. Han, L. Guo, *Nanoscale* **2015**, *7*, 8920–8930.

[9] M. F. Fink, J. Eckhardt, P. Khadke, T. Gerdes, C. Roth, *ChemElectroChem* **2020**, *7*, 4822–4836.

[10] F. D. Speck, P. G. Santori, F. Jaouen, S. Cherevko, *J. Phys. Chem. C* **2019**, *123*, 25267–25277.

[11] I. Roche, E. Chaînet, M. Chatenet, J. Vondrák, *J. Appl. Electrochem.* **2008**, *38*, 1195–1201.

[12] A. H. Tkaczyk, A. Bartl, A. Amato, V. Lapkovskis, M. Petranikova, *J. Phys. D* **2018**, *51*, 203001.

[13] L. Gong, H. Yang, A. I. Douka, Y. Yan, B. Y. Xia, *Adv. Sustainable Syst.* **2021**, *5*, 2000136.

[14] M. Gong, H. Dai, *Nano Res.* **2015**, *8*, 23–39.

[15] Y. Kinemuchi, K. Ishizaka, H. Suematsu, W. Jiang, K. Yatsui, *Thin Solid Films* **2002**, *407*, 109–113.

[16] M. Bałanda, A. Szytuła, Ž. Dimitrijević, J. Todorović, *Phys. Status Solidi* **1969**, *32*, K91–K93.

[17] B. J. Evans, S. S. Hafner, H. P. Weber, *J. Chem. Phys.* **1971**, *55*, 5282–5288.

[18] D. Carta, M. F. Casula, A. Falqui, D. Loche, G. Mountjoy, C. Sangregorio, A. Corrias, *J. Phys. Chem. C* **2009**, *113*, 8606–8615.

[19] A. H. Morr, K. Haneda, *J. Appl. Phys.* **1981**, *52*, 2496–2498.

[20] V. Šepelák, A. Feldhoff, P. Heitjans, F. Krumeich, D. Menzel, F. J. Litterst, I. Bergmann, K. D. Becker, *Chem. Mater.* **2006**, *18*, 3057–3067.

[21] V. Šepelák, I. Bergmann, A. Feldhoff, P. Heitjans, F. Krumeich, D. Menzel, F. J. Litterst, S. J. Campbell, K. D. Becker, *J. Phys. Chem. C* **2007**, *111*, 5026–5033.

[22] M. Atif, M. Nadeem, M. Siddique, *Appl. Phys. A* **2015**, *120*, 571–578.

[23] C. Simon, J. Timm, D. Tetzlaff, J. Jungmann, U.-P. Apfel, R. Marschall, *ChemElectroChem* **2021**, *8*, 227–239.

[24] S. Ahmadian-Fard-Fini, D. Ghanbari, M. Salavati-Niasari, *Composites Part B* **2019**, *161*, 564–577.

[25] U. Lüders, M. Bibes, J.-F. Bobo, M. Cantoni, R. Bertacco, J. Fontcuberta, *Phys. Rev. B* **2005**, *71*, 134419.

[26] A. K. Taylor, I. Andreu, M. Louie, B. D. Gates, *ACS Appl. Mater. Interfaces* **2020**, *3*, 387–400.

[27] Y. Li, K. Guo, J. Li, X. Dong, T. Yuan, X. Li, H. Yang, *ACS Appl. Mater. Interfaces* **2014**, *6*, 20949–20957.

[28] J. Zhou, J. Ma, C. Sun, L. Xie, Z. Zhao, H. Tian, Y. Wang, J. Tao, X. Zhu, *J. Am. Ceram. Soc.* **2005**, *88*, 3535–3537.

[29] J. Wang, F. Ren, B. Jia, X. Liu, *Solid State Commun.* **2010**, *150*, 1141–1144.

[30] K. Maaz, S. Karim, A. Mumtaz, S. K. Hasanain, J. Liu, J. L. Duan, *J. Magn. Magn. Mater.* **2009**, *321*, 1838–1842.

[31] I. Bilecka, M. Niederberger, *Nanoscale* **2010**, *2*, 1358–1374.

[32] N. Pinna, G. Garnweitner, M. Antonietti, M. Niederberger, *J. Am. Chem. Soc.* **2005**, *127*, 5608–5612.

[33] I. Bilecka, I. Djerdj, M. Niederberger, *Chem. Commun.* **2008**, 886–888.

[34] K. Kirchberg, A. Becker, A. Bloesser, T. Weller, J. Timm, C. Suchomski, R. Marschall, *J. Phys. Chem. C* **2017**, *121*, 27126–27138.

[35] A. Becker, K. Kirchberg, R. Marschall, *Zeitschrift für Phys. Chemie* **2020**, *234*, 645–654.

[36] A. Bloesser, H. Kurz, J. Timm, F. Wittkamp, C. Simon, S. Hayama, B. Weber, U.-P. Apfel, R. Marschall, *ACS Appl. Nano Mater.* **2020**, *3*, 11587–11599.

[37] P. Dolcet, K. Kirchberg, A. Antonello, C. Suchomski, R. Marschall, S. Diodati, R. Muñoz-Espí, K. Landfester, S. Gross, *Inorg. Chem. Front.* **2019**, *6*, 1527–1534.

[38] C. Suchomski, B. Breitung, R. Witte, M. Knapp, S. Bauer, T. Baumbach, C. Reitz, T. Brezesinski, *Beilstein J. Nanotechnol.* **2016**, *7*, 1350–1360.

[39] A. Bloesser, J. Timm, H. Kurz, W. Milius, S. Hayama, J. Breu, B. Weber, R. Marschall, *Solar RRL* **2020**, *4*, 1900570.

[40] X. Gu, W. Zhu, C. Jia, R. Zhao, W. Schmidt, Y. Wang, *Chem. Commun.* **2011**, *47*, 5337–5339.

[41] L. M. Ombaka, R. Dillert, L. Robben, D. W. Bahnemann, *APL Mater.* **2020**, *8*, 031105.

[42] A. Ahlawat, V. G. Sathe, *J. Raman Spectrosc.* **2011**, *42*, 1087–1094.

[43] W. B. White, B. A. DeAngelis, *Spectrochim. Acta Part A Mol. Spectrosc.* **1967**, *23*, 985–995.
[44] D. L. A. de Faria, S. Venâncio Silva, M. T. de Oliveira, *J. Raman Spectrosc.* **1997**, *28*, 873–878.
[45] S. Maensiri, C. Masingboon, B. Boonchom, S. Seraphin, *Scr. Mater.* **2007**, *56*, 797–800.
[46] M. C. Biesinger, B. P. Payne, A. P. Grosvenor, L. W. M. Lau, A. R. Gerson, R. S. C. Smart, *Appl. Surf. Sci.* **2011**, *257*, 2717–2730.
[47] M. Fondell, M. Gorgoi, M. Boman, A. Lindblad, *J. Electron Spectrosc. Relat. Phenom.* **2018**, *224*, 23–26.
[48] J. Liu, M.-S. Cao, Q. Luo, H.-L. Shi, W.-Z. Wang, J. Yuan, *ACS Appl. Mater. Interfaces* **2016**, *8*, 22615–22622.
[49] J. Chappert, R. B. Frankel, *Phys. Rev. Lett.* **1967**, *19*, 570–572.
[50] C. S. Kim, S. W. Lee, S. I. Park, J. Y. Park, Y. J. Oh, *J. Appl. Phys.* **1996**, *79*, 5428–5430.
[51] G. K. Reddy, P. Boolchand, P. G. Smirniotis, *J. Phys. Chem. C* **2012**, *116*, 11019–11031.
[52] M. Etier, Y. Gao, V. V. Shvartsman, A. Elsukova, J. Landers, H. Wende, D. C. Lupascu, *Ferroelectrics* **2012**, *438*, 115–122.
[53] H. R. Rechenberg, E. C. Sousa, J. Depeyrot, M. H. Sousa, R. Aquino, F. A. Tourinho, R. Perzynski, *Hyperfine Interact.* **2008**, *184*, 9–14.
[54] P. Laokul, V. Amornkitbamrung, S. Seraphin, S. Maensiri, *Curr. Appl. Phys.* **2011**, *11*, 101–108.
[55] M. George, A. Mary John, S. S. Nair, P. A. Joy, M. R. Anantharaman, *J. Magn. Magn. Mater.* **2006**, *302*, 190–195.
[56] C. N. Chinnasamy, A. Narayanasamy, N. Ponpandian, K. Chattopadhyay, K. Shinoda, B. Jeyadevan, K. Tohji, K. Nakatsuka, T. Furubayashi, I. Nakatani, *Phys. Rev. B* **2001**, *63*, 184108.
[57] M. Artus, L. Ben Tahar, F. Herbst, L. Smiri, F. Villain, N. Yaacoub, J.-M. Grenèche, S. Ammar, F. Fiévet, *J. Phys. Condens. Matter* **2011**, *23*, 506001.
[58] R. J. Tackett, A. W. Bhuiya, C. E. Botez, *Nanotechnology* **2009**, *20*, 445705.
[59] K. Junge Puring, D. Siegmund, J. Timm, F. Möllenbruck, S. Schemme, R. Marschall, U. Apfel, *Adv. Sustainable Syst.* **2021**, *5*, 2000088.
[60] M. Nagao, *J. Phys. Chem.* **1971**, *75*, 3822–3828.
[61] D. Siegmund, N. Blanc, M. Smialkowski, K. Tschulik, U. Apfel, *ChemElectroChem* **2020**, *7*, 1514–1527.
[62] D. Siegmund, S. Metz, V. Peinecke, T. E. Warner, C. Cremers, A. Grevé, T. Smolinka, D. Segets, U.-P. Apfel, *JACS Au* **2021**, jacsau.1c00092.
[63] A. S. Bin Mohd Najib, M. Iqbal, M. B. Zakaria, S. Shoji, Y. Cho, X. Peng, S. Ueda, A. Hashimoto, T. Fujita, M. Miyauchi, et al., *J. Mater. Chem. A* **2020**, *8*, 19788–19792.
[64] M. B. Zakaria, D. Zheng, U. Apfel, T. Nagata, E.-R. S. Kenawy, J. Lin, *ACS Appl. Mater. Interfaces* **2020**, *12*, 40186–40193.
[65] Y. Zhou, Y. Du, S. Xi, Z. J. Xu, *Electrocatalysis* **2018**, *9*, 287–292.
[66] R. D. L. Smith, M. S. Prévot, R. D. Fagan, Z. Zhang, P. A. Sedach, M. K. J. Siu, S. Trudel, C. P. Berlinguette, *Science* **2013**, *340*, 60–63.
[67] X. Chen, X. Zhang, L. Zhuang, W. Zhang, N. Zhang, H. Liu, T. Zhan, X. Zhang, X. She, D. Yang, *Chem. Asian J.* **2020**, *15*, 3995–3999.
[68] Z. Fu, S. Liu, Z. Mai, Z. Tang, D. Qin, Y. Tian, X. Wang, *Chem. Asian J.* **2020**, *15*, 3568–3574.
[69] Q. Chen, R. Wang, F. Lu, X. Kuang, Y. Tong, X. Lu, *ACS Omega* **2019**, *4*, 3493–3499.
[70] D. Lim, H. Kong, N. Kim, C. Lim, W. S. Ahn, S. H. Baeck, *ChemNanoMat* **2019**, *5*, 1296–1302.
[71] A. R. Stokes, A. J. C. Wilson, *Math. Proc. Cambridge Philos. Soc.* **1942**, *38*, 313–322.

Manuscript received: May 21, 2021
Accepted manuscript online: July 6, 2021
Version of record online: August 4, 2021

Chemistry–A European Journal

Supporting Information

Magnetic $NiFe_2O_4$ Nanoparticles Prepared via Non-Aqueous Microwave-Assisted Synthesis for Application in Electrocatalytic Water Oxidation

Christopher Simon, Mohamed Barakat Zakaria, Hannah Kurz, David Tetzlaff, André Blösser, Morten Weiss, Jana Timm, Birgit Weber, Ulf-Peter Apfel, and Roland Marschall*

Table S 1: Elemental compositions of $NiFe_2O_4$ nanoparticles prepared at 225 °C with the microwave-assisted synthesis strategy, estimated *via* EDXS. From each sample, four spots were investigated, showing averaged values with standard deviations as error bars.

	C / at %	O / at %	Fe / at %	Ni / at %	Ni:Fe ratio
as-synthesized	13.5 (5.9)	54.2 (6.5)	22.5 (5.3)	9.6 (1.6)	0.43 (0.03)
300 °C	9.5 (2.2)	51.0 (1.6)	27.7 (1.9)	11.8 (0.8)	0.42 (0.00)
400 °C	5.5 (0.9)	52.1 (2.1)	29.3 (1.9)	13.2 (0.7)	0.45 (0.03)
500 °C	7.7 (3.7)	46.8 (2.4)	31.8 (4.5)	13.8 (1.5)	0.44 (0.02)

Table S 2: Elemental compositions of $NiFe_2O_4$ nanoparticles prepared at 225 °C with the microwave-assisted synthesis strategy, estimated *via* XPS.

	C / at %	O / at %	Fe / at %	Ni / at %	Ni:Fe ratio
as-synthesized	29.0	48.3	15.1	7.5	0.50
300 °C	23.4	50.1	17.8	8.7	0.49
400 °C	23.5	50.5	17.7	8.3	0.47
500 °C	23.1	49.4	18.6	9.0	0.48

Table S 3: Parameters obtained from ^{57}Fe Mössbauer spectroscopy.

		298 K				80 K			
	fit	δ / mm s^{-1}	ΔE_Q / mm s^{-1}	B_0 / T	*Rel. Area*	δ / mm s^{-1}	ΔE_Q / mm s^{-1}	B_0 / T	*Rel. Area*
as-synthesized	1	0.35	0.98	-	0.45	0.46	1.47	-	0.32
	2	0.35	0.55	-	0.55	0.46	0.63	-	0.68
	overall	0.35	0.64	-		0.46	0.66	-	
300 °C	1	0.33	0.98	-	0.32	0.43	-	48.2	0.26
	2	0.33	0.49	-	0.68	0.43	-	-	0.74
	overall	0.33	0.55	-		0.43	-	47.6	
400 °C	1	0.32	1.56	-	0.24	0.46	-	54.1	0.15
	2	0.32	0.53	-	0.76	0.46	-	50.0	0.85
	overall	0.32	0.54	-		0.46	-	50.8	
500 °C	1	0.28	-	50.4	0.25	0.36	-	54.8	0.33
	2	0.28	-	47.0	0.75	0.36	-	50.2	0.67
	overall	0.28	-	47.5		0.36	-	54.1	

Table S 4: Comparison of the oxygen evolution performance of microwave-derived $NiFe_2O_4$ nanoparticles from this work with other recently reported spinel $NiFe_2O_4$ electrocalalysts. Overpotentials are estimated at a current density of 10 mA cm^{-2}.

description	synthesis	calcination	overpotential	Tafel slope	electrolyte	ref.
particles	hydrothermal	800 °C	570 mV	93 mV/dec	0.1M KOH	[1]
fibres	solution blow spinning	800 °C	433 mV	134 mV/dec	1.0M KOH	[2]
mesoporous	soft templating	400 °C	410 mV	50 mV/dec	1.0M KOH	[3]
nanoparticles (O deficient)	hydrothermal, H_2 treatment	-	389 mV	64 mV/dec	1.0M KOH	[4]
particles	sol-gel	700 °C	381 mV	47 mV/dec	1.0M KOH	[5]
nanorods	thermal decomposing	350 °C	342 mV	44 mV/dec	1.0M KOH	[6]
nanoparticles	sol-gel	500 °C	290 mV	42 mV/dec	1.0M KOH	[7]
quantum dots	electro-deposition	-	262 mV	37 mV/dec	1.0M KOH	[8]
this work	microwave	400 °C	380 mV	63 mV/dec	1.0M KOH	-

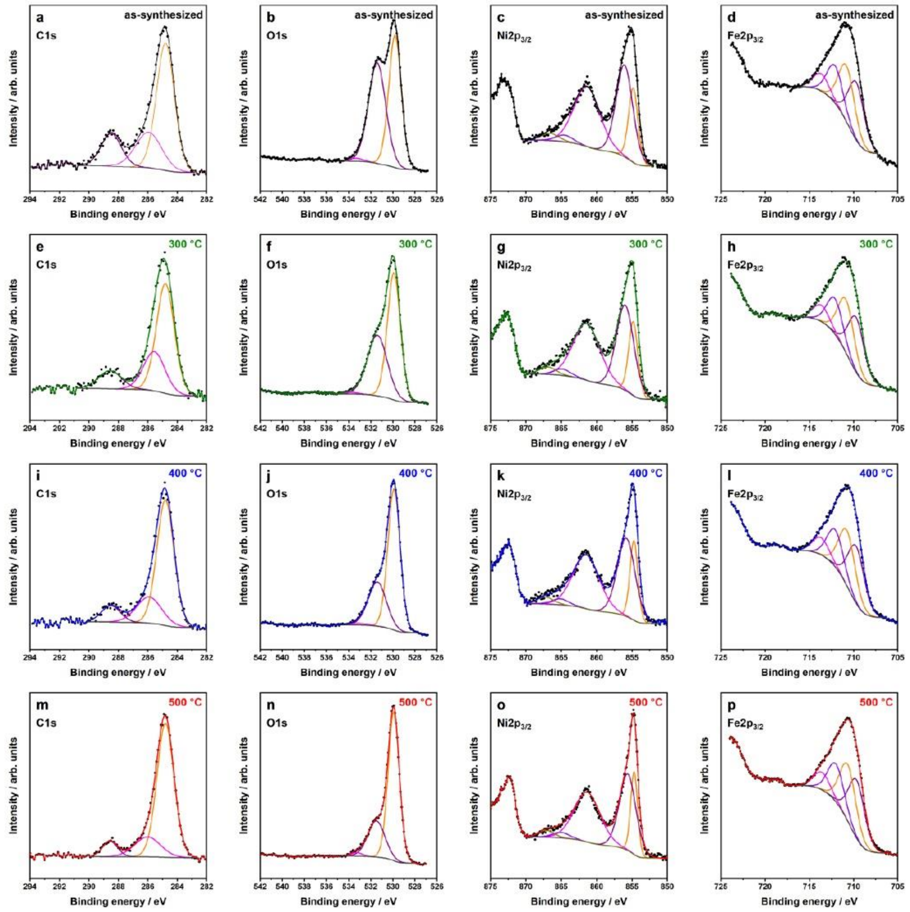

Figure S1: XP spectra fits of the C 1s, O 1s, Ni 2p$_{3/2}$, plus Fe 2p$_{3/2}$ core levels of as-synthesized (a-d) and calcined (300 °C: e-h, 400 °C: i-l, 500 °C: m-p) NiFe$_2$O$_4$ nanoparticles.

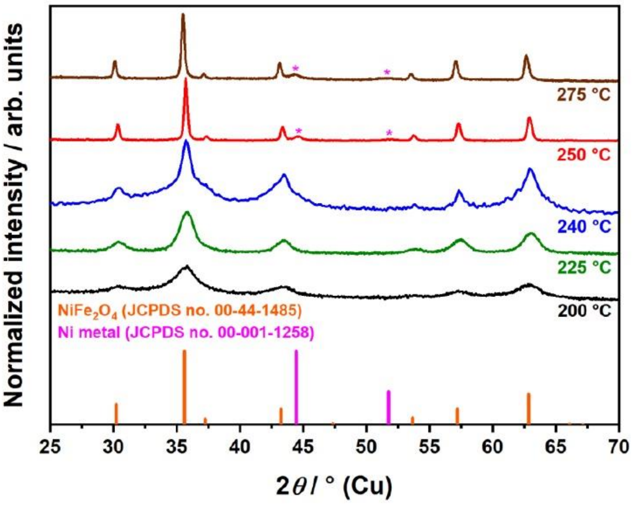

Figure S2: PXRD patterns of as-synthesized $NiFe_2O_4$ nanoparticles prepared at different temperatures *via* the microwave-based synthesis. For better comprehensibility, intensities were normalized with respect to the most intensive reflection at 35.6 ° 2*θ*. At 250 and 275 °C, a Ni metal by-phase can be observed. Here, Ni nuclei form during microwave treatment. Since metallic Ni is an excellent microwave absorbing material, superheating occurs, coupled with an unusual pressure increase. Another result of superheating is an increased crystallinity, which is reflected by sharpened reflections. The possible temperature range of the synthesis is therefore 200-240 °C.

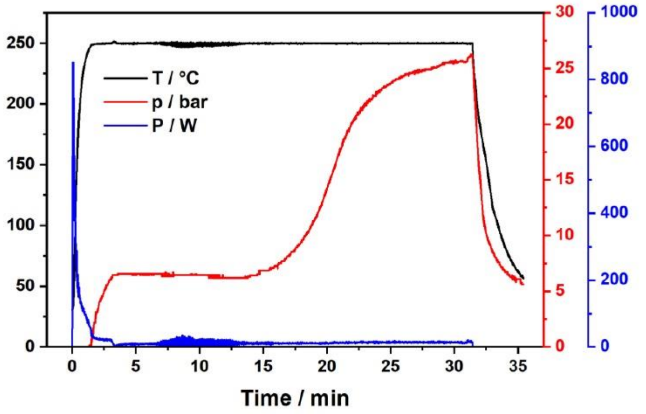

Figure S3: Microwave data (temperature measured *via* IR sensor, evolved pressure, and applied power) of a run performed at 250 °C. The unusual pressure increase beginning after approx. 15 min origins in superheating processes due to metallic Ni deposits, which are excellent absorbers of microwave irradiation. At the standard reaction temperature of 225 °C, the pressure stays constant during the whole reaction time.

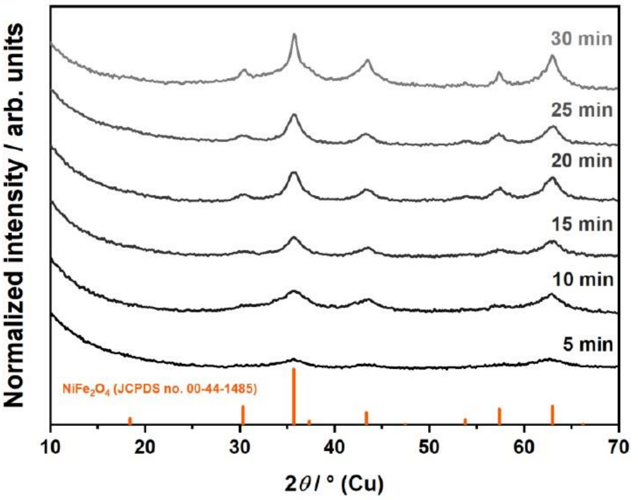

Figure S4: PXRD pattern of as-synthesized $NiFe_2O_4$ nanoparticles prepared at a temperature of 240 °C in the microwave-based synthesis. For better comprehensibility, intensities were normalized with respect to the most intensive reflection at 35.6 ° 2*θ*. In this experiment, the reaction time was changed in a range of 5-30 min within steps of 5 min.

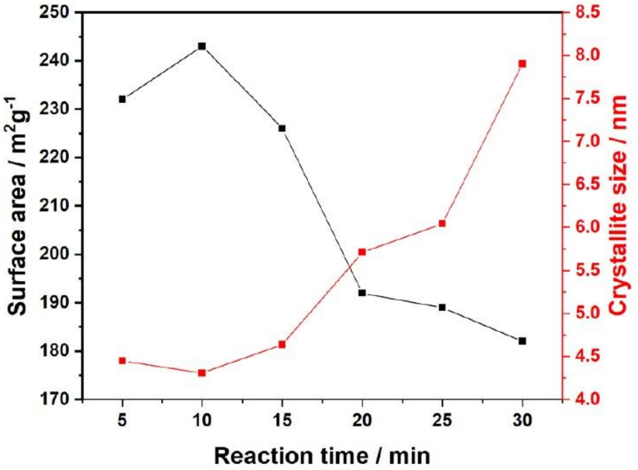

Figure S5: Surface areas determined *via* BET analysis of nitrogen physisorption data and crystallite sizes of as-synthesized $NiFe_2O_4$ nanoparticles prepared at 240 °C. The reaction time was changed in a range of 5-30 min within steps of 5 min.

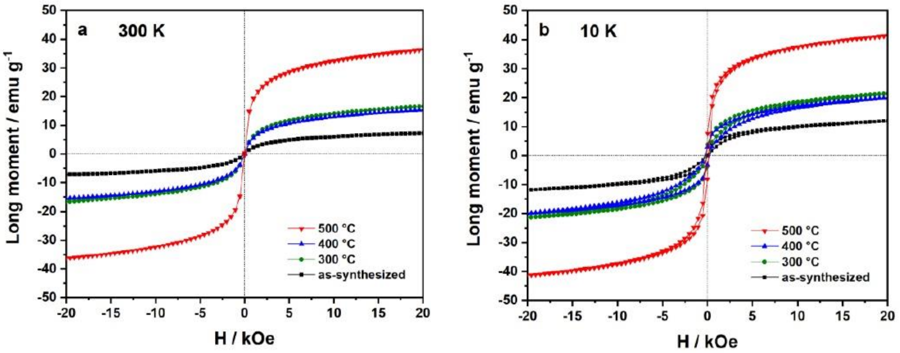

Figure S6: Uncorrected magnetization curves of $NiFe_2O_4$ nanoparticles at 300 K (a) and 10 K (b), measured *via* SQUID magnetometry.

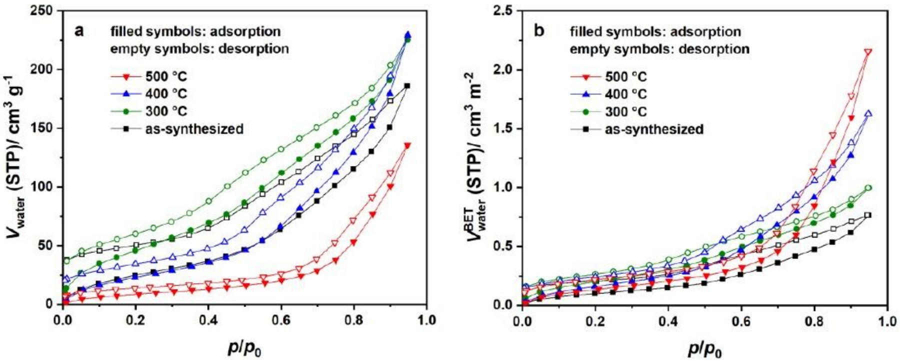

Figure S7: (a) Water vapor physisorption isotherms of $NiFe_2O_4$ nanoparticles prepared at 225 °C and (b) respective surface area-normalized isotherms. Water vapor physisorption experiments were performed at 20 °C.

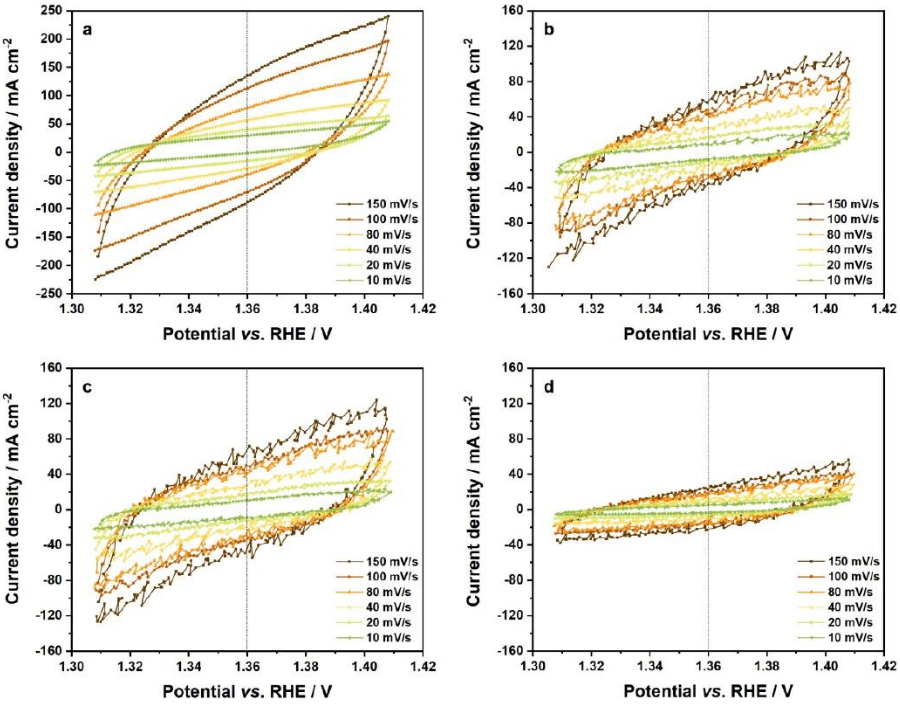

Figure S8: Static cyclic voltammetry curves (CVs) measured at scan rates of 150, 100, 80, 40, 20, and 10 mV s^{-1} for as-synthesized (a) plus 300 °C (b), 400 °C (c) and 500 °C (d) calcined $NiFe_2O_4$ nanoparticles. From the data sets, the electrochemical double-layer capacitance c_{DL} could be estimated, which is proportional to the electrochemical active surface area (ECSA).

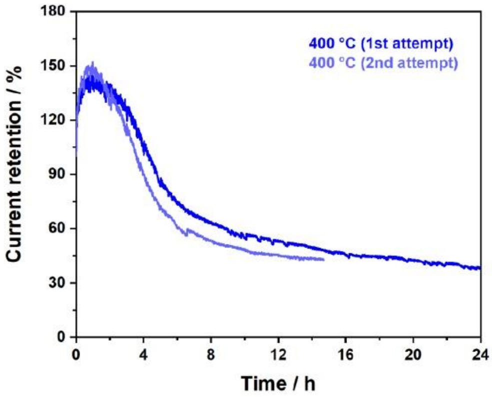

Figure S9: Chronoamperometric long-term stability tests at applied potential (1.56 V *vs.* RHE) with two different electrodes in 1M KOH solution. For both experiments, the most active sample (calcination at 400 °C) was considered.

Additional literature

[1] S. Pal, U. P. Azad, A. K. Singh, D. Kumar, R. Prakash, *Electrochim. Acta* **2019**, *320*, 134584.
[2] V. D. Silva, L. S. Ferreira, T. A. Simões, E. S. Medeiros, D. A. Macedo, *J. Colloid Interface Sci.* **2019**, *540*, 59–65.
[3] C. Simon, J. Timm, D. Tetzlaff, J. Jungmann, U.-P. Apfel, R. Marschall, *ChemElectroChem* **2021**, *8*, 227–239.
[4] D. Lim, H. Kong, N. Kim, C. Lim, W. Ahn, S. Baeck, *ChemNanoMat* **2019**, *5*, 1296–1302.
[5] V. Maruthapandian, M. Mathankumar, V. Saraswathy, B. Subramanian, S. Muralidharan, *ACS Appl. Mater. Interfaces* **2017**, *9*, 13132–13141.
[6] G. Liu, K. Wang, X. Gao, D. He, J. Li, *Electrochim. Acta* **2016**, *211*, 871–878.
[7] N. Dalai, B. Mohanty, A. Mitra, B. Jena, *ChemistrySelect* **2019**, *4*, 7791–7796.
[8] H. Yang, Y. Liu, S. Luo, Z. Zhao, X. Wang, Y. Luo, Z. Wang, J. Jin, J. Ma, *ACS Catal.* **2017**, *7*, 5557–5567.

3.3. Magnetische Untersuchungen und strukturelle Analysen an $MnFe_2O_4$-Nanopartikeln

3.3.1. Synopsis

Die in Kapitel 3.2. dargestellte Mikrowellen-basierte Darstellung von $NiFe_2O_4$-Nanopartikeln lässt sich mit einigen Anpassungen auf weitere oxidische Eisenspinelle übertragen, was in der vorliegenden Publikation in der *Zeitschrift für anorganische und allgemeine Chemie* anhand des Beispiels von Manganferrit ($MnFe_2O_4$) gezeigt wird. Als Präkursor für Mangan wird hierbei $Mn(acac)_2$ eingesetzt. Die Mikrowellenbehandlung erfolgt im Falle von $MnFe_2O_4$ bei 250 °C. Die Synthese führt ebenfalls zu sphärischen Nanopartikeln mit einem Durchmesser von 6 nm und einer spezifischen Oberfläche von 145 $m^2\ g^{-1}$. Röntgendiffraktogramme und transmissionselektronenmikroskopische Aufnahmen beweisen, dass es sich um nanokristalline Partikel handelt. Im Gegensatz zum strukturellen Analogon $NiFe_2O_4$ ist eine thermische Behandlung unter Luft zur Einstellung der Partikelgröße kritisch. Untersuchungen mit der PDF-Methode (englisch *pair size distribution function*), welche aus einem Röntgendiffraktogramm durch Fourier-Transformation ein Histogramm der interatomaren Abstände erzeugt,[158] legen nahe, dass eine Kalzinierung bei 400 °C zur Oxidation von Mn^{2+} zu Mn^{3+} führt. Daraus folgt die Bildung von amorphem Mangan(III)-oxid (α-Mn_2O_3) als Nebenphase und dementsprechend eine Mangan-Verarmung des Spinells. Die bereits beginnende Zersetzung der $MnFe_2O_4$-Nanopartikel bei 400 °C ist nur mit angewandten PDF-Messungen nachweisbar, nicht jedoch anhand der Röntgendiffraktometrie oder spektroskopischen Methoden. Selbst bei den nicht-kalzinierten Nanopartikeln liegt keine perfekte $MnFe_2O_4$-Spinellstruktur vor, da bereits ein struktureller Gradient im Material vorliegt, der zum Beispiel durch unterschiedliche Zusammensetzungen an Partikeloberfläche und -innerem erklärt werden kann. Eine Erhöhung der Kalzinierungstemperatur zu 600 °C oder 800 °C führt schließlich zur vollständigen Zersetzung der Spinellstruktur von $MnFe_2O_4$ in die thermodynamisch stabilen binären Phasen α-Mn_2O_3 und α-Fe_2O_3. Zum Vergleich dazu führt eine solche Temperaturbehandlung der $NiFe_2O_4$-Nanopartikel zu keiner Zersetzung in die binären Phasen, sondern lediglich zu einem Kristallitwachstum. Interessant ist $MnFe_2O_4$ insbesondere wegen der magnetischen Beschaffenheit. Die magnetischen $3d^5$ Mn^{2+}- und Fe^{3+}-Kationen in der partiell inversen Spinellstruktur führen zu ausgeprägten ferrimagnetischen Eigenschaften, verursacht durch die antiferromagnetische Kopplung beider Untergitter. Dadurch, dass beide beteiligten Kationen dieselbe Elektronenkonfiguration aufweisen, ist der Einfluss des Inversionsgrades auf die Sättigungsmagnetisierung in der Theorie weniger ausgeprägt als bei anderen Eisenspinellen, wie zum Beispiel beim $NiFe_2O_4$-Spinell. Die bestimmte Sättigungsmagnetisierung der nicht-kalzinierten $MnFe_2O_4$-Nanopartikel beträgt 63,5 emu g^{-1} (2,62 μ_B pro Formeleinheit) bei 10 K. Damit erreichen die hergestellten Nanopartikel nicht den Literaturwert für $MnFe_2O_4$ (3,3-4,5 μ_B),[56–58] was im Zusammenhang mit einer veränderten Kationenverteilung und Oberflächeneffekten stehen dürfte. Durch die Zersetzung des Spinells durch die thermische Behandlung an Luft ist die Untersuchung des Zusammenhangs von Partikelgröße und Magnetismus nicht möglich, da durch den Verlust der Spinellstruktur die magnetischen Austauschwechselwirkungen zwischen Kationen in beiden Subgittern wegfallen. Für die Anwendung, zum Beispiel als magnetisches Fluid, ist die Dispergierbarkeit der Nanopartikel von Bedeutung. Durch die *post*-synthetische Modifizierung mit verschiedenen Reagenzien, wie beispielsweise Ölsäure kombiniert Oleylamin oder Zitronensäure, können stabile Dispersionen in unpolaren und polaren Medien erzeugt werden. Ein wichtiges Ergebnis des Artikels ist, dass die Mikrowellensynthese von $NiFe_2O_4$-Nanopartikeln mit einigen Anpassungen auf Manganeisenspinelle des Typs $MnFe_2O_4$ anwendbar ist.

3.3.2 Veröffentlichung in *Zeitschrift für anorganische und allgemeine Chemie*

Christopher Simon,[a] André Blösser,[a] Mirco Eckardt,[a] Hannah Kurz,[a] Birgit Weber,[a] Mirijam Zobel+,[a] Roland Marschall[a]

Magnetic properties and structural analysis on spinel $MnFe_2O_4$ nanoparticles *via* non-aqueous microwave synthesis

Veröffentlicht in: *Zeitschrift für anorganische und allgemeine Chemie* **2021**, *647*, 2061-2072.

Einflussfaktor *Zeitschrift für anorganische und allgemeine Chemie* (2021): 1,492
https://doi.org/10.1002/zaac.202100190

[a] Department of Chemistry, University of Bayreuth, Universitaetsstrasse 30, 95447 Bayreuth, Germany
[+] Institute of Crystallography, RWTH Aachen University, Jaegerstrasse 17-19, 52066 Aachen, Germany (aktuelle Adresse)

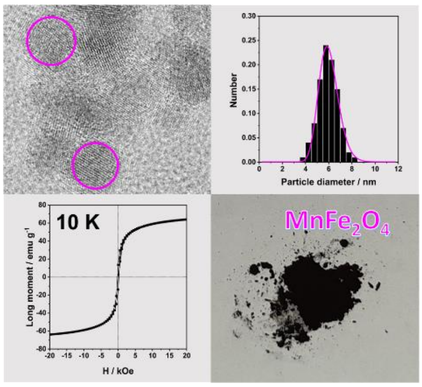

Individuelle Beiträge:

Das grundlegende Konzept der Publikation wurde erarbeitet von Prof. Dr. Mirijam Zobel, Prof. Dr. Birgit Weber, Prof. Dr. Roland Marschall und mir. Verfasst wurde das Manuskript in der Hauptsache von mir mit größeren Beiträgen von allen Co-Autoren. Die Synthesearbeiten wurden größtenteils von mir durchgeführt, ebenso wie die grundlegende Charakterisierung der Proben mittels Röntgendiffraktometrie (Kupferanode), energiedispersiver Röntgenspektroskopie, Transmissionselektronenmikroskopie, UV/Vis- sowie Infrarotspektroskopie und dynamischer Lichtstreuung. Mirco Eckardt hat die Röntgendiffraktometrie-Experimente an der Silberröhre durchgeführt, mittels PDF-Analyse ausgewertet und den entsprechenden Abschnitt im Manuskript verfasst. Die Messungen am *superconducting quantum interference device*-Magnetometer (SQUID) wurden von Dr. Hannah Kurz ausgeführt sowie ausgewertet, ebenso wie die Mössbauerspektroskopie. Jonas Jungmann (AG Marschall, Universität Bayreuth) hat die Physisorptionsmessungen durchgeführt. Die quantitative Auswertung der Röntgenphotoelektronenspektren oblag Dr. Morten Weiss (AG Marschall, Universität Bayreuth). Die Ramanspektren wurden von Dr. Holger Schmalz (Keylab Synthesis and Molecular Characterization, Bayerisches Polymerinstitut) gemessen. Die thermogravimetrischen Analysen wurden durchgeführt von Lena Geiling (AG Roth, Universität Bayreuth). Alle Autoren haben mit wissenschaftlicher Diskussion zum Manuskript beigetragen.

Mein Beitrag zum Manuskript beträgt ca. **60 %**.

Journal of Inorganic and General Chemistry
ZAAC
Zeitschrift für anorganische und allgemeine Chemie
doi.org/10.1002/zaac.202100190
ARTICLE

Magnetic properties and structural analysis on spinel $MnFe_2O_4$ nanoparticles prepared *via* non-aqueous microwave synthesis

Christopher Simon,[a] André Blösser,[a] Mirco Eckardt,[a] Hannah Kurz,[a] Birgit Weber,[a] Mirijam Zobel+,[a] and Roland Marschall*[a]

Dedicated to Prof. Dr. Josef Breu on the occasion of his 60th birthday

Phase-pure 6 nm spinel $MnFe_2O_4$ nanoparticles with high specific surface area of 145 $m^2 g^{-1}$ were successfully prepared *via* microwave-assisted non-aqueous sol-gel synthesis. The phase evolution during postsynthetic thermal treatment was investigated systematically by various methods, including powder X-ray diffraction (PXRD), pair distribution function (PDF) analysis, and Raman spectroscopy. Our results show that the material decomposes to non-spinel binary compounds α-Mn_2O_3 and α-Fe_2O_3 at temperatures between 400 and 600 °C. The application potential of $MnFe_2O_4$ nanoparticles with $3d^5$ Mn(II) and Fe(III) ions with respect to the magnetic properties was demonstrated by superconducting quantum interference device (SQUID) magnetometry, with the as-synthesized nanoparticles reaching a high saturation magnetization of 2.62 μ_B per formula unit (63.5 $Am^2 kg^{-1}$) at 10 K. We further highlight the visible-light response of synthesized powders, making the materials promising for light-related applications, *e.g.* photocatalytic hydrogen evolution. An important additional feature of $MnFe_2O_4$ nanoparticles is their good dispersibilty in polar or non-polar media, as a result of postsynthetic colloidal stabilization with betaine hydrochloride, oleic acid combined with oleylamine, or citric acid.

Introduction

In the last decades, preparation of inorganic magnetic nanoparticles (MNPs) has received particular attention due to their widespread application range, including biomedicine,[1] imaging,[2] data-storage,[3] spintronics,[4] or homogeneous and heterogeneous catalysis.[5–8] Among the variety of available magnetic nanomaterials, the spinel ferrite class offers a significant saturation magnetization, a high electrical resistance, low electrical losses, and an outstanding chemical stability.[9] In addition, most of these materials can be prepared from earth-abundant and inexpensive precursors.[10] Generally, the structure of spinel ferrites can be written as MFe_2O_4, where M represents divalent cations, *e.g.* Fe(II), Cd(II), Mg(II), Zn(II), Cu(II), Ni(II), Co(II), and Mn(II). The occupation of tetrahedral (A) and octahedral (B) sites in the ccp lattice depends on cationic sizes and crystal field splitting energies and is usually described by the inversion parameter λ, according to the notation $(M_{1-\lambda}Fe_{\lambda})^A(M_{\lambda}Fe_{2-\lambda})^BO_4$. An inversion value of $\lambda = 0$ represents a normal spinel structure (*e.g.* $ZnFe_2O_4$),[11] $\lambda = 1$ points out an inverse spinel structure (*e.g.* $NiFe_2O_4$),[12] and the situation $0 < \lambda < 1$ is referred as partially inverse spinel.

Typically, antiferromagnetic exchange interactions result in a magnetic moment of both sublattices, which are coupled ferrimagnetically. The magnetic moment of a spinel ferrite can therefore be described as the difference of magnetic moments of A and B sublattices, with A–B interactions as the dominant ones, determining the overall antiferromagnetic or ferrimagnetic nature.[13,14] The interaction between B site cations are also antiferromagnetic, but much weaker.[15] Since the magnetism consequently depends on the cationic distributions, tailoring the inversion parameter provides a simple access to tune the magnetic properties of spinel ferrites. The degree of inversion can be modified by establishing non-equilibrium conditions, which can be achieved by preparing nanoparticulate materials. In other words, the particle size of a spinel ferrite directly influences λ, and therefore also the magnetism.[16–19]

Owning $3d^5$ electronic high-spin configuration of Mn(II) and Fe(III) centers,[20] manganese ferrite ($MnFe_2O_4$) is an interesting candidate for a functional material with a remarkable high saturation magnetization of 3.3–4.5 μ_B per formula unit for the bulk state.[21–23] The bulk saturation moment of $MnFe_2O_4$ is significantly higher than for other spinel ferrites, *e.g.* $NiFe_2O_4$ (2.2–2.3 μ_B),[24–26] or $MgFe_2O_4$ (1.1–1.4 μ_B),[17,27,28] and comparable to the ones of Fe_3O_4 (3.7–3.9 μ_B),[29–31] or $CoFe_2O_4$ (3.6–4.0 μ_B).[24,32,33] However, it should be noted that the influence of the inversion parameter on the magnetic properties is less pronounced for $MnFe_2O_4$, compared to other spinel ferrites,

---

[a] *C. Simon, A. Blösser, M. Eckardt, H. Kurz, B. Weber, M. Zobel,+ R. Marschall*
Department of Chemistry, University of Bayreuth, Universitaetsstrasse 30, 95447 Bayreuth, Germany
E-mail: roland.marschall@uni-bayreuth.de

[+] *Present address: Institute of Crystallography, RWTH Aachen University, 52066 Aachen, Germany*

Supporting information for this article is available on the WWW under https://doi.org/10.1002/zaac.202100190

such as $MgFe_2O_4$ or Fe_3O_4. This is based on the fact that Mn(II) (A) and Fe(III) (B) cations exhibit an isoelectronic configuration ($3d^5$). But, theoretical DFT calculations by Huang *et al.* reveal saturation of 5 and $3\,\mu_B$ per formula unit for a normal and inverse spinel, respectively, which was confirmed by Simsa and Brabers experimentally.[15,34] This can be correlated to spin canting phenomena and/or mixed valence.[35,36] Spin canting describes the phenomenon that especially the spins of surface ions feature different orientations leading to altered magnetic moments. This effect is especially observed in nanostructures due to the finite-size effect. For the thermodynamically stable bulk state, degrees of inversion for $MnFe_2O_4$ of $\lambda = 0.15$–0.2 were reported, which are commonly estimated *via* neutron diffraction or Mössbauer spectroscopy. Therefore, $MnFe_2O_4$ crystallizes in a partially inverse spinel structure.[37,38] Non-equilibrium conditions can be established by preparing nanostructured spinel ferrites, with an often-altered degree of inversion. This was, for example, confirmed by Zhang *et al.* and Chen *et al.* for co-precipitated $MnFe_2O_4$ nanoparticles with sizes of <10 nm respective 40 nm, with reported inversion degrees of $\lambda = 0.61$–0.67.[39,40] Thus, preparation of nanosized $MnFe_2O_4$ further allows fine-tuning of its magnetic properties. Moreover, featuring a band gap of 1.75–1.78 eV, $MnFe_2O_4$ is able to absorb large portion of sunlight and convert it into chemical energy.[41] For instance, pristine $MnFe_2O_4$ was already applied as photocatalyst for hydrogen evolution or degradation of methylene blue.[42–44] However, for liquid applications, *e.g.* as magnetic fluid[45] or heterogeneous (photo-)catalyst,[46] the colloidal stabilization of ferrimagnetic $MnFe_2O_4$ nanoparticles could be benefical, resulting in a better dispersibilty in aqueous or non-aqueous media. This would further reduce the risk of releasing harmful nanoparticle dusts into the air.[47] The ferrimagnetic nature of $MnFe_2O_4$ nanoparticles still enables a simple method for recovering. Common functionalization agents for the postsynthetic stabilization of Fe-based nanoparticles are oleic acid combined with oleylamine, betaine hydrochloride, or citric acid.[48–50]

$MnFe_2O_4$ nanoparticles with manifold morphological characteristics can be synthesized by different methods, including ball milling,[51] solvothermal synthesis,[52] hydrothermal synthesis,[53] and co-precipitation.[40,54] Compared to many traditional wet-chemical syntheses, the microwave synthesis as alternative offers high reproducibility, significantly shortened reaction times, efficient heating, and high yields.[55] In contrast to *e.g.* milling down solid-state synthesized materials to the desired particle size, microwave syntheses can yield relatively defect-free particles with function-tailored properties,[56] using a significantly lower energy input.

Following this, we present a fast and energy-saving microwave-assisted synthesis of 6 nm single-phase magnetic $MnFe_2O_4$ nanoparticles, which is based on the sol-gel reaction of the metal acetylacetonates with the high boiling point solvent *rac*-1-phenylethanol,[57,58] which was earlier applied to other spinel ferrite materials, such as $MgFe_2O_4$,[17,50] $ZnFe_2O_4$,[59] and $NiFe_2O_4$.[60] The thermal stability of the obtained $MnFe_2O_4$ nanoparticles was investigated by calcination at 400, 600, and 800 °C, showing that the material decomposes to binary non-spinel compounds α-Mn_2O_3 and α-Fe_2O_3 after calcination at 400 °C or higher. Special attention was paid on the magnetic properties of prepared materials, which can be correlated to both particle morphology and phase composition.

Results and discussion

Crystalline $MnFe_2O_4$ nanoparticles were synthesized *via* simple non-aqueous microwave-assisted synthesis. Therefore, the metal acetylacetonates dissolved in *rac*-1-phenylethanol (boiling point 204 °C) were treated at 250 °C for 30 minutes in a commercial microwave reactor (Figure S1), before precipitating the obtained particles with *n*-pentane. Afterwards, the particles were washed with acetone-water mixtures plus diethyl ether and dried at 80 °C. Subsequent thermal treatment in a muffle furnace at 400, 600, and 800 °C was additionally performed under air atmosphere to remove remaining organic residues completely and to investigate potentially occurring phase transformations.

The morphologies of obtained samples were investigated by Transmission Electron Microscopy (TEM) (Figures 1a–d). Selected Area Electron Diffraction (SAED) patterns of the obtained Mn–Fe–O samples are further presented in Figures 1e–h. Directly after synthesis, strongly agglomerated nanosized particles can be observed. The rings in the corresponding SAED pattern indicate a nanocrystalline nature of obtained particles and can be assigned to the spinel-type structure of *e.g.* manganese ferrite ($MnFe_2O_4$, JCPDS, no. 01-073-1964). However, the assignment to $MnFe_2O_4$ is not straightforward due to the breadth of observed rings. The nanoparticulate morphology, as well as the spinel-type crystal structure, are preserved when calcining the particles at 400 °C. Upon calcination at elevated temperatures (600 or 800 °C), the nanoparticulate morphology is lost. In the corresponding SAED patterns, diffraction spots are dominant instead of rings, which clearly confirm crystallite growth.

HR-TEM images of as-synthesized and 400 °C-treated samples presented in Figures 2a,c underline the high crystallinity of obtained nanoparticles. Lattice planes are visible even for the non-calcined nanoparticles. Associated particle size distributions (Figures 2b,d) were generated by counting of 100 nanoparticles. They can be fitted by a LogNormal function, giving similar particle mean diameters of 6.0 and 6.3 nm for as-synthesized and 400 °C-treated samples, respectively. Thus, no crystallite growth occurs when calcining the as-synthesized particles at 400 °C. The specific surface areas estimated *via* BET (*Brunauer-Emmett-Teller*) evaluation of N_2 physisorption data are 145 (as-synthesized) and $144\ m^2\,g^{-1}$ (400 °C). As expected, specific surface areas decrease upon calcination to 21 (600 °C) and $5\ m^2\,g^{-1}$ (800 °C) due to crystallite growth. Assuming sherical particles and a bulk density of $4.77\ g\,cm^{-3}$ for $MnFe_2O_4$,[61] theoretical particles sizes with such a surface area could be calculated to 8.7 nm for as-synthesized and 400 °C samples, respectively. Due to the high degree of agglomeration (*c.f.* Figures 1a,b), the real particles are smaller.

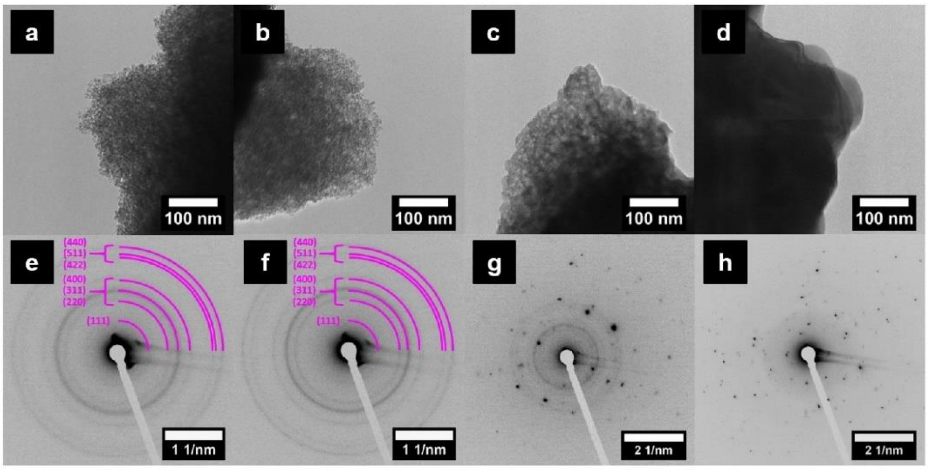

Figure 1. (a-d) Low-magnification TEM images of as-synthesized (left) and calcined (from mid-left to right: 400, 600, 800 °C) Mn–Fe–O samples. Corresponding SAED patterns are presented in (e–h).

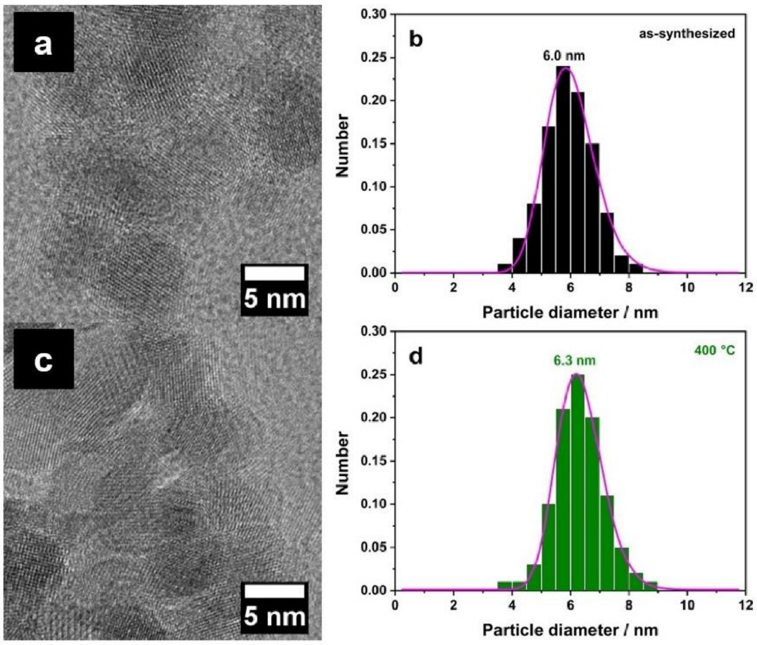

Figure 2. (a,c) HR-TEM images of as-synthesized and 400 °C-treated Mn–Fe–O nanoparticles and (b,d) associated particle size distributions fitted with a LogNormal function.

The phase composition of obtained Mn–Fe–O samples was investigated in detail by various techniques. PXRD patterns measured with silver (Figure 3) and copper (Figure S2) radiation reveal a cubic spinel structure for the as-synthesized and 400 °C-treated samples. Averaging integral breadth analysis of (220), (400), (511), and (440) reflections (Cu PXRD) yields crystallite sizes of 6.2 and 5.9 nm, respectively.[62] Therefore, particle and crystallite sizes are in the same range, which highlights the crystalline nature of prepared spinel nanoparticles.

The positions of the reflections for the as-synthesized nanoparticles are directly in between the ones of the calculated reference patterns for Fe_3O_4 and $MnFe_2O_4$. This could point towards domains of varying composition with Mn and Fe, a co-existence of phases, or an elemental gradient within the nanoparticles. Compared to the as-synthesized sample, the PXRD pattern of the 400 °C sample is shifted to higher *Q*-values, accompanied by the presence of an amorphous signal between 1.5 and 5.5 $Å^{-1}$ (Figure S3). This peak shift matches the modified lattice parameter as determined in PDF refinements. Finally, the sample has transitioned at 600 and 800 °C into co-existing α-Fe_2O_3 (hematite) and α-Mn_2O_3, with some residual spinel phase in the 600 °C sample. This strengthens the point that a phase separation sets in already at 400 °C into presumably an iron-rich spinel phase and nanoscale amorphous domains of manganese oxide.

In contrast to PXRD, which analyses crystal structures in reciprocal space based on Bragg reflections, the pair distribution function (PDF, Figure 4, Figures S4–S5) is gained *via* Fourier Transformation of PXRD data (including both diffuse and Bragg scattering) to real space. The PDF corresponds to a histogram of all interatomic distances in the sample, and is particularly useful when it comes to characterizing short-range order in disordered or nanomaterials. As suggested by PXRD, PDF refinements of the as-synthesized and the 400 °C sample reveal a spinel phase for both samples and a decrease of the lattice parameter caused by calcination. The best fit for the as-synthesized sample is based on two spinel structures, which differ in lattice parameters (and the scale). Since Mn(II) and Fe(III) have isoelectronic configuration, no distinction can be made between Fe_3O_4 and $MnFe_2O_4$ by neither PXRD nor PDF analysis. The stoichiometric ratio of Mn:Fe = 1:2 in $MnFe_2O_4$ was confirmed by energy-dispersive X-ray spectroscopy (EDXS, Figures S6a,c,e,g) and X-ray photoelectron spectroscopy (XPS, Figures S6b,d,f,h) analyses, giving averaged values of 0.51 and 0.47, respectively (EDXS: $Mn_{1.01}Fe_{1.99}O_4$, XPS: $Mn_{0.96}Fe_{2.04}O_4$). This underpins the likeliness of having a compositional or structural gradient in the as-synthesized sample with varying lattice parameters between 8.440 to 8.503 Å. Such gradients could be reflected, for instance, by either a core-shell model with varying lattice parameters from particle surface to core or the co-existence of Fe-rich ($Mn_{1-y}Fe_{2+y}O_4$) and Fe-poor ($Mn_{1+y}Fe_{2-y}O_4$) domains. A defect structure like γ-Fe_2O_3 can be excluded, as the occupancy of the octahedral sites is close to 1, as shown before in PDF refinements on spinel ferrite and iron oxide nanoparticles.[63,64]

While from PXRD data, we could only speculate about the existence of an amorphous Mn_2O_3 phase in the higher background of the 400 °C sample, PDF analysis explicitly confirms the formation of small 0.62 nm α-Mn_2O_3 domains. The addition of a α-Mn_2O_3 phase to the refinement with the spinel phase clearly improves the refinement from a goodness-of-fit R_w of 0.18 to 0.15. This proves that at 400 °C, the spinel phase with a certain distribution of lattice parameters has already started to transform into a spinel phase of shortened lattice parameters

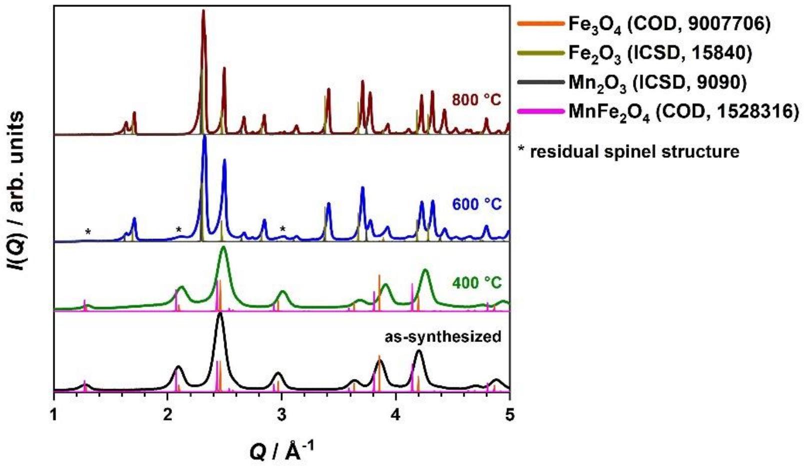

Figure 3. PXRD pattern of samples directly after synthesis and after calcination at 400, 600, and 800 °C. The patterns are stacked and scaled for clarity. Calculated reference patterns of Fe_3O_4, $MnFe_2O_4$, α-Fe_2O_3, and α-Mn_2O_3 are inserted individually at each temperature to highlight existing phases. Reflections of residual spinel structure in the 600 °C sample are marked with a star (*).

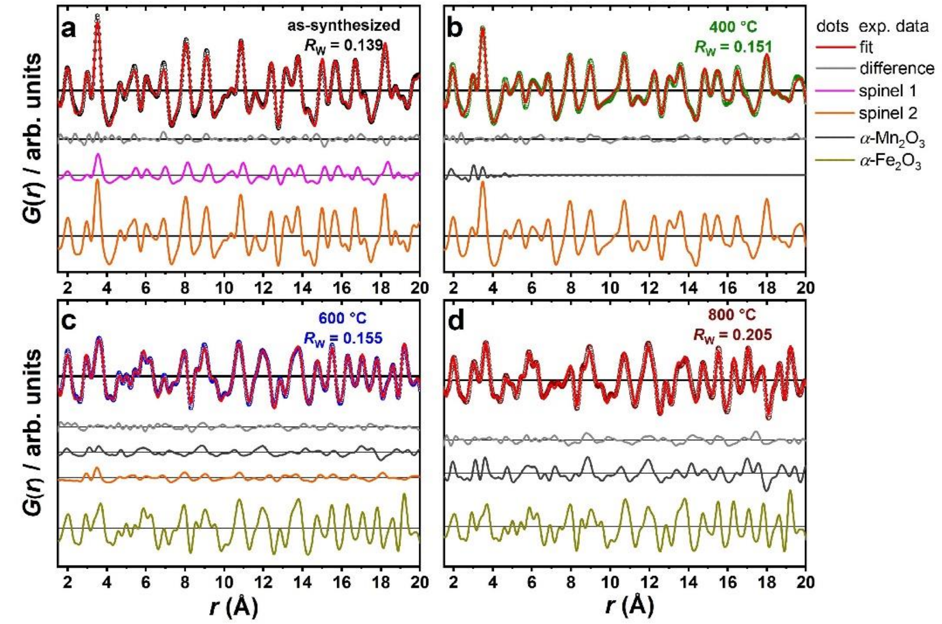

Figure 4. PDF refinements over 1.5 to 50 Å (shown range 1.5 to 20 Å) of the as-synthesized nanoparticles (a) and the ones after calcination at 400 (b), 600 (c), and 800 °C (d). Dots and red solid lines correspond to measured and simulated PDFs. Grey solid lines are the differences. Further solid lines represent the contribution of two different spinel phases, α-Mn_2O_3, and α-Fe_2O_3 to the refinements, respectively. All contributions and differences are plotted in offset, for clarity. The full range PDF refinements over 1.5 to 50 Å are presented in the SI.

accompanied by a manganese oxide phase due to the oxidation of the Mn(II) ions, which only becomes visible by this sophisticated analysis. The refined lattice parameter of 8.343 Å for the spinel phase in the 400 °C sample is even shorter than in bulk Fe_3O_4 (8.394 Å). Considering the resulting molar phase contents in the PDF fits and the Mn : Fe ratio from EDXS of 0.52 (XPS: 0.50), the average spinel sum formula results in $Mn_{0.43}Fe_{2.57}O_4$ (from XPS ratio: $Mn_{0.4}Fe_{2.6}O_4$; for calculation see **eq. S1**). After calcination at 600 °C, highly crystalline α-Fe_2O_3 has formed and the phase fraction of α-Mn_2O_3 increased, with a simultaneous decrease of residual spinel phase with a goodness-of-fit of 0.16. The existence of a α-Mn_2O_3 and a α-Fe_2O_3 phase at 600 °C is coincident with earlier studies on the phase transitions of pure iron and manganese oxide nanoparticles as well as manganese ferrite nanoparticles. They revealed that Mn_5O_8 transforms into α-Mn_2O_3 at 550 °C[64] and Fe_3O_4 transforms into α-Fe_2O_3 between 400 and 500 °C.[65] Evidence for the phase separation of $MnFe_2O_4$ nanoparticles into α-Fe_2O_3 and α-Mn_2O_3 by annealing at 550 °C is also given.[66] A refinement of only the short-range of 1–20 Å (Figure S5a) does not further improve the fit ($R_W = 0.15$), showing that short- and medium-range order are equivalent. The fit of the 800 °C sample results in a higher R_W (0.21) than for the 600 °C sample, although the phase transition has further progressed and the crystallinity and particle size of the hematite phase is expected to be higher given the sharper PXRD Bragg peaks (*cf.* Figure 3). Yet, the difference curve of the PDF fit features structural residuals for $r > 15$ Å. This is substantiated with a better goodness-of-fit $R_W = 0.16$ for the short-range order of 1–20 Å (Figure S5b). The reason for this could be found in possibly polydispersity of the α-Fe_2O_3 and α-Mn_2O_3 domains or crystal defects. During thermal treatment at 600 and 800 °C, the averaged Mn : Fe ratio measured by EDXS stays constant (600 °C: 0.52, 800 °C: 0.51). Since the nanoparticulate structure is lost at such high temperatures, XPS as surface-sensitive technique with low investigation depths (few nm) yields not reliable results concerning the bulk composition.

To conclude, the presented microwave synthesis yields crystalline monomodal $MnFe_2O_4$ nanoparticles with average diameters of 6 nm. However, PXRD and PDF analyses reveal a compositional or structural gradient within the material, which could for example explain varying lattice parameters from particle surface to core or the co-presence of Fe-rich and Fe-poor domains. A subsequent calcination triggers phase transformations. At 400 °C, a spinel-phase with a shortened lattice parameter (presumably magnetite, Fe_3O_4) can be identified as main phase, still forming nanoparticles. Further, small amounts of amorphous α-Mn_2O_3 can be detected, resulting in the Fe-enrichment in the spinel phase. Even higher temperatures (600 and 800 °C) result in the complete decomposition of the spinel structure to the binary compounds α-Fe_2O_3 and α-Mn_2O_3, with some residual spinel at 600 °C.

The four Mn–Fe–O samples were additionally investigated by Raman spectroscopy (Figure 5a). Raman spectra were measured using a green laser (wavelength 532 nm), operated with a low power of 0.3 W to avoid sample fluorescence. The as-synthesized sample features a broad signal at 609 cm^{-1}, which can be assigned to the A_{1g} symmetry mode of spinel-type nanoparticulate $MnFe_2O_4$.[67] According to previous results, a spinel with a shortened lattice parameter is the main phase at a calcination temperature of 400 °C (presumably Fe_3O_4), causing a shift of the A_{1g} signal to higher wavenumbers (653 cm^{-1}).[68] At 600 °C, alongside the Fe_3O_4 spinel (647 cm^{-1}), the prominent Raman bands of α-Fe_2O_3 dominate,[69] while the α-Mn_2O_3 bands additionally appear at 800 °C.[70]

Additional investigations with DRIFT spectroscopy (Figure 5b) reveal that as-synthesized nanoparticles contain organic residues. The –C–H stretching vibration bands at 2967–2860 cm^{-1} clearly indicate the presence of residual acetylacetone on the particle surfaces.[71] Additionally, the prominent bands at 1561 and 1435 cm^{-1} are caused by carbonyl groups of precursor residues.[72,73] The presence of adsorbed water is indicated by –O–H stretching vibrations at 3396 cm^{-1} and the H–O–H bending mode at 1656 cm^{-1}.[74,75] The formation of Fe–O and Mn–O bonds is further confirmed by the bands at 741 and 489 cm^{-1}.[76] The removal of organics on the particle surface can be achieved by a subsequent thermal treatment at 400 °C or higher, but calcination at 600 and 800 °C results in the decomposition of the spinel-type structure.

To prove the presence of organics on the sample surface with a second technique, TG analysis was performed, coupled with mass spectrometry to measure H_2O and CO_2 gas evolution traces (Figure S7). A loss of surface adsorbed water can be observed between 40 and 150 °C. This is followed by the loss of detected organic residues between 200 and 275 °C, as indicated by the delayed signal in the CO_2 mass spectrometry diagram. At a calcination temperature of 400 °C, organic precursor residues are mostly removed, which is also confirmed by DRIFT spectroscopy.

An important feature of $MnFe_2O_4$ nanoparticles for application is their strong magnetism, because of the incorporation of magnetic $3d^5$ high-spin Mn(II) and Fe(III) ions in the partially inverse spinel-type crystal structure. To investigate the influence of particle morphologies and phase compositions on the magnetic properties, synthesized Mn–Fe–O samples were investigated with SQUID magnetometry. The zero field cooled-field cooled (ZFC-FC) magnetization plots measured at 100 Oe are presented in Figure 6a. For the as-synthesized and 400 °C-treated nanoparticles, a characteristic ZFC-FC curve for nanoparticulate soft magnetic materials can be observed.[77,78] Comparatively, the 600 and 800 °C samples exhibit significantly lower magnetic moments in the ZFC-FC curves, which can be correlated to the decomposition of the spinel-type crystal structure into binary compounds α-Mn_2O_3 and α-Fe_2O_3 (*cf.* Figure 3). Consequently, the loss of the spinel-based antiferromagnetic interactions results in an overall reduced magnetic moment. However, the 600 °C sample still contains residual amounts of a spinel-type phase, presumably Fe_3O_4, which would explain the higher magnetic moment, compared to the 800 °C sample.[79] The blocking temperatures (T_B) were estimated by d(ZFC-FC)/d(T) plots,[80] which are depicted in Figure 6b. The blocking temperature of as-synthesized 6 nm $MnFe_2O_4$ nanoparticles is 32 K, which agrees well with previous results reported by Masala *et al.*[81] For the 400 °C sample, the blocking temperature is in the same range (53 K). At even higher calcination temperature (600 °C), the maximum gets broader (81–96 K), which can be correlated to particle growth and an increasing magnetic anisotropy. No blocking temperature can be estimated for the 800 °C sample, which shows a rather small magnetic moment.

The antiferromagnetic exchange interactions between A and B site cations with a 1:2 ratio in Mn–Fe spinels result in ferrimagnetic properties, compared to non-spinel binary compounds α-Mn_2O_3 and α-Fe_2O_3, which are both antiferromagnets.

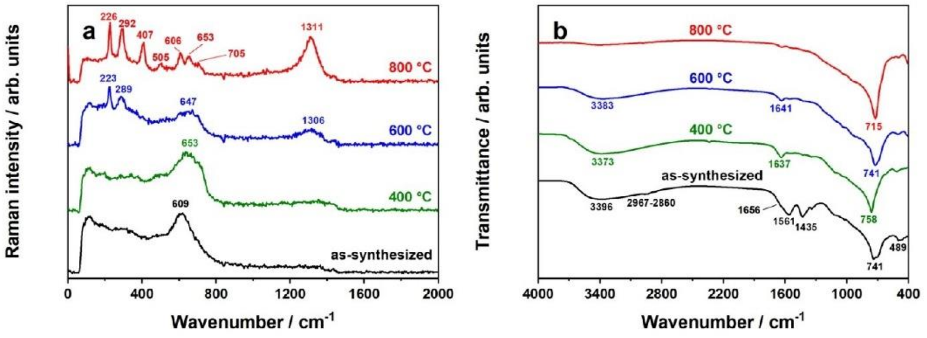

Figure 5. (a) Raman and (b) diffuse reflectance infrared Fourier transform (DRIFT) spectra of as-synthesized and calcined (400, 600, 800 °C) Mn–Fe–O samples. The spectra are stacked and scaled for clarity.

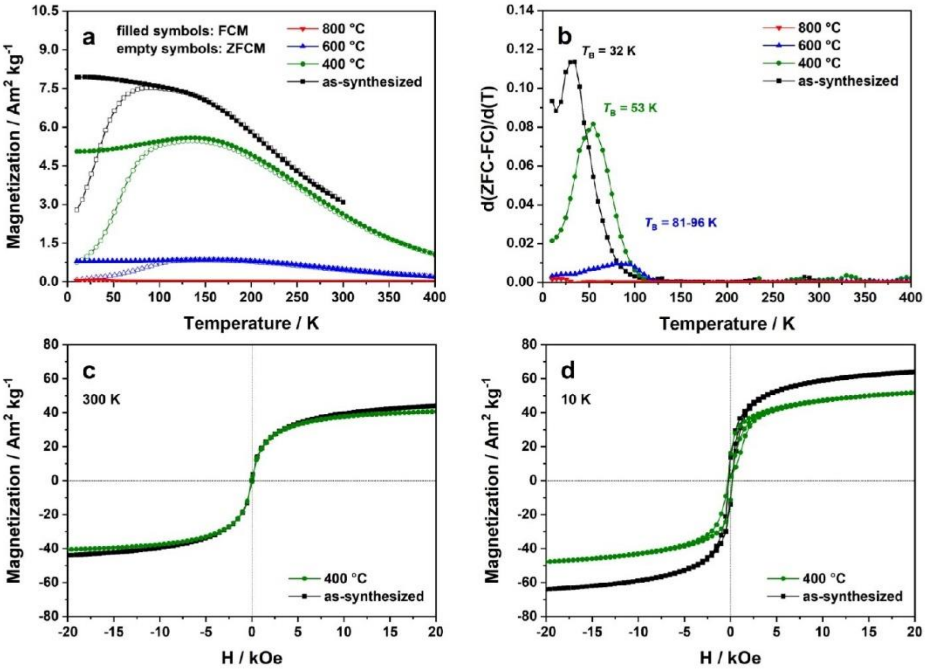

Figure 6. (a) Zero field cooled-field cooled (ZFC-FC) magnetization curves measured at 100 Oe and (b) d(ZFC-FC)/d(T) plots for as-synthesized and calcined (400, 600, 800 °C) Mn–Fe–O samples. Field scans were performed at 300 (c) and 10 K (d) for as-synthesized and 400 °C-treated samples and corrected with respect to the weight loss of diamagnetic components during calcination.

Thus, magnetization curves of as-synthesized and 400 °C nanoparticles were collected at 300 and 10 K (Figures 6c,d). For both samples, the magnetization curves were corrected with respect to the mass loss of diamagnetic carbon-containing residues (as-synthesized: 6.3 wt.-%, 400 °C: 1.3 wt.-%, *cf.* Figure S7). The uncorrected magnetization curves are additionally shown in Figures S8a,b. The saturation magnetizations (M_S) for both uncorrected and corrected data are summarized comparatively in Table 1. By applying the exponential LangevinMod fit,[63] corrected saturation magnetizations of as-synthesized $MnFe_2O_4$ nanoparticles could be estimated to 1.84 (300 K) and 2.62 μ_B (10 K) per formula unit (f.u.), respectively, which is equivalent to 44.5 (300 K) and 63.5 $Am^2 kg^{-1}$ (10 K). Thus, full saturation is not reached at 300 K. Compared to the maximum bulk value for $MnFe_2O_4$ of 3.3–4.5 μ_B,[21–23] the measured saturation magnetization for the 6 nm particles is significantly lower due to modified cationic distributions in the spinel structure and additional surface effects, like surface spin disorder.[82] In

Table 1. Saturation magnetizations of spinel nanoparticles, measured via SQUID magnetometry. The star (*) marks values, which were not corrected for the mass loss of diamagnetic carbon species. For the as-synthesized (as-syn) sample, a formula unit of $MnFe_2O_4$ (M = 230.63 g mol^{-1}) and a unit cell of $Mn_8Fe_{16}O_{32}$ (M = 1845.01 g mol^{-1}) were assumed. Due to progressing phase transitions to Fe_3O_4 at 400 °C, a formula unit of Fe_3O_4 (M = 231.53 g mol^{-1}) and a unit cell of $Fe_{24}O_{32}$ (M = 1852.24 g mol^{-1}) were presumed here.

	size/nm	300 K M_S*/μ_B f.u.$^{-1}$	M_S/μ_B f.u.$^{-1}$	M_S/μ_B u.c.$^{-1}$	10 K M_S*/μ_B f.u.$^{-1}$	M_S/μ_B f.u.$^{-1}$	M_S/μ_B u.c.$^{-1}$
as-syn	6.0	1.96	1.84	14.69	2.80	2.62	20.98
400 °C	6.3	1.73	1.71	13.68	2.07	2.05	16.36
	size/nm	M_S*/Am^2 kg^{-1}	M_S/Am^2 g^{-1}	M_S/kAm^2 mol^{-1}	M_S*/Am^2 g^{-1}	M_S/Am^2 g^{-1}	M_S/kAm^2 mol^{-1}
as-syn	6.0	47.5	44.5	82.1	67.8	63.5	117.2
400 °C	6.3	41.8	41.3	76.4	50.0	49.6	91.7

essence, prepared $MnFe_2O_4$ nanoparticles still reach higher saturation moments than other ferrites in the bulk state, *e.g.* $NiFe_2O_4$ or $MgFe_2O_4$.[24,27] The magnetic properties of $MnFe_2O_4$ can consequently be tailored for a particular application by preparing nanosized or bulk materials, which was already observed for other spinel-type materials.[17,83] The saturation magnetization decreases for 400 °C-treated nanoparticles to 1.71 (300 K) and 2.05 μ_B (10 K) per f.u., respectively, which corresponds to 41.3 (300 K) and 49.3 $Am^2 kg^{-1}$ (10 K). One possible explanation could be the transformation to a spinel structure with shortened lattice parameter, such as Fe_3O_4. However, magnetite nanoparticles were reported to reach similar saturation magnetizations like $MnFe_2O_4$.[29,84] But, nanoparticles treated at 400 °C already contain amorphous non-spinel α-Mn_2O_3 domains, which do not contribute to the overall magnetism and thus explain the reduced values satisfactorily. For both nanoparticulate samples, the magnetization curves measured at 10 K exhibit a hysteresis of 400–500 Oe, contrary to the ones collected at 300 K. Hence, synthesized particles are superparamagnetic at room temperature, as already indicated by the ZFC-FC magnetization plots.

In principle, correlations of magnetic properties and cationic distributions in Fe-based spinels can be investigated *via* ^{57}Fe Mössbauer spectroscopy. For this purpose, a magnetic hyperfine splitting in the Mössbauer spectrum is necessary.[8] However, this sextet splitting can only observed when the measurement temperature is lower than the respective blocking temperature (*e.g.* 32 K for the as-synthesized $MnFe_2O_4$ nanoparticles), which is why no inversion parameter could be estimated from the room temperature data (Figure S9). Due to superparamagnetism at room temperature, a broad doublet with a quadrupole splitting of ΔE_Q of 2.67 $mm\,s^{-1}$ was observed. The broadness with a FWHM $=$ 1.94 $mm\,s^{-1}$ is based on the very small particle size of the sample. For the nanoparticles treated at 400 °C, the room temperature Mössbauer spectrum is even less defined and no fitting was possible. This is in line with the small particle size and the structural inhomogeneity of the spinel as observed by PXRD and PDF analysis.

Through the pronounced magnetism of microwave-derived manganese ferrite nanoparticles, they can be used as inorganic magnetic nanoparticles (MNPs) for numerous applications. Beyond this, the interesting properties of $MnFe_2O_4$ open further application fields. A special highlight is the use as visible-light responsive photocatalyst for hydrogen production or degradation reactions.[42–44] The optical properties of synthesized nanoparticles were therefore investigated by diffuse reflectance UV-Vis-NIR spectroscopy (Figure S10a). From the Kubelka Munk plot (Figure S10b),[85] the optical band gap energy of as-synthesized particles could be estimated to 1.6 eV (794 nm). Band gaps could be estimated more precisely by Tauc plots,[86] which are presented in Figures S10c,d for both direct and indirect behavior. Considering $MnFe_2O_4$ as indirect semiconductor,[87] Tauc analysis of as-synthesized $MnFe_2O_4$ nanoparticles reveals a band gap of 1.5 eV (821 nm). These findings highlight their ability to harvest sunlight. The estimated band gap value is in the same range with the literature value of 1.75–1.78 eV for $MnFe_2O_4$.[41] The progressing decompostion beginning at 400 °C to spinel Fe_3O_4 respective α-Mn_2O_3 and α-Fe_2O_3 effects a further shift of the band edge to the NIR range.

The use of $MnFe_2O_4$ nanoparticles for many applications, *e.g.* as ferrofluid or photocatalyst, requires a colloidal stabilization to achieve an improved dispersibilty in aqueous and non-aqueous media. Therefore, different stabilization strategies were applied. Since as-synthesized nanoparticles contain organic surface residues (*cf.* Figure 5b), postsynthetic stabilization with oleic acid/oleylamine (OA/OLA) seems reasonable to achieve dispersibilty in non-polar solvents, such as toluene.[48] Figure 7a shows the size distribution of OA/OLA-coated as-synthesized $MnFe_2O_4$ nanoparticles dispersed in toluene, measured *via* DLS. The size distribution is relatively sharp, with a mean hydrodynamic diameter of 33 nm, which shows that the particles are less agglomerated. The phase-transfer to polar media (*e.g.* water) was achieved by the exchange of the OA/OLA ligands with citric acid (Figure 7b).[49] The degree of agglomeration is significantly higher, which is reflected by the mean hydrodynamic diameter of 164 nm and the second signal at 500–1300 nm in the DLS measurement. Here, ligand stripping of $MnFe_2O_4$ nanoparticle surfaces with a Meerwein's salt could be helpful, prior to the coating with *e.g.* citric acid.[88] Another possibility of the stabilization of as-synthesized $MnFe_2O_4$ nanoparticles is the functionalization with betaine hydrochloride, which does however not improve the dispersibility in polar solvents (Figure 7c). Obviously, the organic residues on the nanoparticle surface hinder the betaine functionalization. To prove this suggestion, spinel nanoparticles calcined at 400 °C were also stabilized with betaine hydrochloride. Upon calcination at 400 °C, these organics are removed from the nanoparticle surface successfully, resulting in a more hydrophilic surface. Hence, the functionalization of calcined nanoparticles with betaine hydrochloride is possible, which is reflected by the corresponding DLS data (Figure 7d). The mean hydrodynamic diameter of 24 nm indicates a very low degree of agglomeration, and therefore a better dispersibilty.

Conclusion

Phase-pure $MnFe_2O_4$ nanoparticles were successfully synthesized *via* non-aqueous microwave-based sol-gel technique. Directly after synthesis, crystalline nanoparticles with 6 nm in diameter were obtained. Structural analysis reveals a spinel-type structure, with a lattice parameter near the literature value for $MnFe_2O_4$. The slight deviation could be explained with varying lattice parameters from particle surface to core or the co-presence of Fe-rich and Fe-poor domains. The as-synthesized $MnFe_2O_4$ nanoparticles are superparamagnetic at room temperature and ferrimagnetic at 10 K, reaching a saturation magnetization of 2.62 μ_B per formula unit (63.5 $Am^2 kg^{-1}$) at this temperature. Calcination at 400 °C effects no significant morphological changes. But, due to the early formation of amorphous α-Mn_2O_3, the spinel gets Fe richer. The lattice parameter shortens and fits better to Fe_3O_4, compared to $MnFe_2O_4$. The beginning phase decomposition diminishes the applicability of 400 °C-treated particles, which is, inter alia,

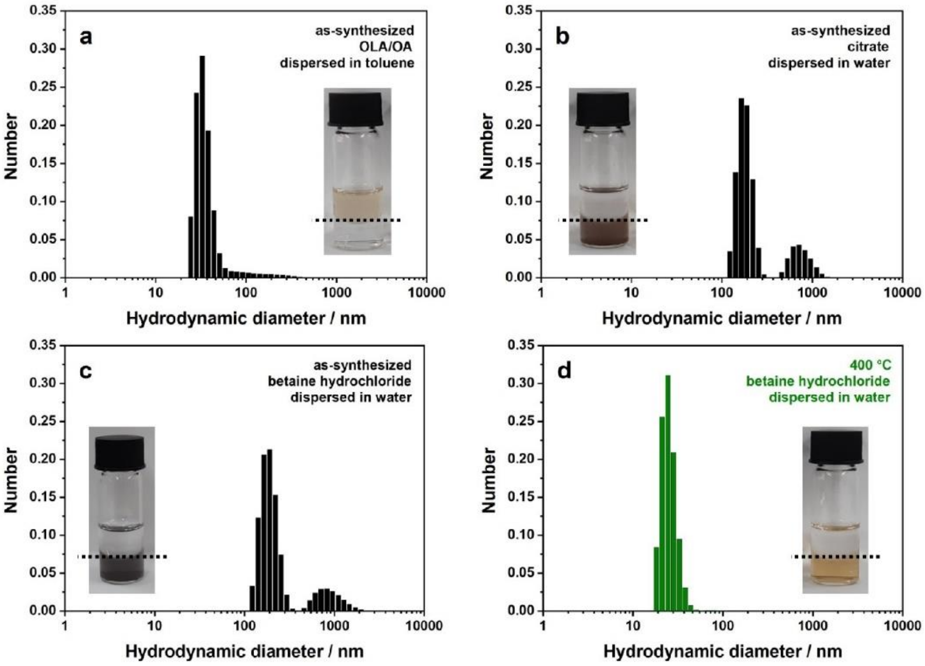

Figure 7. DLS measurements of as-synthesized $MnFe_2O_4$ nanoparticles, which were postsynthetically functionalized with oleic acid/oleylamine (OA/OLA) (a), citric acid (b), and betaine hydrochloride (c). The 400 °C-treated particles were also stabilized with betaine hydrochloride (d). Sample were dispersed in water (below) or toluene (above the broken line in insets), depending on the applied stabilization technique.

reflected by the reduced saturation magnetization of 2.05 μ_B (49.3 $Am^2 kg^{-1}$). At even higher temperature of 600 or 800 °C, the spinel decomposes completely into binary non-spinel compounds α-Mn_2O_3 and α-Fe_2O_3, which is coupled with the loss of the typical magnetic properties of spinel ferrite compounds. We have demonstrated the possibility of the postsynthetic stabilization of magnetic 6 nm $MnFe_2O_4$ nanoparticles in polar and non-polar media, using citric acid respective oleic acid/oleylamine as stabilizing agents, which enables their use as *e.g.* ferrofluid or photocatalyst. The 400 °C-treated spinel nanoparticles, which exhibits a slightly changed composition, could also be stabilized in polar media by betaine hydrochloride.

Experimental section

Synthesis

For the synthesis of $MnFe_2O_4$ nanoparticles, a microwave-assisted synthesis of MFe_2O_4 spinel nanoparticles (M = Mg, Zn) published by Kirchberg *et al.* and Dolcet *et al.* was adapted.[50,59] Therefore, 126.6 mg (0.5 mmol) of $Mn(acac)_2$ (*Sigma Aldrich*, ≥97 %) and 353.2 mg (1.0 mmol) of $Fe(acac)_3$ (*Acros Organics*, >99 %) were dissolved in 15 mL of *rac*-1-phenylethanol (*Sigma Aldrich*, 98 %) using ultrasonification. The obtained solution was transferred into a 30 mL borosilicate glass vessel and heated to 250 °C using a laboratory microwave reactor (*Anton Paar* Monowave 400 with MAS autosampler, frequency 2.45 GHz). The reaction temperature was kept for 30 minutes, before cooling to 55 °C with compressed air. During the microwave treatment, the solution was constantly stirred (600 rpm). The particles were subsequently precipitated with *n*-pentane, washed with acetone-water mixtures (3×) and diethyl ether. Finally, the nanoparticles were dried at 80 °C overnight. Optional thermal treatment of dried particles was performed in a muffle furnace under air atmosphere at 400, 600, and 800 °C for 1 h (heating rate: 10 $K min^{-1}$).

Postsynthetic colloidal stabilization

The stabilization tests were performed according to experimental protocols published by Kirchberg *et al.*[50] For postsynthetic stabilization of as-synthesized $MnFe_2O_4$ nanoparticles in non-polar solvents (*e.g.* toluene), 41.8 mg of $MnFe_2O_4$ were added to a solution of 2 mL of oleic acid (OA, *Sigma Aldrich*, 90 %), 2 mL of oleylamine (OLA, *Sigma Aldrich*, ≥98 %), and 20 mL of toluene (*VWR*, AnalaR Normapur®). The mixture was then refluxed at 116 °C for 48 hours. The nanoparticles were afterwards precipitated with methanol (*VWR*, AnalaR Normapur®) and dried at 80 °C. For the phase-transfer into polar solvents (*e.g.* water), 25.6 mg of citric acid monohydrate (*Carl Roth*, ≥99.5 %) were dissolved in 1.9 mL of 1,2-dichlorobenzene (*Alfa Aesar*, 99 %) and 1.9 mL of *N,N*-dimethylformamide (*Alfa Aesar*, 99.8 %). Then, 29.1 mg of the OA/OLA-coated $MnFe_2O_4$ nanoparticles were added to this solution. The mixture was heated to 100 °C for 22 hours. Finally, the citrate-stabilized particles were precipitated with diethyl ether, washed with acetone (3x), and dried at 80 °C.

As-synthesized $MnFe_2O_4$ nanoparticles were further stabilized in polar media using betaine hydrochloride. Therefore, 21.5 mg of $MnFe_2O_4$ were dissolved in 20 mL of a 2 wt.-% solution of betaine hydrochloride (*TCI*, >98 %) in water. After stirring for 6 hours, particles were precipitated with acetone and dried at 80 °C. This procedure was additionally performed for the 400 °C-treated nanoparticles.

Characterization techniques

Transmission electron microscopy (TEM) and selected area electron diffraction (SAED) were performed on a 200 kV JEOL JEM-2200FS EFTEM from *JEOL GmbH*, additionally equipped with Schottky FEG and In-Column Omega Energyfilter. Prior to the measurements, approximately 1 mg of the sample were dispersed in ethanol (*Acros Organics*, extra dry, 99.5 %), before dropping 4 µL of the dispersion on a carbon film-coated TEM grid (*ScienceServices*, 200 Mesh). Then, the sample was allowed to dry at room temperature. TEM images and SAED patterns were edited using ImageJ 1.52a.

For N_2 physisorption analysis at 77 K, an *Anton Paar* QUADRASORB evo surface area & pore size analyzer was used. Specific surface areas were estimated by applying the BET model (*Brunauer-Emmett-Teller*).[89] Samples were degassed in vacuum at 120 °C for 12 hours before the measurements. Data were evaluated with ASiQwin 4.0®.

Energy-dispersive X-ray spectroscopy (EDXS) was performed on a *Zeiss* Leo 1530 scanning electron microscope, combined with an UltraDry-EDX detector (*Thermo Fisher Scientific* NS7). Prior to the measurements, samples were sputtered with platinum with a Cressington Sputter Coater 208 HR. An acceleration voltage of 15 kV was applied during the measurements. The working distance was set to 8.0 mm.

X-ray photoelectron spectroscopy (XPS) was measured using a *Physical Electronics* PHI VersaProbe III Scanning XPS Microprobe equipped with a monochromatic aluminum K_α source. The survey scans were measured with a pass energy of 226 eV, a step size of 0.4 eV and a time of 50 ms per step, applying a beam diameter of 100 µm. All samples were flooded with low energy electrons and argon ions to prevent surface charging. The recorded data was evaluated with CasaXPS.

Ag powder X-ray diffraction (PXRD) data for PDF analysis was collected at room temperature on a *STOE* STADI P Mythen2 4 K diffractometer (Ag $K\alpha_1$, $\lambda = 0.5594$ Å).[90] Samples were measured in 0.5 mm diameter glass capillaries (*Hilgenberg* glass number 10) for 22 h each in a *Q*-range of 0.3 to 20.4 $Å^{-1}$. PDF processing was carried out with xPDFsuite[91] using a sample-dependent Q_{max} of 13.0 to 17.5 $Å^{-1}$, and fitting was done with PDFgui.[92] Refined parameters are the scale, lattice parameters, crystallite size, correlated atomic motion parameter λ_2, occupancy of octahedral sites in spinel structures and thermal parameters.

Cu PXRD (Cu $K\alpha_1$, $\lambda = 1.5405$ Å and Cu $K\alpha_2$, $\lambda = 1.5444$ Å) was performed on a *Malvern PANanalytical* Empyrean diffractometer with PixCel 1D detector. The device was operated at an acceleration voltage of 40 kV and an emission current of 40 mA. To reduce X-ray fluorescence, the pulse-height-discrimination (PHD) levels were changed to 8.05 and 11.27 keV, respectively. Data were recorded in a range of 10–70 2θ.

A *WITec* alpha 300 RA+ imaging system was employed for Raman measurements, equipped with a UHTS 300 spectrometer and a back-illuminated *Andor Newton* 970 EMCCD camera. The measurements were conducted at an excitation wavelength of $\lambda = 532$ nm, using a laser power of 0.3 mW, an integration time of 5 s and typically 20–30 accumulations (50x *Zeiss* objective, NA = 0.7, software *WITec* Control FIVE 5.3). All spectra were subjected to a cosmic ray removal routine and baseline correction.

For diffuse reflectance infrared Fourier transform (DRIFT) spectroscopy, a *Bruker* alpha II device was used. Data were collected with a spectral resolution of 10 cm^{-1} and 200 co-additions per scan.

Thermogravimetric (TG) analysis in synthetic air was performed using a *Netzsch* Jupiter STA 449 C thermo-balance, which was coupled with a *Netzsch* Aeolos QMS 403 C quadrupol mass spectrometer (MS) for detecting gaseous substances, such as H_2O (18) and CO_2 (44). The heating ramp was set to 10 $K\,min^{-1}$.

Magnetic measurements were performed on a superconducting quantum interference device (SQUID) MPMS-XL5 from *Quantum Design*. Prior to the measurements, samples were prepared in gelatin capsules, which were held by a plastic straw. The field measurements at 10 and 300 K were performed from 100 to 20000 to −20000 Oe (hysteresis mode), with a step width of 500 Oe. Data were corrected for the diamagnetism of the sample holder and the weight loss during thermal treatment. For estimation of the saturation magnetizations M_s, an exponential LangevinMod fit was applied, with the C parameter giving M_s. Saturation magnetizations were converted to units of μ_B per formula unit (f.u.) throughout the text. For recording zero field cooled-field cooled (ZFC-FC) magnetization data, samples were cooled in the SQUID cavity without applying an external magnetic field. The temperature scans were performed from 10 to 300/400 to 10 K in the sweep mode with a velocity of 5 K (applied field 100 Oe).

^{57}Fe Mössbauer spectroscopy was performed in a transmission geometry at constant acceleration with a conventional Mössbauer spectrometer with a ^{57}Co source (50 mCi), embedded in Rh. The spectra were fitted using *Recoil* 1.05 Mössbauer analysis software. The isomer shift values were corrected with respect to α-Fe as a reference at room temperature.

A *PerkinElmer* Lambda 750 device with Praying Mantis mirror unit was applied for diffuse reflectance (DR) UV-Vis-NIR measurements. Data were collected from 200 to 3000 nm, with a step size of 1 nm.

Dynamic light scattering (DLS) was used to determine the hydrodynamic diameter of the dispersed nanoparticles (0.5 $mg\,mL^{-1}$). After ultrasonic treatment, the dispersions were analysed in quartz cuvettes with a *Malvern* ZS Nano Zetasizer (20 °C, equilibration time 2 min, backscattering angle 173°). A refractive index of 2.39 was assumed for data evolution.[50] For each sample, three individual measurements were performed.

Acknowledgements

A.B. and R.M. gratefully acknowledge financial support from the AiF within the program for promoting the Industrial Collective Research (IGF) of the German Federal Ministry of Economic Affairs and Energy (BMWi), based on a resolution of the German Parliament (project "QuinoLight", 18904N1-5). C.S. and R.M. further acknowledge funding by the German Research Foundation DFG (MA 5392/7-1). M.E. and M.Z. acknowledge funding by the DFG *via* SFB 840, project C7, and a scholarship of the Young Academy of the Bavarian Academy of Sciences and Humanities. H.K. gratefully acknowledges financial support from the MINT Lehramt Plus and the BayNAT program. The authors thank the Bavarian Polymer Institute KeyLab Electron and Optical Microscopy for the use of the EM setups. Further thanks go to Jonas Jungmann (University of Bayreuth, Department of Chemistry) for N_2 physisorption measurements, Michael Furtmair (University of Bayreuth, Department of Chemistry) for his help with DLS measurements, Dr. Holger Schmalz (University of Bayreuth, Keylab Synthesis and Molecular Characterization, Bavarian Polymer institute) for Raman-AFM analysis, and Lena Geiling (University of Bayreuth, Faculty of Engineering) for performing TG-MS experiments. We finally thank Bavarian Polymer Institute KeyLab Device Engineering and Dr. Morten Weiss (University of Bayreuth, Department of Chemistry) for the XPS measurements. Open Access funding enabled and organized by Projekt DEAL.

Conflict of Interest

The authors declare no conflict of interest.

Keywords: Spinel ferrites · magnetic nanoparticles · pair distribution function · colloidal stabilization · microwave synthesis

[1] V. F. Cardoso, A. Francesko, C. Ribeiro, M. Bañobre-López, P. Martins, S. Lanceros-Mendez, *Adv. Healthcare Mater.* **2018**, *7*, 1700845.
[2] Z. Zhou, L. Yang, J. Gao, X. Chen, *Adv. Mater.* **2019**, *31*, 1804567.
[3] S. Sun, *Science* **2000**, *287*, 1989–1992.
[4] C. Jiang, C. W. Leung, P. W. T. Pong, *Appl. Surf. Sci.* **2017**, *419*, 692–696.
[5] J. Govan, Y. Gun'ko, *Nanomaterials* **2014**, *4*, 222–241.
[6] F. Davodi, E. Mühlhausen, M. Tavakkoli, J. Sainio, H. Jiang, B. Gökce, G. Marzun, T. Kallio, *ACS Appl. Mater. Interfaces* **2018**, *10*, 31300–31311.
[7] D. Beketova, M. Motola, H. Sopha, J. Michalicka, V. Cicmancova, F. Dvorak, L. Hromadko, B. Frumarova, M. Stoica, J. M. Macak, *ACS Appl. Nano Mater.* **2020**, *3*, 1553–1563.
[8] C. Simon, J. Timm, D. Tetzlaff, J. Jungmann, U. Apfel, R. Marschall, *ChemElectroChem* **2021**, *8*, 227–239.
[9] R. Valenzuela, *Phys. Res. Int.* **2012**, *2012*, 1–9.
[10] L. B. Railsback, *Geology* **2003**, *31*, 737–740.
[11] Y. Goto, *Jpn. J. Appl. Phys.* **1964**, *3*, 309–313.
[12] J. M. Hastings, L. M. Corliss, *Rev. Mod. Phys.* **1953**, *25*, 114–119.
[13] M. L. Néel, *Ann. Phys. (Paris).* **1948**, *12*, 137–198.
[14] D. S. Mathew, R.-S. Juang, *Chem. Eng. J.* **2007**, *129*, 51–65.
[15] J.-R. Huang, C. Cheng, *J. Appl. Phys.* **2013**, *113*, 33912.
[16] Y. Wang, L. Li, Y. Zhang, X. Chen, S. Fang, G. Li, *J. Phys. Chem. C* **2017**, *121*, 19467–19477.
[17] A. Bloesser, H. Kurz, J. Timm, F. Wittkamp, C. Simon, S. Hayama, B. Weber, U.-P. Apfel, R. Marschall, *ACS Appl. Nano Mater.* **2020**, *3*, 11587–11599.
[18] S. M. Ansari, B. B. Sinha, D. Phase, D. Sen, P. U. Sastry, Y. D. Kolekar, C. V. Ramana, *ACS Appl. Nano Mater.* **2019**, *2*, 1828–1843.
[19] K. Vamvakidis, M. Katsikini, D. Sakellari, E. C. Paloura, O. Kalogirou, C. Dendrinou-Samara, *Dalton Trans.* **2014**, *43*, 12754–12765.
[20] M. J. Thompson, K. J. Blakeney, S. D. Cady, M. D. Reichert, J. Del Pilar-Albaladejo, S. T. White, J. Vela, *Chem. Mater.* **2016**, *28*, 1668–1677.
[21] G. Balaji, N. Gajbhiye, G. Wilde, J. Weissmüller, *J. Magn. Magn. Mater.* **2002**, *242–245*, 617–620.
[22] M. Zheng, X. Wu, B. Zou, Y. Wang, *J. Magn. Magn. Mater.* **1998**, *183*, 152–156.
[23] Z. X. Tang, C. M. Sorensen, K. J. Klabunde, G. C. Hadjipanayis, *Phys. Rev. Lett.* **1991**, *67*, 3602–3605.
[24] A. Berkowitz, J. Lahut, C. VanBuren, *IEEE Trans. Magn.* **1980**, *16*, 184–190.
[25] A. Ceylan, S. Ozcan, C. Ni, S. Ismat Shah, *J. Magn. Magn. Mater.* **2008**, *320*, 857–863.
[26] M. Y. Rafique, M. Ellahi, M. Z. Iqbal, Q. Javed, L. Pan, *Mater. Lett.* **2016**, *162*, 269–272.
[27] V. Šepelák, I. Bergmann, D. Menzel, A. Feldhoff, P. Heitjans, F. J. Litterst, K. D. Becker, *J. Magn. Magn. Mater.* **2007**, *316*, e764–e767.
[28] S. Maensiri, M. Sangmanee, A. Wiengmoon, *Nanoscale Res. Lett.* **2009**, *4*, 221–228.
[29] G. F. Goya, T. S. Berquó, F. C. Fonseca, M. P. Morales, *J. Appl. Phys.* **2003**, *94*, 3520–3528.
[30] O. Schneeweiss, R. Zboril, N. Pizurova, M. Mashlan, E. Petrovsky, J. Tucek, *Nanotechnology* **2006**, *17*, 607–616.
[31] D. H. Han, J. P. Wang, H. L. Luo, *J. Magn. Magn. Mater.* **1994**, *136*, 176–182.
[32] R. Pauthenet, *Ann. Phys. (Paris).* **1952**, *12*, 710–747.
[33] M. Gonzalez-Sandoval, A. Beesley, M. Miki-Yoshida, L. Fuentes-Cobas, J. Matutes-Aquino, *J. Alloys Compd.* **2004**, *369*, 190–194.
[34] Z. Simsa, V. Brabers, *IEEE Trans. Magn.* **1975**, *11*, 1303–1305.
[35] F. Nesa, A. K. M. Zakaria, M. A. S. Khan, S. M. Yunus, A. K. Das, S.-G. Eriksson, M. N. I. Khan, M. A. Hakim, *World J. Condens. Matter Phys.* **2012**, *2*, 27–35.
[36] H. Štěpánková, B. Sedlák, V. Chlan, P. Novák, Z. Šimša, *Phys. Rev. B* **2008**, *77*, 92416.
[37] J. M. Hastings, L. M. Corliss, *Phys. Rev.* **1956**, *104*, 328–331.
[38] U. König, *Solid State Commun.* **1971**, *9*, 425–427.
[39] Z. J. Zhang, Z. L. Wang, B. C. Chakoumakos, J. S. Yin, *J. Am. Chem. Soc.* **1998**, *120*, 1800–1804.
[40] J. P. Chen, C. M. Sorensen, K. J. Klabunde, G. C. Hadjipanayis, E. Devlin, A. Kostikas, *Phys. Rev. B* **1996**, *54*, 9288–9296.
[41] A. Mary Jacintha, A. Manikandan, K. Chinnaraj, S. Arul Antony, P. Neeraja, *J. Nanosci. Nanotechnol.* **2015**, *15*, 9732–9740.
[42] K. Dhanalaxmi, R. Yadav, S. K. Kundu, B. M. Reddy, V. Amoli, A. K. Sinha, J. Mondal, *Chem. A Eur. J.* **2016**, *22*, 15639–15644.
[43] M. Pal, R. Rakshit, K. Mandal, *ACS Appl. Mater. Interfaces* **2014**, *6*, 4903–4910.
[44] H. B. Desai, L. J. Hathiya, H. H. Joshi, A. R. Tanna, *Mater. Today: Proc.* **2020**, *21*, 1905–1910.
[45] S. R. Patade, D. D. Andhare, S. B. Somvanshi, S. A. Jadhav, M. V. Khedkar, K. M. Jadhav, *Ceram. Int.* **2020**, *46*, 25576–25583.
[46] X. Wu, Y. Niu, B. Feng, Y. Yu, X. Huang, C. Zhong, W. Hu, C. M. Li, *ACS Appl. Mater. Interfaces* **2018**, *10*, 20440–20447.
[47] R. E. Hewitt, H. F. Chappell, J. J. Powell, *Curr. Opin. Toxicol.* **2020**, *19*, 93–98.
[48] R. M. Patil, P. B. Shete, N. D. Thorat, S. V. Otari, K. C. Barick, A. Prasad, R. S. Ningthoujam, B. M. Tiwale, S. H. Pawar, *RSC Adv.* **2014**, *4*, 4515–4522.
[49] M. Lattuada, T. A. Hatton, *Langmuir* **2007**, *23*, 2158–2168.
[50] K. Kirchberg, A. Becker, A. Bloesser, T. Weller, J. Timm, C. Suchomski, R. Marschall, *J. Phys. Chem. C* **2017**, *121*, 27126–27138.

[51] B. Aslibeiki, P. Kameli, H. Salamati, M. Eshraghi, T. Tahmasebi, *J. Magn. Magn. Mater.* **2010**, *322*, 2929–2934.
[52] Y. Wang, R. Cheng, Z. Wen, L. Zhao, *Eur. J. Inorg. Chem.* **2011**, *2011*, 2942–2947.
[53] M. M. Cruz, L. P. Ferreira, J. Ramos, S. G. Mendo, A. F. Alves, M. Godinho, M. D. Carvalho, *J. Alloys Compd.* **2017**, *703*, 370–380.
[54] J. Azadmanjiri, H. K. Salehani, *Phys. Status Solidi* **2007**, *4*, 253–255.
[55] I. Bilecka, M. Niederberger, *Nanoscale* **2010**, *2*, 1358.
[56] V. Šepelák, U. Steinike, D. C. Uecker, S. Wißmann, K. D. Becker, *J. Solid State Chem.* **1998**, *135*, 52–58.
[57] R. Deshmukh, M. Niederberger, *Chem. A Eur. J.* **2017**, *23*, 8542–8570.
[58] L. Zhang, G. Garnweitner, I. Djerdj, M. Antonietti, M. Niederberger, *Chem. Asian J.* **2008**, *3*, 746–752.
[59] P. Dolcet, K. Kirchberg, A. Antonello, C. Suchomski, R. Marschall, S. Diodati, R. Muñoz-Espí, K. Landfester, S. Gross, *Inorg. Chem. Front.* **2019**, *6*, 1527–1534.
[60] C. Simon, M. B. Zakaria, H. Kurz, D. Tetzlaff, A. Blösser, M. Weiss, J. Timm, B. Weber, U. Apfel, R. Marschall, *Chem. A Eur. J.* **2021**, doi.org/10.1002/chem.202101716.
[61] L. Passerini, *Gazz. Chim. Ital.* **1930**, *60*, 389–99.
[62] J. I. Langford, A. J. C. Wilson, *J. Appl. Crystallogr.* **1978**, *11*, 102–113.
[63] M. Eckardt, S. L. J. Thomä, M. Dulle, G. Hörner, B. Weber, S. Förster, M. Zobel, *ChemistryOpen* **2020**, *9*, 1214–1220.
[64] S. R. Cooper, R. O. Candler, A. G. Cosby, D. W. Johnson, K. M. Ø. Jensen, J. E. Hutchison, *ACS Nano* **2020**, *14*, 5480–5490.
[65] U. Topal, M. A. Aksan, *J. Magn. Magn. Mater.* **2016**, *406*, 123–128.
[66] F. Al-Mokdad, R. S. Hassan, R. Awad, *Curr. Nanomater.* **2019**, *4*, 125–136.
[67] W. Wang, Z. Ding, X. Zhao, S. Wu, F. Li, M. Yue, J. P. Liu, *J. Appl. Phys.* **2015**, *117*, 17A328.
[68] N. H. Hai, N. D. Phu, N. H. Luong, N. Chau, H. D. Chinh, L. H. Hoang, D. L. Leslie-Pelecky, *J. Korean Phys. Soc.* **2008**, *52*, 1327–1331.
[69] D. L. A. de Faria, S. Venâncio Silva, M. T. de Oliveira, *J. Raman Spectrosc.* **1997**, *28*, 873–878.
[70] R. Naeem, M. Ali Ehsan, R. Yahya, M. Sohail, H. Khaledi, M. Mazhar, *Dalton Trans.* **2016**, *45*, 14928–14939.
[71] S. F. Tayyari, T. Bakhshi, S. J. Mahdizadeh, S. Mehrani, R. E. Sammelson, *J. Mol. Struct.* **2009**, *938*, 76–81.
[72] B. Eckhardt, E. Ortel, D. Bernsmeier, J. Polte, P. Strasser, U. Vainio, F. Emmerling, R. Kraehnert, *Chem. Mater.* **2013**, *25*, 2749–2758.
[73] C. R. Vestal, Z. J. Zhang, *J. Am. Chem. Soc.* **2003**, *125*, 9828–9833.
[74] A. M. Turek, I.E. Wachs, E. DeCanio, *J. Phys. Chem.* **1992**, *96*, 5000–5007.
[75] N. Gajbhiye, G. Balaji, *Thermochim. Acta* **2002**, *385*, 143–151.
[76] Q. Chen, J. Zheng, Q. Yang, Z. Dang, L. Zhang, *ACS Appl. Mater. Interfaces* **2019**, *11*, 15478–15488.
[77] P. A. Joy, P. S. Anil Kumar, S. K. Date, *J. Phys. Condens. Matter* **1998**, *10*, 11049–11054.
[78] C. Liu, B. Zou, A. J. Rondinone, Z. J. Zhang, *J. Phys. Chem. B* **2000**, *104*, 1141–1145.
[79] M. Ahmadzadeh, C. Romero, J. McCloy, *AIP Adv.* **2018**, *8*, 56807.
[80] K. L. Livesey, S. Ruta, N. R. Anderson, D. Baldomir, R. W. Chantrell, D. Serantes, *Sci. Rep.* **2018**, *8*, 11166.
[81] O. Masala, R. Seshadri, *Chem. Phys. Lett.* **2005**, *402*, 160–164.
[82] R. H. Kodama, A. E. Berkowitz, E. J. McNiff, S. Foner, *J. Appl. Phys.* **1997**, *81*, 5552–5557.
[83] D. K. Dinkar, B. Das, R. Gopalan, B. S. Dehiya, *Mater. Chem. Phys.* **2018**, *218*, 70–76.
[84] Y. Wei, B. Han, X. Hu, Y. Lin, X. Wang, X. Deng, *Procedia Eng.* **2012**, *27*, 632–637.
[85] P. Kubelka, F. Munk, *Z. Tech. Phys.* **1931**, *12*, 593–601.
[86] J. Tauc, *Mater. Res. Bull.* **1968**, *3*, 37–46.
[87] A. R. O. Rodrigues, J. M. F. Ramos, I. T. Gomes, B. G. Almeida, J. P. Araújo, M. J. R. P. Queiroz, P. J. G. Coutinho, E. M. S. Castanheira, *RSC Adv.* **2016**, *6*, 17302–17313.
[88] A. Dong, X. Ye, J. Chen, Y. Kang, T. Gordon, J. M. Kikkawa, C. B. Murray, *J. Am. Chem. Soc.* **2011**, *133*, 998–1006.
[89] S. Brunauer, P. H. Emmett, E. Teller, *J. Am. Chem. Soc.* **1938**, *60*, 309–319.
[90] S. L. J. Thomae, N. Prinz, T. Hartmann, M. Teck, S. Correll, M. Zobel, *Rev. Sci. Instrum.* **2019**, *90*, 43905.
[91] X. Yang, P. Juhas, C. L. Farrow, S. J. L. Billinge, *J. Appl. Crystallogr.* **2014**, arXiv:1402.3163v3.
[92] C. L. Farrow, P. Juhas, J. W. Liu, D. Bryndin, E. S. Božin, J. Bloch, T. Proffen, S. J. L. Billinge, *J. Phys. Condens. Matter* **2007**, *19*, 335219.

Manuscript received: May 31, 2021
Revised manuscript received: August 30, 2021
Accepted manuscript online: September 3, 2021

Zeitschrift für
anorganische und
allgemeine Chemie

Supporting Information

Magnetic properties and structural analysis on spinel $MnFe_2O_4$ nanoparticles prepared *via* non-aqueous microwave synthesis

Christopher Simon, André Blösser, Mirco Eckardt, Hannah Kurz, Birgit Weber, Mirijam Zobel[+], and Roland Marschall*

Supporting Information

Magnetic properties and structural analysis on spinel $MnFe_2O_4$ nanoparticles prepared *via* non-aqueous microwave synthesis

Christopher Simon[a], André Blösser[a], Mirco Eckardt[a], Hannah Kurz[a], Birgit Weber[a], Mirijam Zobel[a] and Roland Marschall[a]*

[a] Department of Chemistry, University of Bayreuth, Universitaetsstrasse 30, 95447 Bayreuth, Germany
E-mail: roland.marschall@uni-bayreuth.de

Calculation of the sum formula of the spinel phase in the 400 °C sample

Mn/Fe – ratio according to SEM-EDX: 0.52

Refined molar phase contents according to PDF: Mn_2O_3: 0.312

spinel: 0.688

Sum formula for a Fe-rich spinel structure: $Mn_{1-y}Fe_{2+y}O_4$

➔ $\frac{n(Mn)}{n(Fe)} = 0.52 = \frac{0.312*2+0.688*(1-y)}{0.688*(2+y)};$ **(eq. S1)**

➔ $0.358*(2+y) = 0.624 + 0.688*(1-y);$

➔ $0.716 + 0.358*y = 0.624 + 0.688 - 0.688*y;$

➔ $y = 0.57$

Mn/Fe – ratio according to XPS: 0.50

Refined molar phase contents according to PDF: Mn_2O_3: 0.312

spinel: 0.688

Sum formula for a Fe-rich spinel structure: $Mn_{1-y}Fe_{2+y}O_4$

➔ $\frac{n(Mn)}{n(Fe)} = 0.50 = \frac{0.312*2+0.688*(1-y)}{0.688*(2+y)}$

➔ $0.344*(2+y) = 0.624 + 0.688*(1-y);$

➔ $0.688 + 0.344*y = 0.624 + 0.688 - 0.688*y;$

➔ $y = 0.60$

Additional figures

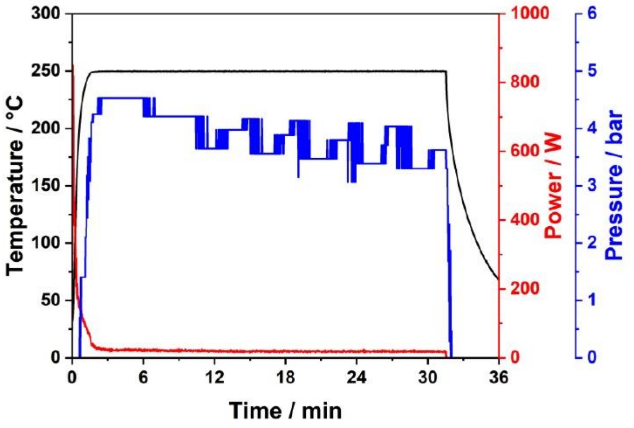

Figure S 1. Microwave synthesis of $MnFe_2O_4$ nanoparticles. During the reaction, temperature (IR sensor), applied power and evolved pressure were recorded.

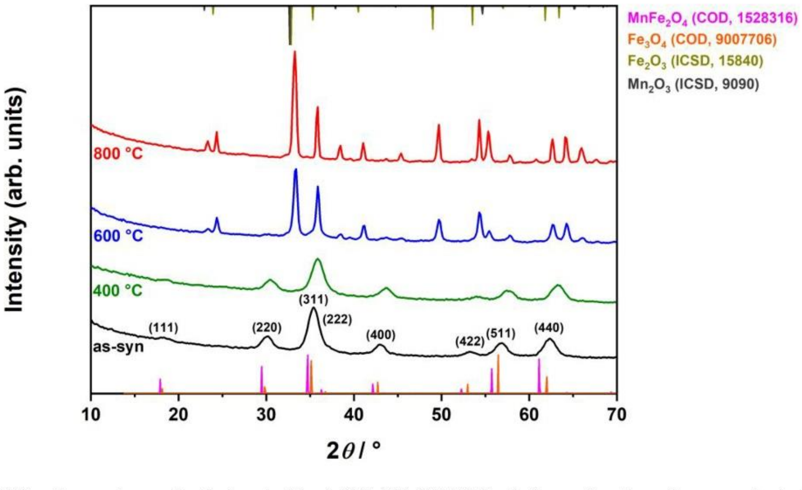

Figure S 2. Cu PXRD patterns of as-synthesized and calcined (400, 600, 800 °C) Mn-Fe-O samples. The patterns are stacked for clarity.

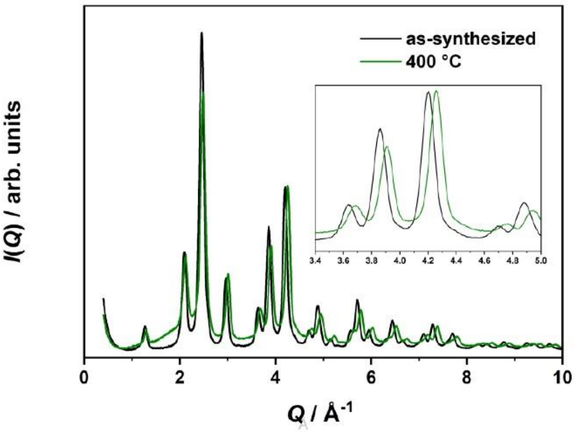

Figure S 3. Ag PXRD patterns of as-synthesized and 400 °C samples to highlight the shift in reflex positions and the occurrence of the amorphous signal between 1.5 and 5.5 Å^{-1}. The inset magnifies the Q-range between 3.4 and 5.0 Å^{-1} to make the shift visible.

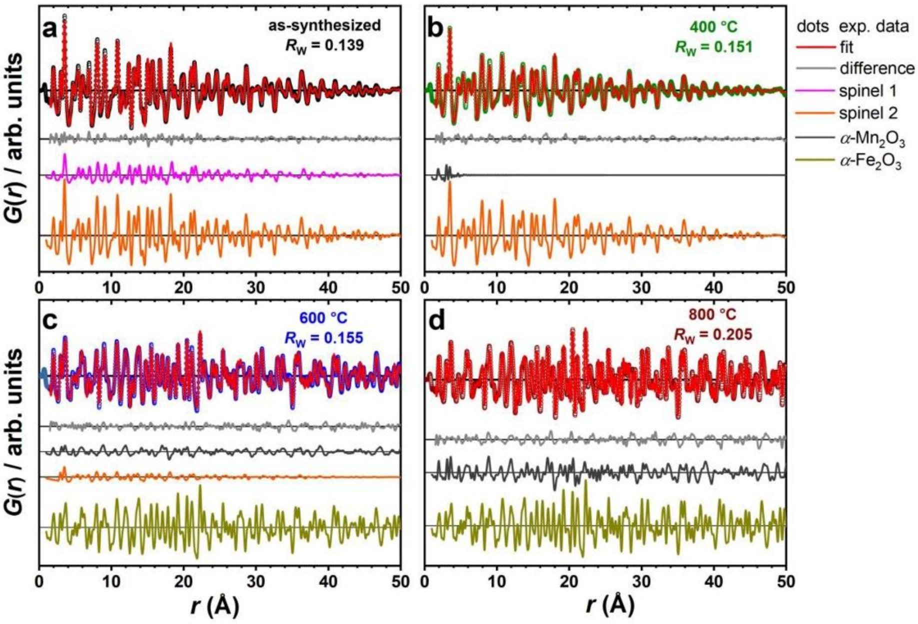

Figure S 4. PDF refinements over 1.5 to 50 Å of the as-synthesized nanoparticles (a) and the ones after calcination at 400 (b), 600 (c) and 800 °C (d). Dots and red solid lines correspond to measured and simulated PDFs. Grey solid lines are the differences. Further solid lines represent the contribution of two different spinel phases, α-Mn_2O_3, and α-Fe_2O_3 to the refinements, respectively. All contributions and differences are plotted in offset, for clarity.

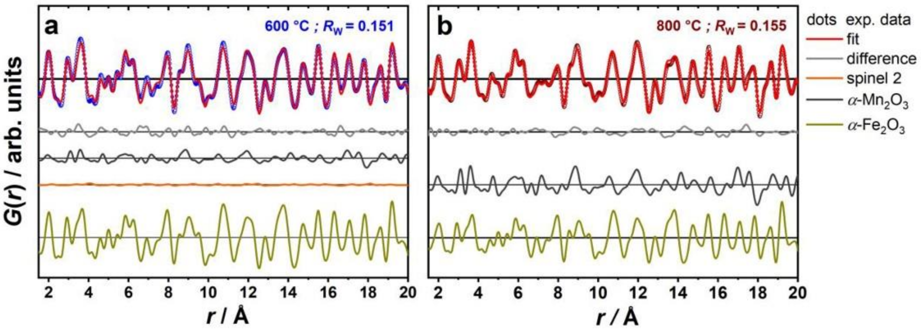

Figure S 5. Short-range PDF refinements (1.5 to 20 Å) after calcination at 600 (a) and 800 °C (b). The R_W value of the short-range refinement of the 600 °C sample is nearly equal to the 50 Å fit. For the 800 °C sample, the R_W is significantly lower for the short-range refinement.

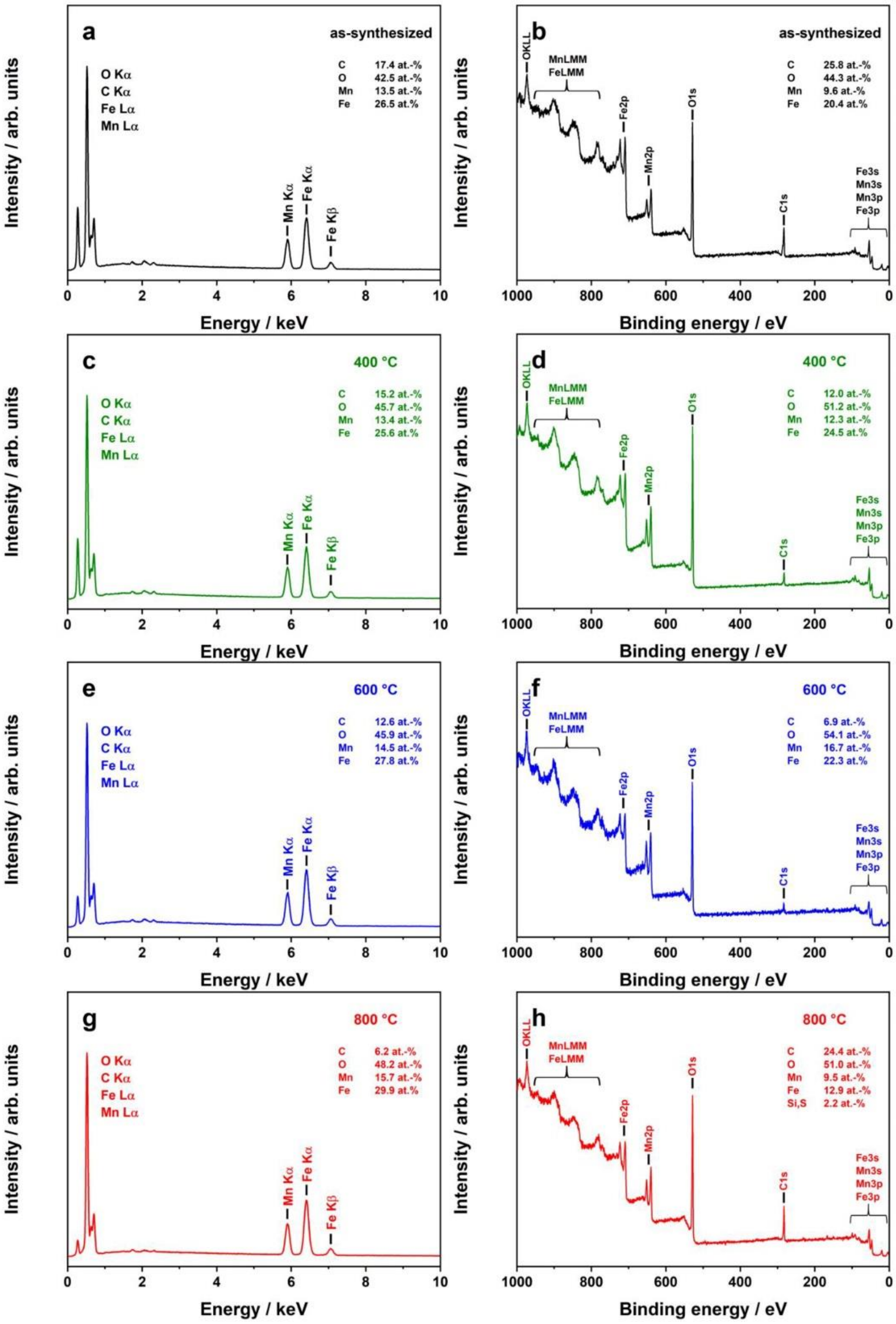

Figure S 6. Elemental compositions of different treated Mn-Fe-O samples, estimated *via* EDXS (a,c,e,g) and XPS (b,d,f,h).

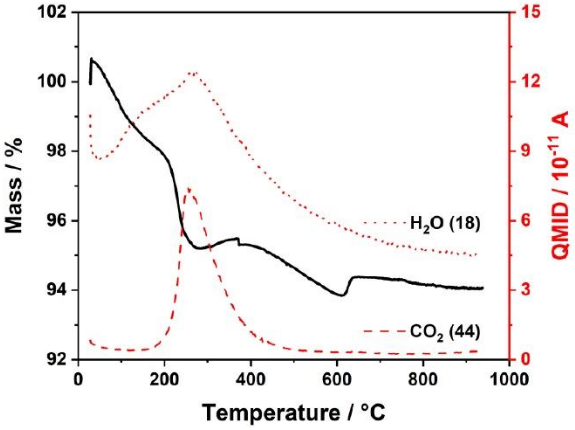

Figure S 7. Thermogravimetric analysis of microwave-derived $MnFe_2O_4$ nanoparticles. During heating, H_2O (*m/e* 18) und CO_2 (*m/e* 44) gas evolution rates were measured *via* online mass spectrometry.

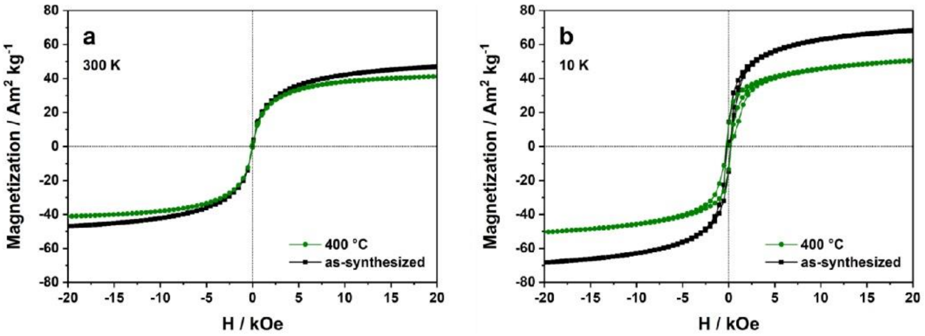

Figure S 8. Field scans performed at 300 (c) and 10 K (d) for as-synthesized and 400 °C-treated samples. Both data sets were not corrected with respect to the weight loss of diamagnetic components during calcination.

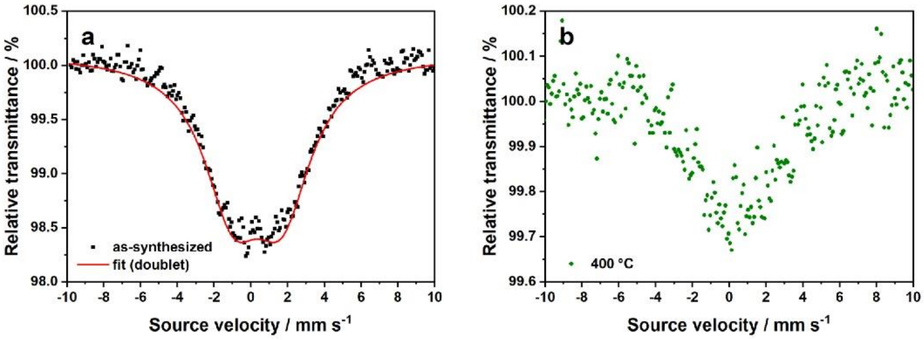

Figure S 9. (a) Room temperature ^{57}Fe Mössbauer spectrum of microwave-derived as-synthesized $MnFe_2O_4$ nanoparticles. Data points were fitted with one doublet (red, quadrupole splitting $\Delta E_Q = 2.67$ mm s^{-1}). The isomer shift of $\delta = 0.37$ mm s^{-1} clearly confirms the presence of Fe(III). (b) Room temperature ^{57}Fe Mössbauer spectrum of the 400 °C spinel nanoparticles. Due to the data quality, no fitting was possible.

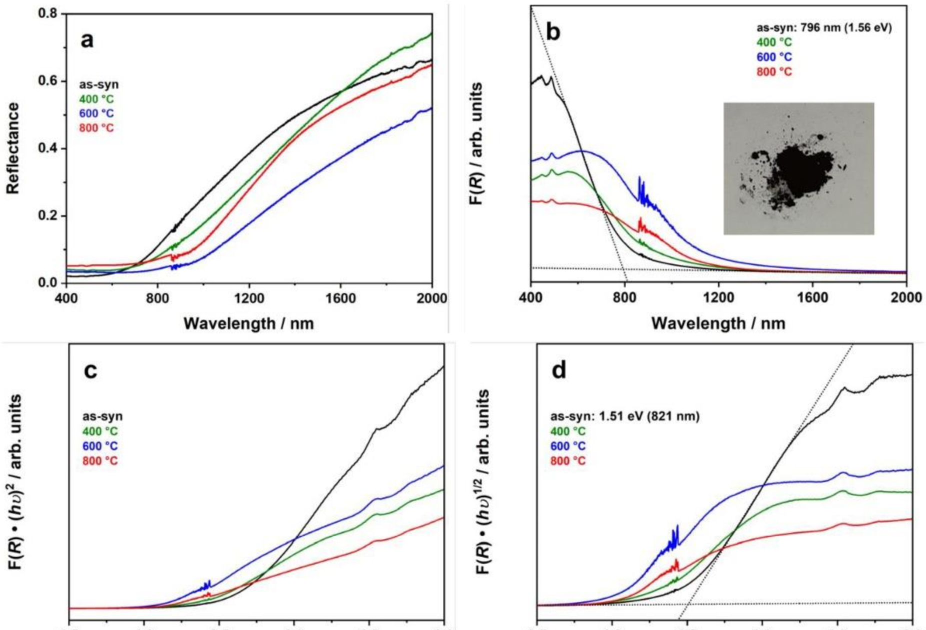

Figure S 10. (a) Diffuse reflectance (DR) UV-Vis-NIR spectra of for as-synthesized and calcined (400, 600, 800 °C) Mn-Fe-O samples and (b) corresponding Kubelka Munk plots. The inserted image shows the dark-brownish as-synthesized $MnFe_2O_4$ nanoparticles. Tauc plots assuming (c) direct and (d) indirect behaviour. Optical band gaps were determind from the Kubelka Munk and Tauc plots, assuming that $MnFe_2O_4$ is an indirect semiconductor.

3.4. Elektrochemische Reduktion von Kohlenstoffdioxid mit Ni_2FeS_4

3.4.1. Synopsis

Die beschriebene Darstellung von Eisenspinell-Nanopartikeln des Typs MFe_2O_4 (M = Ni^{2+}, Mn^{2+}) durch eine Mikrowellensynthese basiert auf einem nukleophilen Angriff von Benzylalkohol oder eines Derivats an ein Metall-Acetylacetonat, wie $Ni(acac)_2$, $Mn(acac)_2$ und $Fe(acac)_3$. Es handelt sich um eine nicht-wässrige Synthesestrategie. Das für die Bildung eines Metalloxids benötigte Sauerstoff-Anion wird dabei vom Lösungsmittel Benzylalkohol zur Verfügung gestellt. Wird nun Benzylalkohol durch das Schwefel-Analogon Benzylmercaptan partiell ersetzt, ist es möglich, einen schwefelhaltigen Eisenspinell herzustellen. Die prinzipielle Eignung der Herstellung von Eisen-basierten Thiospinellen wird anhand des Beispiels von Ni_2FeS_4 in der Veröffentlichung in *ACS Applied Energy Materials* thematisiert. Die Reaktion ausgehend von $Ni(acac)_2$ und $Fe(acac)_3$, welche in einem Gemisch aus *rac*-1-Phenylethanol und Benzylmercaptan gelöst werden, erfolgt bei 200 °C. Höhere Temperaturen sind wegen einer starken Druckentwicklung (>20 bar) nicht möglich. Die Kombination verschiedener Messtechniken (unter anderem Röntgendiffraktometrie, energiedispersive Röntgenspektroskopie, Röntgenphotoelektronenmikroskopie) beweist eindeutig, dass es sich bei dem hergestellten Pulver um den phasenreinen Ni_2FeS_4-Thiospinell handelt. Im Lösungsmittelgemisch ist ein Anteil von ≥ 40 Volumenprozent Benzylmercaptan notwendig, um die Phasenreinheit zu gewährleisten, ansonsten entstehen Komposite aus $NiFe_2O_4$ und Ni_2FeS_4. Erwähnenswert ist, dass im Thiospinell Nickel als dreiwertiges Kation (Ni^{3+}) vorliegt, während Eisen als zweiwertiges Kation (Fe^{2+}) auftritt. Im Vergleich zum Oxid $NiFe_2O_4$ sind die Oxidationsstufen umgekehrt. Während der Mikrowellenreaktion wird dementsprechend Nickel oxidiert und Eisen reduziert. Bemerkenswert ist die Synthese auch deshalb, da der Syntheseaufwand und der Energiebedarf im Vergleich zu traditionellen Hydrothermalsynthesen von Ni_2FeS_4 beziehungsweise Metallsulfiden allgemein minimal ist.[159–161] Bei der Synthese entstehen keine Nanopartikel, sondern plättchenartige Strukturen (Nanoschichten), was elektronenmikroskopische Untersuchungen darlegen. Die spezifische Oberfläche der Nanoschichten beträgt $80\ m^2\ g^{-1}$. Der Wert ist verglichen mit den nicht-kalzinierten oxidischen Nanopartikeln zwar vergleichsweise niedrig, dennoch bietet das Material genug aktive Zentren für eine Anwendung in der heterogenen Katalyse. Das Material Ni_2FeS_4 ist in Laugen nicht stabil, was aus dem Phasendiagramm des Fe-Ni-S-O Systems (**Abbildung 5**) hervorgeht.[46] Daher ist eine Anwendung in der alkalischen Wasseroxidation im Gegensatz zum oxidischen Vertreter $NiFe_2O_4$ nicht sinnvoll. Als anorganisches Analogon der Kohlenmonoxiddehydrogenase (CODH), welche [Ni-4Fe-5S] Cluster enthält, ist das Material in der CO_2-zu-CO-Elektroreduktion aktiv. Die entsprechenden Experimente durchgeführt in einer mit CO_2 gesättigten Kaliumhydrogencarbonat-Lösung zeigen, dass mit den Ni_2FeS_4-Nanoschichten als Elektrokatalysator Synthesegas (Kohlenstoffmonoxid und Wasserstoff) hergestellt werden kann. Bei einem Potential von −0,7 V gegen die reversible Wasserstoffelektrode (*reversible hydrogen electrode*, RHE) beträgt die Selektivität für Kohlenstoffmonoxid (CO) 6,0 %, was einer Faraday-Effizienz von 5,9 % entspricht. Mit einem entsprechenden experimentellen Setup kann an den Nanoschichten auch reiner Wasserstoff aus Wasser dargestellt werden (HER). Die Ergebnisse legen zusammenfassend dar, dass eine weitere Optimierung notwendig ist, um die Wirtschaftlichkeit der elektrochemischen Reduktion von CO_2 und der Wasserstoffentwicklung an Ni_2FeS_4-Nanoschichten zu erreichen. Allerdings enthält die Publikation ein *proof-of-principle*, dass die Synthese von Eisen-basierten ternären Thiospinellen mit Benzylmercaptan als Schwefel-Quelle funktioniert, was bisher nur für binäre Systeme bekannt war.[151]

3.4.2. Veröffentlichung in *ACS Applied Energy Materials*

Christopher Simon,[a] Judith Zander,[a] Tintula Kottakkat,[b] Morten Weiss,[a] Jana Timm,[a] Christina Roth,[b] Roland Marschall[a]

Fast Microwave Synthesis of Phase-Pure Ni_2FeS_4 Thiospinel Nanosheets for Application in Electrochemical CO_2 Reduction

Veröffentlicht in: *ACS Applied Energy Materials* **2021**, *4*, 8702-8708.
Einflussfaktor *ACS Applied Energy Materials* (2021): 6,024

https://doi.org/10.1021/acsaem.1c01341

[a] Department of Chemistry, University of Bayreuth, Universitaetsstrasse 30, 95447 Bayreuth, Germany
[b] Faculty of Engineering, University of Bayreuth, Universitaetsstrasse 30, 95447 Bayreuth, Germany

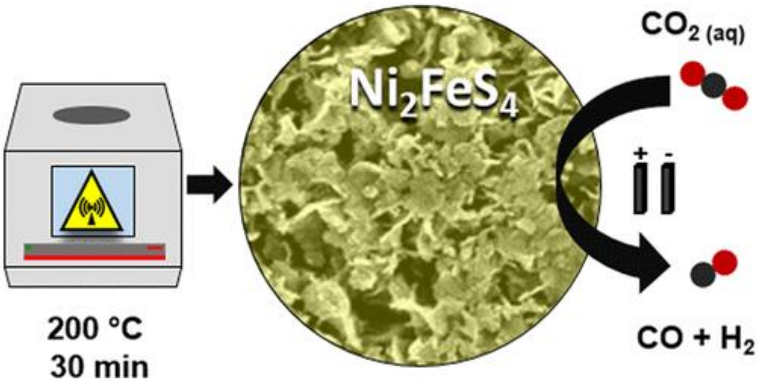

Individuelle Beiträge:

Das Konzept des Beitrags stammt von Prof. Dr. Roland Marschall und mir. Verfasst wurde das Manuskript größtenteils von mir mit Beiträgen von allen Co-Autoren. Die Idee der Mikrowellensynthese von Ni_2FeS_4 wurde von mir entwickelt und praktisch umgesetzt. Die meisten Charakterisierungsexperimente an den hergestellten Nanoschichten wurden ebenfalls von mir durchgeführt und ausgewertet (Röntgendiffraktometrie mit Kupferröhre einschließlich Rietveld-Verfeinerung, Rasterelektronenmikroskopie gekoppelt mit energiedispersiver Röntgenspektroskopie, Transmissionselektronenmikroskopie gekoppelt mit Röntgenbeugung). Judith Zander hat gemeinsam mit Dr. Tintula Kottakkat sämtliche Messungen rund um die elektrochemische Reduktion von Kohlenstoffdioxid und Wasser durchgeführt und die entsprechenden Daten in Zusammenarbeit mit mir ausgewertet. Dr. Morten Weiss hat die Röntgenphotoelektronenspektren aufgenommen und ausgewertet und mich bei der Rietveld-Verfeinerung unterstützt. Dr. Jana Timm hat die Morphologie der Nanoschichten durch Stickstoff- und Wasserdampf-Physisorptionsmessungen analysiert. Auch die Messung des Röntgendiffraktogramms mit der Silberröhre und dessen Auswertung oblag Dr. Jana Timm. Die thermogravimetrischen Untersuchungen an den Proben wurden von Lena Geiling (AG Roth, Universität Bayreuth) ausgeführt. Alle Autoren haben mit wissenschaftlicher Diskussion zum Manuskript beigetragen.

Mein Beitrag zum Manuskript beträgt ca. **70 %**.

ACS APPLIED ENERGY MATERIALS

www.acsaem.org Letter

Fast Microwave Synthesis of Phase-Pure Ni_2FeS_4 Thiospinel Nanosheets for Application in Electrochemical CO_2 Reduction

Christopher Simon, Judith Zander, Tintula Kottakkat, Morten Weiss, Jana Timm, Christina Roth, and Roland Marschall*

Cite This: ACS Appl. Energy Mater. 2021, 4, 8702–8708 Read Online

ACCESS | Metrics & More | Article Recommendations | Supporting Information

ABSTRACT: Phase-pure spinel Ni_2FeS_4 nanosheets with a specific surface area of 80 m^2 g^{-1} were successfully prepared via fast and energy-saving microwave-assisted nonaqueous sol−gel synthesis, starting from metal acetylacetonates and benzyl mercaptan as the sulfur source. Synthesized nanosheets were characterized thoroughly by X-ray diffraction including Rietveld refinement, X-ray photoelectron spectroscopy, energy-dispersive X-ray spectroscopy, electron microscopy, nitrogen and water vapor physisorption measurements, and thermogravimetric analysis coupled with mass spectrometry. Such noble metal free Ni_2FeS_4 nanosheets were successfully applied as electrocatalyst for the aqueous carbon dioxide reduction reaction, yielding selectively the syngas components hydrogen and carbon monoxide.

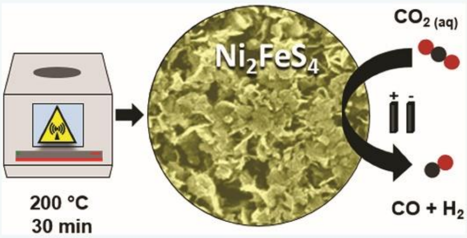

KEYWORDS: *electrocatalysis, CO_2 reduction, metal sulfides, thiospinels, microwave synthesis*

In times of rising carbon dioxide (CO_2) levels in the Earth's atmosphere, converting the greenhouse gas into valuable chemicals or energy-rich fuels is a hot topic in recent research. Reduction of CO_2 via electrolysis to useful C1-components such as CO or formic acid has received increasing attention considering its potential impact on a sustainable energy economy. CO_2 reduction is generally a thermodynamically and kinetically challenging process, requiring highly negative potentials due to the inert nature of CO_2 and proceeding via several proton coupled electron transfers.[1] Furthermore, the formation of different carbon-containing product classes is possible.[2] Therefore, the choice of electrocatalysts that on the one hand selectively generate only one product and on the other hand operate at low overpotentials is severely limited. Among the variety of available compounds, bimetallic transition metal sulfides (TMSs) are cost-effective alternatives to replace state-of-the-art (noble) metal-based electrocatalysts. Especially, nickel cobalt sulfides (Ni−Co−S),[3] iron-based sulfides (Fe−M−S),[4] copper-based sulfides (Cu−M−S),[5] and molybdenum-based sulfides (Mo−M−S)[6] have gained attention in the field of electrocatalysis.

One class of highly conductive electrocatalysts can be prepared from sulfur and the earth-abundant metals nickel and iron, which additionally feature excellent redox properties. Piontek et al. have shown the feasibility of this concept using the mineral pendlandite $Ni_{4.5}Fe_{4.5}S_8$ for electrochemical CO_2 reduction, which is nature-inspired by the carbon monoxide dehydrogenase containing [Ni−4Fe−5S] active clusters.[4] Another promising material in the Ni−Fe−S system is that of Ni_2FeS_4, which is often referred to as mineral violarite. However, in contrast to solid-state-synthesized $Ni_{4.5}Fe_{4.5}S_8$, the ability of pristine Ni_2FeS_4 to electrocatalyze the CO_2 reduction reaction has only scarcely been studied before.[7] Ni_2FeS_4 is of a metallic nature and possesses an inverse thiospinel structure, wherein Fe(II) cations in the low-spin state occupy octahedral sites, while Ni(III) cations are located in both tetrahedral and octahedral sites (Supporting Information (SI) Figure S1).[8] The cubic space group of Ni_2FeS_4 is $Fd\bar{3}m$.[9] Commonly, synthetic violarite Ni_2FeS_4 is prepared via a hydrothermal approach, requiring long reaction times, typically in the range of days. For example, Jørgensen et al. suggested a hydrothermal synthesis for 45 h at 130 °C, starting from nickel(II) acetate, iron(II) acetate, and D,L-penicillamine to prepare nonstoichiometric violarite $Ni_{2.36}Fe_{0.31}S_4$.[10] Mitchell et al. presented a 12 h batch synthesis at 310 °C for the preparation of phase-pure $(Ni,Fe)_3S_4$ powders, based on nickel(II) acetylacetonate, iron(II) acetylacetonate, and sublimed sulfur. The reaction was, however, carried out in oleylamine under nitrogen atmosphere.[11] An et al. described an alternative two-step

Received: May 10, 2021
Accepted: August 12, 2021
Published: August 26, 2021

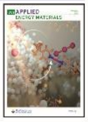

https://doi.org/10.1021/acsaem.1c01341
ACS Appl. Energy Mater. 2021, 4, 8702–8708

pathway for the synthesis of $NiFe_2O_4/Ni_2FeS_4$ heterostructured nanosheets.[12] First, nickel(II) nitrate, iron(III) nitrate, urea, and ammonium fluoride were treated hydrothermally at 120 °C for 12 h to form $NiFe_2O_4$ nanosheets. The subsequent sulfidation step with sodium sulfide at 100 °C for 1−9 h yielded $NiFe_2O_4/Ni_2FeS_4$ heterostructures, but complete sulfidation was also possible when extending the sulfidation step to 12 h.[12]

Generally, compared to traditional hydrothermal syntheses, microwave syntheses offer several advantages, such as significantly shortened reaction times, efficient heating, reproducibility, and improved yields.[13] In this context, we present a novel and fast microwave-assisted sol−gel synthesis for the preparation of synthetic violarite. In contrast to previous hydrothermal or batch syntheses of violarite, our presented facile microwave synthesis of stoichiometric and phase-pure violarite Ni_2FeS_4 only requires a reaction time of 30 min at 200 °C, which offers at least a 24-fold time-saving. Moreover, the use of sulfur precursor, benzyl mercaptan, as solvent component does not require an additional sulfidation step. The short reaction time further implies energetic advantages, and the precursors for the incorporated elements are relatively cheap, which makes the synthesis economically viable.

The applied microwave synthesis is an adaptation of the well-known nonaqueous synthesis of metal oxide nanoparticles, including ternary metal oxides (TMOs), such as $ZnFe_2O_4$[14] or $MgFe_2O_4$ spinels.[15] In short, this method includes an ester elimination step as direct consequence of a nucleophilic attack of benzyl alcohol or a derivate thereof on a metal acetylacetonate. In that process, an oxygen atom of the benzyl alcohol molecule is transferred to the metal cation.[16]

The (partial) replacement of benzyl alcohol or a derivate thereof with the sulfur-analogue benzyl mercaptan results in the incorporation of sulfur instead of oxygen in the crystal structure of the formed product. A first feasibility study on the extension of the benzyl alcohol method to binary metal sulfides was reported by Ludi et al. for the case of ZnS and SnS_2.[17]

For the one-step microwave synthesis of phase-pure Ni_2FeS_4 (Scheme 1, for experimental details see SI), stoichiometric amounts of nickel(II) acetylacetonate and iron(III) acetylacetonate were dissolved in 10 mL of a mixture of *rac*-1-phenylethanol and benzyl mercaptan. The reaction was performed in a microwave reactor under constant stirring at 200 °C for only 30 min, which is the shortest reaction time for the preparation of synthetic phase-pure Ni_2FeS_4 reported ever.[10−12] The obtained powder was precipitated with *n*-pentane, washed with acetone−water mixtures and diethyl ether, and finally dried at 80 °C. During the reaction, reduction of Fe^{3+} and oxidation of Ni^{2+} occur, which might involve benzyl mercaptan acting as electron shuttle.

Scheme 1. Microwave-Assisted Preparation Route of Violarite Nanosheets with Benzyl Mercaptan as Sulfur Precursor

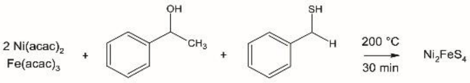

Different solvent ratios of *rac*-1-phenylethanol and benzyl mercaptan were tested for the synthesis of Ni_2FeS_4, with benzyl mercaptan concentrations ranging between 0 and 50 vol %. Investigations by X-ray powder diffraction (XRPD) point out that a benzyl mercaptan fraction of at least 40 vol % is necessary to obtain phase-pure Ni_2FeS_4 (Figure 1a and Figure S2) with high reproducibility. Lower benzyl mercaptan concentrations result in the formation of a $NiFe_2O_4$ by-phase. Hence, it can be concluded that the formation mechanism proceeds faster for benzyl mercaptan, compared to *rac*-1-phenylethanol. As a consequence of different reaction kinetics (and mechanisms), benzyl mercaptan concentrations as low as 40 vol % are sufficient for the synthesis of phase-pure Ni_2FeS_4.

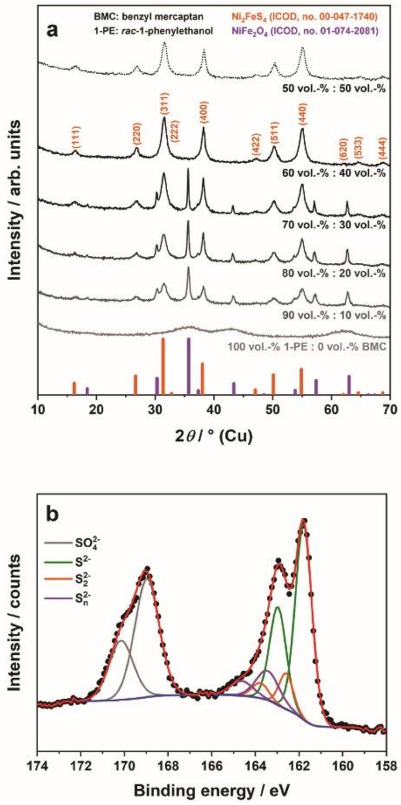

Figure 1. (a) XRPD patterns of microwave-derived powders prepared with different solvent ratios of *rac*-1-phenylethanol and benzyl mercaptan. The amount of benzyl mercaptan was varied in a range of 0−50 vol %, showing that 40 vol % are crucial to obtain phase-pure violarite. (b) XP spectrum of phase-pure Ni_2FeS_4. The black dots represent measured data points, the red line is the overall fit, and the blue line corresponds to the background.

In the following, only samples prepared with a fraction of 40 vol % benzyl mercaptan in the solvent mixture will be discussed regarding phase composition, morphology, stability, and application in the CO_2 electroreduction, because of their phase-pure nature. In XRPD, all observed reflections can be ascribed to the cubic thiospinel Ni_2FeS_4 (ICOD No. 00-047-1740), excluding the presence of any by-phases. Additional XRPD with a silver X-ray tube was performed to reduce the background due to sample fluorescence and confirm absolute phase-purity (Figure S3). Analysis of the integral breadth of (220), (400), (511), and (440) single reflections reveals a crystallite domain size of 8.6 ± 1.0 nm. By Rietveld refinement (Figure S4), the lattice constant of the cubic crystal structure was determined to be 9.47 Å, which is in good agreement with recent literature.[9] Further, calculated domain size via Rietveld refinement is 9.7 ± 1.2 nm, which is matching with the value obtained from integral breadth analysis. The composition was further investigated by X-ray photoelectron spectroscopy (XPS; Figure S5). The quantitative analysis of the survey XP spectrum is summarized in Table S1. The estimated iron to nickel ratio of 0.53 matches well with the theoretical value of 0.5. However, the metal to sulfur ratio of 0.56 slightly deviates from the ideal value of 0.75. XPS as a surface-sensitive technique reveals a higher sulfur content than expected from the sum formula, which could be explained by benzyl mercaptan residues on the Ni_2FeS_4 surface. Therefore, the S 2p region was analyzed in detail via high-resolution XPS (Figure 1b). In the relevant S 2p region, two main signal groups are dominant. The signals in the region 160.4−165.7 eV can be assigned to sulfides. The sulfide signal can be deconvoluted into three individual doublets, representing the spin−orbit splitting of S $2p_{3/2}$ and S $2p_{1/2}$ lines. The doublets can be correlated to the presence of three different sulfur species, including monosulfide, disulfide, and polysulfide, and could explain the slight differences in the mentioned metal to sulfur ratio.[18]

In addition, the other signals (167.3−171.7 eV) can be assigned to sulfate species.[19] Hence, sulfates are clearly present on the sample surface. Observed signals are in good agreement with the XPS profile of violarite reported by Mitchell et al.[11] The presence of sulfur in the reaction product is moreover confirmed by energy-dispersive X-ray (EDX) spectroscopy, as well as the homogeneous distributions of incorporated elements (Figures S6 and S7). For a semiquantitative analysis with EDX spectroscopy (Table S1), five individual spots were considered. In agreement with XPS, the iron to nickel ratio of 0.49 fits to the expected value, while the sulfur content (metal to sulfur ratio, 0.86) is slightly larger than expected. EDXS is a semibulk method, which verifies an enrichment of sulfur in the Ni_2FeS_4 bulk, compared to the surface. The thermal stability of prepared Ni_2FeS_4 was checked by thermogravimetric analysis coupled with online mass spectrometry (TG-MS), showing that the material is air-stable up to approximately 200 °C. Beyond that, Ni_2FeS_4 decomposes gradually upon temperature increase, finally yielding $NiFe_2O_4$ and NiO at 900 °C (Figures S8 and S9).

Concluding the phase analysis, phase-pure Ni_2FeS_4 thiospinel can be prepared by a simple, one-step microwave synthesis in only 30 min.

The morphology of obtained Ni_2FeS_4 was examined with scanning electron microscopy (SEM; Figures 2a and S10) and transmission electron microscopy (TEM; Figures 2b and S11a−d). The depicted SEM images clearly reveal a sheet-like morphology, which is confirmed by TEM analysis. The sheets exhibit diameters of approximately 100−200 nm. The thickness is less than 10 nm, which is in the range of estimated crystallite domain size from XRPD. The HR-TEM image (Figure S11e) further shows lattice planes of Ni_2FeS_4, which can be correlated to the high crystallinity of prepared nanosheets, as already indicated by XRPD analysis. The rings in the corresponding selected area electron diffraction pattern (SAED; Figure S11f) can be assigned unambiguously to the spinel-type structure of Ni_2FeS_4. The nanosheet-like morphology of synthetic Ni_2FeS_4 is further confirmed by the shape of the corresponding nitrogen physisorption isotherm, which is presented in Figure S12. A strong increase in the adsorbed volume and a narrow hysteresis can be observed only at a high relative pressure of >0.9. The slight hysteresis at high relative pressure further underlines the SEM and TEM observations due to the fact that nonporous, nonrigid plate-like particles/sheets could form such an isotherm and are caused by condensation of nitrogen in interparticular voids.[20] The nanosheets are nonporous, but the assembly of the nanosheets leads to an interparticle porosity. The high specific surface area of 80 $m^2\ g^{-1}$ obtained from BET (Brunauer−Emmett−Teller) analysis further demonstrates the assembled, nanostructured morphology of synthesized Ni_2FeS_4 nanosheets resulting in voids between the sheets. The specific surface area is quite remarkable for a Ni−Fe−S material with a high density of 4.65 $cm^3\ g^{-1}$, which is underlined by the comparison with $Ni_{0.7}Fe_{0.3}S_2$ microflowers (11 $m^2\ g^{-1}$)[21] and Ni-doped FeS_2 nanoparticles (26 $m^2\ g^{-1}$).[22]

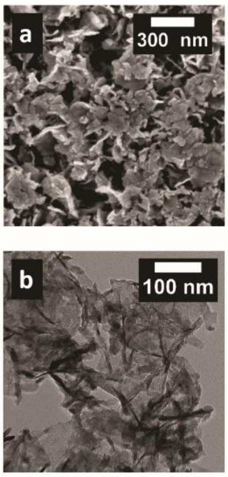

Figure 2. (a) SEM and (b) TEM images of phase-pure Ni_2FeS_4 nanosheets, prepared via the microwave-based sol−gel technique.

These are very important features since the performance of an electrocatalyst can be controlled by tuning size, composition, morphology, and architecture of applied materials.[23] Nanostructuring can be beneficial, as it increases the volume to bulk ratio and thus the number of active surface sites.

In electrochemical CO_2 reduction in aqueous media, the two-phase boundary contact between the catalyst surface and the CO_2-saturated aqueous phase is crucial to avoid further impediments from the catalyst side. The two-phase contact between both is influenced in turn by the surface properties of the catalyst, with a hydrophobic surface being potentially impeding for the performance due to minimized interfacial contact.[24]

Thus, water vapor physisorption measurements were performed for microwave-derived Ni_2FeS_4 (Figure S13). Since the electrochemical experiments employed Ni_2FeS_4 electrodes supported on carbon paper, water vapor measurements were additionally conducted on a respective electrode with a catalyst loading of 2.2 mg cm^{-2}, as well as on bare carbon paper. The area of the working electrodes was limited to 1 cm_2 geometric area by using Kapton tape. The microwave-derived Ni_2FeS_4 nanopowder exhibits a high water vapor uptake of 805 cm^3 g^{-1} at 0.95 relative pressure (95% humidity), owing to its high porosity and surface area and preferable bulk hydrophilicity plus wettability. The hydrophilicity can be explained with the sulfate surface groups, which were identified via XPS. The main uptake of water occurs at a relative pressure of >0.75. The combination of the hydrophobic carbon paper (only water uptake of 20 cm^3 g^{-1} at 0.95 p/p_0) and small amounts of the hydrophilic Ni_2FeS_4 nanopowder leads to an increased water uptake ability (water uptake of Ni_2FeS_4 on carbon paper of 152 cm^3 g^{-1} at 0.95 p/p_0) compared to pure carbon paper. The hydrophilicity of the Ni_2FeS_4 nanopowder improves attractive interactions between the aqueous electrolyte and the catalyst to enhance the performance of the electrocatalytic CO_2 reduction.[24]

The CO_2 electroreduction experiments were performed in a two-compartment electrochemical cell, using a typical three-electrode setup. A CO_2-saturated 0.1 M $KHCO_3$ solution (pH = 6.8) was used as the electrolyte and constantly purged with carbon dioxide at a flow rate of 20 mL min^{-1}. For electrode preparation, as-synthesized sulfide was drop-cast onto a porous carbon paper substrate (for experimental details see the SI). Cyclic voltammetry (CV) was employed to investigate the suitable potential range for the reaction (Figure S14). A change in the current response could be observed starting from −0.5 V vs RHE at pH 0, indicating CO_2 reduction below this potential. A pronounced current increase at more negative potentials suggests accelerated reduction reactions, assuming mostly the hydrogen evolution reaction (HER). To investigate the selectivity and activity dependence on the potential, the reaction was carried out for 15 min each at −0.6 to −0.9 V vs RHE. Although pristine carbon paper as support material itself is conductive, the chronoamperometric measurement exhibits no marked current response in the examined potential range, because of its inactivity for the CO_2 electroreduction. On the contrary, the chronoamperometric curves of the Ni_2FeS_4-modified carbon paper electrodes show a stable current response during 15 min (Figure 3a) of operation. Subsequently, the product gases were analyzed via gas chromatography (GC). The main products of electrochemical CO_2 reduction with Ni_2FeS_4 are carbon monoxide (CO) and hydrogen (H_2). Trace amounts of methane and liquid-phase products such as methanol, ethanol, or isopropanol were observed, however the concentrations were too low for quantification (Figure S15). For each potential, the CO and H_2 formation rates are presented in Figure 3b. The formation rate was normalized to the mass loading. Calculated Faradaic efficiencies (FEs) and gas-phase selectivities for CO gas evolution are depicted in Figure 3c. Selectivities were calculated on the assumption that only CO and H_2 are formed. Averaged gas evolution rates, FEs, and selectivities for CO production and the corresponding standard deviations of the mean are further summarized comparatively in Table S2.

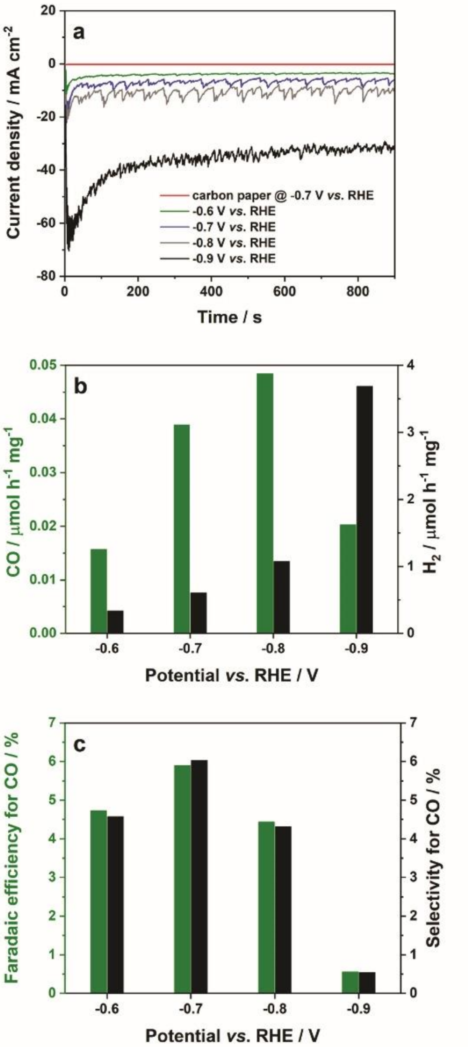

Figure 3. (a) Chronoamperometric responses of Ni_2FeS_4-modified carbon paper electrodes measured for 15 min at constant potentials ranging from −0.6 to −0.9 V vs RHE. (b) Carbon monoxide and hydrogen formation rates after a reaction period of 15 min, as a function of applied potential. (c) Faradaic efficiencies (FEs) plus gaseous product selectivities for CO evolution as a function of applied potential.

The highest FE of 5.9% was observed at a potential of −0.7 V vs RHE. At potentials below −0.8 V vs RHE, a significant drop in the CO Faradaic efficiency is apparent, indicating preferred HER at this potential. In case the reaction was performed on bare carbon paper electrodes, trace amounts of H_2 were produced and no carbonaceous reduction products were detected, confirming the inactivity of pristine carbon paper for the CO_2 reduction. Another noticeable observation from the CV curves is the current density decrease in the second cycle compared to the first, for both Ni_2FeS_4-loaded electrodes before the CO_2 reduction reaction. This might be an indication of surface cleaning processes.[25] To evaluate the stability of the catalyst during the measurement in more detail, the duration of the constant potential application was extended to 1 h at −0.7 V vs RHE (Figure S16a). The current density decreases slightly over time and a measurement of gaseous products at 10 min and 1 h of chronoamperometry reveals a slow deactivation of the Ni_2FeS_4-modified carbon paper working electrode. However, the Faradaic efficiency and gaseous product selectivity for CO remain the same, which means that CO and H_2 formation rates decrease simultaneously. A potential explanation could be a decreased contact between catalyst and carbon paper support material due to a visible detachment process. A stable current density for longer periods up to 5 h could be achieved by using an optimized Nafion binder composition during electrode preparation. Ni_2FeS_4 attachment on the carbon paper substrate was significantly improved by this, suggesting an increase in the actual Nafion content, which concurrently resulted in a slightly lower current density, due to the decreased conductivity and reduced number of active sites, but ultimately in a very stable long-time measurement (Figure S16b).[26] In order to exclude possible phase transformations during the reaction, the working electrode was examined by XRPD after the electrochemical reduction reaction (Figure S17). Alongside the Ni_2FeS_4 thiospinel phase, two broad reflections appear at 34.2 and 60.5° 2θ, showing that the material is not entirely stable during electrochemical CO_2 reduction. Although unambiguous reflection assignment is not possible due to weak intensities, the complete reduction to Ni^0 or Fe^0 can be excluded. Possibly, partial decomposition of Ni_2FeS_4 to $NiSO_4$ and FeS_2 occurs, coupled with the simultaneous oxidation of sulfide anions to elemental sulfur,[27] which would explain brown-greenish residues on the working electrode and the sulfur-like odor after electrocatalytic tests. The decomposition products may not contribute to the CO_2 reduction activity (catalytic area loss); selectivity for H_2 in the CO_2 electroreduction to CO from potassium bicarbonate was already reported for related compounds, such as pendlandite $Ni_{4.5}Fe_{4.5}S_8$. Applying $Ni_{4.5}Fe_{4.5}S_8$ as electrocatalyst, product distributions and selectivities could be adjusted precisely by the process conditions, i.e., by the choice of the solvent.[4] Such solvent dependence for Ni_2FeS_4 will be investigated in future studies. A different product distribution was observed in the CO_2 electroreduction from aqueous $KHCO_3$ solution with FeS_2/NiS nanocomposites, yielding methanol as the main product alongside hydrogen gas.[28] Since both Ni and Fe feature a low overpotential for the hydrogen evolution reaction, H_2 evolution will always be expected alongside CO_2 reduction.[29] The hydrogen production efficiency was illustrated in a comparative experiment employing the same electrocatalyst, electrolyte, and potential, but conducting the experiment in Ar atmosphere (Figure S18). A very low overpotential of only −0.2 V was observed.

In conclusion, Ni_2FeS_4 thiospinel nanosheets with a high specific surface area of 80 $m^2\,g^{-1}$ were successfully prepared via a simple and fast one-step microwave synthesis at 200 °C, starting from $Ni(acac)_2$ and $Fe(acac)_3$ using benzyl mercaptan as sulfur precursor. The reaction time of 30 min is significantly shorter than for any other syntheses reported in literature so far. A benzyl mercaptan volume fraction of at least 40% in the solvent mixture (benzyl mercaptan/*rac*-1-phenylethanol) is necessary to obtain phase-pure Ni_2FeS_4. Otherwise, $NiFe_2O_4$/Ni_2FeS_4 heterostructures were observed. Phase-purity of synthesized Ni_2FeS_4 was thoroughly investigated and confirmed by multiple analysis techniques. Electrocatalytic CO_2 reduction in CO_2-saturated aqueous $KHCO_3$ was used as a test reaction and yielded the syngas components CO and H_2 on these Ni_2FeS_4 nanosheets. At a potential −0.7 V vs RHE, a gaseous product selectivity of 6.0% for CO generation was achieved, which corresponds to a Faradaic efficiency of 5.9%.

■ ASSOCIATED CONTENT

Supporting Information

The Supporting Information is available free of charge at https://pubs.acs.org/doi/10.1021/acsaem.1c01341.

> Ag-XRPD; Rietveld refinement; survey XP and EDX spectroscopy results; TG-MS; nitrogen physisorption and water vapor physisorption data; CVs; chronoamperometric stability tests with XRPD patterns; HER testing; further experimental details and information about the applied characterization methods (PDF)

■ AUTHOR INFORMATION

Corresponding Author

Roland Marschall − *Department of Chemistry, University of Bayreuth, 95447 Bayreuth, Germany;* orcid.org/0000-0002-1057-0459; Email: roland.marschall@uni-bayreuth.de

Authors

Christopher Simon − *Department of Chemistry, University of Bayreuth, 95447 Bayreuth, Germany*
Judith Zander − *Department of Chemistry, University of Bayreuth, 95447 Bayreuth, Germany*
Tintula Kottakkat − *Faculty of Engineering, University of Bayreuth, 95447 Bayreuth, Germany*
Morten Weiss − *Department of Chemistry, University of Bayreuth, 95447 Bayreuth, Germany*
Jana Timm − *Department of Chemistry, University of Bayreuth, 95447 Bayreuth, Germany*
Christina Roth − *Faculty of Engineering, University of Bayreuth, 95447 Bayreuth, Germany*

Complete contact information is available at: https://pubs.acs.org/10.1021/acsaem.1c01341

Author Contributions

C.R. and R.M planned the study and experiments. C.S. developed the microwave synthesis of Ni_2FeS_4. C.S., M.W., and J.T. performed the characterization experiments. J.Z. and T.K. measured the electrochemical CO_2 reduction with Ni_2FeS_4. C.S. wrote the manuscript with the support from J.Z., M.W., J.T., T.K., C.R., and R.M. All authors discussed the results and contributed to the final manuscript.

Notes

The authors declare no competing financial interest.

■ ACKNOWLEDGMENTS

We thank Lena Geiling (University of Bayreuth, Faculty of Engineering) for performing TG-MS experiments. Further thanks go to Jonas Jungmann (University of Bayreuth, Department of Chemistry) for nitrogen physisorption measurement. We acknowledge available SEM and TEM devices by the Bavarian Polymer Institute KeyLab Electron and Optical Microscopy. We also thank the XPS/UPS facility at the Bavarian Polymer Institute KeyLab Device Engineering for use of the XPS device (PHI 5000 VersaProbe III system). C.S. and R.M. gratefully acknowledge funding by the German Research Foundation DFG (Grant MA 5392/7-1). C.R. gratefully acknowledges funding by the German Research Foundation DFG (Grant RO 2454/16-2).

■ REFERENCES

(1) (a) Liu, G.; Tran-Phu, T.; Chen, H.; Tricoli, A. A Review of Metal- and Metal-Oxide-Based Heterogeneous Catalysts for Electroreduction of Carbon Dioxide. *Adv. Sustain. Syst.* **2018**, 2 (8−9), 1800028. (b) Yu, F.; Wei, P.; Yang, Y.; Chen, Y.; Guo, L.; Peng, Z. Material Design at Nano and Atomic Scale for Electrocatalytic CO2 Reduction. *Nano Mater. Sci.* **2019**, *1* (1), 60−69.

(2) (a) Kim, H.; Jeon, H. S.; Jee, M. S.; Nursanto, E. B.; Singh, J. P.; Chae, K.; Hwang, Y. J.; Min, B. K. Contributors to Enhanced CO2 Electroreduction Activity and Stability in a Nanostructured Au Electrocatalyst. *ChemSusChem* **2016**, *9* (16), 2097−2102. (b) Li, Q.; Wang, Z.; Zhang, M.; Hou, P.; Kang, P. Nitrogen Doped Tin Oxide Nanostructured Catalysts for Selective Electrochemical Reduction of Carbon Dioxide to Formate. *J. Energy Chem.* **2017**, *26* (5), 825−829. (c) Cave, E. R.; Shi, C.; Kuhl, K. P.; Hatsukade, T.; Abram, D. N.; Hahn, C.; Chan, K.; Jaramillo, T. F. Trends in the Catalytic Activity of Hydrogen Evolution during CO2 Electroreduction on Transition Metals. *ACS Catal.* **2018**, *8* (4), 3035−3040.

(3) Zhang, Z.; Wang, X.; Cui, G.; Zhang, A.; Zhou, X.; Xu, H.; Gu, L. NiCo2S4 Sub-Micron Spheres: An Efficient Non-Precious Metal Bifunctional Electrocatalyst. *Nanoscale* **2014**, *6* (7), 3540−3544.

(4) Piontek, S.; junge Puring, K.; Siegmund, D.; Smialkowski, M.; Sinev, I.; Tetzlaff, D.; Roldan Cuenya, B.; Apfel, U.-P. Bio-Inspired Design: Bulk Iron−Nickel Sulfide Allows for Efficient Solvent-Dependent CO2 Reduction. *Chem. Sci.* **2019**, *10* (4), 1075−1081.

(5) Chauhan, M.; Reddy, K. P.; Gopinath, C. S.; Deka, S. Copper Cobalt Sulfide Nanosheets Realizing a Promising Electrocatalytic Oxygen Evolution Reaction. *ACS Catal.* **2017**, *7* (9), 5871−5879.

(6) Shit, S.; Jang, W.; Bolar, S.; Murmu, N. C.; Koo, H.; Kuila, T. Effect of Ion Diffusion in Cobalt Molybdenum Bimetallic Sulfide toward Electrocatalytic Water Splitting. *ACS Appl. Mater. Interfaces* **2019**, *11*, 21634−21644.

(7) Yamaguchi, A.; Yamamoto, M.; Takai, K.; Ishii, T.; Hashimoto, K.; Nakamura, R. Electrochemical CO2 Reduction by Ni-Containing Iron Sulfides: How Is CO2 Electrochemically Reduced at Bisulfide-Bearing Deep-Sea Hydrothermal Precipitates? *Electrochim. Acta* **2014**, *141*, 311−318.

(8) Townsend, M. G.; Gosselin, J. R.; Horwood, J. L.; Ripley, L. G.; Tremblay, R. J. Violarite, a'metallic Natural Spinel. *Phys. Status Solidi* **1977**, *40* (1), K25−K29.

(9) Craig, J. R. Violarite Stability Relations. *Am. Mineral.* **1971**, *56*, 1303−1311.

(10) Jørgensen, W. H.; Toftlund, H.; Warner, T. E. Hydrothermal Precipitation of Artificial Violarite. *Hydrometallurgy* **2012**, *115−116*, 98−103.

(11) Mitchell, C. E.; Santos-Carballal, D.; Beale, A. M.; Jones, W.; Morgan, D. J.; Sankar, M.; de Leeuw, N. H. The Role of Surface Oxidation and Fe−Ni Synergy in Fe−Ni−S Catalysts for CO2 Hydrogenation. *Faraday Discuss.* **2021**, *230*, 30.

(12) An, L.; Zhang, Z.; Feng, J.; Lv, F.; Li, Y.; Wang, R.; Lu, M.; Gupta, R. B.; Xi, P.; Zhang, S. Heterostructure-Promoted Oxygen Electrocatalysis Enables Rechargeable Zinc−Air Battery with Neutral Aqueous Electrolyte. *J. Am. Chem. Soc.* **2018**, *140* (50), 17624−17631.

(13) (a) Bilecka, I.; Djerdj, I.; Niederberger, M. One-Minute Synthesis of Crystalline Binary and Ternary Metal Oxide Nanoparticles. *Chem. Commun.* **2008**, 886−888. (b) Pinna, N.; Garnweitner, G.; Antonietti, M.; Niederberger, M. A General Nonaqueous Route to Binary Metal Oxide Nanocrystals Involving a C−C Bond Cleavage. *J. Am. Chem. Soc.* **2005**, *127* (15), 5608−5612. (c) Bilecka, I.; Niederberger, M. Microwave Chemistry for Inorganic Nanomaterials Synthesis. *Nanoscale* **2010**, *2*, 1358−1374.

(14) (a) Dolcet, P.; Kirchberg, K.; Antonello, A.; Suchomski, C.; Marschall, R.; Diodati, S.; Muñoz-Espí, R.; Landfester, K.; Gross, S. Exploring Wet Chemistry Approaches to ZnFe2O4 Spinel Ferrite Nanoparticles with Different Inversion Degrees: A Comparative Study. *Inorg. Chem. Front.* **2019**, *6* (6), 1527−1534. (b) Suchomski, C.; Breitung, B.; Witte, R.; Knapp, M.; Bauer, S.; Baumbach, T.; Reitz, C.; Brezesinski, T. Microwave Synthesis of High-Quality and Uniform 4 Nm ZnFe2O4 Nanocrystals for Application in Energy Storage and Nanomagnetics. *Beilstein J. Nanotechnol.* **2016**, *7* (1), 1350−1360.

(15) (a) Bloesser, A.; Kurz, H.; Timm, J.; Wittkamp, F.; Simon, C.; Hayama, S.; Weber, B.; Apfel, U.-P.; Marschall, R. Tailoring the Size, Inversion Parameter, and Absorption of Phase-Pure Magnetic MgFe2O4 Nanoparticles for Photocatalytic Degradations. *ACS Appl. Nano Mater.* **2020**, *3* (11), 11587−11599. (b) Kirchberg, K.; Becker, A.; Bloesser, A.; Weller, T.; Timm, J.; Suchomski, C.; Marschall, R. Stabilization of Monodisperse, Phase-Pure MgFe2O4 Nanoparticles in Aqueous and Nonaqueous Media and Their Photocatalytic Behavior. *J. Phys. Chem. C* **2017**, *121* (48), 27126−27138.

(16) (a) Zhang, L.; Garnweitner, G.; Djerdj, I.; Antonietti, M.; Niederberger, M. Generalized Nonaqueous Sol−Gel Synthesis of Different Transition-Metal Niobate Nanocrystals and Analysis of the Growth Mechanism. *Chem. - Asian J.* **2008**, *3* (4), 746−752. (b) Deshmukh, R.; Niederberger, M. Mechanistic Aspects in the Formation, Growth and Surface Functionalization of Metal Oxide Nanoparticles in Organic Solvents. *Chem. - Eur. J.* **2017**, *23* (36), 8542−8570.

(17) Ludi, B.; Olliges-Stadler, I.; Rossell, M. D.; Niederberger, M. Extension of the Benzyl Alcohol Route to Metal Sulfides: "Nonhydrolytic" Thio Sol-Gel Synthesis of ZnS and SnS2. *Chem. Commun.* **2011**, *47* (18), 5280−5282.

(18) (a) Buckley, A. N.; Woods, R. X-Ray Photoelectron Spectroscopy of Oxidised Pyrrhotite Surfaces. *Appl. Surf. Sci.* **1985**, *20* (4), 472−480. (b) Pratt, A. R.; Muir, I. J.; Nesbitt, H. W. X-Ray Photoelectron and Auger Electron Spectroscopic Studies of Pyrrhotite and Mechanism of Air Oxidation. *Geochim. Cosmochim. Acta* **1994**, *58* (2), 827−841.

(19) Siriwardane, R. V.; Poston, J. A., Jr; Fisher, E. P.; Shen, M.-S.; Miltz, A. L. Decomposition of the Sulfates of Copper, Iron (II), Iron (III), Nickel, and Zinc: XPS, SEM, DRIFTS, XRD, and TGA Study. *Appl. Surf. Sci.* **1999**, *152* (3−4), 219−236.

(20) (a) Thommes, M.; Kaneko, K.; Neimark, A. V.; Olivier, J. P.; Rodriguez-Reinoso, F.; Rouquerol, J.; Sing, K. S. W. Physisorption of Gases, with Special Reference to the Evaluation of Surface Area and Pore Size Distribution (IUPAC Technical Report). *Pure Appl. Chem.* **2015**, *87* (9−10), 1051−1069. (b) Schlumberger, C.; Thommes, M. Characterization of Hierarchically Ordered Porous Materials by Physisorption and Mercury Porosimetry—A Tutorial Review. *Adv. Mater. Interfaces* **2021**, *8* (4), 2002181.

(21) Yu, J.; Cheng, G.; Luo, W. Ternary Nickel−Iron Sulfide Microflowers as a Robust Electrocatalyst for Bifunctional Water Splitting. *J. Mater. Chem. A* **2017**, *5* (30), 15838−15844.

(22) Nguyen, H. Q.; Phan, T. H. T.; Ho, D. Q.; Nguyen, H. Du; Le, T. T.; Nguyen, T. M.; Pham, V. T.; Duong, N. H.; Nguyen, T. Q. H. A Comparasion of Photocatalytic Activity Between FeS2, Ni-Doped FeS2 Nanoparticles and Un-Doped FeS2/RGO Composite. *J. Electron. Mater.* **2020**, *49* (11), 6474−6482.

(23) (a) Kang, Y.; Yang, P.; Markovic, N. M.; Stamenkovic, V. R. Shaping Electrocatalysis through Tailored Nanomaterials. *Nano Today* **2016**, *11* (5), 587−600. (b) Simon, C.; Timm, J.; Tetzlaff, D.; Jungmann, J.; Apfel, U.-P.; Marschall, R. Mesoporous NiFe2O4 with Tunable Pore Morphology for Electrocatalytic Water Oxidation. *ChemElectroChem* **2021**, *8* (1), 227−239.

(24) Junge Puring, K.; Siegmund, D.; Timm, J.; Möllenbruck, F.; Schemme, S.; Marschall, R.; Apfel, U. Electrochemical CO2

https://doi.org/10.1021/acsaem.1c01341
ACS Appl. Energy Mater. 2021, 4, 8702−8708

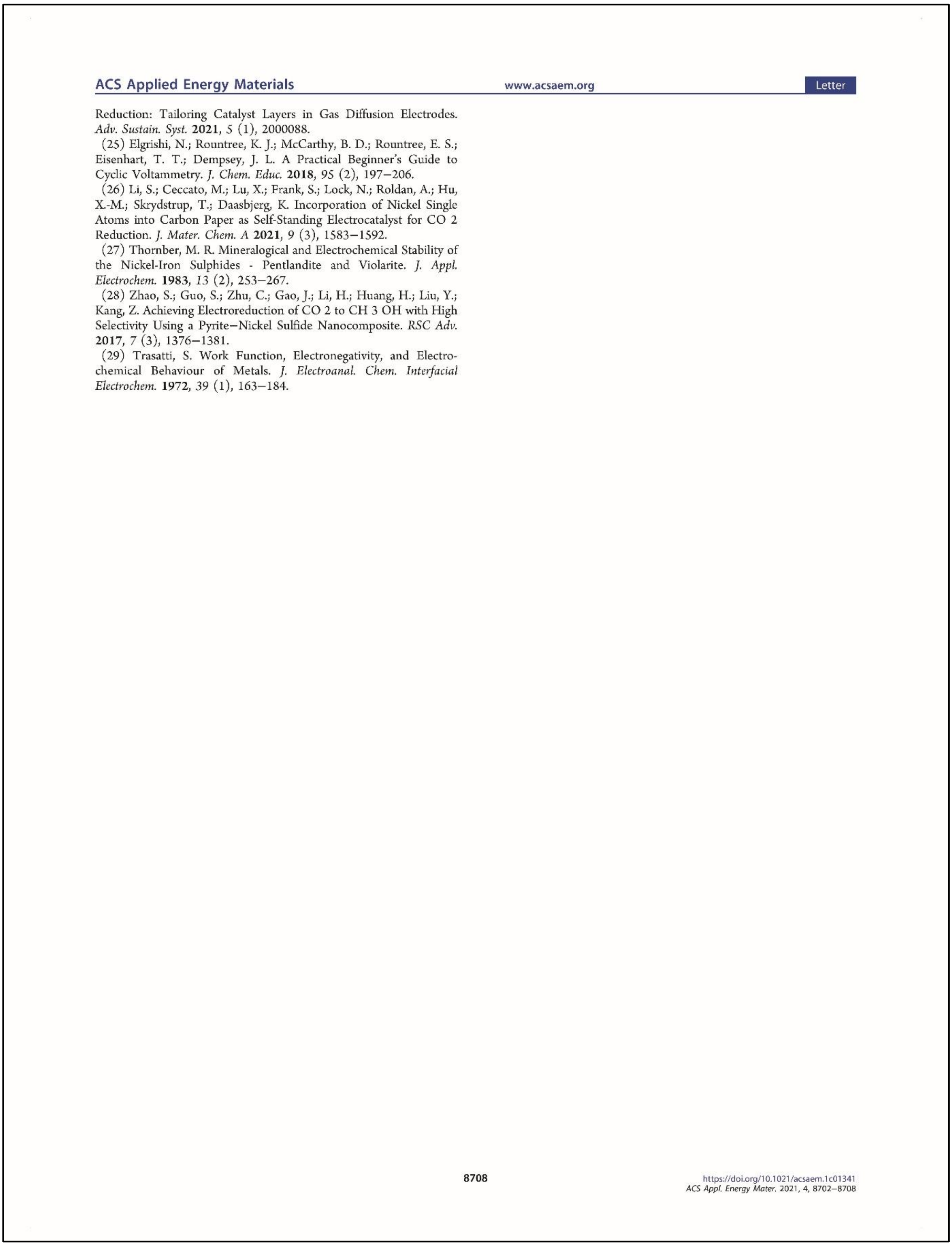

Reduction: Tailoring Catalyst Layers in Gas Diffusion Electrodes. *Adv. Sustain. Syst.* **2021**, *5* (1), 2000088.

(25) Elgrishi, N.; Rountree, K. J.; McCarthy, B. D.; Rountree, E. S.; Eisenhart, T. T.; Dempsey, J. L. A Practical Beginner's Guide to Cyclic Voltammetry. *J. Chem. Educ.* **2018**, *95* (2), 197−206.

(26) Li, S.; Ceccato, M.; Lu, X.; Frank, S.; Lock, N.; Roldan, A.; Hu, X.-M.; Skrydstrup, T.; Daasbjerg, K. Incorporation of Nickel Single Atoms into Carbon Paper as Self-Standing Electrocatalyst for CO 2 Reduction. *J. Mater. Chem. A* **2021**, *9* (3), 1583−1592.

(27) Thornber, M. R. Mineralogical and Electrochemical Stability of the Nickel-Iron Sulphides - Pentlandite and Violarite. *J. Appl. Electrochem.* **1983**, *13* (2), 253−267.

(28) Zhao, S.; Guo, S.; Zhu, C.; Gao, J.; Li, H.; Huang, H.; Liu, Y.; Kang, Z. Achieving Electroreduction of CO 2 to CH 3 OH with High Selectivity Using a Pyrite−Nickel Sulfide Nanocomposite. *RSC Adv.* **2017**, *7* (3), 1376−1381.

(29) Trasatti, S. Work Function, Electronegativity, and Electrochemical Behaviour of Metals. *J. Electroanal. Chem. Interfacial Electrochem.* **1972**, *39* (1), 163−184.

Supporting Information

Fast microwave synthesis of phase-pure Ni_2FeS_4 thiospinel nanosheets for application in electrochemical CO_2 reduction

Christopher Simon[†], *Judith Zander*[†], *Tintula Kottakkat*[‡], *Morten Weiss*[†], *Jana Timm*[†], *Christina Roth*[‡], *and Roland Marschall*[*,†]

†Department of Chemistry, University of Bayreuth, Universitaetsstrasse 30, 95447 Bayreuth, Germany

‡Faculty of Engineering, University of Bayreuth, Universitaetsstrasse 30, 95447 Bayreuth, Germany

Corresponding Author
* Prof. Dr. Roland Marschall, Department of Chemistry, University of Bayreuth, Universitaetsstrasse 30, 95447 Bayreuth, Germany; roland.marschall@uni-bayreuth.de

Experimental section

Mircowave synthesis of Ni_2FeS_4

For the preparation of Ni_2FeS_4 nanosheets, 128.5 mg (0.5 mmol) of Ni(acac)$_2$ (*SigmaAldrich*, for synthesis) and 88.3 mg (0.25 mmol) of Fe(acac)$_3$ (*Acros Organics*, +99%) were dissolved in 5-10 mL of *rac*-1-phenylethanol (*SigmaAldrich*, 98%) using ultrasonification, before transferring the solution into a 30 mL borosilicate microwave glass vessel. Subsequently, 0-5 mL of benzyl mercaptan (*SigmaAldrich*, 99%) were added under rigorous stirring (800 rpm). Then, the reaction mixture was heated to 200 °C for 30 minutes using microwave irradiation (*Anton Paar Monowave 400* with *MAS24* autosampler) under constant stirring (800 rpm). During the heating process, the power was limited to 20-25 W to avoid overheating. After cooling down the reaction solution to 55 °C with compressed air, obtained particles were precipitated with *n*-pentane and washed with acetone-water mixtures (3:1, 12:1, 12:1) plus diethyl ether. Finally, obtained nanosheets were dried at 80 °C overnight in a heating oven.

Electrode preparation and electrochemical measurements

Electrodes for the electrochemical reduction of CO_2 were prepared *via* drop-casting of 50 µL of an ink containing the Ni_2FeS_4 sample onto carbon paper (*Freudenberg H2315-C2*). The carbon paper was cut into stripes measuring 1x2.5 cm and covered with Kapton-tape, leaving 1 cm^2 free for coverage with the Ni_2FeS_4 catalyst. For the ink preparation, 10 mg of Ni_2FeS_4 were dispersed in 300 µL of *i*-propanol, under addition of 20 µL of a 5 wt.% solution of Nafion in water/1-propanol (*Alfa Aesar*) as a binder. The dispersion was ultrasonicated for at least 1 h prior to drop-casting. The electrodes were left to dry at room temperature for 1 day. The carbon paper substrate was weighed before and after sulfide deposition to determine the amount of catalyst on the electrode.

The electrochemical CO_2 reduction was performed in a custom made two compartment cell, separated by a *Selemion AMV-N* anion-exchange membrane purchased from the *AGC group*. A *Gamry Reference 3000* potentiostat and the software *Gamry Framework* were employed for all electrochemical measurements. The reduction was carried out in a 0.1M aqueous $KHCO_3$ solution, which was continuously purged with CO_2 gas from the bottom of the working compartment at a flow rate of 20 mL/min using a calibrated mass flow controller (*Bronkhorst*). The electrolyte was saturated with CO_2

(99.995 volume%, *Air* Liquide) for 10 min prior to the measurement (pH 6.8). The potential was measured against an Ag/AgCl reference electrode and a Pt mesh was used as the counter electrode. After potential application for a certain time (15 min if not otherwise specified) at room temperature, gaseous products were analyzed by gas chromatography (*Shimadzu GC-2014*), using a *HayeSep Q* and a *HayeSep R* column in series and two detectors. A thermal conductivity detector (TCD) was employed for the analysis of H_2, whereas a methanizer in series with a flame ionization detector (FID) was used for the detection of CO and hydrocarbons. Grade 5 Ar was used as the carrier gas. All potentials were converted to RHE at pH 0 and corrected by iR. Liquid products in the electrolyte were analyzed using a high performance liquid chromatograph (*Shimadzu, Nexera*) equipped with a *Shim-pack GIST C18-AQ* column that flushed with 5 mM H_2SO_4 at a flow rate of 0.5 mL/min and a *SPD-40* UV-Vis detector, for the analysis of carboxylic acids. Additionally, a gas chromatograph (*Shimadzu, GC-2030*), equipped with a *SH-Stabilwax* column and a FID detector was employed for the detection of alcohols and aldehydes. The Faradaic efficiency (FE) was calculated from the partial current for CO, that was derived from the CO yield and the total current, by averaging over the last 10 s before injection.

$$I_{\mathrm{CO}} = x_{\mathrm{CO}} \cdot z_{\mathrm{CO}} \cdot F \cdot \dot{n} \qquad\qquad FE\,[\%] = \frac{I_{\mathrm{CO}}}{I_{\mathrm{total}}} \cdot 100$$

With I_i: partial current, I_{total}: total current, x_i: volume fraction, z_i: number of electrons for the particular reaction, F: Faraday constant, $\dot{n}$: molar gas flow.

The relative gaseous product selectivity FS_i was calculated by dividing the partial current by the sum of the partial current of all considered products, here H_2 and CO, respectively.

$$FS_{\mathrm{i}}\,[\%] = \frac{x_{\mathrm{i}} \cdot z_{\mathrm{i}}}{\sum x_{\mathrm{i}} \cdot z_{\mathrm{i}}} \cdot 100$$

Cyclic voltammetry (CV) was measured in the same setup as used for the CO_2 reduction. The solution was saturated with CO_2 using a flow rate of 20 mL/min for 10 min. During the CV measurements, the flow was reduced to 5 mL/min in order to avoid perturbation in the measurements. The potential was swept in a window from -0.4 to -1.6 V *vs*. Ag/AgCl, using a scan rate of 10 mV/s.

Hydrogen evolution was performed in the same setup, but using Ar instead of CO_2 at a flow rate of 20 mL/min. The working electrode compartment was flushed for minimum 15 min with Ar before a potential was applied. The pH of the Ar purged electrolyte was determined to be 9.8.

Characterization methods

X-ray powder diffraction (XRPD) patterns were measured with a *Malvern PANanalytical Empyrean* device with *PixCel 1D* detector using Cu Kα irradiation with $\lambda_1 = 1.54046$ Å and $\lambda_2 = 1.54439$ Å. Hereby, acceleration voltage and emission current were set to 40 kV and 40 mA, respectively. To avoid X-ray fluorescence, pulse-height discrimination (PHD) settings were adjusted to 8.05 keV (lower level) and 11.27 keV (upper level). X-ray diffraction with Ag radiation was carried out with a STOE STADI P Mythen2 4K diffractometer equipped with a Ge(111) monochromator, Ag $K\alpha_1$ radiation with $\lambda = 0.5594$ Å and four Dectris MYTHEN2 R 1K strip detectors in Debye–Scherrer geometry (transmission).[1] The sample was sealed in a glass capillary (Hilgenberg, $\varnothing = 1$ mm).

Rietveld analysis was executed using the program *FullProf* (version September-20). The instrumental resolution was determined with a LaB_6 standard (*NIST SRM 660c*). For reflection modelling, the Thompson-Cox-Hastings pseudo-Voigt function was applied.[2] The background was modelled using a Chebychev polynomial. The Rietveld refinement was based on the crystallographic information file published by *Vaughan* and *Craig*.[3]

X-ray photoelectron (XP) spectra were collected on a *VersaProbe III Scanning XPS Microprobe* device (*Physical Electronics*) with a monochromatic Al Kα source. The survey scans were measured with a pass energy of 224 eV, a step size of 0.8 eV, and a step time of 50 ms per step. For high-resolution spectra in the S2p region, the pass energy was decreased to 26 eV, with a step size of 0.1 eV, and step time of 50 ms. The beam diameter was 100 μm for all measurements. During the measurements, samples were flooded with low energy electrons and argon ions, in order to prevent surface charging. Samples were not argon ion sputter-cleaned to prevent reduction of iron and nickel. Collected data points were evaluated with the program *CasaXPS* with Gaussian-Lorentzian (GL30) line shapes and Shirley backgrounds. Here, the C1s signal was set to 284.8 eV for charge correction.

Thermogravimetric (TG) analysis in synthetic air was performed with a *Netzsch Jupiter STA 449C* thermo-balance, which was additionally coupled with a *Netzsch Aeolos QMS 403C* quadrupol mass spectrometer (MS) for recording gaseous compounds, *i.e.* H_2O (18), CO_2 (44), and SO_2 (64).

Scanning electron microscopy (SEM) images were taken on a *Zeiss Leo 1530* instrument at an acceleration voltage of 3 kV. The working distance was set to approximately 5 mm. For the measurements, samples were placed on conductive carbon pads, before sputtering with Pt using a *Cressington Sputter Coater 208 HR*. SEM images were processed with the program *ImageJ 1.52a*. For energy-dispersive X-ray (EDX) spectroscopy with an UltraDry-EDX detector (model *Thermo Fisher Scientific 7*), acceleration voltage and working distance were changed to 15 kV and 8 mm, respectively.

Transmission electron microscopy (TEM) and selected area electron diffraction (SAED) were performed on a 200 kV *JEOL JEM-2200FS EFTEM*, equipped with Schottky FEG and In-Column Omega Energyfilter. For sample preparation, the powders were dispersed in ethanol (*Merck, LiChrosolv®, gradient grade for liquid chromatography*), before dropping a small amount onto a carbon film coated Cu TEM grid (200 Mesh). TEM images and SAED patterns were edited with *ImageJ 1.52a*.

Nitrogen physisorption isotherms were collected on a *QUADRASORB evo surface area & pore size analyzer* from *Anton Paar*. The measurement temperature was 77 K. Specific surface areas were calculated using the model from Brunauer, Emmett, and Teller (BET). Prior to the measurements, samples were pre-treated in vacuum at 100 °C for 6 hours. The program *ASiQwin 4.0®* was used for data evalution.

Volumetric H_2O vapor physisorption measurements were performed with the *ASiQMP-MP-AG setup* (*Anton Paar QuantaTec*, Boynton Beach, USA) at 20 °C and constant $p_0 = 2317.67$ Pa (17.384 Torr). Prior to the measurement, the samples were degassed at 100 °C for 6 h. *ASiQwin 4.0®* was used for data evaluation.

Additional data

Table S 1. Elemental composition of microwave-derived Ni_2FeS_4, estimated *via* X-ray photoelectron spectroscopy (XPS) and energy-dispersive X-ray (EDX) spectroscopy.

	C / at.%	O / at.%	S / at.%	Fe / at.%	Ni / at.%
XPS	27.3	31.4	26.5	5.1	9.7
EDXS	11.2	36.1	28.3	8.0	16.4

Table S 2. Carbon monoxide and hydrogen formation rates during electrochemical CO_2 reduction with Ni_2FeS_4-modified carbon paper working electrodes after a reaction period of 15 minutes, depending on the applied potential. Faradaic efficiencies (FE) and selectivities for CO evolution were calculated. Given values are averaged from different runs, allowing error calculations (standard error of the mean). For a potential of -0.7 V *vs*. RHE, only one run was performed.

Potential (RHE) / V	Faradaic efficiency / %	Selectivity / %	CO / µmol/h/mg	H_2 / µmol/h/mg
-0.6	4.73 (1.08)	4.58 (0.90)	0.016 (0.003)	0.335 (0.016)
-0.7	5.90 (0.37)	6.03 (0.41)	0.039 (0.004)	0.605 (0.057)
-0.8	4.44	4.31	0.048	1.074
-0.9	0.56 (0.06)	0.54 (0.06)	0.020 (0.005)	3.686 (0.200)

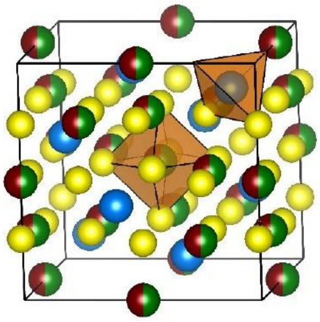

Figure S 1. Cubic inverse spinel-type crystal structure of Ni_2FeS_4. Yellow balls represent S^{2-}, brown ones Fe^{2+}, blue ones Ni^{3+} in tetrahedral sites, and green ones Ni^{3-} in octahedral sites.

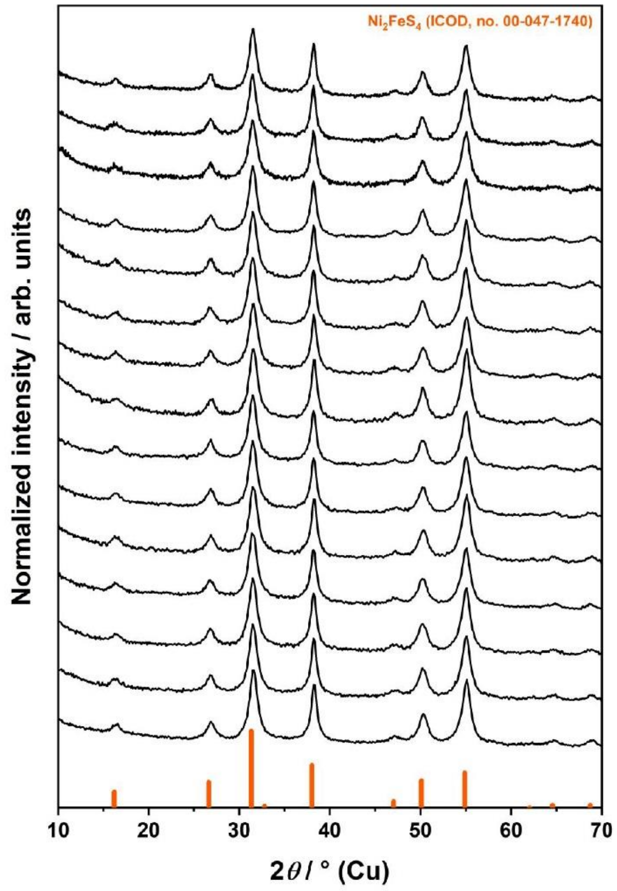

Figure S 2. Reproducibility of synthesis. X-ray powder diffraction (XRPD) patterns of synthesized Ni_2FeS_4 samples. The microwave-assisted synthesis was carried out 15 times to confirm reproducibility of the presented procedure.

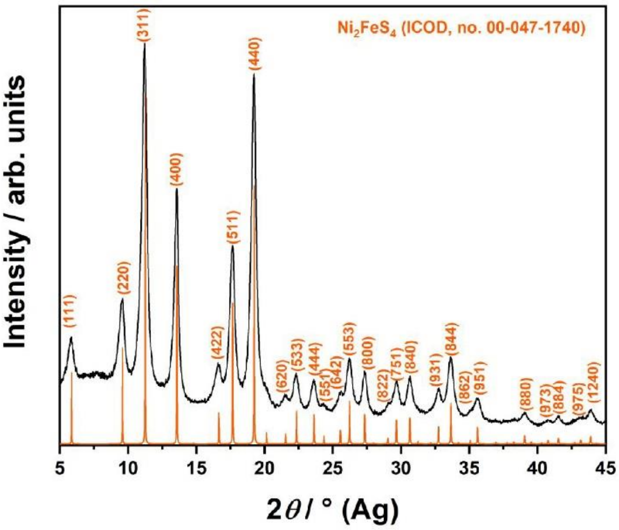

Figure S 3: X-ray powder diffraction (XRPD) pattern of phase-pure Ni_2FeS_4, measured with a silver tube.

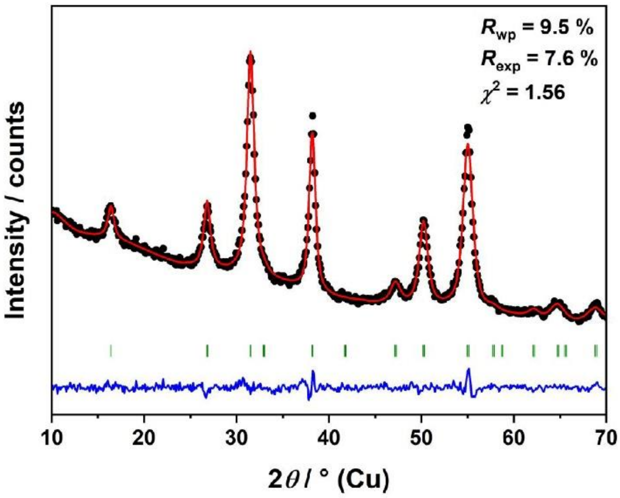

Figure S 4. Rietveld refinement of microwave-derived phase-pure Ni_2FeS_4 inverted thiospinel. Black dots indicate measured data points. The red line corresponds to the calculated pattern, while the blue line represents the difference between measured data and calculated pattern. Green signs further mark the theoretical reflection positions of Ni_2FeS_4.

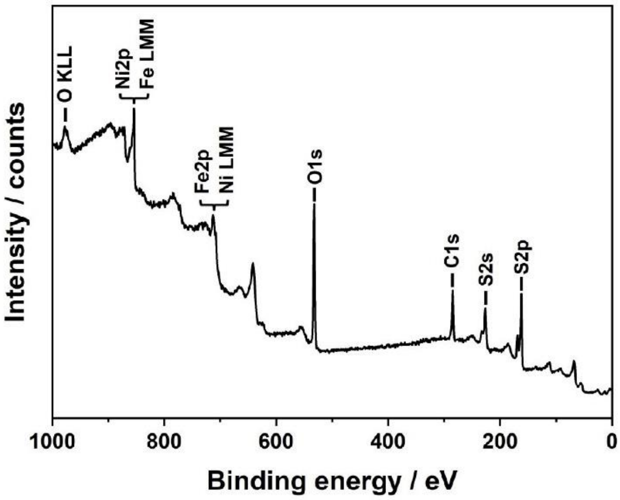

Figure S 5. Survey X-ray photoelectron spectrum of phase-pure Ni_2FeS_4 with assignments of most relevant XP spectroscopy signals.

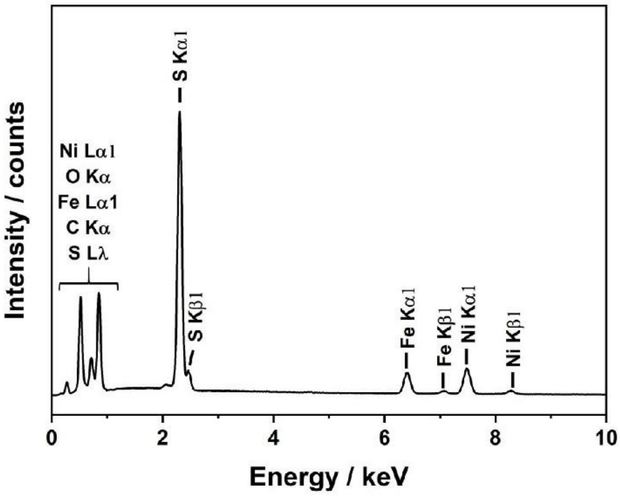

Figure S 6. Energy-dispersive X-ray (EDX) spectrum of phase-pure violarite with assignments of observed lines.

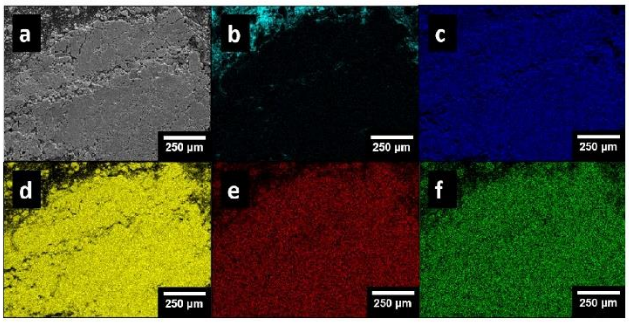

Figure S 7. (a) Large area scanning electron microscopy (SEM) image of Ni_2FeS_4 thiospinel. The area was used for energy-dispersive X-ray (EDX) spectroscopy elemental mapping of phase-pure Ni_2FeS_4 for carbon (b), oxygen (c), sulfur (d), iron (e), and nickel (f).

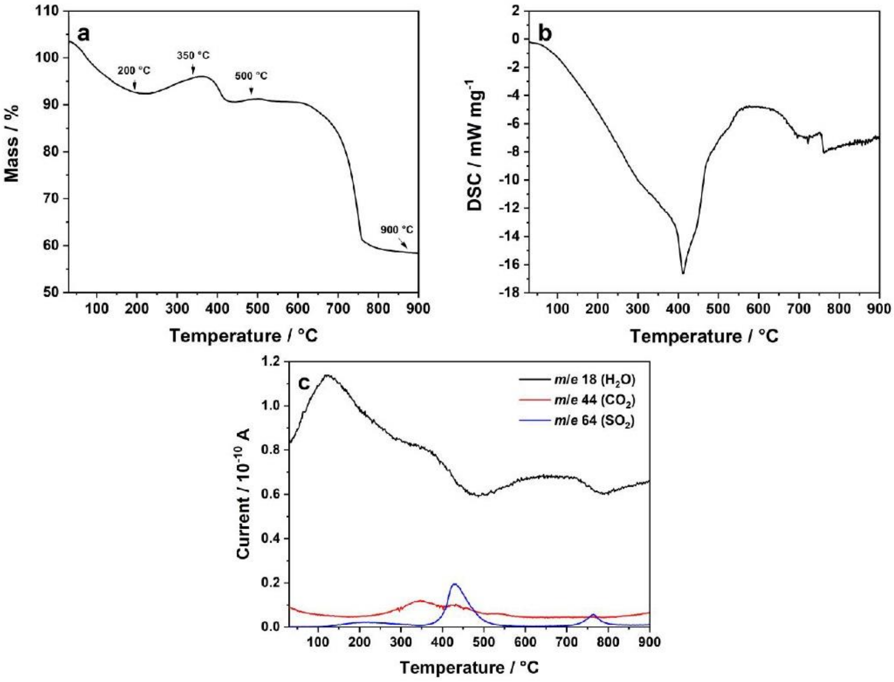

Figure S 8. (a) Thermogravimetric (TG) analysis, (b) differential scanning calorimetry (DSC) analysis, and (c) gas evolution curves during TG analysis, here monitored *via* mass spectrometry (MS). The experiment was performed in synthetic air with a heating rate of 5 °C min^{-1}.

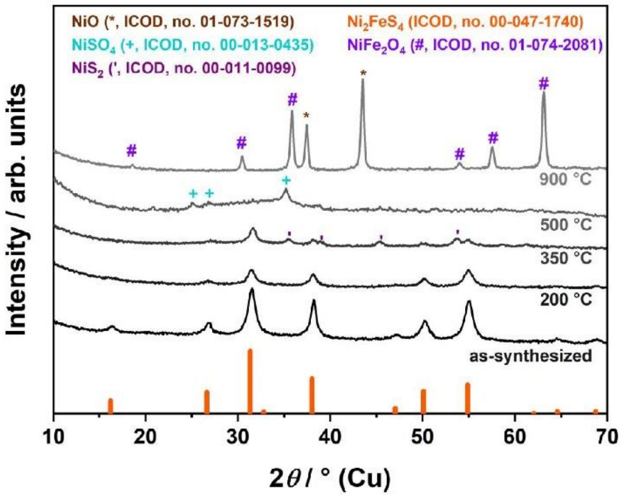

Figure S 9. X-ray powder diffraction (XRPD) patterns of calcined Ni_2FeS_4 powders. Heating experiments were performed in a muffle furnace under air atmosphere, with a heating ramp of 5 °C min^{-1} and 5 h holding time.

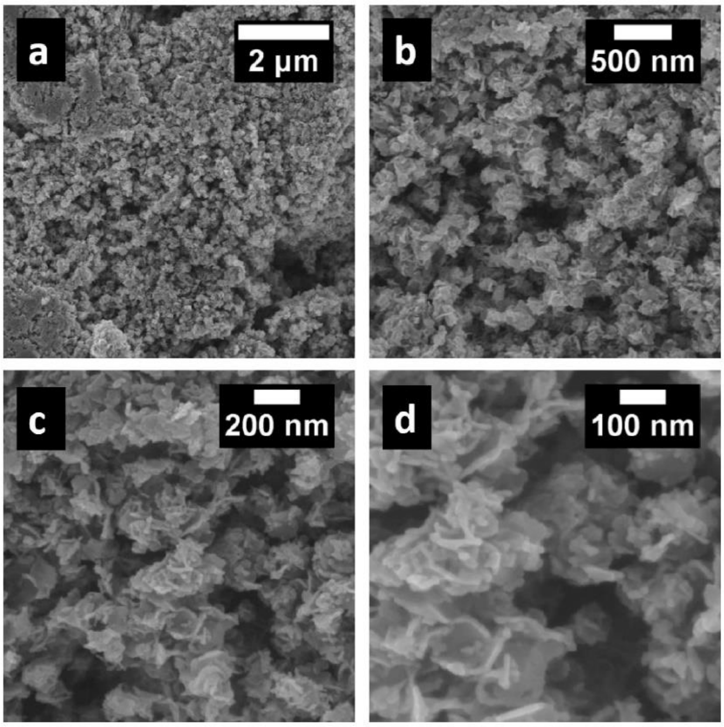

Figure S 10. Additional SEM images of microwave-derived Ni_2FeS_4 thiospinel nanosheets.

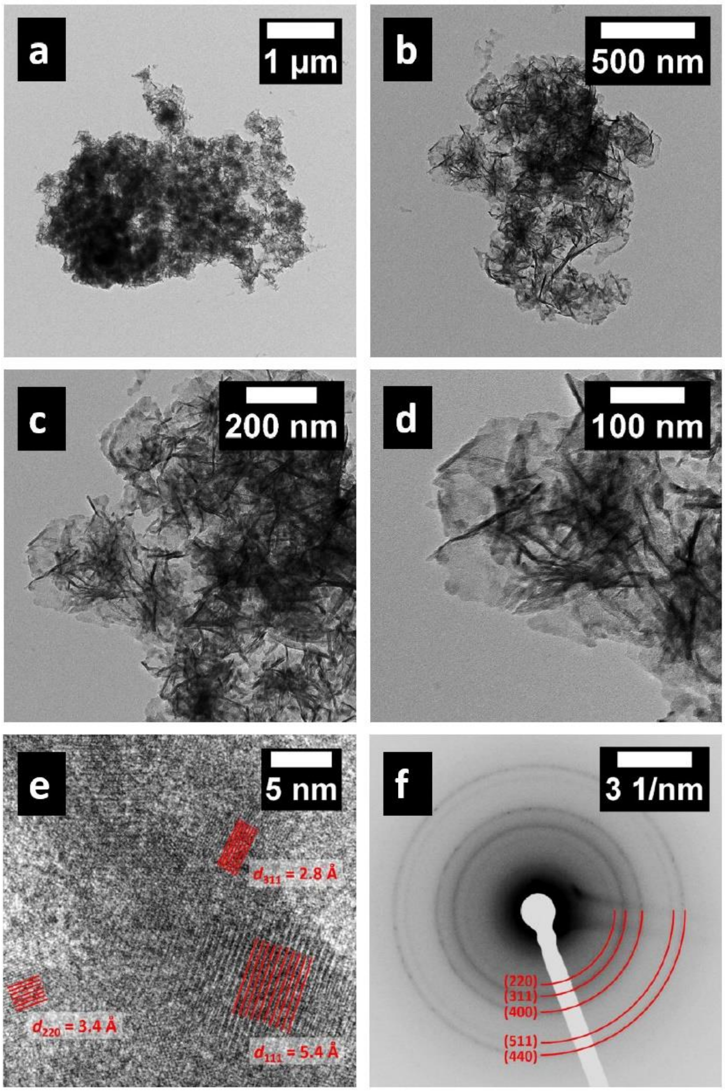

Figure S 11. (a-d) Additional LR-TEM images of microwave-derived Ni_2FeS_4 thiospinel nanosheets. A HR-TEM image is presented in (e), showing lattice planes of Ni_2FeS_4 (red marked). The SAED pattern of prepared nanosheets (f) exhibits rings, which consists of small dots. The rings could be assigned unambiguously to the (220), (311), (400), (511), and (440) reflections of spinel-type Ni_2FeS_4 (ICOD, no. 00-047-1740).

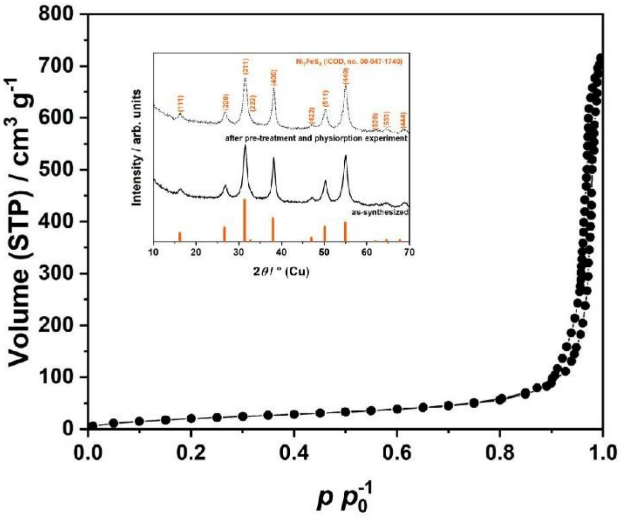

Figure S 12: Nitrogen physisorption isotherm of microwave-derived phase-pure Ni_2FeS_4, measured at 77 K. Sample was pre-treated at 100 °C for 6 h before the measurement to remove adsorbed water. BET evalution yields a specific surface area of 80 m^2 g^{-1}. To exclude any structural changes during N_2 physisorption analysis, XRPD pattern of the sample after the nitrogen physisorption analysis was measured (Inset).

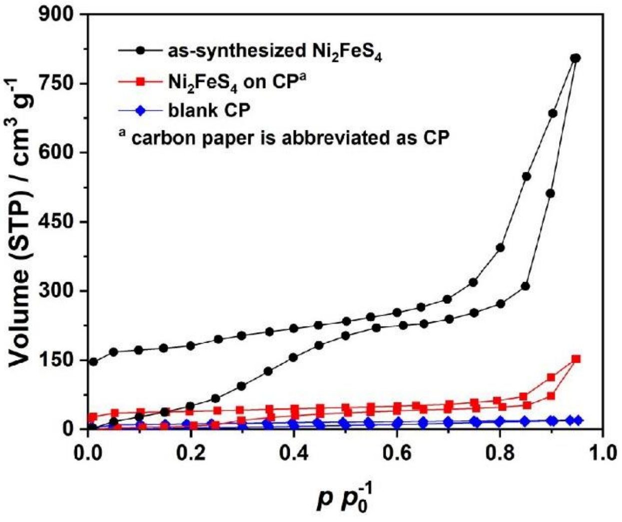

Figure S 13. Water vapor physisorption isotherms of microwave-derived Ni_2FeS_4, carbon paper modified with 2.2 mg cm^{-1} Ni_2FeS_4 and blank carbon paper as reference. The adsorbed volumes at 0.95 relative pressure are: 805 cm^3 g^{-1} (as-synthesized Ni_2FeS_4), 152 cm^3 g^{-1} (Ni_2FeS_4 on carbon paper), and 20 cm^3 g^{-1} (blank carbon paper).

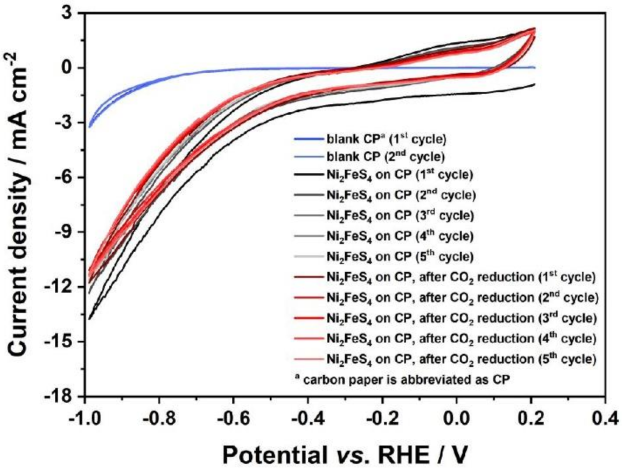

Figure S 14. Cyclic voltammetry (CV) responses of blank carbon paper and Ni_2FeS_4-modified carbon paper working electrodes, measured in 0.1M $KHCO_3$ with a scan rate of 10 mV s^{-1}. CV was also measured for Ni_2FeS_4-modified electrodes after five consecutive CO_2 reduction measurements (-0.7 V *vs*. RHE) for 15 min. Five cycles in succession were measured for each run. The electrolyte was continuously purged with CO_2 at a flow rate of 5 mL/min during the measurement.

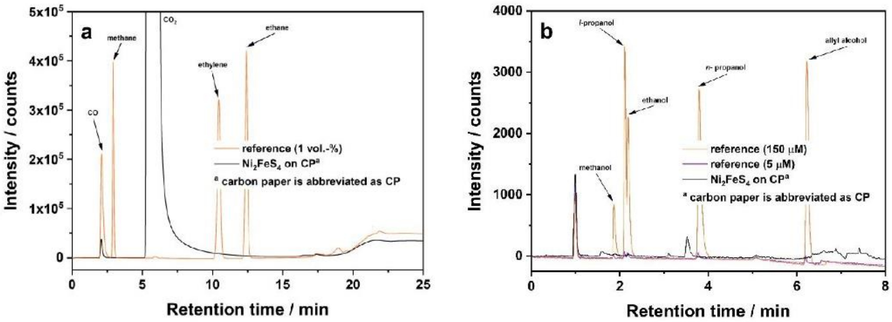

Figure S 15. Trace amount detection of methane and liquid-phase products (methanol, ethanol, *iso*-propanol) in the CO_2 electroreduction with Ni_2FeS_4 on carbon paper from CO_2-satured 0.1M $KHCO_3$ solution, measured *via* (a) gas chromatography (GC) and (b) liquid gas chromatography (LGC). Reference chromatograms for conceivable reaction products (gaseous and liquid) are included. Prior to the measurements, a constant potential of -0.9 V *vs*. RHE was applied for 15 minutes (GC) and for 1 h (LGC), respectively.

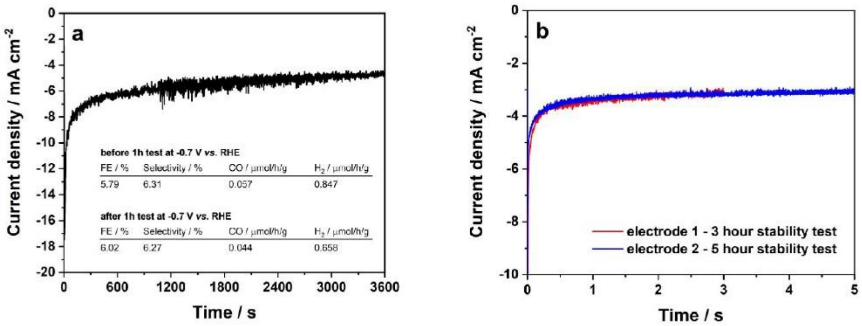

before 1h test at -0.7 V *vs.* RHE

FE / %	Selectivity / %	CO / µmol/h/g	H_2 / µmol/h/g
5.79	6.31	0.057	0.847

after 1h test at -0.7 V *vs.* RHE

FE / %	Selectivity / %	CO / µmol/h/g	H_2 / µmol/h/g
6.02	6.27	0.044	0.658

Figure S 16. (a) Chronoamperometric responses of a Ni_2FeS_4-modified carbon paper electrode measured for 60 minutes at a constant potential of -0.7 *vs*. RHE. Prior to this run, the same potential was applied for 15 min. At the end of first 15 min run and the second 60 minutes, gaseous reaction products were analyzed *via* GC. Faradaic efficiencies (FE) and selectivities for carbon monoxide were also calculated (inserted Table). (b) Additional chronoamperometric stability tests were conducted at -0.7 *vs*. RHE with two different Ni_2FeS_4-modified carbon paper electrodes. Here, the duration was extended to three and five hours, respectively. For electrode preparation, a fresh Nafion solution was used, containing more binder. Thereby, the adhesion of the catalyst layer was improved, enabling longer reaction periods, while concurrently the current density decreased, due to the lower conductivity and reduced number of active sites.

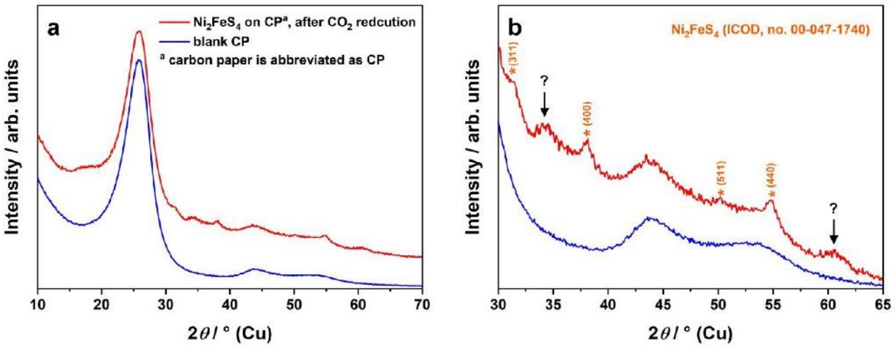

Figure S 17. (a) X-ray diffraction patterns of blank carbon paper and Ni_2FeS_4-modified carbon paper electrodes, measured after electrochemical 15 min CO_2 reduction experiments at a negative applied potentials of -0.6/-0.7 V *vs*. RHE and (b) enlarged view of same XRD patterns. Electrode was prepared with a catalyst loading of 4.3 mg cm^{-2}. After the CO_2 reduction with Ni_2FeS_4 on carbon paper, two broad reflections appear arise at 34.2 and 60.5 ° 2θ, which cannot be assigned to thiospinel Ni_2FeS_4, while all other reflections can be assigned to (311), (400), (511), and (440) reflections of Ni_2FeS_4. However, reflections at 34.2 and 60.5 ° 2θ cannot assigned unambiguously due to the low intensity.

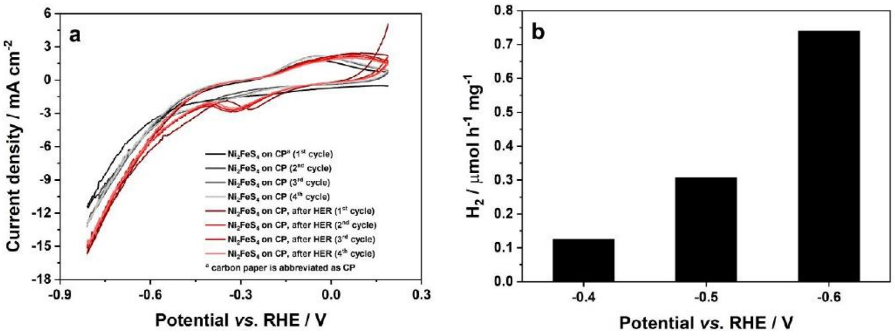

Figure S 18. Hydrogen evolution experiments with Ni_2FeS_4 nanosheets. (a) Cyclic voltammetry (CV) responses of Ni_2FeS_4-modified carbon paper working electrodes, measured in 0.1M $KHCO_3$ with a scan rate of 10 mV s^{-1}. The electrolyte was constantly purged with Ar gas (20 mL min^{-1}). CV was also measured for Ni_2FeS_4-modified electrodes after chronoamperometry at -0.7 V *vs*. RHE for 1h. Four cycles in succession were measured for each run. The overpotential for the HER is clearly lower than for the CO2RR. The evolving reduction peak might perhaps be attributed to a slow reduction of Ni(III) over the course of the measurement, possibly alongside hydroxide formation that is favoured at higher pH (compared to that of the CO2RR).[4] Alternatively, it could be a result of changes in the electrolyte composition due to partial conversion of HCO_3^- to CO_2 and changes in the solution pH. (b) H_2 evolution rates after a reaction period of 15 min.

Additional literature

(1) Thomae, S. L. J.; Prinz, N.; Hartmann, T.; Teck, M.; Correll, S.; Zobel, M. Pushing Data Quality for Laboratory Pair Distribution Function Experiments. *Rev. Sci. Instrum.* **2019**, *90* (4), 043905. https://doi.org/10.1063/1.5093714.

(2) Thompson, P.; Cox, D. E.; Hastings, J. B. Rietveld Refinement of Debye–Scherrer Synchrotron X-Ray Data from Al2O3. *J. Appl. Crystallogr.* **1987**, *20* (2), 79–83. https://doi.org/10.1107/S0021889887087090.

(3) Vaughan, D. J.; Craig, J. R. The Crystal Chemistry of Iron-Nickel Thiospinels. *Am. Mineral.* **1985**, *70* (9–10), 1036–1043.

(4) Zakaria, S. N. A.; Hollingsworth, N.; Islam, H. U.; Roffey, A.; Santos-Carballal, D.; Roldan, A.; Bras, W.; Sankar, G.; Hogarth, G.; Holt, K. B.; de Leeuw, N. H. Insight into the Nature of Iron Sulfide Surfaces During the Electrochemical Hydrogen Evolution and CO2 Reduction Reactions. *ACS Appl. Mater. Interfaces* **2018**, *10* (38), 32078–32085. https://doi.org/10.1021/acsami.8b08612.

4. Bibliographie

[1] M. E. Schlesinger, *Int. J. Environ. Stud.* **1983**, *20*, 103–114.

[2] R. E. Zeebe, A. Ridgwell, J. C. Zachos, *Nat. Geosci.* **2016**, *9*, 325–329.

[3] BP, *Statistical Review of World Energy* **2022**.

[4] *https://ourworldindata.org/energy-mix* **2022**, 05.07.2022, 19:46 Uhr.

[5] J. Rockström, O. Gaffney, J. Rogelj, M. Meinshausen, N. Nakicenovic, H. J. Schellnhuber, *Science* **2017**, *355*, 1269–1271.

[6] *https://www.smard.de/home* **2022**, 05.07.2022, 19:01 Uhr.

[7] H. Schüle, *Stromproduktion und Stromverbrauch im Jahre 2021 der Bundesrepublik Deutschland* **2021**.

[8] N. Khan, S. Dilshad, R. Khalid, A. R. Kalair, N. Abas, *Energy Storage* **2019**, *1*, 1–49.

[9] G. Eisenbeiß, *Phys. unserer Zeit* **2005**, *36*, 135–140.

[10] *https://www.wissenschaft.de/allgemein/energiedichte-verschiedener-kraftstoffe* **2022**, 14.04.2022, 10:17 Uhr.

[11] A. Züttel, *Mater. Today* **2003**, *6*, 24–33.

[12] A. Züttel, P. Wenger, S. Rentsch, P. Sudan, P. Mauron, C. Emmenegger, *J. Power Sources* **2003**, *118*, 1–7.

[13] J. Andersson, S. Grönkvist, *Int. J. Hydrogen Energy* **2019**, *44*, 11901–11919.

[14] M. Ball, M. Weeda, *Int. J. Hydrog. Energy* **2015**, *40*, 7903–7919.

[15] T. L. LeValley, A. R. Richard, M. Fan, *Int. J. Hydrogen Energy* **2014**, *39*, 16983–17000.

[16] M. Wang, Z. Wang, X. Gong, Z. Guo, *Renew. Sustain. Energy Rev.* **2014**, *29*, 573–588.

[17] S. Fürnsinn, H. Hofbauer, *Chem. Ing. Tech.* **2007**, *79*, 579–590.

[18] M. E. Royer, *Comptes rendus l'Académie des Sci.* **1870**, *70*, 731–735.

[19] M.-Y. Lee, K. T. Park, W. Lee, H. Lim, Y. Kwon, S. Kang, *Crit. Rev. Environ. Sci. Technol.* **2020**, *50*, 769–815.

[20] Q. Lu, F. Jiao, *Nano Energy* **2016**, *29*, 439–456.

[21] K. Chan, *Nat. Commun.* **2020**, *11*, 5954.

[22] M. Todoroki, K. Hara, A. Kudo, T. Sakata, *J. Electroanal. Chem.* **1995**, *394*, 199–203.

[23] A. Vasileff, X. Zhi, C. Xu, L. Ge, Y. Jiao, Y. Zheng, S.-Z. Qiao, *ACS Catal.* **2019**, *9*, 9411–9417.

[24] R. J. Hill, J. R. Craig, G. V. Gibbs, *Phys. Chem. Miner.* **1979**, *4*, 317–339.

[25] D. H. Taffa, R. Dillert, A. C. Ulpe, K. C. L. Bauerfeind, T. Bredow, D. W. Bahnemann, M. Wark, *J. Photonics Energy* **2016**, *7*, 012009.

[26] D. Carta, M. F. Casula, A. Falqui, D. Loche, G. Mountjoy, C. Sangregorio, A. Corrias, *J. Phys. Chem. C* **2009**, *113*, 8606–8615.

[27] G. A. Sawatzky, F. Van Der Woude, A. H. Morrish, *Phys. Rev.* **1969**, *187*, 747–757.

[28] A. V. Humbe, S. D. Birajdar, J. M. Bhandari, N. N. Waghule, V. R. Bhagwat, K. M. Jadhav, *AIP Conf. Proc.* **2015**, *1665*, 050138.

[29] G. Xian, S. Kong, Q. Li, G. Zhang, N. Zhou, H. Du, L. Niu, *Front. Chem.* **2020**, *8*, 1–11.

[30] U. Lüders, A. Barthélémy, M. Bibes, K. Bouzehouane, S. Fusil, E. Jacquet, J.-P. Contour, J.-F. Bobo, J. Fontcuberta, A. Fert, *Adv. Mater.* **2006**, *18*, 1733–1736.

[31] Z. Li, S. X. Wang, Q. Sun, H. L. Zhao, H. Lei, M. B. Lan, Z. X. Cheng, X. L. Wang, S. X. Dou, G. Q. Max Lu, *Adv. Healthc. Mater.* **2013**, *2*, 958–964.

[32] D. Makovec, A. Košak, A. Žnidaršič, M. Drofenik, *J. Magn. Magn. Mater.* **2005**, *289*, 32–35.

[33] C. Chen, *Magnetism and Metallurgy of Soft Magnetic Materials*, Dover Publications, Inc., New York, **1986**.

[34] C. M. Sorensen, K. J. Klabunde, *Nanoscale Materials in Chemistry*, John Wiley & Sons, Inc., New York, **2001**.

[35] V. Tsurkan, H.-A. Krug von Nidda, J. Deisenhofer, P. Lunkenheimer, A. Loidl, *Phys. Rep.* **2021**, *926*, 1–86.

[36] C. R. Vestal, Z. J. Zhang, *ChemInform* **2004**, *35*, 240–263.

[37] M. L. Néel, *Ann. Phys.* **1948**, *12*, 137–198.

[38] D. S. Mathew, R.-S. Juang, *Chem. Eng. J.* **2007**, *129*, 51–65.

[39] S. E. Shirsath, S. S. Jadhav, B. G. Toksha, S. M. Patange, K. M. Jadhav, *J. Appl. Phys.* **2011**, *110*, 013914.

[40] A. Berkowitz, J. Lahut, C. VanBuren, *IEEE Trans. Magn.* **1980**, *16*, 184–190.

[41] A. Ceylan, S. Ozcan, C. Ni, S. Ismat Shah, *J. Magn. Magn. Mater.* **2008**, *320*, 857–863.

[42] M. Y. Rafique, M. Ellahi, M. Z. Iqbal, Q. Javed, L. Pan, *Mater. Lett.* **2016**, *162*, 269–272.

[43] V. Šepelák, I. Bergmann, A. Feldhoff, P. Heitjans, F. Krumeich, D. Menzel, F. J. Litterst, S. J. Campbell, K. D. Becker, *J. Phys. Chem. C* **2007**, *111*, 5026–5033.

[44] F. Majid, J. Rauf, S. Ata, I. Bibi, A. Malik, S. M. Ibrahim, A. Ali, M. Iqbal, *Mater. Chem. Phys.* **2021**, *258*, 123888.

[45] J. Jacob, M. A. Khadar, *J. Appl. Phys.* **2010**, *107*, 114310.

[46] A. Pring, C. Tenailleau, B. Etschmann, J. Brugger, B. Grguric, *Regolith* **2005**, 252–255.

[47] C. C. L. McCrory, S. Jung, J. C. Peters, T. F. Jaramillo, *J. Am. Chem. Soc.* **2013**, *135*, 16977–16987.

[48] S. Mehrabani, J. P. Singh, R. Bagheri, A. G. Wattoo, Z. Song, K. H. Chae, M. M. Najafpour, *Nanoscale Adv.* **2019**, *1*, 686–695.

[49] M. B. Askari, P. Salarizadeh, *Int. J. Hydrogen Energy* **2020**, *45*, 27482–27491.

[50] G. Rekhila, Y. Bessekhouad, M. Trari, *Int. J. Hydrogen Energy* **2013**, *38*, 6335–6343.

[51] C. Jia, Y. Zhang, Q. Kong, Q. Wang, G. Chen, H. T. Guam, C. Dong, *J. Mater. Sci. Mater. Electron.* **2020**, *31*, 6000–6007.

[52] J. M. Hastings, L. M. Corliss, *Phys. Rev.* **1956**, *104*, 328–331.

[53] K. Vamvakidis, M. Katsikini, D. Sakellari, E. C. Paloura, O. Kalogirou, C. Dendrinou-Samara, *Dalton Trans.* **2014**, *43*, 12754–12765.

[54] M. Muroi, R. Street, P. G. McCormick, J. Amighian, *Phys. Rev. B* **2001**, *63*, 184414.

[55] J.-R. Huang, C. Cheng, *J. Appl. Phys.* **2013**, *113*, 033912.

[56] G. Balaji, N. S. Gajbhiye, G. Wilde, J. Weissmüller, *J. Magn. Magn. Mater.* **2002**, *242–245*, 617–620.

[57] M. Zheng, X. C. Wu, B. S. Zou, Y. J. Wang, *J. Magn. Magn. Mater.* **1998**, *183*, 152–156.

[58] Z. X. Tang, C. M. Sorensen, K. J. Klabunde, G. C. Hadjipanayis, *Phys. Rev. Lett.* **1991**, *67*, 3602–3605.

[59] A. Bloesser, H. Kurz, J. Timm, F. Wittkamp, C. Simon, S. Hayama, B. Weber, U.-P. Apfel, R. Marschall, *ACS Appl. Nano Mater.* **2020**, *3*, 11587–11599.

[60] V. Šepelák, I. Bergmann, D. Menzel, A. Feldhoff, P. Heitjans, F. J. Litterst, K. D. Becker, *J. Magn. Magn.*

Mater. **2007**, *316*, 764–767.

[61] S. Maensiri, M. Sangmanee, A. Wiengmoon, *Nanoscale Res. Lett.* **2009**, *4*, 221–228.

[62] G. F. Goya, T. S. Berquó, F. C. Fonseca, M. P. Morales, *J. Appl. Phys.* **2003**, *94*, 3520–3528.

[63] O. Schneeweiss, R. Zboril, N. Pizurova, M. Mashlan, E. Petrovsky, J. Tucek, *Nanotechnology* **2006**, *17*, 607–616.

[64] D. H. Han, J. P. Wang, H. L. Luo, *J. Magn. Magn. Mater.* **1994**, *136*, 176–182.

[65] R. Pauthenet, *Ann. Phys.* **1952**, *12*, 710–747.

[66] M. P. Gonzalez-Sandoval, A. M. Beesley, M. Miki-Yoshida, L. Fuentes-Cobas, J. A. Matutes-Aquino, *J. Alloys Compd.* **2004**, *369*, 190–194.

[67] T. Pandiarajan, S. Ravichandran, L. J. Berchmans, *RSC Adv.* **2014**, *4*, 64364–64370.

[68] Y. Zhou, Y. Du, S. Xi, Z. J. Xu, *Electrocatalysis* **2018**, *9*, 287–292.

[69] F. Jiang, X. Du, S. Zhao, J. Guo, B. Huang, X. Huang, Q. Su, J. Zhang, G. Du, *J. Nanoparticle Res.* **2015**, *17*, 173.

[70] J. H. L. Beal, S. Prabakar, N. Gaston, G. B. Teh, P. G. Etchegoin, G. Williams, R. D. Tilley, *Chem. Mater.* **2011**, *23*, 2514–2517.

[71] D. Santos-Carballal, A. Roldan, R. Grau-Crespo, N. H. De Leeuw, *Phys. Rev. B* **2015**, *91*, 1–13.

[72] X. Zheng, J. Jiang, T. Bi, F. Jin, M. Li, *ACS Appl. Energy Mater.* **2021**, *4*, 3288–3296.

[73] C. S. Kim, J. Childress, C. L. Chien, *J. Appl. Phys.* **1988**, *64*, 5886–5888.

[74] S. Haider, R. Grau-Crespo, A. J. Devey, N. H. De Leeuw, *Geochim. Cosmochim. Acta* **2012**, *88*, 275–282.

[75] C. Tenailleau, B. Etschmann, R. M. Ibberson, A. Pring, *Am. Mineral.* **2006**, *91*, 1442–1447.

[76] H. Dobbek, V. Svetlitchnyi, L. Gremer, R. Huber, O. Meyer, *Science* **2001**, *293*, 1281–1285.

[77] S. Piontek, K. junge Puring, D. Siegmund, M. Smialkowski, I. Sinev, D. Tetzlaff, B. Roldan Cuenya, U.-P. Apfel, *Chem. Sci.* **2019**, *10*, 1075–1081.

[78] A. Yamaguchi, M. Yamamoto, K. Takai, T. Ishii, K. Hashimoto, R. Nakamura, *Electrochim. Acta* **2014**, *141*, 311–318.

[79] T. F. Yi, T. T. Wei, J. Mei, W. Zhang, Y. Zhu, Y. G. Liu, S. Luo, H. Liu, Y. Lu, Z. Guo, *Adv. Sustain. Syst.* **2020**, *4*, 1900137.

[80] S. Thirumaran, G. Gurumoorthy, R. Arulmozhi, S. Ciattini, *Appl. Organomet. Chem.* **2020**, *34*, 5761.

[81] J. Shen, J. Ji, P. Dong, R. Baines, Z. Zhang, P. M. Ajayan, M. Ye, *J. Mater. Chem. A* **2016**, *4*, 8844–8850.

[82] P. Karthick Kannan, B. Dinesh, C. Y. An, C.-H. Chung, *ChemistrySelect* **2017**, *2*, 1967–1973.

[83] T. E. Warner, N. M. Rice, N. Taylor, *Hydrometallurgy* **1996**, *41*, 107–118.

[84] A. J. Bard, L. R. Faulkner, *Electrochemical Methods - Fundamentals and Applications*, New York, **2001**.

[85] M. Zeng, Y. Li, *J. Mater. Chem. A* **2015**, *3*, 14942–14962.

[86] A. Paets van Troostwijk, J. R. Deimann, *J. Phys.* **1790**, *2*, 130–141.

[87] G. Sandstede, *Chem. Ing. Tech.* **1991**, *63*, 575–592.

[88] A. Eftekhari, *Mater. Today Energy* **2017**, *5*, 37–57.

[89] M. Tahir, L. Pan, F. Idrees, X. Zhang, L. Wang, J.-J. Zou, Z. L. Wang, *Nano Energy* **2017**, *37*, 136–157.

[90] J. Kibsgaard, T. F. Jaramillo, *Angew. Chem. Int. Ed.* **2014**, *53*, 14433–14437.

[91] W. Hu, Q. Shi, Z. Chen, H. Yin, H. Zhong, P. Wang, *ACS Appl. Mater. Interfaces* **2021**, *13*, 8337–8343.

[92] C. C. L. McCrory, S. Jung, I. M. Ferrer, S. M. Chatman, J. C. Peters, T. F. Jaramillo, *J. Am. Chem. Soc.* **2015**, *137*, 4347–4357.

[93] D. H. Kweon, M. S. Okyay, S.-J. Kim, J.-P. Jeon, H.-J. Noh, N. Park, J. Mahmood, J.-B. Baek, *Nat. Commun.* **2020**, *11*, 1278.

[94] H. J. Song, H. Yoon, B. Ju, D. Kim, *Adv. Energy Mater.* **2021**, *11*, 2002428.

[95] L. Yang, G. Yu, X. Ai, W. Yan, H. Duan, W. Chen, X. Li, T. Wang, C. Zhang, X. Huang, J.-S. Chen, X. Zou, *Nat. Commun.* **2018**, *9*, 5236.

[96] X. Miao, L. Zhang, L. Wu, Z. Hu, L. Shi, S. Zhou, *Nat. Commun.* **2019**, *10*, 3809.

[97] C. C. L. McCrory, S. Jung, J. C. Peters, T. F. Jaramillo, *J. Am. Chem. Soc.* **2013**, *135*, 16977–16987.

[98] M. Gong, H. Dai, *Nano Res.* **2015**, *8*, 23–39.

[99] C. E. Frey, P. Kurz, *Chem. Eur. J.* **2015**, *21*, 14958–14968.

[100] F. Švegl, B. Orel, I. Grabec-Švegl, V. Kaučič, *Electrochim. Acta* **2000**, *45*, 4359–4371.

[101] Y. Yang, Y. Xiong, M. E. Holtz, X. Feng, R. Zeng, G. Chen, F. J. DiSalvo, D. A. Muller, H. D. Abruña, *Proc. Natl. Acad. Sci. U.S.A.* **2019**, *116*, 24425–24432.

[102] T. Priamushko, R. Guillet-Nicolas, M. Yu, M. Doyle, C. Weidenthaler, H. Tüysüz, F. Kleitz, *ACS Appl. Energy Mater.* **2020**, *3*, 5597–5609.

[103] C. Guo, Y. Shi, S. Lu, Y. Yu, B. Zhang, *Chinese J. Catal.* **2021**, *42*, 1287–1296.

[104] I. Terashima, S. Yanagisawa, H. Sakakibara, *Plant Cell Physiol.* **2014**, *55*, 237–240.

[105] *https://www.co2.earth/daily-co2* **2022**, 15.07.2022, 16:18 Uhr.

[106] R. F. Keeling, C. D. Keeling, *Atmospheric Monthly In Situ CO2 Data - Mauna Loa Observatory, Hawaii. In Scripps CO2 Program Data. UC San Diego Library Digital Collections*, **2017**.

[107] W. Steffen, J. Rockström, K. Richardson, T. M. Lenton, C. Folke, D. Liverman, C. P. Summerhayes, A. D. Barnosky, S. E. Cornell, M. Crucifix, J. F. Donges, I. Fetzer, S. J. Lade, M. Scheffer, R. Winkelmann, H. J. Schellnhuber, *Proc. Natl. Acad. Sci. U.S.A.* **2018**, *115*, 8252–8259.

[108] X. Zhang, S.-X. Guo, K. A. Gandionco, A. M. Bond, J. Zhang, *Mater. Today Adv.* **2020**, *7*, 100074.

[109] W. Zhang, Y. Hu, L. Ma, G. Zhu, Y. Wang, X. Xue, R. Chen, S. Yang, Z. Jin, *Adv. Sci.* **2018**, *5*, 1700275.

[110] H. Kim, H. S. Jeon, M. S. Jee, E. B. Nursanto, J. P. Singh, K. Chae, Y. J. Hwang, B. K. Min, *ChemSusChem* **2016**, *9*, 2097–2102.

[111] W. Luo, Q. Zhang, J. Zhang, E. Moioli, K. Zhao, A. Züttel, *Appl. Catal. B Environ.* **2020**, *273*, 119060.

[112] T. Yuan, Z. Hu, Y. Zhao, J. Fang, J. Lv, Q. Zhang, Z. Zhuang, L. Gu, S. Hu, *Nano Lett.* **2020**, *20*, 2916–2922.

[113] X. Yao, Y. Guo, B. Liu, P. Wang, J. Sun, W. Li, C. Zhao, *ChemElectroChem* **2021**, *8*, 592–602.

[114] Z. Tao, Z. Wu, Y. Wu, H. Wang, *ACS Catal.* **2020**, *10*, 9271–9275.

[115] M. Le, M. Ren, Z. Zhang, P. T. Sprunger, R. L. Kurtz, J. C. Flake, *J. Electrochem. Soc.* **2011**, *158*, E45.

[116] D. Karapinar, C. E. Creissen, J. G. Rivera de la Cruz, M. W. Schreiber, M. Fontecave, *ACS Energy Lett.* **2021**, *6*, 694–706.

[117] S. Y. Lee, H. Jung, N.-K. Kim, H.-S. Oh, B. K. Min, Y. J. Hwang, *J. Am. Chem. Soc.* **2018**, *140*, 8681–8689.

[118] J. Wu, S. Ma, J. Sun, J. I. Gold, C. Tiwary, B. Kim, L. Zhu, N. Chopra, I. N. Odeh, R. Vajtai, A. Z. Yu, R. Luo, J. Lou, G. Ding, P. J. A. Kenis, P. M. Ajayan, *Nat. Commun.* **2016**, *7*, 13869.

[119] H. Mistry, A. S. Varela, S. Kühl, P. Strasser, B. R. Cuenya, *Nat. Rev. Mater.* **2016**, *1*, 16009.

[120] X. Zhang, X. Cheng, Q. Zhang, *J. Energy Chem.* **2016**, *25*, 967–984.

[121] C. Joachim, *Nat. Mater.* **2005**, *4*, 107–109.

[122] G. Garnweitner, M. Niederberger, *J. Am. Ceram. Soc.* **2006**, *89*, 1801–1808.

[123] M. Thommes, K. Kaneko, A. V. Neimark, J. P. Olivier, F. Rodriguez-Reinoso, J. Rouquerol, K. S. W. Sing, *Pure Appl. Chem.* **2015**, *87*, 1051–1069.

[124] B. Zdravkov, J. Čermák, M. Šefara, J. Janků, *Open Chem.* **2007**, *5*, 385–395.

[125] N. Ortiz Peña, D. Ihiawakrim, M. Han, B. Lassalle-Kaiser, S. Carenco, C. Sanchez, C. Laberty-Robert, D. Portehault, O. Ersen, *ACS Nano* **2019**, *13*, 11372–11381.

[126] Y. Wang, T. Zhou, K. Jiang, P. Da, Z. Peng, J. Tang, B. Kong, W. Bin Cai, Z. Yang, G. Zheng, *Adv. Energy Mater.* **2014**, *4*, 1–7.

[127] M. Zhen, B. Zhou, Y. Ren, *Front. Environ. Sci. Eng.* **2013**, *7*, 341–355.

[128] J. Timm, R. Marschall, *Adv. Sustain. Syst.* **2018**, *2*, 1700170.

[129] W. Li, D. Zhao, *Chem. Commun.* **2013**, *49*, 943–946.

[130] H. Yen, Y. Seo, R. Guillet-Nicolas, S. Kaliaguine, F. Kleitz, *Chem. Commun.* **2011**, *47*, 10473–10475.

[131] F. Schüth, *Angew. Chem. Int. Ed.* **2003**, *42*, 3604–3622.

[132] N. Pal, A. Bhaumik, *Adv. Colloid Interface Sci.* **2013**, *189–190*, 21–41.

[133] Y. Shi, Y. Wan, D. Zhao, *Chem. Soc. Rev.* **2011**, *40*, 3854.

[134] A. V Kabanov, E. V Batrakova, V. Y. Alakhov, *J. Control. Release* **2002**, *82*, 189–212.

[135] G. Wanka, H. Hoffmann, W. Ulbricht, *Macromolecules* **1994**, *27*, 4145–4159.

[136] A. Pitto-Barry, N. P. E. Barry, *Polym. Chem.* **2014**, *5*, 3291–3297.

[137] Y. Zheng, J. Liu, J. Liang, M. Jaroniec, S. Z. Qiao, *Energy Environ. Sci.* **2012**, *5*, 6717.

[138] D. Gu, F. Schüth, *Chem. Soc. Rev.* **2014**, *43*, 313–344.

[139] M. Bernicke, B. Eckhardt, A. Lippitz, E. Ortel, D. Bernsmeier, R. Schmack, R. Kraehnert, *ChemistrySelect* **2016**, *1*, 482–489.

[140] B. Eckhardt, E. Ortel, D. Bernsmeier, J. Polte, P. Strasser, U. Vainio, F. Emmerling, R. Kraehnert, *Chem. Mater.* **2013**, *25*, 2749–2758.

[141] K. Kirchberg, A. Becker, A. Bloesser, T. Weller, J. Timm, C. Suchomski, R. Marschall, *J. Phys. Chem. C* **2017**, *121*, 27126–27138.

[142] A. V. Nikam, B. L. V. Prasad, A. A. Kulkarni, *CrystEngComm* **2018**, *20*, 5091–5107.

[143] R. Krishnakanth, G. Jayakumar, A. Albert Irudayaraj, A. Dhayal Raj, *Mater. Today Proc.* **2016**, *3*, 1370–1377.

[144] D.-S. Wang, T. Xie, Q. Peng, S.-Y. Zhang, J. Chen, Y.-D. Li, *Chem. Eur. J.* **2008**, *14*, 2507–2513.

[145] D. Chen, R. Xu, *Mater. Res. Bull.* **1998**, *33*, 1015–1021.

[146] I. Bilecka, M. Niederberger, *Nanoscale* **2010**, *2*, 1358–1374.

[147] L. Zhang, G. Garnweitner, I. Djerdj, M. Antonietti, M. Niederberger, *Chem. – An Asian J.* **2008**, *3*, 746–752.

[148] R. Deshmukh, M. Niederberger, *Chem. Eur. J.* **2017**, *23*, 8542–8570.

[149] C. Suchomski, B. Breitung, R. Witte, M. Knapp, S. Bauer, T. Baumbach, C. Reitz, T. Brezesinski, *Beilstein J. Nanotechnol.* **2016**, *7*, 1350–1360.

[150] P. Dolcet, K. Kirchberg, A. Antonello, C. Suchomski, R. Marschall, S. Diodati, R. Muñoz-Espí, K. Landfester, S. Gross, *Inorg. Chem. Front.* **2019**, *6*, 1527–1534.

[151] B. Ludi, I. Olliges-Stadler, M. D. Rossell, M. Niederberger, *Chem. Commun.* **2011**, *47*, 5280–5282.

[152] E. Riedel, *Anorganische Chemie*, 3. Auflage, De Gruyter, Berlin, **1994**.

[153] M. J. Winter, *J. Chem. Educ.* **2011**, *88*, 1507–1510.

[154] *https://institut-seltene-erden.de/seltene-erden-und-metalle/basismetalle/nickel* **2022**, 16.07.2022, 17:20 Uhr.

[155] M. Thommes, K. Kaneko, A. V. Neimark, J. P. Olivier, F. Rodriguez-Reinoso, J. Rouquerol, K. S. W. Sing, *Pure Appl. Chem.* **2015**, *87*, 1051–1069.

[156] P. Taheri, J. C. Lang, J. Kenvin, P. Kroll, *Phys. Chem. Chem. Phys.* **2021**, *23*, 5422–5430.

[157] Y. Qiu, H. Yang, B. Wen, L. Ma, Y. Lin, *J. Colloid Interface Sci.* **2021**, *590*, 561–570.

[158] S. J. L. Billinge, *Philos. Trans. R. Soc. A* **2019**, *377*, 20180413.

[159] W. H. Jørgensen, H. Toftlund, T. E. Warner, *Hydrometallurgy* **2012**, *115–116*, 98–103.

[160] C. E. Mitchell, D. Santos-Carballal, A. M. Beale, W. Jones, D. J. Morgan, M. Sankar, N. H. de Leeuw, *Faraday Discuss.* **2021**, *230*, 30–51.

[161] L. An, Z. Zhang, J. Feng, F. Lv, Y. Li, R. Wang, M. Lu, R. B. Gupta, P. Xi, S. Zhang, *J. Am. Chem. Soc.* **2018**, *140*, 17624–17631.

5. Danksagung

Ich möchte zunächst meinem Doktorvater Prof. Dr. Roland Marschall herzlich für die Chance danken, verschiedene Forschungsmodule, Abschlussarbeiten und meine Promotion in seiner Arbeitsgruppe auf den Gebieten Festkörperchemie und heterogene Elektro- beziehungsweise Photokatalyse absolvieren zu dürfen. Vielen Dank auch für die Übernahme der Betreuung während der Promotion. Die wissenschaftliche und persönliche Unterstützung während der gesamten Promotionszeit war mir stets eine große Stütze. Ich konnte während der Promotion viel dazu lernen, was ich größtenteils dir zu verdanken habe. Ich bedanke mich zudem für die Möglichkeit, einige nationale sowie internationale Konferenzen zu besuchen und an der Messzeit am Synchroton *Diamond Light Source* in England teilzunehmen. Besonders hervorheben möchte ich auch die gute Arbeitsatmosphäre, die in der AG Marschall herrscht. Die vielen gemeinsamen Aktivitäten werden in besonderer Erinnerung bleiben, wie zum Beispiel das gemeinsame Eislaufen oder auch unser LaserTech-Abend.

Entsprechend möchte ich allen ehemaligen und aktuellen Mitgliedern der AG Marschall danken. Es war wirklich eine schöne Zeit mit euch! Ich danke Jana Timm, insbesondere für die Physisorptionsmessungen, aber auch für die stetige persönliche Unterstützung während meiner Promotion. Mein Dank gilt André Bloesser für die unzähligen Diskussionen über die Eisenspinelle und die Ratschläge, wenn Mikrowelle oder Glovebox wieder mal streikten. Ich danke Morten Weiss insbesondere für die Hilfe bei der Rietveld-Auswertung und für die zahlreichen XPS-Messungen. Anja Hofmann danke ich ebenfalls für die Unterstützung während der Promotionszeit. Ich möchte ferner Judith Zander für die fruchtbare Zusammenarbeit auf dem Gebiet der elektrochemischen Reduktion von CO_2 danken. Bei Michael Furtmair bedanke ich mich für die abendlichen Biergarten-Ausflüge, wo es oftmals auch um private Themen ging. Herzlichen Dank auch nochmal für das ausführliche Fehlerlesen meiner Dissertation an Jana, Morten, Judith, Anja, Yolanda Kleiner (CMBlu Energy AG) und Clarissa Glaser (Justus-Liebig-Universität Giessen).

Die Betreuung von Studierenden während der Promotion hat mir stets viel Freude bereit. Erwähnen möchte ich Paula Wolf und Judith, da beide mehrwöchige Forschungspraktika unter meiner Betreuung absolviert haben. Mein Dank gilt allen, die in meinem Auftrag Messungen durchgeführt haben. Stellvertretend möchte ich an dieser Stelle Dr. Hannah Kurz (Universität Bayreuth, AG Weber) und Lena Geiling (Universität Bayreuth, AG Roth) nennen und mich für die Magnetmessungen beziehungsweise Experimente mit der TGA-MS bedanken!

Für die Finanzierung meiner Promotion bedanke ich mich bei der Deutschen Forschungsgemeinschaft (DFG). Meinen Bochumer Projektpartnern im Rahmen des DFG-Projekts MA 5392/7-1 *Electro- and Photocatalytic CO_2 Reduction with [FeNi]-Chalcogenides* David Tetzlaff, Mohamed Barakat Zakaria und Prof. Dr. Ulf-Peter Apfel danke ich für die stets fruchtbare Zusammenarbeit, was vier gemeinsame Paper eindrucksvoll unterstreichen.

Ich möchte meinen Eltern Reiner und Claudia, meiner Schwester Lea und meinen Großeltern Karl-Heinz und Irmgard für die durchgehende und vollumfängliche Unterstützung danken, insbesondere während meiner Promotionszeit, die ich fernab der Heimat absolviert habe. Eure Besuche in Bayreuth haben immer viel Spaß gemacht und haben mich stets motiviert. Abschließend gilt mein Dank meiner Freundin Clarissa. Trotz der Fernbeziehung hast du mich immer bedingungslos unterstützt und mir Rückhalt gegeben. Wir haben es trotz steigender Spritpreise ja auch meistens geschafft, uns alle zwei Wochen zu sehen.

Ich bedanke mich zuletzt bei den Mitgliedern des Prüfungsausschusses: Prof. Dr. Roland Marschall (Gutachter), Prof. Dr. Birgit Weber (Gutachterin), Prof. Dr. Matthias Breuning (Vorsitz) und Jun.-Prof. Dr. Anna Schenk.
Mein Dank gilt natürlich auch allen, die an der Stelle vergessen wurden.

6. Beiträge und Teilnahmen

Beiträge in Zeitschriften

- C. Simon, J. Timm, D. Tetzlaff, J. Jungmann, U.-P. Apfel, R. Marschall, *ChemElectroChem* **2021**, *8*, 227-239.
- C. Simon, M. B. Zakaria, H. Kurz, D. Tetzlaff, A. Blösser, M. Weiss, J. Timm, B. Weber, U.-P. Apfel, R. Marschall, *Chem. Eur. J.* **2021**, *27*, 16990-17001.
- C. Simon, A. Blösser, M. Eckardt, H. Kurz, B. Weber, M. Zobel, R. Marschall, *Z. Anorg. Allg. Chem.* **2021**, 647, 2061-2072.
- C, Simon, J. Zander, T. Kottakkat, M. Weiss, J. Timm, C. Roth, R. Marschall, *ACS Appl. Energy Mater.* **2021**, *4*, 8702-8708.
- D. Tetzlaff, C. Simon, D. S. Achilleos, M. Smialkowski, K. junge Puring, A. Bloesser, S. Piontek, H. Kasap, D. Siegmund, E. Reisner, R. Marschall, U.-P. Apfel, *Faraday Discuss.* **2019**, *215*, 216-226.
- R. A. Henning, P. Uredat, C. Simon, A. Bloesser, P. Cop, M. T. Elm, R. Marschall, *J. Phys. Chem. C* **2019**, *123*, 18240-18247.
- A. Blößer, H. Kurz, J. Timm, F. Wittkamp, C. Simon, S. Hayama, B. Weber, U.-P. Apfel, R. Marschall, *ACS Appl. Nano. Mater.* **2020**, *3*, 11587-11599.
- D. Tetzlaff, V. Alagarasan, C. Simon, D. Siegmund, K. junge Puring, R. Marschall, U.-P. Apfel, *Energies* **2022**, *15*, 543.

Die vorliegende kumulative Dissertation basiert auf den vier erstgenannten Beiträgen in dieser Liste.

Teilnahmen an Konferenzen

- 19th International Symposium on the Reactivity of Solids, 15.-18.07.2018, Universität Bayreuth
- 31. Deutsche-Zeolith-Tagung, 06.-08.03.2019, Technische Universität Dresden

  C. Simon, R. Marschall, *Preparation of mesoporous nickel ferrite ($NiFe_2O_4$) via soft templating for application in photocatalysis* (Posterbeitrag)
- Bunsen-Tagung 2019, 30.05.-01.06.2019, Friedrich-Schiller-Universität Jena

  C. Simon, J. Timm, R. Marschall, *Preparation of mesoporous nickel ferrite ($NiFe_2O_4$) via soft-templating for application in photocatalysis* (Posterbeitrag)
- 7th International Conference on Semiconductor Photochemistry, 11.-14.09.2019, Universität Mailand

  D. Tetzlaff, C. Simon, D. S. Achilleos, M. Smialkowski, K. junge Puring, A. Bloesser, S. Piontek, H. Kasap, D. Siegmund, E. Reisner, R. Marschall, U.-P. Apfel, *Fe/Ni sulphide photocatalysts for solar-driven hydrogen production?* (Posterbeitrag)
- Electrochemistry Undercover 2020, 23.-24.09.2020, Onlineevent

  C. Simon, J. Timm, D. Tetzlaff, J. Jungmann, U.-P. Apfel, R. Marschall, *Accessible surface area determining the electrocatalytic water oxidation activity of mesoporous $NiFe_2O_4$* (Posterbeitrag)

- Inaugural CataLight Young Scientist Symposium on Light-Driven Catalysis, 10.-26.11.2020, Onlineevent
- 32. Deutsche-Zeolith-Tagung, 10.-11.03.2021, Onlineevent
- International solar fuels conference 2021, 26.-29.07.2021, Onlineevent

Teilnahmen an Workshops und Messzeiten

- PerkinElmer HPUV Anwenderseminar, 23.10.2019, Rodgau
- Besuch am Diamond Light Source, 25.-29.11.2019, Chilton, Vereinigtes Königreich
- Mitbetreuung des C#NaT-Programms der Universität Bayreuth im WS2019/20, 10.03.2020, Bayreuth

7. (Eidesstaatliche) Versicherungen und Erklärungen

Gemäß der Promotionsordnung für die Bayreuther Graduiertenschule für Mathematik und Naturwissenschaften (BayNAT) vom 25. Januar 2021

(§9 Satz 2 Nr. 3 PromO BayNAT)
Hiermit versichere ich eidesstattlich, dass ich die Arbeit selbstständig verfasst und keine anderen als die von mir angegebenen Quellen und Hilfsmittel benutzt habe (vgl. Art. 64 Abs. 1 Satz 6 BayHSchG).

(§9 Satz 2 Nr. 3 PromO BayNAT)
Hiermit erkläre ich, dass ich die Dissertation nicht bereits zur Erlangung eines akademischen Grades eingereicht habe und dass ich nicht bereits diese oder eine gleichartige Doktorprüfung endgültig nicht bestanden habe.

(§9 Satz 2 Nr. 4 PromO BayNAT)
Hiermit erkläre ich, dass ich Hilfe von gewerblichen Promotionsberatern bzw. -vermittlern oder ähnlichen Dienstleistern weder bisher in Anspruch genommen habe noch künftig in Anspruch nehmen werde.

(§9 Satz 2 Nr. 7 PromO BayNAT)
Hiermit erkläre ich mein Einverständnis, dass die elektronische Fassung meiner Dissertation unter Wahrung meiner Urheberrechte und des Datenschutzes einer gesonderten Überprüfung unterzogen werden kann.

(§9 Satz 2 Nr. 8 PromO BayNAT)
Hiermit erkläre ich mein Einverständnis, dass bei Verdacht wissenschaftlichen Fehlverhaltens Ermittlungen durch universitätsinterne Organe der wissenschaftlichen Selbstkontrolle stattfinden können.

……
Ort, Datum, Unterschrift